Aerodynamic Performance of Turbine Rim Sealing Flows

Anna Bru Revert

St Anne's College

Department of Engineering Science

University of Oxford

A thesis submitted in partial fulfilment of the requirements of the degree of

Doctor of Philosophy at the University of Oxford

Trinity Term 2020

Acknowledgments

First of all, I would like to thank everyone who has contributed to making this thesis possible with their professional, technical and personal support. To all of those who have stayed by my side from the beginning, joined halfway through my journey or have only been part of this recently.

I would like to thank EPSRC, industry sponsors and universities for setting up the CDT in Gas Turbine Aerodynamics that I have been lucky to be part of. This adventure would have never taken place without the trust of Kam Chana who gave me the opportunity to undertake this research. The contribution of Paul Beard assisting and closely monitoring my work has been invaluable and I am very much in debt. In addition, I would like to acknowledge the support provided by the collaborators of the project, John Chew, Feng Gao and Donato Palermo from the University of Surrey and Sebastiaan Bottenheim and Peter Smout from Rolls-Royce plc. Thank you very much for contributing with your insight, guidance and expertise.

Special mention to the wonderful people who have been part of my life in Oxford, the Osney boyz who have been by my side supporting me through the ups and downs. To the CDT people and to the Oxford crew who have shared this growing process with me. To Mike, Amir, Alex and Francesco who welcomed me with open arms and left a big void in my life when they moved on. To Mathias, willing to go the extra dance for me and to Laura and Bea for the peer pressure outside of the lab with the funniest workouts.

The assistance of all the staff at the Oxford Thermofluids Institute has made this research a reality, from the admin staff and technicians to the students and other academics, thanks to everyone. Thanks to Paul Cox and the maintenance team for their always prompt response to urgent requests. The help of Greg King, Dave O'Dell and the entire workshop is greatly acknowledged. In particular I would like to thank the technical (but also personal) support of James Carter setting up the facility and Sunny Chana with the long hours in the control room.

Last but not least, I must acknowledge my support net away from Oxford. To my person Mariadel, unconditional ally who has always been by my side making me laugh in the worst moments, you taught me the meaning of true selfless friendship. To Eleni, always ready to go on our next trip and keeping the spirits high from our preferred handball position. To Laura, my patient link with my origins and to my people in Agullent for not giving up on me. None of this would have happened without the backing of my relatives who believed in me when not even I did. Thanks for always being ready to jump on a plane to come for a visit, for the unconditional love and support, but most importantly the unlimited patience and understanding. I cannot be prouder and more thankful of the extremely caring, kind, selfless, loving and supporting big family I had the luck to grow up in. Thanks to every single member of the families Revert-Tarrega and Valles-Bru for always being there for me.

The most special of all of the acknowledgments to my parents for giving me everything in life, for always encouraging me to pursue my ambitions and relentlessly supporting me. To my siblings Jordi and Laia, their love and admiration have been the motivation that has kept me going these years. Thanks for bringing light to my life in the darkest times and for encouraging me to never give up. This degree is as much yours as it is mine.

Abstract

An investigation of the hot gas ingestion phenomenon in the Oxford Rotor Facility examined rotor disc rotation, mainstream pressure asymmetries and unsteady structures in the cavity as main drivers. The facility underwent major modifications to allow different annulus flow configurations, higher resolution in the low and high bandwidth pressure instrumentation and the installation of a new system to quantify the sealing effectiveness using the tracer gas technique (± 0.0068 uncertainty). Rotationally-driven ingestion was simulated with a bladeless annulus and conditions of pressure-driven ingestion with nozzle guide vanes. By decoupling each contribution, the fundamentals of hot gas ingestion are addressed. A chute rim seal arrangement has been studied with two gap sizes. The influence of non-dimensional purge flow, C_{w}, rotational Reynolds number, Re_{ϕ}, axial Reynolds number, $\mathrm{Re}_{\mathrm{ax}}$, and seal clearance, s_c, has been examined through the mean cavity pressure coefficient, C_{p}, sealing effectiveness, ε, and frequency spectra of the unsteady pressure signals. The maximum Re_{ϕ} was 3.3×10^6 with a flow coefficient of 0.45 with NGVs. The mean pressure field in the cavity revealed the existence of two vortices. Values of sealing effectiveness showed good agreement with the disc pumping orifice model at low flow coefficients, suggesting operation in the rotationally-induced regime. This finding challenges the extended assumption that pressure-driven ingestion dominates when asymmetries exist in the annulus. However, this hypothesis matched the experimental data at high flow coefficients. The frequency spectra of the high bandwidth pressure signals revealed two sources of unsteadiness in the rim seal region: the large-scale flow features due to rotation of the disc and the interaction between the annulus and purge flows.

Contents

Acknowledgments **i**

Abstract **iii**

List of Figures **viii**

List of Tables **xvi**

1 Introduction **2**

1.1 Background 2

1.2 Motivation 6

1.3 Objectives 7

1.4 Research approach 8

1.5 Thesis structure 10

2 Literature review **12**

2.1 Hot gas ingestion 13

2.1.1 Cavity flow physics 13

2.2 Historic overview 17

2.3 Rotationally-induced ingestion 20

2.4 Externally-induced ingestion 24

2.5 Rim seal instabilities in ingestion 29

2.5.1 Early research 30

2.5.2 Rim seal instabilities . . . 32
2.5.3 Limitations in numerical modelling . . . 36
2.5.4 Source of unsteadiness . . . 37
2.6 Spoiling effect on turbine aerodynamics . . . 40
2.7 Other studies . . . 41
2.8 Summary . . . 43

3 Experimental method 44
3.1 The Oxford Rotor Facility . . . 44
3.1.1 Original ORF design . . . 44
3.1.2 ORF for secondary air systems research . . . 47
3.1.3 Modifications to the ORF . . . 48
3.2 Instrumentation set up . . . 64
3.2.1 Low bandwidth data . . . 65
3.2.2 Sealing effectiveness data . . . 72
3.2.3 High bandwidth data . . . 86
3.2.4 Data acquisition system . . . 89
3.3 Summary . . . 92

4 Rotationally-induced ingestion 93
4.1 Test matrix . . . 94
4.2 Mean cavity flow . . . 95
4.2.1 Validation of new working section . . . 95
4.2.2 Steady cavity flow behaviour . . . 97
4.3 Sealing performance . . . 100
4.3.1 Disc pumping results . . . 100
4.3.2 Effect of mainstream annulus flow . . . 102
4.3.3 Effect of rotor disc speed . . . 103
4.3.4 Effect of seal clearance . . . 105

4.3.5 Effect of purge flow . . . 106
4.4 Summary . . . 110

5 Externally-induced ingestion 112
5.1 Test matrix . . . 113
5.2 Mean flow structure . . . 114
5.2.1 Annulus pressure asymmetry . . . 114
5.2.2 Steady cavity flow behaviour . . . 117
5.3 Sealing performance . . . 121
5.3.1 Effect of mainstream flow conditions . . . 121
5.3.2 Overall sealing effectiveness dependencies . . . 125
5.3.3 Comparison to previous work . . . 132
5.3.4 Effect of relative position to NGV trailing edge . . . 134
5.4 Spoiling effect on the mainstream aerodynamics . . . 136
5.5 Summary . . . 139

6 Unsteady rim seal flow structures 142
6.1 Test matrix . . . 143
6.2 Methodology . . . 144
6.3 Cavity flow structure . . . 148
6.3.1 Validation of new working section . . . 149
6.3.2 Unsteady cavity flow behaviour . . . 151
6.3.3 Phase analysis . . . 171
6.4 Summary . . . 177

7 Conclusions 180
7.1 Experimental method . . . 180
7.2 Rotationally-induced ingestion . . . 181
7.3 Externally-induced ingestion . . . 182
7.4 Unsteady rim seal flow structures . . . 183

7.5 Future research studies 185
7.6 Research impact 188

Appendix A **190**

Bibliography **202**

List of Figures

1.1 Secondary air system paths. 3

1.2 Breakout of the gas turbine engine components and highlight of the high pressure turbine and secondary air system interface in the turbine rim seal region. 5

1.3 Relationship between component life and temperature [3]. 5

1.4 Research approach. 9

2.1 Cavity flow behaviour in rotating cavity with (a) only egress, (b) simultaneous ingress and egress. 16

2.2 Examples of rim seal geometrical arrangements [4]. 18

2.3 Driving mechanisms of rim seal ingestion. 19

2.4 Disc pumping effect as the driving mechanism of rim seal ingestion. 21

2.5 Circumferential pressure asymmetries as the driving mechanism of ingestion. 25

2.6 Rim seal instabilities (depicted as inertial waves) as the driving mechanism of hot gas ingestion. 30

2.7 Contours of velocity inside the cavity showing rim seal instabilities, Cao *et al.* [15] (left) and rotor-stator cavity modes from Jakoby *et al.* [45] (right). 32

2.8 Development of Kelvin-Helmholtz instabilities. 38

2.9 Inertial waves representation [20]. 39

3.1 Schematic of the Oxford Rotor Facility. 45

3.2 Photograph of the Oxford Rotor Facility in the Oxford Thermofluids Institute. 46
3.3 Basic design sketch for 1D calculations. 51
3.4 Examples of geometries investigated for the reduced annulus with velocity contours for each one. 54
3.5 Domain geometry of the 2D models with original and reduced annulus casing lines with zoomed view of the axial velocity distributions at the rim seal. 55
3.6 Longitudinal cross section of the CAD model. 56
3.7 (a)Details of the working section geometry and purge flow supply, (b) details of the rim seal geometry (mm), (c) relevant dimensions for the small gap size, $s_c = 0.0042$, and (d) relevant dimensions for the large gap size, $s_c = 0.0078$. 58
3.8 Schematic of the mainstream and purge air feed system for (a) $\mathrm{Re_{ax}} = 0$ (Stage 1) and (b) $\mathrm{Re_{ax}} = 2.6 \times 10^5$ (Stages 2 and 3). 60
3.9 (a) Pressure reducing valve and flow limiter assembly, (b) feed distributor plate and (c) feed distributor assembly in the ORF. 61
3.10 (a) Operation principle of the flow limiter and pressure regulator and (b) typical air feed system pressures and mass flows. 61
3.11 Photographs of (a) SLA NGVs, (b) assembly of NGVs in casing mounting ring with static pressure tappings visible and (c) casing mounting ring. . . 64
3.12 (a) Pressure and temperature instrumentation in the main gas path, feed and inner cavities and (b) view of the casing wall circumferential points for axisymmetric and non-axisymmetric annulus flow configurations above the rim seal. 66
3.13 Typical upstream pressures ensuring axisymmetric flow in the annulus. . . 67
3.14 Pressure instrumentation in the stator ring. 68
3.15 Dispersive (left) and non-dispersive (right) infrared technology operation. . 73

3.16 ORF sealing effectiveness measurement system for high purge flow rates. . 76
3.17 View of the ORF equipment distribution. 77
3.18 Gas analyser software interface. 79
3.19 Example of the gas analyser calibration curve. 80
3.20 Response of the gas analyser for different dwell times. 81
3.21 (a) Position of the circumferentially-distributed cavity pressure tappings and (b) relative position of the cavity measurement points respect to the NGVs. 83
3.22 (a) CAD view of the annulus measurement probe assembly and (b) downstream view of the annulus measurement probe installed in the ORF. . . . 85
3.23 High bandwidth pressure measurements distribution in the NGV ring. . . . 87
3.24 DAQ cabinet. 90
3.25 Instrumentation systems. 91

4.1 Disc pumping effect as the driving mechanism of rim seal ingestion. 93
4.2 Radial distribution of the mean pressure coefficient in the rim seal and stator-rotor cavity for $C_{\mathrm{w}} = 0$, $s_c = 0.0042$ and $\mathrm{Re}_\phi = 3 \times 10^6$. 96
4.3 Effect of purge flow, C_{w}, and rotor disc speed, Re_ϕ, in the radial distribution of the mean pressure coefficient in the rim seal cavity for $s_c = 0.0042$: (a) $\mathrm{Re}_{\mathrm{ax}} = 0$ and (b) $\mathrm{Re}_{\mathrm{ax}} = 2.6 \times 10^5$. 98
4.4 Effect of the external flow, Re_ϕ and s_c in the mean pressure coefficient at the rim, $r/b = 0.99$, correlated against the turbulent flow parameter. . . . 99
4.5 (a) Comparison of the sealing effectiveness of different seal geometries against non-dimensional flow ratio at $r/b = 0.96$ and (b) effect of the annulus flow in the sealing effectiveness as a function of $U_{\mathrm{m}}/(\Omega b)$ at $r/b = 0.96$ for two different gap sizes. 101

4.6 Radial distribution of sealing effectiveness and pressure coefficient inside the cavity in absence of annulus flow at different rotational Reynolds numbers for a gap size of $s_c = 0.0078$ at $C_{\mathrm{w}} = 830$ (left) and $C_{\mathrm{w}} = 7400$ (right). 104

4.7 Sealing effectiveness as a function of the non-dimensional flow ratio at $r/b = 0.96$ for $s_c = 0.0078$ (a) in absence of annulus flow, $\mathrm{Re}_{\mathrm{ax}} = 0$, and (b) with axial axisymmetric annulus flow, $\mathrm{Re}_{\mathrm{ax}} = 2.6 \times 10^5$. 105

4.8 Effect of the purge flow on the sealing effectiveness radial distribution at $\mathrm{Re}_\phi = 1.5 \times 10^6$ without and with annulus flow for: (a) $s_c = 0.0042$ and (b) $s_c = 0.0078$. 107

4.9 Effect of the axial annulus flow on the sealing effectiveness and cavity pressure difference as a function of the purge supply at $\mathrm{Re}_\phi = 1.5 \times 10^6$ (left) and $\mathrm{Re}_\phi = 2.7 \times 10^6$ (right) measured at $r/b = 0.99$ and $s_c = 0.0078$. 108

5.1 Circumferential pressure asymmetries as the driving mechanism of ingestion. 112

5.2 Effect of Re_ϕ on $C_{\mathrm{p},\theta}$ over one NGV pitch for $s_c = 0.0042$ and $U_{\mathrm{m}}/U_{\mathrm{ax}} = 0.11$ with $C_{\mathrm{p},\theta}$ referenced to the annulus flow (left) and the rotor disc speed (right). 115

5.3 Effect of purge flow, $U_{\mathrm{m}}/(\Omega b)$, on $C_{\mathrm{p},\theta\mathrm{disc}}$ over one NGV pitch for $s_c = 0.0042$ at $U_{\mathrm{ax}}/(\Omega b) = 1.01$ (left) and $U_{\mathrm{ax}}/(\Omega b) = 0.45$ (right). 116

5.4 Effect of purge flow, $U_{\mathrm{m}}/(\Omega b)$, on the peak-to-peak circumferential pressure coefficient difference $\Delta C_{\mathrm{p},\theta\mathrm{disc}}$ for $s_c = 0.0042$ at (a) $U_{\mathrm{ax}}/(\Omega b) = 1.01$ and (b) $U_{\mathrm{ax}}/(\Omega b) = 0.45$. 116

5.5 Radial profile of C_{p} inside the cavity without annulus flow, with axisymmetric and with non-axisymmetric annulus flow for $s_c = 0.0042$, $U_{\mathrm{m}}/U_{\mathrm{ax}} = 0.08$ at $U_{\mathrm{m}}/(\Omega b) = 0.09$ ($\mathrm{Re}_\phi = 1.5 \times 10^6$) on the left and $U_{\mathrm{m}}/(\Omega b) = 0.045$ ($\mathrm{Re}_\phi = 2.9 \times 10^6$) on the right. 118

5.6 Cavity pressure coefficient as a function of λ_{T} for two seal clearances under axisymmetric and non-axisymmetric conditions of external annulus flow. . 119

5.7 Effect of the external flow conditions in the sealing effectiveness radial distribution at $C_w = 3500$ ($U_m/U_{ax} = 0.08$) at $Re_\phi = 1.5 \times 10^6$ and $s_c = 0.0042$. 122

5.8 Effect of flow coefficient and annulus pressure asymmetries at: (a) $C_w = 3500$ ($U_m/U_{ax} = 0.08$) for $s_c = 0.0042$, (b) $C_w = 4800$ ($U_m/U_{ax} = 0.06$) for $s_c = 0.0078$. 123

5.9 Map of sealing effectiveness against non-dimensional purge flow ratio, $U_m/(\Omega b)$, at $r/b = 0.99$ for different seal-to-axial velocity ratios, U_m/U_{ax}, and flow coefficients, $U_{ax}/(\Omega b)$, under axisymmetric and non-axisymmetric external annulus flow. 125

5.10 Effect of flow coefficient on the sealing effectiveness for (a) a radial seal and (b) an axial seal [71]. 127

5.11 Comparison of test conditions of published experimental studies ([29] and [71]) on the influence of the flow coefficient over the sealing performance. . 128

5.12 Map of sealing effectiveness against the seal-to-rotor disc speed velocity ratio, $U_m/(\Omega b)$, under axisymmetric and non-axisymmetric external flow at: (a) $r/b = 0.99$ and $s_c = 0.0042$, (b) $r/b = 0.84$ and $s_c = 0.0042$, (c) $r/b = 0.99$ and $s_c = 0.0078$ and (d) $r/b = 0.84$ and $s_c = 0.0078$. 130

5.13 Comparison of sealing performance of the ORF chute seal under different external flow conditions at $r/b = 0.96$ against the chute seal from Horwood *et al.* [53] and the disc pumping correlation from Chew [25]. 132

5.14 Comparison of experimental data against prediction from [30] and [25]. . . 134

5.15 Comparison of the sealing effectiveness radial profiles in configuration of Stage 3 for two different circumferential locations $\Delta\theta_{NGV} = -4°$ and $\Delta\theta_{NGV} = +1°$ at $U_m/U_{ax} = 0.08$ and $s_c = 0.0042$. 135

5.16 Radial profiles of repeat tests for cavity points at $\Delta\theta_{NGV} = +1°$ taken at $U_m/U_{ax} = 0.08$ and $s_c = 0.0042$. 136

5.17 Influence of flow coefficient, radial position and purge-to-annulus flow rate on the circumferential variation of sealing effectiveness in the main gas path. 137

5.18 Distribution of ε in a traverse plane in the main gas path downstream of the NGVs for two flow coefficients and two ratios of purge-to-mainstream mass flow. 138

6.1 Unsteady rim seal flow structures as the driving mechanism of ingestion. . 142

6.2 Schematic of the rotating cavity flow structure [59]. 145

6.3 Example of histogram (a) with a dominant time lag and (b) with large spread. 146

6.4 Summary plot for $s_c = 1$ mm, $\mathrm{Re}_\phi = 3 \times 10^6$ and $C_\mathrm{w} = 3400$ [19]. 147

6.5 Frequency spectra of the unsteady pressure signals at three radial positions inside the cavity ($r/b = 0.95, 0.97, 0.99$) across test campaigns at $C_\mathrm{w} = 3500$ and $\mathrm{Re}_\phi = 3 \times 10^6$ in the full annulus configuration with bolts (top) and in the reduced annulus without bolts (bottom). 149

6.6 Peak amplitude of the distinct cavity frequency against radial position within the cavity at $C_w = 3400$ and $\mathrm{Re}_\phi = 3 \times 10^6$ for $s_c = 0.0042$ in absence of external flow. 150

6.7 Mean pressure coefficient radial distribution obtained in the steady and unsteady runs at $U_\mathrm{m}/(\Omega b) = 0.04$ and $s_c = 0.0042$ for: (a) no external annulus flow, (b) axial axisymmetric annulus flow and (c) non-axisymmetric annulus flow. 152

6.8 Frequency spectra in absence of external flow at different radial positions inside the cavity at (a) $U_\mathrm{m}/(\Omega b) = 0.037$, $s_c = 0.0042$ and (b) $U_\mathrm{m}/(\Omega b) = 0.036$, $s_c = 0.0078$. 153

6.9 Effect of the purge supply on the frequency spectra at $r/b = 0.95$ in absence of external annulus flow for constant $\mathrm{Re}_\phi = 3 \times 10^6$, $s_c = 0.0042$. 157

6.10 Effect of the rotational Reynolds number on the frequency spectra for constant $C_w = 3500$ at $r/b = 0.95$, $s_c = 0.0042$ in absence of external annulus flow. 158

6.11 Non-dimensional pressure and frequency of the distinct peak for different rotational Reynolds numbers and $U_m/(\Omega b)$ in absence of annulus flow at two gap sizes (a) $s_c = 0.0042$ and (b) $s_c = 0.0078$. 160

6.12 Effect of the purge supply on the frequency spectra at $r/b = 0.95$ with external axisymmetric flow at $\mathrm{Re}_\phi = 3.1 \times 10^6$, $s_c = 0.0078$. 161

6.13 Effect of the rotational Reynolds number on the frequency spectra for constant $C_w = 3500$ at $r/b = 0.95$, $s_c = 0.0042$ in absence of external annulus flow, under an axisymmetric annulus flow and under non-axisymmetric annulus flow. 163

6.14 Frequency spectra for constant $C_w = 3500$, $\mathrm{Re}_\phi = 3 \times 10^6$ at $r/b = 0.95$, $s_c = 0.0042$ in absence of external annulus flow, under an axisymmetric annulus flow and under non-axisymmetric annulus flow. 165

6.15 Effect of the external annulus flow conditions on the frequency spectra for constant $C_w = 3500$ and $s_c = 0.0042$ at (a) $U_{ax}/(\Omega b) = 1.05$ and (b) $U_{ax}/(\Omega b) = 0.45$. 167

6.16 Effect of the circumferential position on the the frequency spectra for constant $C_w = 3500$, $s_c = 0.0042$ in absence of external annulus flow. 170

6.17 (a) Example of an unfiltered (top) and filtered (bottom) FFT case and (b) model cross-correlation distribution for $\alpha = 10°$. 172

6.18 Summary plots of cross-correlation results for $C_w = 3500$ in absence of external flow at (a) $\mathrm{Re}_\phi = 1.5 \times 10^6$ and $s_c = 0.0042$, (b) $\mathrm{Re}_\phi = 3 \times 10^6$ and $s_c = 0.0042$, (c) $\mathrm{Re}_\phi = 1.5 \times 10^6$ and $s_c = 0.0078$ and (d) $\mathrm{Re}_\phi = 3 \times 10^6$ and $s_c = 0.0078$. 173

6.19 Summary plots of cross-correlation results at $\mathrm{Re}_\phi = 3\times10^6$ and $s_c = 0.0042$ in (a) axisymmetric annulus flow at $C_\mathrm{w} = 3800$, (b) axisymmetric annulus flow at $C_\mathrm{w} = 31800$, (c) non-axisymmetric annulus flow at $C_\mathrm{w} = 3800$ and (d) non-axisymmetric annulus flow at $C_\mathrm{w} = 20800$. 175

List of Tables

3.1 Original Oxford Rotor Facility operating conditions [73]. 46

3.2 Oxford Rotor Facility operating conditions at the NGV hub exit [73]. . . . 48

3.3 List of modified components in the ORF shown in Fig.3.6. 57

3.4 Purge flow nozzle diameter for axisymmetric annulus flow (Stage 2). 63

3.5 Purge flow nozzle diameter for non-axisymmetric annulus flow (Stage 3). . 63

3.6 Summary of steady pressure measurements in the cavity. 69

3.7 Summary of steady pressure measurements. 70

3.8 Summary of temperature measurements. 71

3.9 Sample values from the gas analyser calibration. 80

3.10 Summary of concentration measurement data points in the second stator ring. 84

3.11 Summary of concentration measurement points in the annulus traverse. . . 86

3.12 Angles resulting of the pairing of any two unsteady pressure sensors. . . . 88

3.13 Summary of unsteady pressure measurements. 88

4.1 Test conditions for experiments under rotationally-induced ingestion. . . . 95

5.1 Experimental test matrix for externally-induced ingestion investigation (*denotes test condition for non-axisymmetric annulus flow only). 113

5.2 Rotational Reynolds number and flow coefficient at tested rotor speeds for experiments with non-axisymmetric annulus flow. 114

List of Tables

6.1 Experimental test matrix for unsteady-induced ingestion investigation (*denotes test condition for non-axisymmetric annulus flow only). 144

6.2 Summary of rotating flow structures. 177

7.1 Design point conditions for uncertainty analysis. 191

7.2 Design point conditions for the cavity pressure coefficient uncertainty analysis. 194

7.3 Bias error of variables for C_{p}. 194

7.4 Precision error of variables for C_{p}. 194

7.5 Uncertainty quantification for the mass flow through Stage 2 nozzles. . . . 196

7.6 Uncertainty quantification for the mass flow through Stage 3 nozzles. . . . 196

7.7 Design point conditions for the C_{w} uncertainty analysis. 197

7.8 Bias error of variables for C_{w}. 197

7.9 Precision error of variables for C_{w}. 198

Nomenclature

Romans

A	area, m^2
b	disc radius, m
B	bias error
c	tracer gas concentration, %
C_{ax}	axial chord, m
C_d	discharge coefficient
C_w	non-dimensional purge flow rate $= \dot{m}/(\mu\, b)$
C_p	cavity pressure coefficient $= (p - p_{1011})/(0.5\rho(\Omega\, b)^2)$
$C_{p,\theta disc}$	circumferential pressure coefficient $= (p_\theta - \bar{p_\theta})/(0.5\,\rho\,(\Omega\, b)^2)$
$C_{p,\theta ann}$	circumferential pressure coefficient $= (p_\theta - \bar{p_\theta})/(0.5\,\rho\,(U_{ann})^2)$
d	diameter, m
dp	differential pressure, Pa
f	frequency, Hz
g	rim seal gap, m
k	empirical constant
L	number of lobes
$\dot{m}$	mass flow rate, kg/s
M	Mach number
N	rotor speed, rpm
p	pressure, Pa
r	radial position, m
Q	example variable
R	gas constant, J/(kg K)
Re_{ax}	axial flow Reynolds number $= \rho\, U_{ax}\, C_{ax}/\mu$
Re_ϕ	rotational Reynolds number $= \rho\,\Omega\, b^2/\mu$
s_c	non-dimensional rim seal clearance $= g/b$
S	precision error
S_{ref}	Sutherland law reference temperature, K
t	time, s
T	temperature, K
U	velocity, m/s
U_m	mean flow velocity through seal in $r - z$ plane $= \dot{m}/(\rho\, 2\pi\, b\, s_c)$
V	voltage, V
Vol	volume, m^3

Greeks

α	angle between pressure probes, $^\circ$
$\alpha_{\mathrm{NGVexit}}$	flow angle at the exit of the NGV, $^\circ$
β	angle between unsteady flow structures, $^\circ$
ε	sealing effectiveness
$\Delta\theta$	relative circumferential position
Δt_α	time lag between two probes, s
Δt_β	time lag between two flow structures, s
γ	ratio of specific heats
λ_{T}	turbulent flow parameter
μ	dynamic viscosity, Pa s
η	thermodynamic efficiency
ρ	fluid density, kg/m^3
Ω	angular speed of rotor disc, rad/s
ω	angular speed of unsteady flow structures, rad/s
Φ	flow ratio
Ψ	flow coefficient
θ	circumferential coordinate, $^\circ$

Subscripts and Superscripts

0	total condition
1	turbine/working section inlet condition
12	rim seal condition
2	turbine inlet condition in reduced annulus
3	turbine inlet condition in plenum
4	turbine exit condition
ann	annulus value
ax	axial component value
dyn	dynamic value
fd	free disc value
max	maximum value
min	minimum value
NGV	nozzle guide vane value
nozzle	nozzle value
p	peak value
purge	purge flow value
rakes	rakes value
ref	reference value
rim	rim value
s	sample value
seal	seal value
stator	stator wall value
throat	throat value
upstream	upstream condition

wall	wall value
θ	circumferential component
$*$	choked condition

Acronyms

1D	one dimensional
2D	two dimensional
AC	alternating current
CAD	computer aided design
CFD	computational fluid dynamics
CI	combined ingestion
CO_2	carbon dioxide
DC	direct current
DAQ	data acquisition
EI	externally-induced ingestion
FFT	fast Fourier transform
FS	full scale
FTIR	Fourier transform infrared
GA	gas analyser
HPT	high pressure turbine
IR	infrared
LES	large eddy simulations
NDIR	non-dispersive infrared
NGV	nozzle guide vane
ORF	Oxford Rotor Facility
PIV	particle image velocimetry
ppm	particles per million
PS	pressure side
RANS	Reynolds-averaged Navier-Stokes
RI	rotationally-induced ingestion
SA	Spallart-Almaras turbulence model
SLA	stereolithography
SS	suction side
URANS	unsteady Reynolds-averaged Navier-Stokes
WMLES	wall-modelled large eddy simulation

Chapter 1

Introduction

The purpose of this chapter is to introduce the problem of hot gas ingestion in gas turbine engines and highlight the relevance of rim sealing flows within the secondary air system. The challenges encountered in current design methods are exposed before defining the motivation to conduct this study. The research goals of this project are listed followed by a detailed description of the research approach established to achieve the objectives.

1.1 Background

In recent years, an increase in transport-related emissions has been registered despite all efforts to reduce the impact over climate change. This is due to the higher volume of transport of which, according to the European Union Aviation and Safety Agency Enviromental Report [1], aviation represents 13.4% (in 2016) of the total. The airflow going through the core of the engine (compressor, combustor and turbine) is referred to as mainstream flow. Historically, the effort of gas turbine designers has primarily focused on improving the gas turbine cycle efficiency with increased pressure ratios and turbine entry temperature in the mainstream. This performance gain led to a reduction in emissions at a cost of more expensive cooling requirements. Moreover, this approach endangers the integrity and life of the turbine components as hot air can penetrate into flow paths which are not protected against the high temperatures of the hot mainstream flow.

In a modern gas turbine, up to 25% of the intake mass flow is channelled through a secondary air system that bypasses the combustion chamber. The secondary air is bled from several points along the compressor stages with various offtakes depending on the air pressure and temperature requirements, see Fig.1.1.

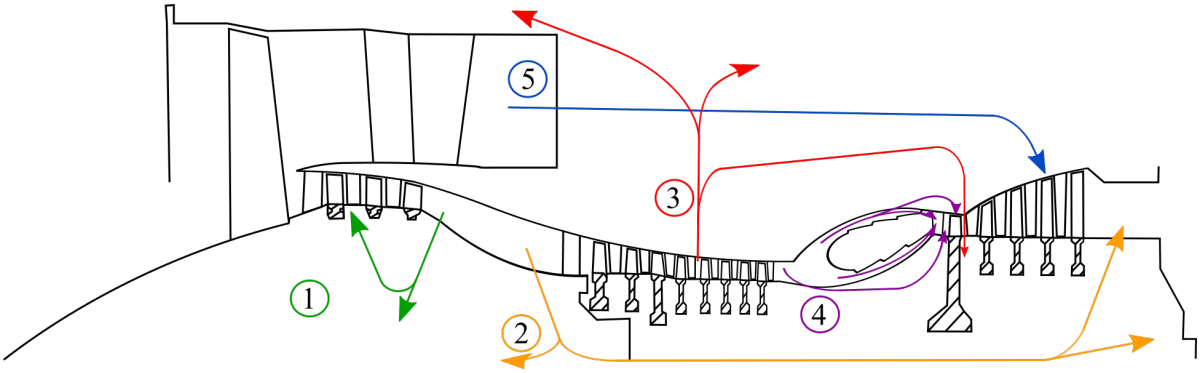

Figure 1.1: Secondary air system paths.

Fig.1.1 provides a clear illustration of the relevance of the secondary air system and its many uses. Air is bled from the low pressure compressor at positions 1 and 2 and is used to cool the low pressure compressor and turbine, pressurise and seal the front and rear bearing chambers and provide further cooling to the high pressure disc drums underneath the hub line. In addition, this air is responsible for balancing the bearing loads of the engine spools and dissipating the heat originating from windage. Air at higher pressure is taken from location 3 to satisfy the more demanding cooling and sealing requirements of the high pressure turbine. A part of this bleed is diverted to cover the demands of the nacelle and wing anti-icing systems as well as the pressurised cabin air. The most expensive flow extracted from station 4 is used for the first high pressure turbine stage cooling and purge. Seals provide rotordynamic stability to the turbomachinery of the gas turbine engine controlling leakages and coolant flows. Most seals and interfaces are passive, but in the high pressure turbine they may also be actively controlled. This is represented by flow path number 5 in Fig.1.1, where some of the bypassed intake flow of the fan is used in the low pressure turbine for active tip clearance control. The air bleed allows the turbine blades to operate in an environment in which the gas temperature is

well above their metal melting temperature with sophisticated cooling technologies. After cooling components and/or purging cavities, the secondary air re-enters the main gas path at various points in the turbine stage thus interacting with the high temperature mainstream flow. Though necessary, the secondary air system infers an efficiency penalty in the thermodynamic cycle that is agravated by the ever more demanding cooling requirements. Firstly, the compressor stages consume power to condition the flow thus any bleeding reduces the amount of fluid available to extract energy from in the operating process. Secondly, it derives in aerodynamic losses from the spoiling effect originated by the mixing of the mainstream and cooling flows in the main gas path. Thus, the amount of coolant air bled from the compressor must be kept to a minimum. Moore [2] estimated that a 1% reduction of the engine bleed can lead to a 0.4% saving in the specific fuel consumption that reflects in a reduction of emissions.

The current research focuses on the study of the interface between the high pressure turbine and the secondary air system, particularly in turbine rim sealing flows. A break-out of the region and the most relevant components are represented in Fig.1.2. A small gap in the turbine annulus hub line is required to allow for the relative movement of the rows of rotating blades and stationary nozzle guide vanes (NGVs). Nonetheless, this consented clearance must be sealed with coolant air to prevent the hot gas exiting the combustor from reaching the stator-rotor disc cavity.

The rotor discs beneath the hub platform are exposed to high mechanical loads but they are not protected against thermal loads (unlike the rotor blades in the main gas path). Failing to seal the cavity volume would extend the need for additional cooling systems to the discs in order to maintain acceptable under-platform and disc metal temperatures. Overheating of the discs and drums could yield to unforeseen mechanical cracks with potential to trigger a catastrophic event. In addition, the operating life and reliability of discs are predicted based on the thermal loading and the flight envelope of the engine.

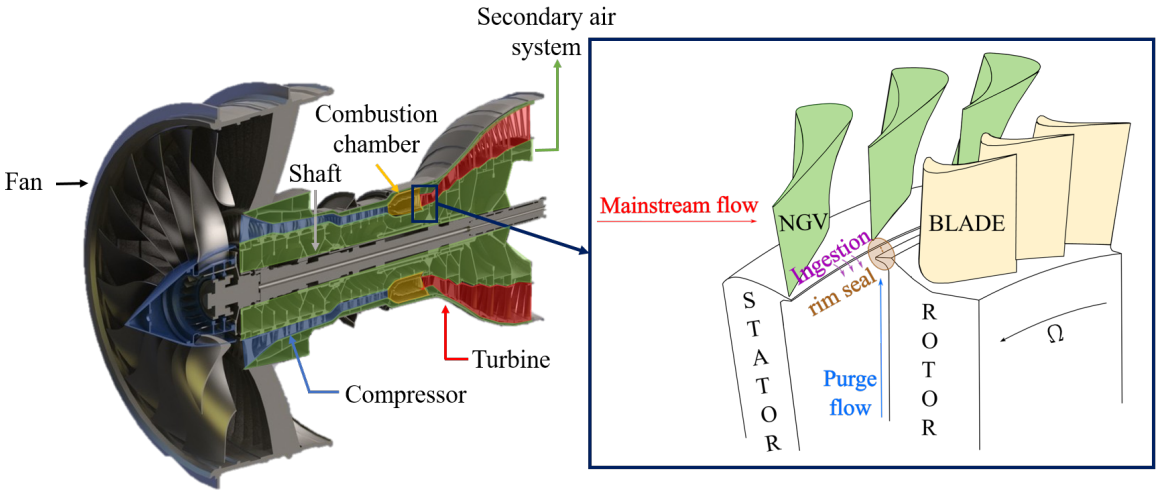

Figure 1.2: Breakout of the gas turbine engine components and highlight of the high pressure turbine and secondary air system interface in the turbine rim seal region.

Service intervals are scheduled considering the cumulative loss of component life, which is closely linked to the operating temperatures, Fig.1.3. Understanding the sealing flow requirements and heat transfer between the purge flow, ingested flow and metal discs is paramount for accurate predictions of the disc loads and component life. Otherwise, shortened inspection intervals would lead to increased maintenance costs. Higher rates of purge through the cavity intensify the cooling effect but they cause a larger penalty on the cycle efficiency. The challenge lays on finding the minimum coolant flow that can guarantee safe temperatures in the cavity walls through prevention of ingress.

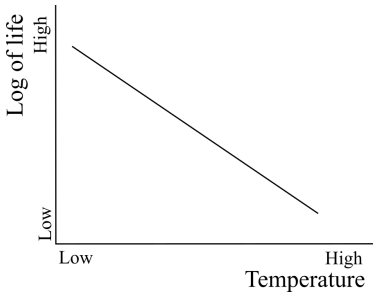

Figure 1.3: Relationship between component life and temperature [3].

The undesirable scenario in which hot air penetrates the cavity is known as hot gas ingestion. To assist the sealing process, engine designers often include a lip at the periphery of the stator disc that protrudes into the gap providing blockage to entrainment of

external flow whilst still allowing the purge flow to be expelled. This feature is referred to as a rim seal and its design is aimed at preventing hot air from being drawn into the cavity whilst minimising the mixing losses with the mainstream flow.

1.2 Motivation

Over the years, turbine rim seals have been designed based on semi-empirical correlations even though some attempts to replace them with numerical simulations have been addressed. Despite these efforts, neither approach seems reliable enough. Numerical predictions have been shown to underpredict the amount of ingested gas whilst the lack of engine-realistic conditions in the experiments questions the extrapolation of the results to real gas turbine engines. Failing to control, or accurately predict, hot gas ingestion can jeopardise the integrity and reliability of the rotating components in the hot section throughout their operating life. The urge for developing an adequate design method highlights the need for more accurate predictive techniques. In order to achieve this, computational simulations or empirical correlations must include the unsteady flow physics affecting the phenomenon of hot gas ingestion under engine-representative conditions.

In recent years, gas turbine designers have gained awareness of the complexity of the secondary air system, the potential performance gains achievable from the optimisation of the secondary air usage and the possibility to reduce the costs inferred from hot gas ingestion (redesign of damaged parts, maintenance and operation). Research on rim sealing flows has been undertaken for decades and several types of simple and complex turbine geometries as well as different configurations of rim seals have been studied under a variety of operating conditions. Yet, the phenomenon of hot gas ingestion is not fully comprehended. As a consequence, interest in improving the understanding of sealing flows has significantly increased both in industry and academia. Considerable resources are being put into researching many aspects of the secondary air system, turbine rim sealing

standing out due to the severity of the potential consequences. Some research groups are conducting more fundamental studies in order to gain insight into the physics and effects over engine performance while others are prioritising the collection of experimental data and validation of numerical models to allow the development of more accurate design tools.

1.3 Objectives

The aim of the research was to investigate the fluid dynamics associated with the sealing of turbine rims. A staged approach was planned in order to decouple the different drivers leading to hot gas ingestion to better comprehend the individual and synergetic effects of the disc pumping effect, the annulus circumferential pressure asymmetries and the unsteady rim seal instabilities.

This project planned to acquire the capability to study the sealing performance of a chute seal in steady state conditions through redesign of the test facility and the installation of a brand new measurement system. Moreover, the modifications to the working section aspired to allow an investigation covering a wide range of operating points at design and off-design conditions to provide high quality experimental data.

The fundamental goal of this project was to identify the unsteady flow structures in the cavity that may exacerbate ingestion in order to improve the comprehension of the underlying physics of the rim seal instabilities. In order to achieve this, high bandwidth instrumentation was installed in the stator cavity wall to characterise the flow structures in detail across a broad range of test conditions.

One of the objectives was also to provide high quality experimental data for use in the development of more accurate design methods and validation of CFD predicting tools.

The outcome of this research was expected to contribute to expand the knowledge of the fluid dynamic phenomena developing in the rim seal region. An improved understanding would directly impact the design of sealing arrangements in the secondary air system inferring a benefit in the engine performance. Ultimately, good quality experimental data could be extrapolated to engine conditions and used as a predictive tool by the engine designer, leading to an optimisation of the sealing and cooling flows. Overall, better usage of the secondary air would yield higher cycle efficiencies which translates into more environmentally-friendly engines.

1.4 Research approach

The investigation conducted for this doctoral thesis proposes an experimental study considering the coupling between the secondary air system (cool sealing flow) and the primary gas path (hot mainstream flow) to understand the underlying physics and characterise the fluid dynamics of turbine rim sealing flows. This study focuses on the inherent unsteadiness of rim seal flows, rather than that imposed by the rotating blades. Therefore, the facility is operated in different configurations to decouple the effect of the pressure asymmetries introduced in the annulus by the existence of vanes and blades from that originated by the sole influence of the rotation of the rotor disc and analyse them separately. To do so, the project followed a staged methodology that gradually built up the complexity of the system, see Fig.1.4.

The first stage of the project was defined by a clean main gas path in which the vanes and blades were removed and no annulus flow was provided. Stage 1 only featured the purge flow and rotor disc rotation. Still with a clean annulus free from any blading, the addition of an axial axisymmetric annulus flow passing through the main gas path determined the beginning of the second stage. Next, the installation of NGVs in the main gas path introduced a swirl component into the mainstream inducing pressure and potential

field asymmetries in a non-axisymmetric annulus flow. The project would have culminated with the addition of the rotor blades in the fourth and last stage, thus representing the most complex scenario with the presence of purge flow, mainstream annulus flow, stator vanes and rotor blades. However, due to the interesting findings obtained during Stage 3 it was decided to investigate further the third configuration instead of progressing to Stage 4.

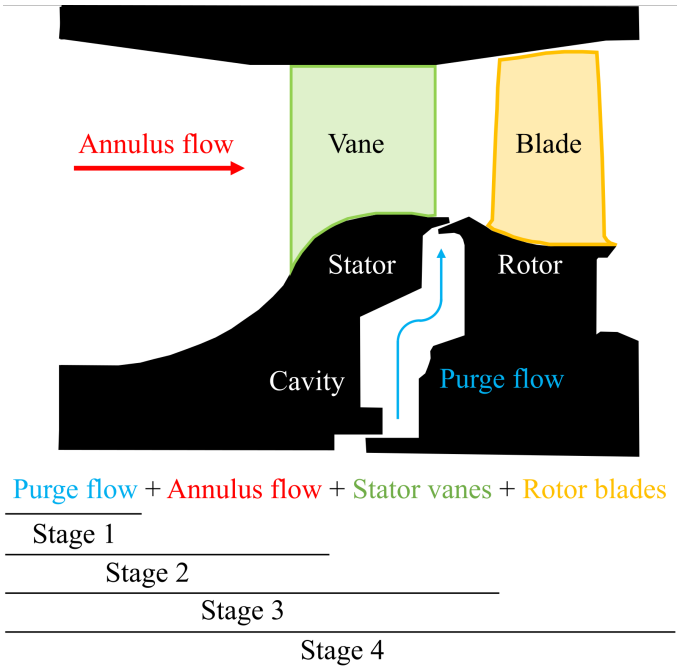

Figure 1.4: Research approach.

The two initial phases simulate the scenario of rotationally-induced ingestion in absence of annulus flow and with an axial mainstream flow. The third stage represents the most complex configuration considered within this research where the pressure asymmetries in the main gas path govern the ingestion of hot gas into the cavity. This scenario is referred to as pressure-driven or externally-driven ingestion.

The project here described covered a range of sealing flow rates and rotational Reynolds numbers with the mainstream flow (when present) scaled to match engine representative conditions of axial Mach number and axial Reynolds number with a full turbine stage. Nonetheless, the engine-realistic environment was not simulated during this research since

these fundamental studies are part of a longer-term campaign. A chute rim seal arrangement with simultaneous radial and axial overlap was investigated as a representative design of modern aero gas turbine engines. Two sizes of seal clearance were studied representing the design operating point and off-design operation. In total, the effects of four main variables were analysed through the non-dimensional purge flow rate, C_{w}, or flow ratio, $U_{\mathrm{m}}/(\Omega b)$, axial Reynolds number, $\mathrm{Re}_{\mathrm{ax}}$, rotational Reynolds number, Re_{ϕ}, and seal clearance, s_c, respectively. Low and high bandwidth pressure sensors were installed in the cavity and a new system to acquire gas concentration data was deployed. The output variables examined to conduct the analysis of the cavity aerodynamics and sealing performance were the mean pressure coefficient, C_{p}, sealing effectiveness, ε, and frequency spectra of the unsteady pressure signals.

1.5 Thesis structure

An overview of the thesis structure is provided in this section. Chapter 2 summarises the most relevant findings in the topic of hot gas ingestion that are available in the open literature. The flow physics behind the phenomenon of hot gas ingestion are described in detail and a breakdown of the main driving mechanisms is included. A review of previous work (numerical and experimental) is also presented.

The experimental set up of the Oxford Rotor Facility (ORF) is described in chapter 3. Modifications to the original test section are detailed here as well as the new air supply system installed. The measurement equipment used during this investigation together with the data acquisition system are also thoroughly covered.

Chapter 4 presents the results obtained during Stage 1 with a clean annulus under purely rotationally-induced ingestion. The pressure and sealing effectiveness data of the baseline test case in absence of annulus flow are compared against the measurements ob-

tained with the second configuration to study how an axial axisymmetric annulus flow affects the mean cavity flow aerodynamics and the sealing performance.

Chapter 5 thoroughly analyses the results for the third stage of the test campaign in which nozzle guide vanes were fitted in the main gas path, therefore featuring non-axisymmetric annulus flow. The experimental results under pressure-driven ingestion are studied in detail and contrasted against those reported in chapter 4. Further discussion is included to help understand the effects of the flow coefficient on the sealing capability of the chute seal.

In chapter 6, the high bandwidth pressure measurements taken in the ORF are analysed in the frequency domain to investigate the presence of large-scale unsteady flow structures rotating inside the cavity. These have been logged and studied in all three annulus configurations. A phase analysis revealed the number and angular speed at which they travel in the cavity.

The conclusions of this research are summarised in chapter 7 followed by a brief suggestion of next steps for potential future research studies.

The output of this investigation has been submitted for publication. The first paper covers the results presented in chapter 4 and it has been accepted at the 18th International Symposium on Transport Phenomena and Dynamics of Rotating Machinery. The second paper, reporting large part of the results discussed in chapter 5, has been accepted for presentation at Turbo Expo 2020. After being peer reviewed, this last paper has been recommended for journal publication.

Chapter 2

Literature review

This chapter reviews the literature available on hot gas ingestion. A thorough description of the flow physics governing the phenomenon is provided. The possible mechanisms that can lead to this outcome are introduced and the most relevant discussed in depth.

Rotating disc systems are found in a wide variety of engineering applications, including turbomachinery. For years, common practice within gas turbine engine designers was to target higher turbine entry temperatures for improved cycle efficiency, translating into a reduction of emissions. This practice poses a technological challenge for the designers of the cooling system as they face more demanding requirements that penalise engine performance. One of the purposes of the secondary air is to seal the space between rotor and stator discs underneath the annulus platform. This stream of cold air is reinserted into the mainstream gas path through the clearance that allows for the relative movement between the rotating and stationary components. Entrainment of the hot gas exiting the combustor into the cavity through this clearance is undesirable. The heavy discs to which the rotor blades are attached withstand high mechanical stresses derived from rotation at high angular speeds. Ingestion of hot air would superpose a thermodynamic load to this already challenging mechanical load that could lead to a catastrophic event. Good understanding of the phenomena of hot gas ingestion is therefore paramount.

2.1 Hot gas ingestion

The foundations of the hot gas ingestion phenomenon are explained in this section. The flow behaviour inside the cavity is described and then the physical principles behind it thoroughly discussed. The different mechanisms that can lead to hot gas ingestion are then briefly exposed before being described in more detail in the following sections.

2.1.1 Cavity flow physics

In rotating systems, the case of a disc which is immersed in a stationary fluid and rotates perpendicular to its axis is known as the free disc. A boundary layer develops on the disc surface and shear transfers angular momentum from the disc to the adjacent fluid which acquires the disc tangential velocity. Away from the disc, in the free stream, the tangential velocity is zero due to the no-slip condition. In a free rotating disc, the viscous forces, through the Reynolds number, define the flow. The radial velocity is zero at the disc surface and in the free stream. Shear between the rotating disc and the surrounding fluid induces a centrifugal force that pumps the flow in the disc boundary layer radially out. Axial flow enters the rotor disc boundary layer to satisfy mass conservation and provide the radially outward flow. This phenomenon is known as the free-disc pumping effect. The flow in the boundary layer may be laminar or turbulent depending on the angular speed of the disc.

In an enclosed stator-rotor system of co-axial discs, this is with a stationary shroud in the periphery of the cavity introduced to prevent ingress, boundary layers are expected to grow on the surface of the stator and the rotor discs. A core of fluid rotating at a fraction of the rotor disc develops in between. For turbulent flow, the fluid core is predicted to rotate at $\sim 40\%\,\Omega$ with Ω being the angular speed of the rotor disc, and $\sim 30\%\,\Omega$ if the flow is laminar [4]. The angular velocity of the rotating fluid core reduces when the separation between the stator and rotor discs is large. Nonetheless, at small gaps

the axial component is suppressed and the tangential velocity is significant, leading to Couette flow. The Coriolis forces that emerge as a consequence of the rotational motion confine the flow towards the boundary layer in the disc surface. Again, friction and the centrifugal force accelerate the fluid in the rotor boundary layer up to the disc speed pumping it radially out. The effect of the centrifugal force over the core fluid is balanced by a radial pressure gradient. Consequence of the radial gradient, the minimum pressure will be found inside of the cavity rising with proximity to the shroud. In the situation where the pressure inside the cavity falls below that in the outside environment, external flow from the surroundings is drawn into the cavity to replenish the volume and satisfy conservation of mass. This phenomenon is referred to as hot gas ingestion. Injecting a radially outwards flow of cooling air between the stator and rotor discs (purge or sealing air) pressurises the volume and discourages the hot mainstream gases from entering the cavity. In the unfavourable scenario in which ingress occurs, the coolant aims to dilute the ingested flow to maintain the temperature of the discs within acceptable limits. Protrusions in the periphery of the cavity shroud are fitted at the rim of either disc to reduce the available clearance and minimise the amount of purge flow required to seal the cavity.

The entrained fluid flows radially inwards in the stator boundary layer after mixing with the sealing flow at the top of the volume. The viscous and turbulent effects can be neglected if sufficient clearance exists between the stationary and rotating walls and the fluid core outside the boundary layers can be considered inviscid [6].

Initially, it was proposed that the flow structure inside the cavity contained fluid from the stator boundary layer that axially migrated through the rotating core, spinning at a fraction of the rotor angular speed, to entrain the rotor disc boundary layer. This flow structure is known as the Batchelor flow. However, a few years later the hypothesis of a non-rotating core was proposed and referred to as Stewartson flow. Owen and Rogers [6] solved the controversy highlighting that the flow structure within the cavity

could be Batchelor or Stewartson type of flow depending on the turbulent flow parameter, $\lambda_{\mathrm{T}} = C_{\mathrm{w}}/\mathrm{Re}_{\phi}^{0.8}$, defined from the purge flow and rotational Reynolds number. Nevertheless, ingestion and the sealing flow can change the flow pattern in the cavity. Sufficient sealing flow pressurises the cavity volume thus reducing the extent of the core region, shifting its position radially upwards or even completely suppressing it (leading to Stewartson flow). Therefore, the turbulent flow parameter determines transition from Batchelor to Stewartson type of flow. Nonetheless, the temperature distribution on the discs can have a significant impact on the flow structure [4]. The conclusion was that a Batchelor flow structure is expected at the core region, whilst the Stewartson type of flow with no core rotation appears at low radii (source region in Fig.2.1). Bayley *et al.* [7] outlined that high rotational speeds and strong temperature gradients may induce significant variations in the boundary layers, although changes in disc geometry appeared not to affect them.

Daily and Nece [8] studied the flow mechanics in an enclosed volume with an axial seal clearance and a plane rotating disc. They found that the seal clearance, s_c, and rotational Reynolds number, Re_{ϕ}, were paramount. A characterisation of the cavity flow structure in four regimes was then defined based on these two non-dimensional parameters:

1. Laminar flow, small clearance, merged boundary layers.
2. Laminar flow, large clearance, separate boundary layers.
3. Turbulent flow, small clearance, merged boundary layers.
4. Turbulent flow, large clearance, separate boundary layers.

Research for turbulent flow in merged boundary layers (Dahlqvist *et al.* [9], Bohn *et al.* [10]) for narrow cavity volumes has shown different behaviour than that found in gas turbine engines where turbulent flow in separate boundary layers develop. The cavity flow structure corresponding to regime 4 is described below since it is the one expected in the experimental conditions of this research.

Four different aerodynamic regions can be identified inside a rotating cavity with an outward superimposed flow, Fig.2.1(a): (i) source or inner region where the flow enters the cavity, (ii) boundary layers at each side of the cavity (stator and rotor discs respectively), (iii) a central core and (iv) a sink/outer section. In case of mainstream flow entering the cavity volume, the outer region acts as the mixing zone where the ingressed flow blends with the egressed flow.

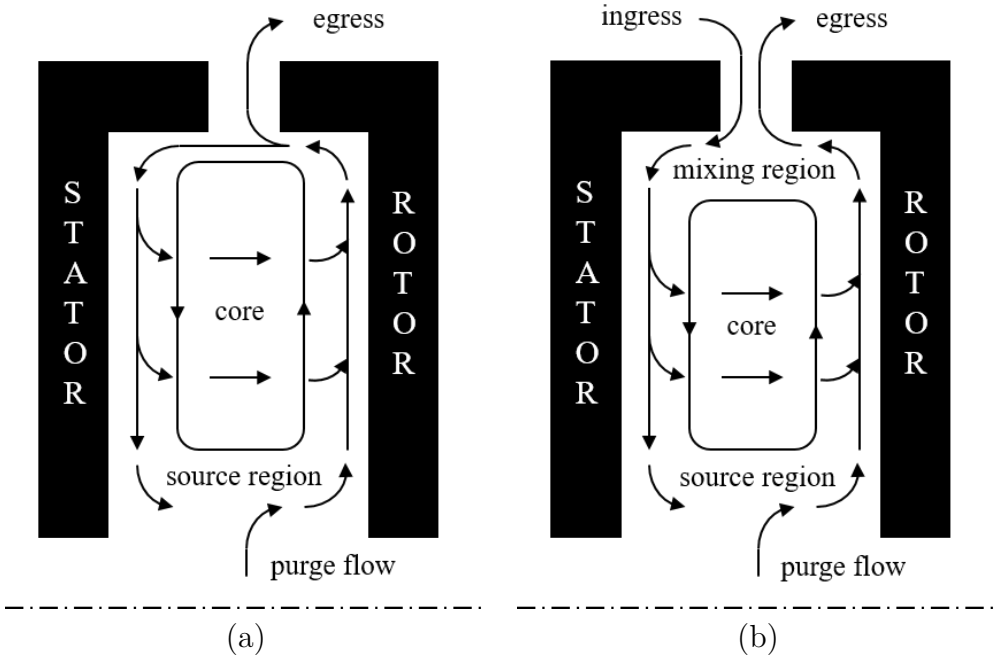

Figure 2.1: Cavity flow behaviour in rotating cavity with (a) only egress, (b) simultaneous ingress and egress.

Flow is introduced into the cavity through the inner source region and then feeds the two boundary layers at either disc. Once all the supplied fluid has entrained the steady boundary layers, they become non-entraining regions where the viscous forces are negligible. The term Ekman layer is used to refer to these regions, which act as solid boundaries to the rotating fluid. In the case of outward flow, the sink region is found at the top of the cavity. The boundary layers merge at the sink region to exit the cavity. In between the Ekman layers, the cavity volume is filled with an inviscid core of rotating fluid.

The flow structure strongly depends on whether there is flow radially inwards or

outwards through the cavity. Throughout this project simultaneous regions of radial ingress and egress have been assumed and therefore the cavity flow structure is likely to be as shown in Fig.2.1(b).

2.2 Historic overview

Early studies of rim seal ingress focused on the disc pumping effect that leads to rotationally-induced ingestion. The earliest published data on turbine rim sealing was obtained by Bayley and Owen [11]. They considered rotationally-induced ingestion for a simple axial seal clearance and produced a correlation for the minimum flow required to prevent ingestion. The importance of the annulus flow was acknowledged shortly after and attention subsequently shifted to the impact of turbine vanes and blades which create circumferential flow asymmetries in the main gas path and drive ingestion irrespective of the disc pumping. In the open literature, Abe *et al.* [12] were the first to recognise the relevance of the pressure asymmetries in the annulus gas path in driving hot gas ingestion. Further to this, Phadke and Owen [13] and [14] defined two regimes based on the dominating mechanism in hot gas ingestion: rotationally-induced ingestion would occur when the disc pumping effects prevail, whilst externally-induced ingestion would take place when the external pressure asymmetries govern ingress. In isolation, the rotation of the disc can still draw mainstream flow into the cavity with an axisymmetric environment (in absence of pressure asymmetries in the external flow field).

From the more basic experimental set ups only comprising a rotating disc, the complexity of the system was increased over the years until it represented a full turbine stage with annulus flow, sealing flow, nozzle guide vanes, rotor blades and even different flow temperatures and other leakage flows. Multiple rim seal arrangements have been investigated in a wide range of operating conditions, see Fig.2.2. Previous research concluded that in an engine-realistic system, externally-induced ingestion would predominantly prevail over

the disc pumping effect. However, under certain conditions such as the off-design operation of a gas turbine engine, the effects of rotationally-induced ingestion can no longer be neglected and it is considered to coexist with the externally-induced ingestion. Some authors have referred to this regime as combined ingestion.

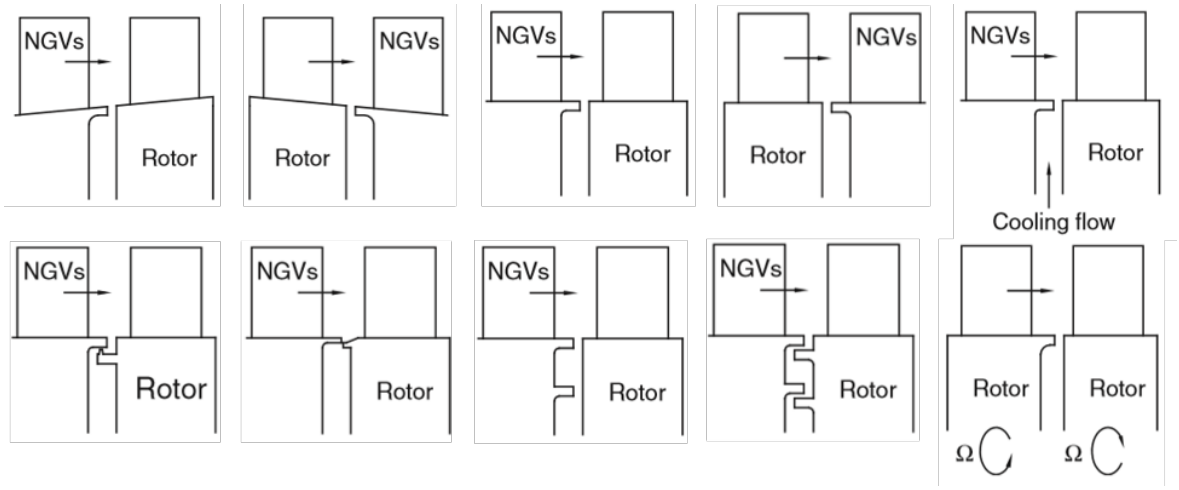

Figure 2.2: Examples of rim seal geometrical arrangements [4].

Multiple research groups have conducted numerical and experimental investigations to assess the various factors affecting rim seal flows. Over the last two decades, unsteady computational fluid dynamics (CFD) and fast response pressure measurements have revealed that rim seal flows are subject to rotating flow modes or inertial waves. This has provided an explanation for the limitations of steady CFD and more elementary models, and has stimulated new research aimed at clarifying the flow physics and reassessing the mechanisms that drive hot gas ingestion. The presence of large-scale unsteady flow features in the cavity was first reported by Cao *et al.* [15] in a combined experimental and numerical study. The CFD results indicated that, for the turbine studied, ingestion was rotationally-driven rather than pressure-driven.

Johnson *et al.* [16] listed disc pumping, periodic pressure field in the annulus, geometrical 3D features within the rim seal region, asymmetries in the rim seal geometry, turbulent transport and flow entrainment as the main mechanisms that intervene in rim seal ingestion. The presence of large-scale unsteady flow features inside the cavity had not

been detected at the time of this review. However, the research by Cao *et al.* [15], showed that they can also dominate the ingestion mechanism and should therefore be added to the list. In the most complex scenario, the hot gas ingestion mechanism in turbine rims becomes four-dimensional, being space and time-dependent.

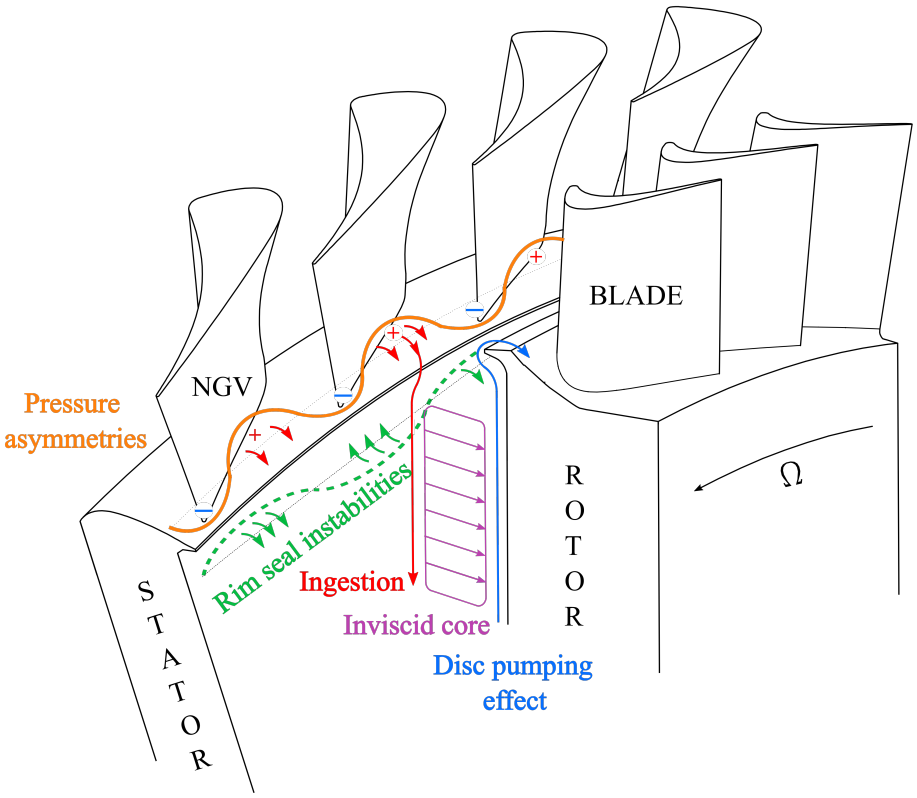

Figure 2.3: Driving mechanisms of rim seal ingestion.

Several studies have been conducted in order to investigate each one of these drivers under different operating conditions, rim seal geometries and experimental configurations. The mainstream flow is unsteady by nature due to the interaction of the rotor-stator potential field combined with the wakes from the rows of vanes and rotor blades sweeping downstream into subsequent stages. The cavity flow was also found to be inherently unsteady therefore hugely increasing the complexity of the system. This highlighted the need to clarify the synergetic effect of the interaction in the rim seal region. Scobie *et al.* [17] and Chew *et al.* [18] recently published thorough reviews of the work done in the field.

The current project focuses on studying the three driving mechanisms shown in Fig.2.3: the disc pumping effect (rotationally-induced ingestion), the pressure asymmetries in the annulus gas path (externally-induced ingestion) and the rim seal instabilities (depicted as inertial waves in Fig.2.3). Each one of these is described in more detail in sections 2.3, 2.4 and 2.5 respectively.

Interest in this topic has increased in recent years as gas turbine designers seek to improve the overall cycle efficiency by reducing the penalty derived from the secondary air system. An experimental study by Beard *et al.* [19] confirmed the presence of rotating flow modes in a chute seal subject to rotationally-driven ingestion. This work drew the attention of the sponsors and set the grounds for the investigation conducted within this thesis. Subsequently, Gao *et al.* [20] computationally explored the physics behind the rim seal unsteadiness as the third major driver for hot gas ingestion, sparking new questions regarding the effects of rotation. This study aims to investigate the isolated and combined effect of all three drivers.

2.3 Rotationally-induced ingestion

Research on the fluid dynamics of turbine rim seals commenced after several studies of free rotating discs showed some interesting effects. A rotating disc immersed in a fluid environment imposes its rotation to the surrounding fluid. Consequently, the flow in the boundary layer on the rotating disc will be ejected radially outwards owing to the centrifugal force. This phenomenon is referred to as the disc pumping effect, see Fig.2.4.

The initial investigations started with a basic scenario in which a radial outflow was supplied through an open stator-rotor system. The external environment, the main gas path in a gas turbine engine, was dismissed. Such studies aimed to quantify the minimum flow rate necessary to completely isolate the cavity from a quiescent external environment.

This led to empirical correlations of the minimum non-dimensional flow rate required to fully seal the cavity, $C_{\mathrm{w,min}}$, for what is now known as rotationally-driven or rotationally-induced ingestion. For example, Bayley and Owen [11] and Phadke and Owen [21] considered axial and radial seals respectively showing that, for the same minimum clearance, the radial seal required less sealing flow than the axial seal. These initial studies concluded that the flow structure in the disc cavities is a strong function of the seal arrangement but independent of the cavity geometry. In addition, a linear relationship of proportionality between $C_{\mathrm{w,min}}$ and Re_{ϕ} was demonstrated.

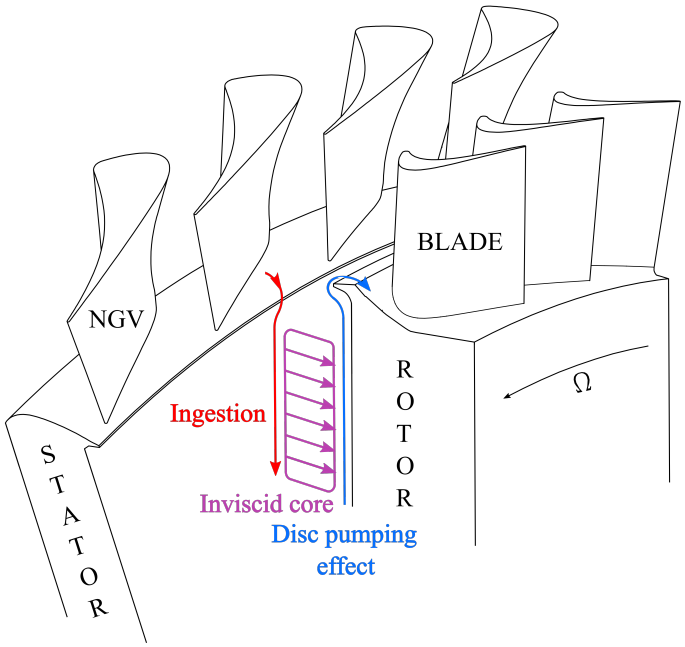

Figure 2.4: Disc pumping effect as the driving mechanism of rim seal ingestion.

The results of a more complete experimental set up featuring mainstream and purge flow came into conflict with those previously published by Bayley and Owen. Tests performed by Abe *et al.* [12] suggested that $C_{\mathrm{w,min}}$ was independent of the rotor rotational speed and was instead controlled by the velocity of the external annulus flow. Unavoidably, this outcome casted doubt on the methods used by Bayley and Owen. Subsequently, they extended their research to include the mainstream annulus flow aiming to confirm/dismiss the findings of Abe *et al.* Towards this goal, Phadke and Owen [13], [14], [22] carried out an extensive investigation to examine how the presence of annulus flow

and the pressure asymmetries affected the rim seal performance. They combined pressure measurements, gas concentration data and flow visualisation techniques to study the flow field and concluded that pressure-based results overpredicted $C_{\mathrm{w,min}}$.

In the second of this three-part study, Phadke and Owen [14] aimed to generate an axisymmetric annulus flow exempt of circumferential asymmetries, but a quasi-axisymmetric flow was investigated instead due to experimental limitations. Yet, they reported that a weak annulus flow would enhance the sealing capability up to a certain threshold in which the circumferential pressure asymmetries in the external flow would dominate and larger $C_{\mathrm{w,min}}$ would be required to seal the cavity. Flow visualisation techniques revealed that the ingested fluid generated a separation bubble at the edge of the shroud that reduced the effective clearance thereby improving the sealing performance under a quasi-axisymmetric flow. This behaviour was not shown in those conditions in which the circumferential pressure asymmetries were large and $C_{\mathrm{w,min}}$ would be proportional to the external flow. The amount of purge flow required to prevent ingestion was found to be strongly linked to the amplitude of the annulus pressure asymmetries. Further to this, Phadke and Owen defined two regimes that dominated in hot gas ingestion: rotationally-induced ingestion would occur at low $\mathrm{Re_{ax}}/\mathrm{Re}_\phi$ when the disc pumping effects prevail, whilst externally-induced ingestion would take place when the ratio $\mathrm{Re_{ax}}/\mathrm{Re}_\phi$ is large and the external pressure asymmetries govern ingress. The latter scenario would imply predominance of external flow conditions and independence (or negligible effect) of Re_ϕ, expected to be a few orders of magnitude lower.

Dadkhah *et al.* [23] stated that any ingested flow would entrain the stator boundary layer and travel across the cavity volume through the fluid core to join the rotor boundary layer. They identified the largest dilution of the seeded flow (indicative of ingestion of external flow) at the top of the cavity, with uncontaminated purge flow at the lowest radial positions. The interaction of the axisymmetric annulus flow with the ejected sealing

flow proved to have a significant impact over ingestion. Shortly after, Daniels *et al.* [24] concluded that the effect of the swirl in the external flow on ingestion was minimal. In addition, their experimental study included a test case with an axisymmetric external flow in which the purge flow required to prevent ingestion was found to be independent of rotational speed, agreeing with Abe *et al.* Most importantly, the study by Dadkhah *et al.* concluded that a slight reduction in the purge flow does not cause a critical decrease of sealing performance. Indeed, they suggested that a 35% saving in purge flow would be possible if rim sealing effectiveness of 0.95 could be accepted.

Further experimental studies on rotationally-induced ingestion provided data for a number of seal types and use of gas concentration measurements allowed sealing effectiveness to be quantified for flow rates $C_{\mathrm{w}} < C_{\mathrm{w,min}}$. Assuming the flow in the turbine disc cavity to be largely controlled by disc pumping, Chew [25] developed a model to correlate experimental data and estimate sealing effectiveness for different seal designs in absence of external annulus flow. For the small clearance seals considered, the minimum flow rate required to seal the cavity and the sealing effectiveness for flow rates below this value are given by Eq.2.1. The parameter k is adjusted to fit the data for different rim seal geometries and gives an indication of the sealing performance; low k implies better prevention or suppression of ingestion.

$$\frac{U_{\mathrm{m,min}}}{(\Omega b)} = 0.1214\,k \qquad \varepsilon = \frac{1}{0.8 + 0.024\,k\left(\dfrac{\Omega b}{U_{\mathrm{m}}}\right)} \qquad \text{for} \quad 0 < U_{\mathrm{m}} < U_{\mathrm{m,min}} \tag{2.1}$$

Where U_{m} is the mean seal velocity through the rim based on the supplied purge flow rate, Ω is the rotor angular speed, b is the disc outer radius, and ε is the sealing effectiveness (defined later for experimental measurements). Chew *et al.* [26] estimated the value of k in Eq.2.1 for different geometries and fitted the model to their own experimental data. Good agreement was evident with their results but also with that of other research groups in absence of mainstream flow. For $k = 0.8$, the model gives

$C_{w,min} = 0.61(s_c/b)Re_\phi$, where s_c is the seal clearance, reproducing Bayley and Owen's correlation for a simple axial clearance seal. Phadke and Owen [21] reported a superior sealing performance of the radial seal. Chew *et al.* found that k was lowest for a radial seal thus confirming that the rim seal arrangement most capable of preventing ingestion was the radial seal. Several simple and complex seal geometries have been tested over the years, but the study by Bru Revert *et al.* [27] is thought to be the first investigation of a chute seal configuration purely under disc pumping effect.

A different orifice model for rotationally-induced ingestion was proposed by Owen [5]. The derived theoretical equations suggested that swirl in the annulus would reduce ingestion and swirl inside the cavity would be the driving force for the disc pumping effect, favouring ejection of purge flow at large swirl ratios. Within the same research group, Sangan *et al.* [28] conducted an experimental study and fitted the orifice model to their data showing very good agreement between the experimental and theoretical results. Sangan *et al.* [28] estimated that the sealing mass flow required to seal a radial clearance under rotationally-induced ingestion was 38% lower than for the axial clearance, agreeing with previous research. The sealing effectiveness data identified a mixing region at the top of the cavity where the ingested annulus flow mixed with the sealing flow and then the fluid merged the stator boundary layer to travel radially inbound. A fully mixed flow in the stator boundary layer led to an invariant profile of sealing effectiveness in the stator wall. In the case of incomplete mixing, the sealing effectiveness obtained at the top of the stator wall was lower than that found in the inner part of the cavity.

2.4 Externally-induced ingestion

Johnson *et al.* [16] conducted a thorough study of the most relevant mechanisms of turbine rim seal ingestion. Several reasons were pointed out as possible causes for ingestion: rotor disc pumping, rim seal geometry (3D features or asymmetries), periodic pressure

asymmetries from the mainstream flow (interaction vane-blade), turbulent transport and flow entrainment. Ingestion due to disc pumping occurs because of the centrifugal forces of the fluid in the rotor boundary layer which act to push the fluid radially outwards. When there is not enough purge mass flow pressurising the cavity, a radial pressure gradient is established and, to compensate, the mainstream flow is ingested into the cavity. Some authors have alluded to this phenomena as Rotationally-Induced (RI) ingestion and it is described in section 2.3.

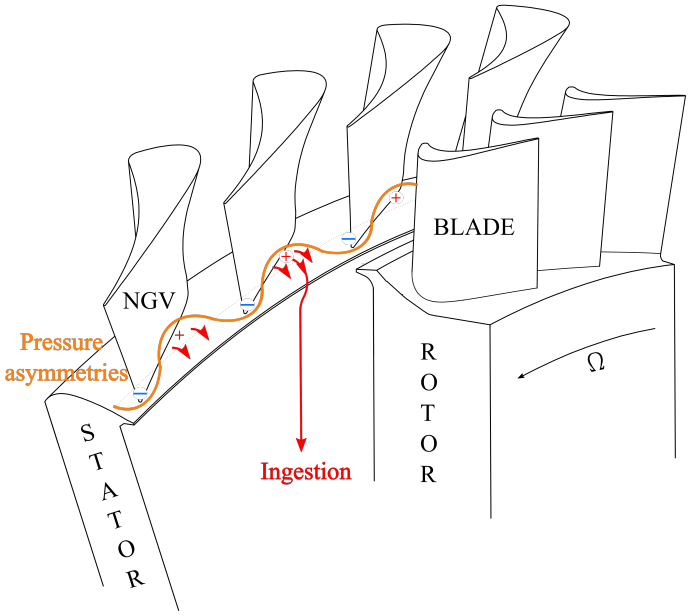

Figure 2.5: Circumferential pressure asymmetries as the driving mechanism of ingestion.

An alternative form of ingestion is named Externally-Induced (EI) or Pressure-Driven ingestion, caused by the circumferential pressure asymmetries in the main gas path. Flow would naturally be sucked in due to the rotation of the disc. Circumferential pressure asymmetries in the annulus severely impact this phenomenon promoting ingress and egress of cavity flow around the seal circumference. Alternating regions of local high and low pressure appear in the annulus as a consequence of the interaction between the pressure fields of NGVs and rotor blades as depicted in Fig.2.5. Wherever the pressure in the main gas path is above the pressure inside the cavity, hot gas ingestion will occur, as the mainstream flow will be sucked into the disc cavity. Pressure-driven ingestion has been

assumed to be the dominating mechanism of ingestion in turbine rim seals when pressure asymmetries exist in the main gas path. Nonetheless, there are many situations in which the disc pumping effect cannot be neglected and an intermediate scenario of coexisting RI and EI is often referred as Combined Ingress (CI).

Phadke and Owen [22] generated pressure asymmetries and proved that $C_{\mathrm{w,min}}$ was correlated with the amplitude of the maximum circumferential pressure difference from the annulus flow. Following the initial studies in which the main gas path was clear of any blading, experimental investigations including a full stage started to emerge. Several attempts to predict the sealing effectiveness under the influence of the pressure asymmetries had been made by numerous research groups with the formulation of orifice models and turbulent transport models. Nonetheless, it should be noted that, as highlighted by Savov *et al.* [29], none of these models offer prediction capability *per se* rather a best fit to experimental data with adjusted parameters. Hamabe and Ishida [30] were amongst the first of many researchers to compare sealing effectiveness based on gas concentration measurements with an elementary orifice model of pressure-driven ingestion. Approximating the circumferential annulus pressure variation (between $p_{\theta\mathrm{min}}$ and $p_{\theta\mathrm{max}}$) as sinusoidal (amongst other distributions) and adopting a uniform cavity pressure, Hamabe and Ishida derived Eq.2.2 to calculate the minimum sealing flow rate. This is obtained by integrating around the annulus assuming local one-dimensional flow through an orifice area corresponding to the seal clearance. With appropriate choice of discharge coefficient, C_{d}, the orifice model may be adjusted to match measured sealing flows and sealing effectiveness. Overall, the models show good fit to most experimental data although significant discrepancies arose when unsteady pressure fluctuations were registered in the cavity.

$$\frac{U_{\mathrm{m,min}}}{(\Omega b)} = C_{\mathrm{d}} \frac{2}{\pi} \sqrt{\frac{(p_{\theta\mathrm{max}} - p_{\theta\mathrm{min}})}{0.5\rho\big(\Omega b\big)^2}} \tag{2.2}$$

Shortly after, Green and Turner [31] aimed to decouple the effect of the nozzle guide vanes and rotor blades in the annulus publishing the first study featuring a complete

turbine stage. In a comprehensive experimental investigation, they demonstrated that the addition of the NGVs promoted ingress due to larger pressure asymmetries. However, they found that introducing the blades smoothed out the NGV pressure asymmetries and therefore provided a more axisymmetric external flow. This resulted in higher sealing effectiveness thus concluding that the rotor blades positively influenced the sealing performance. Furthermore, Green and Turner showed that with a full stage, the levels of ingestion were proportional to the rotor disc speed suggesting that the cavity could be rotationally dominated. They also emphasised the need for experiments at representative engine conditions to avoid misleading conclusions.

Chew *et al.* [32] corroborated that the introduction of weak (asymmetric) annulus flow improved the sealing effectiveness when compared to the quiescent environment. This was previously acknowledged by Phadke and Owen [14] with a quasi-axisymmetric mainstream. Nevertheless, the interaction of high rates of purge with the annulus flow led to sealing effectiveness below unity in all cases, indicating that the cavity was never fully sealed. They speculated that this may be due to turbulent diffusion of the seeded gas through the seal clearance. Bohn *et al.* [33], [34] carried out an extensive combined investigation to experimentally and numerically assess how the phenomenon of hot gas ingestion was affected by the introduction of NGVs and rotor blades in the annulus. They noticed that the cavity could not be fully sealed in real systems with circumferential pressure asymmetries [33]. Therefore, their results supported the findings of Chew *et al.* In [34], Bohn *et al.* found that the rim seal geometry is crucial to determine the influence of the rotor blades on ingestion. Their numerical simulations showed a reasonable qualitative agreement with the data from Green and Turner [31] for one of their configurations, confirming the performance benefit originated from the presence of the blades. These results differed from experiments of their own and were only displayed by one of their configurations - their other arrangement penalised the sealing effectiveness.

The numerical study of Hills *et al.* [35] highlighted that a highly swirled purge flow (with a tangential velocity component closer to that of the rotor disc than to that of the vanes) caused the pressure non-uniformity induced by the rotor blades in the annulus (generally smaller than that of the NGVs) to have a disproportionate effect on ingress. The mismatch between the calculated and experimental values from Gentilhomme *et al.* [36] were attributed to the reduction of swirl flow at higher sealing flow rates. They demonstrated that ingress of highly swirled annulus flow at low rates of purge supply increased the swirl in the cavity and consequently the radial pressure gradient. Recent work suggested that swirling the purge flow could be beneficial to reduce the viscous losses associated with cavity and mainstream flow interaction in the main gas path. Zlatinov *et al.* [37] numerically investigated the effect of swirl in the purge flow and noted that larger purge supply is required to seal the cavity if the purge flow is swirled owing to its synchronisation with the pressure non-uniformities. Nonetheless, they concluded that swirling the purge flow would be beneficial if the ingestion mechanism is driven by the unsteady pressure disturbance at the rim dominated by the NGV pressure non-uniformity.

Comparison of test campaigns under rotationally-induced, externally-induced and combined ingestion for the same operating conditions have been published in several occasions. A theoretical study by Owen *et al.* [5], [38] provided an analytical and numerical solution to the orifice equations for an axial clearance. The experimental counterpart was conducted by Sangan *et al.* [39] and [40] who tested a range of seal configurations (axial, radial and double radial) under different conditions of external flow. The orifice models derived by Owen were fitted to their rig measurements showing remarkable agreement. Moreover, Sangan *et al.* also provided evidence of a lower minimum sealing flow rate to prevent ingress in RI than in EI for both axial and radial clearances (25% and 36% respectively). Despite the good agreement of the predicted analytical values with the measured sealing effectiveness in the RI regime, Owen *et al.* [38] highlighted the need for more experimental data in the regime of combined ingestion for theoretical

(and computational) validation. Recently, Bru Revert *et al.* [41] showed evidence that in the presence of external pressure asymmetries, the disc pumping effect can dominate the ingestion mechanism challenging the definition of the combined ingress regime.

Previous studies with turbulent flow and separate boundary layers showed that under rotationally-induced ingestion, the flow was fully mixed in the stator boundary layer. Sangan *et al.* [28] reported constant levels of sealing effectiveness on the stator wall owing to no unmixed flow being added into the stator boundary layer. Under the influence of the external pressure asymmetries introduced by the stator vanes and rotor blades, radial variations of sealing effectiveness were found. This indicated that the mixing of the entrained annulus flow and the sealing flow at the top of the cavity was incomplete.

2.5 Rim seal instabilities in ingestion

The first studies investigating rim seal ingestion focused on the disc pumping effect that leads to rotationally-induced ingestion. Shortly after, the relevance of the pressure asymmetries in the main gas path, external to the cavity, was acknowledged and the focus shifted towards the so-called externally-induced ingestion. Decades of research later, and despite the developments in computational modelling techniques, differences between experimental and simulated results were still large, indicating that other key elements were being missed. Publications started to provide evidence suggesting the possibility of unsteady phenomena driving hot gas ingestion.

Over the last two decades, unsteady computational fluid dynamics (CFD) and fast response pressure measurements have revealed that rim seal flows are also subject to rotating cavity flow modes or inertial waves as represented in Fig.2.6. This has provided an explanation for the limitations of steady CFD and more elementary models stimulating new research aimed at clarifying the flow physics and reassessment of the driving

mechanisms. The main source of unsteadiness was observed to arise from the vane and blade potential field interaction in the main gas path, but unsteady pressure fluctuations unrelated to the blade passing frequencies were detected inside the cavity. The latter is the focus of this section.

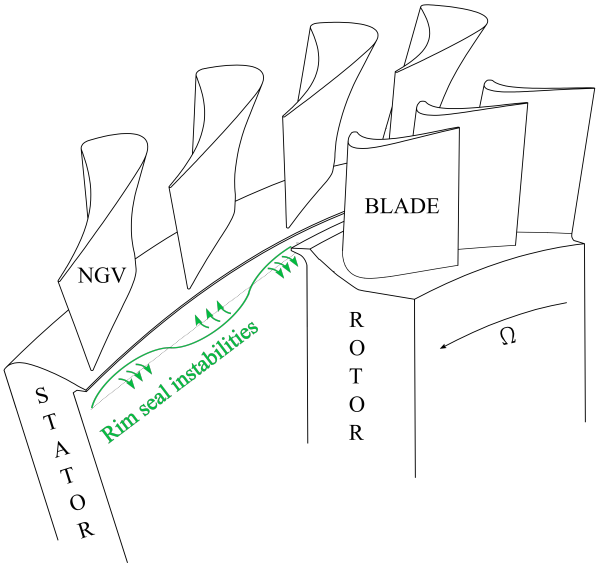

Figure 2.6: Rim seal instabilities (depicted as inertial waves) as the driving mechanism of hot gas ingestion.

2.5.1 Early research

An extensive investigation combining an experimental and numerical approach led Bohn *et al.* [34] to reveal an ingestion zone rotating at half the rotor speed which was not present in the steady simulations previously reported in [33]. Similarly, Roy *et al.* [42] identified a large mismatch between their unsteady pressure measurements and predictions with steady CFD models. The source of disagreement was attributed to unsteady effects in the rim seal. Several investigations such as those by Hills *et al.* [35] and Gentilhomme *et al.* [36] highlighted the importance of the flow unsteadiness on the ingestion process based on the misalignment between their time-averaged rig measurements and the outcome from their RANS simulations. Indeed, Hills *et al.* demonstrated that unsteady computations (URANS) provided better agreement with the experimental data. More-

over, they pointed to an overestimation of the inertial effects arising from the difference on tangential velocity between the sealing flow and the external annulus flow as the cause for the underprediction of ingestion in CFD. The unsteady phenomena detected at that time was introduced by the vanes and blades in the main gas path. However, some publications started to mention the presence of unsteady flow features unrelated to the blade passing frequency.

Experimentally, the presence of previously unnoticed large-scale pressure fluctuations unrelated to the blade passing frequency with a characteristic length larger than a vane or blade pitch was detected by Smout *et al.* [43]. Following the experimental evidence, some unsteady simulations were carried out to corroborate whether the numerical models detected such structures. The review by Chew *et al.* [18] states that a project within the University of Surrey computationally revealed three-dimensional unsteady flow structures at the rim seal despite the boundary conditions being axisymmetric and steady. Shortly after, Cao *et al.* [15] published the first combined experimental and numerical study reporting the existence of large-scale unsteady flow features in the cavity which were unrelated to the blade passing frequency. They were observed to span over a single vane or blade pitch. The CFD results (with unbladed annulus) indicated that ingestion was rotationally-driven rather than pressure-driven. Cao *et al.* detected a flow pattern of alternating regions of ingress and egress with large-scale structures rotating slightly slower than the disc speed. These were thought to arise from the interaction of the annulus and sealing flows. Further analysis of the unsteady pressure signals revealed that these events were rotating rather than pulsating and that the frequencies related to the flow modes were proportional to the rotor disc speed. Nonetheless, the frequency was found to be a stronger function of the annulus flow swirl velocity than rotor speed.

2.5.2 Rim seal instabilities

Looking at the frequency spectra of the high resolution pressure measurements logged, Roy *et al.* [44] identified a distinctive peak at a frequency lower than the blade passing frequency. The peak was detected at the rim seal region and it was seen to propagate downstream through the domain where it would be modulated by the presence of vanes and blades in the main gas path. Independently of the rim seal flow structures, Jakoby *et al.* [45] detected a stable periodic pattern of large scale rotating structures further inside the cavity. Their computations broadly matched the unsteady pressure measurements and associated the low frequency peak in this region to the cavity modes. Low frequency pulsations of large amplitude were observed at low rates of sealing flow, with the limit at which they disappear proven to be dependent on seal configuration and operating conditions.

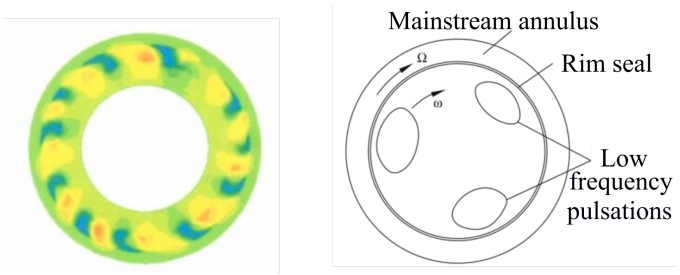

Figure 2.7: Contours of velocity inside the cavity showing rim seal instabilities, Cao *et al.* [15] (left) and rotor-stator cavity modes from Jakoby *et al.* [45] (right).

Roy *et al.* [44] observed that ingress would occur in the circumferential locations under the influence of the vane where the pressure was highest. Therefore, areas with maximum pressure differential across the rim seal would find the largest ingestion of mainstream flow. Julien *et al.* [46] reported that when the large-scale structures appear, the pressure perturbations inside the disc space provoke a much deeper penetration of the flow during ingestion. The influence of this transient phenomenon was significant especially at low coolant rates where larger regions of low pressure would develop. Schadler *et al.* [47] stated that the rim seal instabilities are defined by a local exchange of mass flow of sealing and annulus flow across the seal when ingress/egress occurs. The unsteadiness at

the rim seal was associated to vortex formation and modulation.

Measurements from Roy *et al.* [44] revealed that in absence of purge flow, the large scale flow structures still appeared and represented the most energetic phenomenon in the frequency spectra, whilst the blade passing frequency contained more energy at high rates of sealing flow. This aligned with the findings of other studies conducted independently which showed that the distinct frequency corresponding to the cavity flow structures disappeared as the sealing purge flow increased and the blade passing frequency became the most energetic peak in the frequency spectra (see Julien *et al.* [46] and Horwood *et al.* [48]). Julien *et al.* [46] also found that high rates of sealing flow had a stabilising effect on the cavity pressure fluctuations as it reduced the intensity and count of the unsteady flow structures. Several authors agreed with the theory that unsteady flow structures and the subsequent ingestion of mainstream flow could be mitigated or stabilised at high purge supplies (Chilla *et al.* [49], Schadler *et al.* [47]). Boudet *et al.* [50] speculated that the rim seal instabilities disappeared when the centrifugal force dominated over the pressure gradient inside the cavity, producing an outflow which stabilised the flow field. Consistent with this hypothesis, Schadler *et al.* [47] postulated that the stabilisation of the cavity pressure fluctuations in the rim seal at larger purge rates reduced the energy content of the vortical structures. In addition, they defended that ingress and egress were required to trigger the rim seal instabilities since the phenomena were defined by a flow exchange. Therefore, if the cavity was fully sealed by a high purge flow and only egress was taking place, the unsteadiness was suppressed. A recent study conducted by Queguineur *et al.* [51] concluded that stabilising the cavity or shifting the frequency of the instabilities would require controlling the stator mode through harmonic forcing of its boundary layer.

Nonetheless, the hypothesis of mode stabilisation was not exempt of controversy. Mirzamoghadam *et al.* [52] contradicted these claims arguing that, when external flow pressure asymmetries are present, ingestion can occur even at high purge mass flow rates

due to the highly unstable flow found when EI and RI coexist. Recent studies by Horwood *et al.* [53] showed that in a chute seal, the frequencies below blade passing appeared at all computed purge rates and that the amplitude of the peak increased with higher sealing flow rates although it slightly reduced at $U_{\mathrm{m}}/(\Omega b) = 0.1$. On the contrary, for a radial seal, Horwood *et al.* [48] detected a reduction of the low frequency peak amplitude with increasing purge, with the energy corresponding to the rotating structures being largely suppressed at the same $U_{\mathrm{m}}/(\Omega b) = 0.1$. These apparently opposing outcomes show the complexity of the phenomena and sensitivity to different parameters such as geometrical arrangement.

The inherent unsteadiness was detected in axial clearances ([45], [15], [47]), chute rim seals ([44], [54], [50], [19], [53]), radial seals ([55]) and overlap-type rim seals ([49], [56]) in both experimental and numerical studies. Some of these studies focused on determining the number and rotational speed of the flow structures, few others on investigating their origin and many more on developing computational models with the capability to capture them. The aim of these was to match the accuracy and reliability of the experimental data through inexpensive simulations. After an extensive review of the available literature, Chew *et al.* [18] concluded that axial seals with higher clearances appear to present the distinct peak of the unsteady flow structures at lower frequencies than more complex geometries with tighter clearances. A recent study by Gao *et al.* [20] investigated the unsteady flow structures in an axial, chute and radial seal arrangements with similar cavity volumes and found that the geometry of the latter restricted the radial outflow suppressing the cavity instabilities.

The unsteady flow structures present a wide range of sensitivities. Roy *et al.* [44] listed mainstream, purge flow, rotor disc speed and geometrical features of the rim seal set up as the most influential parameters on the unsteadiness of the three-dimensional flow field. In other words, the ingestion phenomena strongly depends on the velocity

triangle and vice versa. Indeed, Paniagua *et al.* [57] demonstrated that the sealing flow modified the velocity triangles and relative incidence angle at the rotor downstream the cavity. Following this, Boudet *et al.* [50] proved that the higher the supply of purge flow, the stronger the perturbation originated in the incidence angle to the rotor blades. Furthermore, this effect was observed to travel downstream.

The initial study by Cao *et al.* [15] showed that the frequency of the flow structures slightly increased with rotor disc speed although they concluded that the swirled annulus flow had a greater impact. In addition, they found that the lengthscale and strength of the unsteady 3D effects was linked to the dimensions of the cavity (radial extent, axial spacing and gap size). Town *et al.* [58] indicated that the rim seal cavity, rather than the number of vanes and blades in the gas path, would determine the cell size, shape and speed of the flow structures. They showed that large unobstructed clearances would develop less (in number) but larger (in size) structures and vice versa. In a thorough study, Schadler *et al.* [47] concluded that the axial width of the vortical structure will be of the order of magnitude of the distance between stationary and rotating cavity discs.

Gao *et al.* [59] also pointed out that each experimental campaign may also be affected by protrusions in the cavity volume such as boltheads (see Beard *et al.* [19]), eccentricity in the experimental rig (see Savov *et al.* [29]), vibrations and annulus flow conditioning components as potential variables that may distort the recorded unsteadiness.

Furthermore, the phenomena was observed to be time-dependent with a high degree of randomness, which meant that each revolution would have different number and intensity in the flow structures, as noted by Cao *et al.* [15]. Clear evidence of this is provided by the phase analysis methodology suggested by Beard *et al.* [19] that showed summary plots in which the phase lag for each pair of pressure measurements differed for each revolution within the same run.

2.5.3 Limitations in numerical modelling

The intrinsic unsteadiness of the rim seal has been experimentally detected by several research groups ([15], [45], [44], [47], [58], [29], [19]) whose measurements logged low frequencies unrelated to blade passing. The high expense of conducting an experimental campaign positions numerical computations as an appealing alternative to investigate the phenomena at a fraction of the cost. The computational resources in terms of power, modelling capabilities and numerical methods required to simulate such complex scenarios have recently become available. Indeed, since the early days, various investigations have followed a combined numerical-experimental approach to conduct a more in-depth analysis of the flow physics, validate the results from the simulations and complement rig data with flow visualisations from simulations. As a result, the computations of Cao *et al.* [15] and Jakoby *et al.* [45] successfully detected the rotating structures in the cavity measured in their respective experimental facilities.

Numerous studies have agreed that the size of the sector model was limiting the length-scale of the unsteadiness due to the imposed periodicity of the boundary conditions. However, conducting full annulus time-resolved simulations is computationally expensive and therefore a trade-off in accuracy, modelling effort and computational time often results in a smaller sector size being used. Apart from 3D full annulus unsteady simulations, Boudet *et al.* [50] also suggested running Large Eddy Simulations (LES) in views to overcome the previously observed underpredictions of ingested flow. Contrasting results from different modelling strategies and experiments has become common practice (for example [15], [45], [60], [47], [61], [19], [29], [48]). Comparisons of LES-URANS-rig data often show increasing agreement of the LES results with the experimental data although a misalignment in either frequencies or pressure amplitudes tends to still be observed. The source of the mismatch has often been attributed to lack of representative boundary conditions, grid resolution, imposed periodicity, turbulence modelling and the sector size model for URANS. Julien *et al.* [46] also highlighted the challenge on the choice of

time step and duration to reach convergence of the simulations due to the interaction of multiple time-scales. Significant advances in the modelling strategies and computational capabilities have been achieved, yet new investigations yield to the same conclusion as recently shown by Gao *et al.* [59].

2.5.4 Source of unsteadiness

The origin of the aforementioned rim seal pressure fluctuations continues to be investigated since agreement on the physical cause of such phenomenon has not been reached. Nevertheless, three general trends stand out in the published literature pointing to the Taylor-Couette instability, Kelvin-Helmhotz instability or inertial waves as triggers.

Jakoby *et al.* [45] proved that the unsteady pressure fluctuations in the rim cavity were unrelated to the blade passing frequency, and consistently with Cao *et al.*, speculated that they emerged as a consequence of the interaction between the highly swirled mainstream flow and the purge flow. The large-scale flow structures were attributed to the non-linear coupling between the instabilities inside the cavity and the blade passing frequency by Boudet *et al.* [50]. Schuepbach *et al.* [62] seconded this hypothesis years later. Town *et al.* [58] justified them based on the momentum in the rotor boundary layer causing the air in the cavity to swirl therefore creating a pattern of moving high and low pressure cells.

Amongst those who proposed the Taylor-Couette instabilities as the trigger for the rotating structures are Boudet *et al.* [50], O'Mahoney *et al.* [63] and Gao *et al.* [59]. Boudet *et al.* justified that at low rates of purge flow, the cavity flow is governed by opposition between the pressure gradient and the centrifugal force thus satisfying the condition for the Taylor-Couette instability to develop. High supplies of coolant would suppress the instability since the centrifugal force dominates the flow. The numerical evidence for this theory was provided by the instantaneous flow field obtained from the LES study published by Gao *et al.* [59].

Rabs *et al.* [61] defended that the regions of low pressure in the rim seal gap indicated a vortex structure initialised by the Kelvin-Helmholtz instability. Their detailed study determined that the condition for the development of Kelvin-Helmholtz instabilities was the existence of two parallel, superposed flows of different velocities. This requirement is met in the rim seal region when the hot mainstream flow meets the cold egressed sealing air at different velocity and a shear layer forms. An instability arises at the inflection point in the velocity profile thus exciting the shear layer. The Bernouilli equation indicates that the larger velocity of the annulus flow in the upper shear layer leads to a lower pressure than that of the lower layer corresponding to the purge flow. The perturbations increase with distance and the shear layer starts to bend without the need for viscosity. The shear layer rolls up owing to the bend moving in the direction of the flow and Kelvin-Helmholtz vortices occur. The sequence of Kelvin-Helmholtz vortices formation is depicted in Fig.2.8.

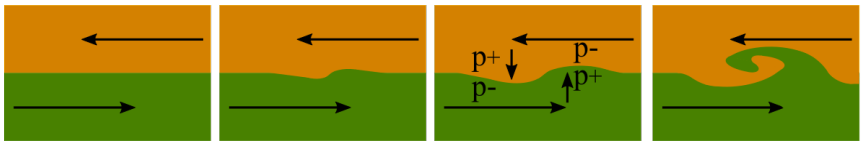

Figure 2.8: Development of Kelvin-Helmholtz instabilities.

The size of the vortices depends on the amount of purge flow, and they are detected with an almost sealed cavity (although with reduced amplitude). The development of these vortices may be suppressed by the interaction of the NGVs and rotor blades in the convoluted potential field. The observations of the vortex shedding process reported by Chilla *et al.* [49] aligned with these principles demonstrating that the unsteadiness disappeared when the difference in tangential velocity was minimised. Most importantly, the Kelvin-Helmholtz instabilities would be suppressed by the interaction of NGVs and rotor blades in a full stage. Similarly, Savov *et al.* [29] justified the formation of unsteady flow structures based on turbulent transport and the roll-up of the shear layer that leads to Kelvin-Helmholtz instabilities. Schadler *et al.* [47] formulated the same principle. Horwood *et al.* [48] provided further evidence of the development of Kelvin-Helmholtz

instabilities due to the tangential shear between purge and mainstream flows with the results by his coauthors Hualca *et al.* [64] being consistent with both hypotheses.

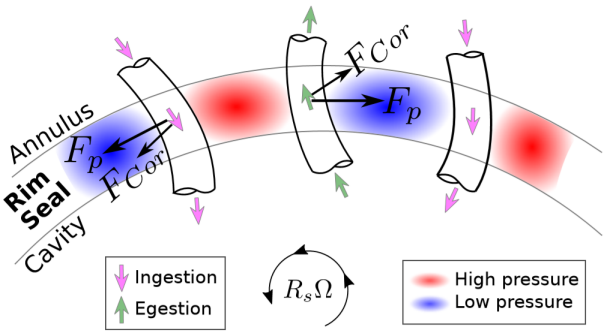

Figure 2.9: Inertial waves representation [20].

A different theory has been recently suggested by Gao *et al.* [20] who explored the physics behind inertial waves as the third major driver for hot gas ingestion, see Fig.2.9. Childs [4] pointed out that similar flow structures develop in rotating cavities in which the coexistence of radial inflow and outflow in a rotating fluid demands for opposition of Coriolis forces (of different sign) generated by alternating areas of cyclonic and anticyclonic circulation. The LES results provided by Gao *et al.* suggest that inertial waves such as those governing atmospheric phenomena could develop in the chute seal they studied. The principle lies in the restoring forces, such as Coriolis forces, that drive inertial waves. Within the three geometrical configurations they investigated, evidence of inertial waves appeared in an axial and chute rim seal arrangement. Interestingly, the radial configuration was shown to suppress the inertial waves. Gao *et al.* attributed this to the seal geometry restricting the radial fluid motion that would, as a consequence, also reduce the Coriolis force. According to Gao *et al.*, waves arise in the axial and chute seals from the interaction of ingested and ejected flow and in these two seal configurations, the Coriolis terms strongly couple the radial and tangential momentum equations. Evidence of the Taylor-Couette vortex pair previously shown by Gao *et al.* [59] did not develop in the radial seal.

2.6 Spoiling effect on turbine aerodynamics

The need to purge and seal the cavity volume to prevent undesired overheating of the discs detriments the cycle efficiency owing to, among others, the impact of ejection on the aerodynamics of the main gas path. Extensive investigations have been conducted to study the sensitivity of the aerodynamic flow field to ingress/egress of cavity flow, mainly to evaluate performance impact and loss generation. During assessments of turbine performance, the interface between the turbine and the secondary air system was often neglected with the rim sealing flows studied separately. An integrated approach is paramount to achieve accurate predictions given the interdependence between the two engine sections.

The strong link between aerodynamic losses and the purge flow was demonstrated by McLean *et al.* [65], [66] who proved that radial ejection caused large losses in efficiency. Furthermore, they showed that high velocity ratios in the purge flow could disrupt the rotor boundary layer potentially leading to an increase in aerodynamic efficiency. Alternatives to reduce the performance penalty derived from the purge supply were suggested by other authors such as an injection with radial and tangential velocity components or increasing the swirl of the purge flow to reduce the severity of the shear between the sealing and annulus flows.

An intensification of the secondary flows on the rotor downstream the rim seal cavity was reported by several research groups such as Paniagua *et al.* [57], Schuepbach *et al.* [62] and Schadler *et al.* [47]. Paniagua *et al.* identified a strengthening of the secondary flows due to entrainment of the purge flow into the hub passage vortex. Moreover, the stronger vortex was found to be pushed upwards in the spanwise direction as a consequence of the ejected cavity flow. Schadler *et al.* [47] observed that the cavity flows migrated radially upwards to up to 30% of the blade span. Furthermore, other researchers such as Boudet *et al.* [50] identified traces of rim seal flows (through tem-

perature measurements) downstream of the rotor blades. Several hypotheses have been postulated to justify the migration of the cold purge flow such as the hub vortex lifting the ejected air, due to negative incidence or overturning leading to a reduced flow velocity.

The spoiling effect of the purge flow was categorised into four sources of aerodynamic loss by Schrewe *et al.* [67]: alteration of the vane flow field, blockage of rotor inlet, increase in secondary flows and modification of rotor incidence. Schuepbach *et al.* noticed that the vortex rotation of the secondary flows was affected by a non-linear combination with the instabilities in the rim region. Chilla *et al.* [49] demonstrated that the rim seal unsteadiness enhanced aerodynamic loss generation. The identification of the close link between the rim instabilities and the loss mechanisms led to the realisation that the performance gain (loss reduction) consequence of reducing the purge supply was weakened by the unsteadiness [47].

2.7 Other studies

Investigations diverging from the common practice that aimed to expand the scope of the understanding about hot gas ingestion in turbine rim seals from a different perspective have also been carried out. Some examples are briefly mentioned in this section to illustrate the complexity of the problem.

Test facilities featuring 1.5 stages of an engine-realistic turbine offered the possibility of studying the front and rear cavities. The experimental and numerical study conducted by Jakoby *et al.* [45] revealed that the front cavity experienced larger ingestion than the rear one. They used the pressure gradient across the cavity as a measure of ingestion and justified this effect based on the swirl of the annulus flow. The large swirl velocity component of the flow between the NGV and rotor blades (front cavity) was transferred into the cavity flow when it was ingested thus leading to an increase in cavity swirl and

pressure gradient. Downstream of the rotor blades, above the back cavity, the angular momentum of the almost axial mainstream flow was very small and as a result, its effect over the cavity pressure distribution was smaller. A decade later, Patinios *et al.* [68] also studied the two cavities in an experimental test facility at the University of Bath and found an improvement of the sealing efficiency on the downstream cavity due to a reduction in the annulus swirl. They speculated that this was due to the mixing of the purge flow exiting the front cavity with the mainstream flow and the presence of the rotor blades.

Schadler *et al.* [47] conducted a noise study based on the acoustic characteristics of the pressure fluctuations in the cavity. Their investigation concluded that the overall noise of a high pressure turbine could be reduced by suppressing the rim seal unsteadiness.

A strong dependency of the steady static pressure at the rim seal on the axial position of the vanes was reported by Hualca *et al.* [64] although the unsteady pressure structures in the cavity showed weak dependency. Similarly, Johnson *et al.* [69] observed that the time-dependent annulus pressure field external to the cavity could dominate the ingestion mechanism if there was close proximity between the stator and rotor blade rows.

Leakage paths in the secondary air system of a gas turbine engine are unavoidable in the interface between structural components, thus the effect of leakages has also sparked the interest of several research groups. For instance, Patinios *et al.* [70] identified two different flow structures in the cavity depending on the relevance of the leakage flows.

Research of hot gas ingestion has typically been conducted at operating conditions that represent the engine design point. Nonetheless, Scobie *et al.* [71] and Savov *et al.* [29] also investigated some experimental off-design conditions that represented other points of the flight envelope. The study conducted by Bru Revert *et al.* [41] included a wide range of flow coefficients that represented design and off-design operating conditions.

2.8 Summary

A detailed review of the literature available in the public domain has been reported in this chapter. The hot gas ingestion mechanism has been described and the cavity flow physics detailed for the cases of a free disc and an enclosed rotor-stator system.

A chronological overview of the published research in rim sealing flows has been addressed from the fundamental early studies to the most recent and complex configurations in which an entire turbine stage typical of a gas turbine engine was investigated. Special focus has been placed on the rotationally-induced, externally-induced and the unsteady flow phenomena in the turbine rim region as the main driving mechanisms for hot gas ingestion.

The most relevant studies conducted to study rotationally-induced ingestion have been reviewed. An analytical orifice model for the disc pumping effect has been described in more detail since it is used for comparison in subsequent chapters.

A summary of the key investigations of externally-induced ingestion has been presented. The fundamental physics of the mechanism have been explained and the impact of the pressure asymmetries on the cavity and mainstream aerodynamics reported. An orifice model which considers the circumferential pressure asymmetries has been detailed since it is later fitted to the data of this investigation. Disagreements between several research studies have been highlighted to emphasise the complexity of the problem.

The most relevant studies that aimed at understanding the rim seal instabilities have been summarised. The early research that pointed at unsteady phenomena as the cause for mismatches in numerical and experimental studies have been briefly commented. A review of the limitations of numerical modelling to capture the unsteady phenomena has been included. The physical origin of the unsteadiness has also been explored.

Chapter 3

Experimental method

This chapter is dedicated to the detailed description of the experimental set up and instrumentation. The Oxford Rotor Facility (ORF) is introduced first, with a brief description of its original capability and the modifications it had to undergo to conduct the research reported in this thesis. Following this, the three different types of instrumentation installed in the facility are thoroughly discussed. Finally, the data acquisition process followed to convert the raw data into meaningful aerodynamic results is briefly explained.

3.1 The Oxford Rotor Facility

All experiments were conducted in the Oxford Rotor Facility, a transient isentropic light piston facility designed to investigate the aero-thermal behavior of transonic high pressure turbines at engine representative conditions [72]. Recently, the use of the facility has focused on research of the turbine secondary air system.

3.1.1 Original ORF design

Initially, the ORF was conceived as a facility to experimentally investigate the quasi-steady and unsteady aero-thermal behaviour of high pressure transonic turbine stages [72]. The working section comprised a 1.5 turbine stage (36 HP NGVs - 60 HP rotor blades -

21 IP NGVs) driven by an isentropic light piston tube for a test duration of quasi-steady aero-thermodynamic behaviour of approximately 80 ms. The ORF was designed to create a realistic engine-like environment by matching the main non-dimensional parameters and using aerodynamic blade designs from a real civil turbofan aero-engine.

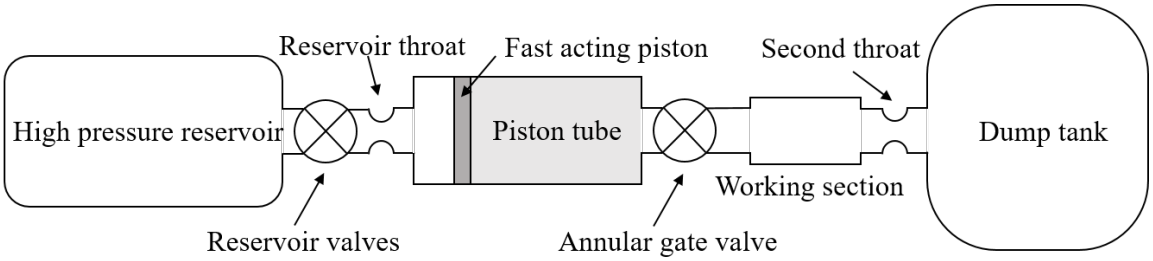

Figure 3.1: Schematic of the Oxford Rotor Facility.

A schematic of the ORF is shown in Fig.3.1. To carry out a test, the reservoir valves allowed the high pressure air from the plenum to go through the reservoir throat and drive the piston along the piston tube. The pressure and temperature of the air increased in the piston tube until the desired conditions were reached. The high pressure air drove the piston isentropically compressing the driven gas. Then, the fast acting annular gate valve opened raising the temperature and pressure in the working section. The working section was isolated from the downstream dump tank by a second throat that also set the pressure ratio across the stage.

Reproducing an engine-realistic environment of the hot end of a large civil turbofan in an experimental facility is prohibitive due to the high pressures and temperatures at the entry of the turbine stage. However, a similar flow field representative of that found in a real engine can be simulated at lower values of pressure and temperature if the non-dimensional parameters of pressure ratio, $\frac{p_{01}}{p_{04}}$, specific speed, $\frac{N}{\sqrt{T_{01}}}$, Reynolds number, Re, and gas-to-wall temperature ratio, $\frac{T_{01}}{T_{\text{wall}}}$, are matched.

$$\frac{\dot{m}\sqrt{T_{01}}}{p_{01}},\ \eta,\ \frac{\Delta T_0}{T_{01}} = f\left\{\frac{p_{01}}{p_{04}},\ \frac{N}{\sqrt{T_{01}}},\ \text{Re},\ \frac{T_{01}}{T_{\text{wall}}}\right\}$$

Table 3.1: Original Oxford Rotor Facility operating conditions [73].

Parameter	Expression	Value	Units
Rotor disc speed	N	9000	rpm
Mass flow rate	$\dot{m}$	29	kg/s
Turbine inlet temperature	T_{01}	374	K
Pressure ratio	$\frac{p_{01}}{p_{04}}$	3	–
Reynolds number (based on NGV C_{ax})	Re	2.7×10^6	–
Gas to wall temperature ratio	$\frac{T_{01}}{T_{\mathrm{wall}}}$	1.3	–
NGV exit Mach number	$\mathrm{M}_{\mathrm{NGV}}$	0.93	–
Specific speed	$\frac{N}{\sqrt{T_{01}}}$	460	rpm $\sqrt{\mathrm{K}}$
Specific mass flow	$\frac{\dot{m}\sqrt{T_{01}}}{p_{01}}$	7.025×10^{-4}	kg/ s $\sqrt{\mathrm{K}}$/Pa

Figure 3.2: Photograph of the Oxford Rotor Facility in the Oxford Thermofluids Institute.

After moving to the new Southwell building, the ORF was re-commissioned to its former capability using EPSRC funds in the Oxford Thermofluids Institute of the University of Oxford, as shown in Fig.3.2. In addition, the facility was upgraded from its original configuration to study turbine rim sealing flows with funding from Rolls-Royce plc. Within this project, the facility had to undergo major modifications in both the air supply systems and the working section to accommodate the new test conditions and configurations that are described in section 3.1.2.

3.1.2 ORF for secondary air systems research

The different research goals of this project required further modifications to the original facility. The staged testing approach demanded accessibility to the working section to allow for quick and easy changes of configuration. Moreover, based on the results of Beard *et al.* [19], additional instrumentation was included further inbound into the cavity. Hot gas ingestion has been historically quantified through sealing effectiveness, derived from measurements of gas concentration. With the aim of quantifying the sealing performance of the rim seal, the ORF was equipped with a system to take gas concentration measurements of the seeded purge flow with a gas analyser that would be converted into sealing effectiveness data. Due to the settling time of the gas analyser, the air system supply was also redesigned in order to achieve a steady state continuous running time of the order of minutes rather than milliseconds.

Gas analysers have a typical time response of a few seconds, but more realistically it adds up to $10 - 15\,\mathrm{s}$ when taking into account the transit time of the sample gas through the pneumatic tubing used to connect the sensor to the measurement location. Therefore, to determine sealing effectiveness through gas concentration measurements, a test period of the order of minutes was essential. An extended run time of duration of minutes was achieved through two main changes. Firstly, a new air delivery system was implemented to supply the air feed to the facility from a $60\,\mathrm{m}^3$ store of ambient temperature air at

27.6 bar. The air feed system is later described in more detail. Secondly, the facility working section was redesigned with an annulus line of reduced radial span to minimise the required mainstream mass flow.

Operating point

Matching the relevant non-dimensional variables ensures the flow field in the experimental facility is representative of that found in a real gas turbine engine. The non-dimensional and pseudo non-dimensional parameters of the original facility reported in Table 3.1 were maintained and the new operating point of the ORF derived from them.

All throughout this study, the facility was operated at room temperature and therefore, based on the specific speed of Table 3.1, the new design speed was $N = 7833\,\text{rpm}$. This was approximated to $N \sim 7850\,\text{rpm}$ and referred to as the nominal speed at design conditions. The new ORF nominal conditions are summarised in Table 3.2.

$$\frac{N}{\sqrt{T_0}} = 460 \quad \rightarrow \quad \text{for} \quad T_0 = 290\,\text{K} \quad \rightarrow \quad N \sim 7850\,\text{rpm}$$

Table 3.2: Oxford Rotor Facility operating conditions at the NGV hub exit [73].

N	M_{ax}	Re_{ax}	$\dot{m}$
7850 rpm	0.342	10^6	29 kg/s

3.1.3 Modifications to the ORF

The new design requirement was a system capable of matching the original ORF test Reynolds number to ensure engine-representative conditions. This was envisioned to be achieved with a new feed system and a reduced annulus casing line. The new air supply system would allow the operation of the facility in steady state and a lower span in the annulus would decrease the mass flow requirement so that longer test runs could be completed with the same volume of air. The feed pressure to the system was estimated at

10 bar (design parameter). A second throat downstream of the working section set the required pressure ratio to provide the desired operating conditions.

The compressed air in the 60 m^3 volume tanks that feed the 27.6 bar air supply line was kept at ambient temperature for these investigations. In order to feed the mainstream flow, a minimum of 10 bar was required upstream of the working section. The available mass of air ($m = pVol/RT$) at the nominal mass flow rate of 29 kg/s would allow a maximum testing time of the order of $\sim$ 40 s. Given that the vanes and rotor blades were removed from the main gas path in the initial stages of the project, there was no need for such a large mainstream flow supply and a reduced annulus section could be utilised to minimise the mass flow demand. This modification was aimed to increase the running time of the facility to at least 6 minutes (with $\dot{m} \leq 6$ kg/s), allowing ample time for gas concentration measurements.

The modified ORF was able to match the mainstream flow Reynolds number. However, owing to the fact that the mainstream Reynolds number was not expected to have a major influence on the cavity flow, the experiments reported in this thesis were run at lower Reynolds number. Two primary reasons supported this decision:

1. A lower air mass flow requirement extended the potential run time (and the number of measurements possible with a single test) thereby allowing an extensive and wide ranging test matrix. Only the parameters expected to have the largest impact were investigated across all three stages of testing. A longer run test was paramount to conduct gas concentration measurements with a multiplexer sequentially sampling from different positions. This is further explained in section 3.2.2.

2. The research group at the University of Surrey were developing, in collaboration with the ORF research group, a CFD method based in LES. The run time of LES simulations with high mainstream Reynolds number would have been prohibitive and very restrictive for this research.

The experiments at lower mainstream Reynolds number were conducted without the second throat in place, with the air flow exhausted to a downstream plenum at atmospheric pressure. The mass flow requirement was then reduced to ~ 1.4 kg/s allowing longer test durations in steady state of the order of 6 minutes.

Reduced annulus

The profile of the casing wall was redesigned and the annulus height reduced to 20% of its original radial span in order to increase the running time of the facility and lower the mass flow requirement. This was performed ensuring unaffected interaction between the mainstream and cavity purge flows whilst preserving the aerodynamic flow conditions above the rim seal between the HP NGV exit and rotor inlet. Matching the axial Mach number in the main gas path regardless of the NGVs or rotor blades being present was of paramount importance to guarantee an engine realistic flow field when a full stage was to be tested. For the scope of this fundamental study, this approach allowed comparison between different experimental configurations. One and two dimensional modelling of the working section of the facility were performed to make sure this requirement was satisfied and the aerodynamic losses were kept to a minimum.

- **1D modelling**

A one-dimensional model consisting of basic calculations of pressures, velocities and areas with the compressible flow equations was used to obtain the first estimations of the aerothermodynamic parameters in the main gas path. The axial Mach number and axial Reynolds number at the hub were obtained from the original set-up and taken as input design parameters. The desired mass flow rate in the main gas path was imposed by the pressure ratio across the test section. The ORF was simplified to a choked nozzle leading to a duct with an acute area contraction to accelerate the flow before dumping it into a plenum tank. A choked plate at the back would set the pressure ratio exhausting the air to the room. A 1D simple sketch can be seen in Fig.3.3.

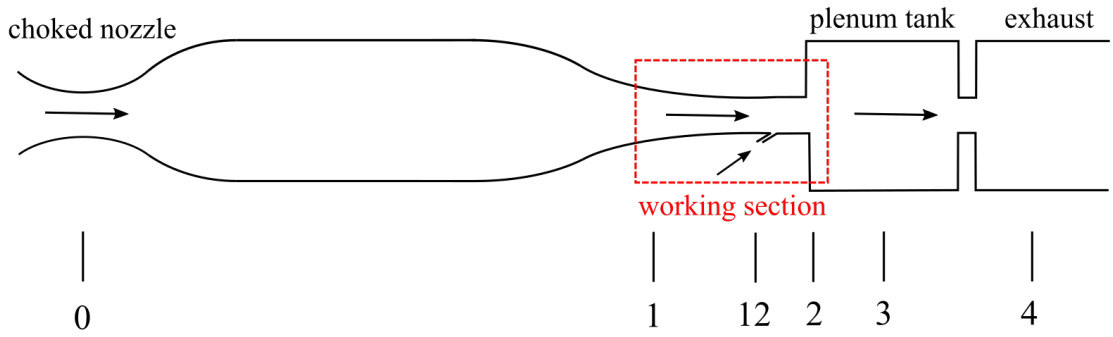

Figure 3.3: Basic design sketch for 1D calculations.

Station 1: With the available information at the entry to the working section ($\mathrm{M}_{\mathrm{ax},1}$, $\mathrm{Re}_{\mathrm{ax},1}$ and T_{01}) and the isentropic compressible flow equations Eq.3.1, Eq.3.2, Eq.3.3 and Eq.3.4 and Eq.3.5 the parameters T_1, p_1, p_{01}, $U_{\mathrm{ax},1}$ and $\dot{m}_1$ were calculated.

$$\frac{T_0}{T} = \left(1 + \frac{\gamma - 1}{2}\mathrm{M}^2\right) \tag{3.1}$$

$$\frac{p_0}{p} = \left(1 + \frac{\gamma - 1}{2}\mathrm{M}^2\right)^{\frac{\gamma}{\gamma - 1}} \tag{3.2}$$

$$U = \mathrm{M}\sqrt{\gamma RT} \tag{3.3}$$

$$\dot{m} = \frac{p}{RT} U_{\mathrm{ax}} A \tag{3.4}$$

$$\mathrm{Re}_{\mathrm{ax}} = \frac{\rho U_{\mathrm{ax}} C_{\mathrm{ax}}}{\mu} \tag{3.5}$$

All experiments were performed at ambient temperature, therefore $T_{01} = 290\,\mathrm{K}$ remained constant throughout the different stations in the 1D model of Fig.3.3. The viscosity was obtained at this temperature from the Sutherland law, Eq.3.6, where T_{ref} is the reference temperature, μ_{ref} is the reference viscosity at the given reference temperature and S is the Sutherland temperature. The coefficients of the Sutherland law for an air medium are $T_{\mathrm{ref}} = 273.15\,\mathrm{K}$, $S_{\mathrm{ref}} = 110.4\,\mathrm{K}$ and $\mu_{\mathrm{ref}} = 1.7894 \times 10^{-5}\,\mathrm{kg/m\,s}$.

$$\mu = \mu_{\text{ref}} \left(\frac{T}{T_{\text{ref}}} \right)^{\frac{3}{2}} \left(\frac{T_{\text{ref}} + S_{\text{ref}}}{T + S_{\text{ref}}} \right) \tag{3.6}$$

Station 12: The velocity through the rim seal was estimated as half of the axial velocity in the gas path, $U_{12} = 0.5\,U_1$. This value was deemed best guess based on previous experience during a discussion with the collaborators in Surrey. The static temperature at the seal, T_{12}, required to calculate the flow density, was obtained from an iterative process using Eq.3.1 with M_{12} and $T_{0,12}$. Assuming that the mixing of the annulus and purge flow occurred at constant static pressure, $p_{12} = p_1$, the sealing mass flow for a certain gap size, $\dot{m}_{12}$, was obtained with Eq.3.4.

Station 0: The design requirement to keep constant mass flow in the annulus determined that the upstream nozzle must be choked, $\mathrm{M}_0 = 1$, and therefore $\dot{m}_0 = \dot{m}_1$ for continuity. An initial guess set the total pressure to 10 bar and allowed an iterative process to run and calculate the diameter of the choked nozzle with expression Eq.3.7.

$$d_{\text{nozzle}} = \sqrt{4/\pi \; \dot{m} \; \frac{\sqrt{R\,T/\gamma}}{p} \left(\frac{\gamma + 1}{2} \right)^3} \tag{3.7}$$

Stations 4, 3 and 2: The main assumption imposed that all the dynamic head was lost when the flow was dumped into the tank ($p_{03} = p_2$) and that the tank exhausted to atmosphere through the choked plate ($p_4 = 1$ bar). The total temperature remained unchanged and mass conservation accounted for the addition of the purge flow into the mainstream $\dot{m}_1 + \dot{m}_{12} = \dot{m}_2 = \dot{m}_3 = \dot{m}_4$. Again, iterations were required to solve the system and obtain the area required to choke the back plate. A first estimation for the back throat area was assumed and then p_{03} was calculated from Eq.3.8 allowing for M_4, p_{04}, T_4 and U_4 to be found.

$$\dot{m}^* = \frac{p_{01} A^*_{\text{throat}}}{\sqrt{T_{01}}} \left(\frac{\gamma}{R} \right)^{1/2} \left(\frac{(\gamma + 1)}{2} \right)^{\frac{-(\gamma+1)}{2(\gamma-1)}} \tag{3.8}$$

The mass flow equation was then solved for M_2, and with it, p_{02}, T_2 and U_2 were obtained. Two conditions must be satisfied in order to complete the iterative process and achieve convergence: that the calculated mainstream mass flow matched the initial one; and that the exit flow conditions calculated from the thermodynamic variables in station 4 agreed with those in station 2. In case of a mismatch, a new value of A^*_{throat} was assumed and the process repeated until the above conditions were satisfied.

Results: An inlet total pressure of 4.13 bar with the original annulus area provided a mainstream mass flow input of 29.26 kg/s (agreeing with Table 3.1). Bringing the casing line down to 20% of the original area reduced the mass flow requirement to 5.8 kg/s, well within target. This value was used as a first approximation for the CFD inlet boundary conditions.

- **2D modelling**

A 2D model was created to assess the flow behaviour in the new working section with the goal of minimising the pressure losses in the reduced annulus design. The geometry was created from the original ORF CAD files using Autodesk© Inventor LT™ and then imported into ANSYS© ICEM CFD™ 17.2 to generate a mesh. Once the domain was discretised it was finally loaded into FLUENT© 17.2 to solve the flow equations. The boundary conditions for the simulations were imposed based on the estimations obtained from the 1D modelling. After convergence was achieved, the results were analysed using MATLAB 2016a and the ANSYS© post-processing tool CFD-POST.

Geometry: A qualitative study to assess the best casing line was performed without including the volume corresponding to the cavity. The convergent shape of the duct induced an acceleration of the flow followed by a diffusion that triggered flow separation downstream of the working section. The original geometry of the working section was modelled and compared to new designs with a reduced casing line. Some examples of geometries and velocity contours are shown in Fig.3.4. The final design featured a constant

casing line after the duct throat to allow a slight diffusion whilst minimising the extension of the separation region and the pressure loss. The geometry labelled *Reduced annulus 1* in Fig.3.4 was selected to be manufactured and installed in the ORF.

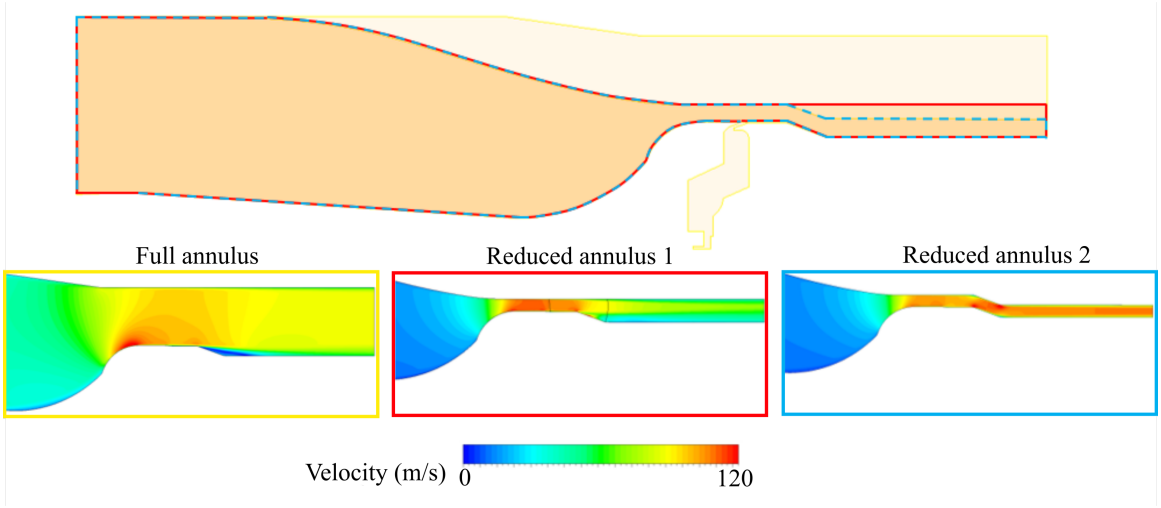

Figure 3.4: Examples of geometries investigated for the reduced annulus with velocity contours for each one.

Fig.3.5 shows the geometry of the original full height annulus of the ORF and the reduced annulus casing line. The dashed lines for the NGV and rotor blades are purely for indication purposes. The axial velocity distribution along the spanwise direction shows in blue that the flow in the hub region (5% of total span) reached the same target axial velocity with the reduced annulus.

Nonetheless, it is important to emphasise that the boundary layers at each endwall of the annulus would cover a large portion of the annulus span thus hindering the development of secondary flows. Moreover, the reduced annulus NGVs have not been scaled to achieve a representative loading. As a consequence, this configuration would not be adequate to study the aerodynamics of the main gas path but it is considered representative in the rim seal and hub region.

Mesh: A mesh sensitivity study concluded that a structured mesh of 55 000 elements provided a grid independent solution for flow velocity, static pressure and mass flow. The

first cell height at the hub was set at 7×10^{-3} mm to provide a $y^+ < 7$ and a maximum cell aspect ratio of 66.

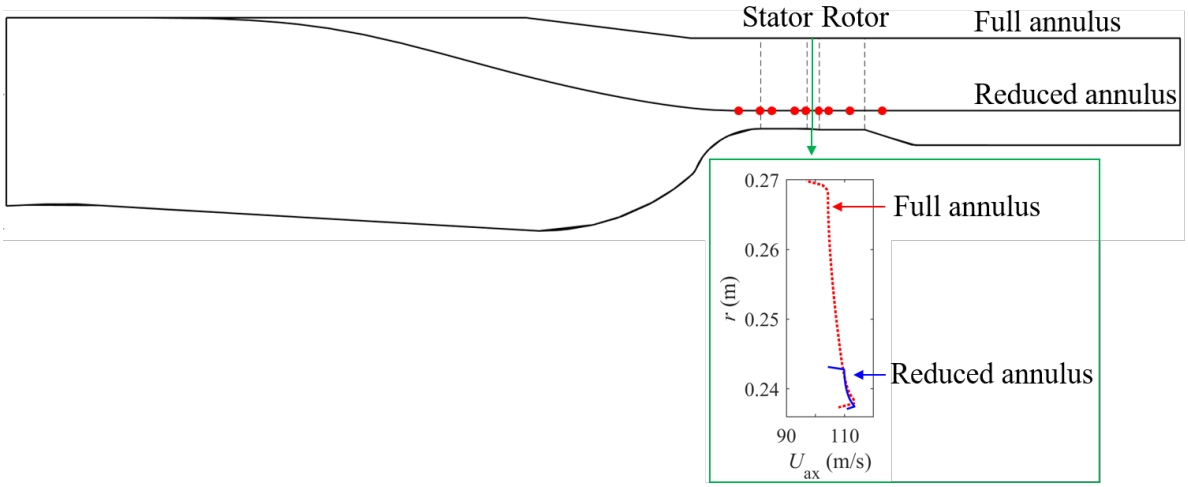

Figure 3.5: Domain geometry of the 2D models with original and reduced annulus casing lines with zoomed view of the axial velocity distributions at the rim seal.

Solver: A two dimensional density based steady solver with axisymmetric swirl using a k-ω SST turbulence model was used to evaluate the performance of a number of modified casing annulus lines. An implicit method and second order upwind spatial discretisation were implemented whilst boundary conditions of inlet mass flows (purge and mainstream) and exit static pressure with radial equilibrium were applied. The results from the 1D model were used as an initial guess but an iterative process was required to finally achieve the target hub axial velocity of 115 m/s at the exit of the NGV. The 2D study concluded that the constant annulus line downstream of the rim seal provided the minimum pressure loss and it was therefore implemented into the CAD model as shown in Fig.3.6.

Facility working section design

Following the design of the reduced annulus casing line, a total of 25 components were re-designed to accommodate the test configurations of the following stages and to allow easy changes of set up. Installation of new and more extensive instrumentation was also considered. The new components are listed in Table 3.3 and numbered in Fig.3.6.

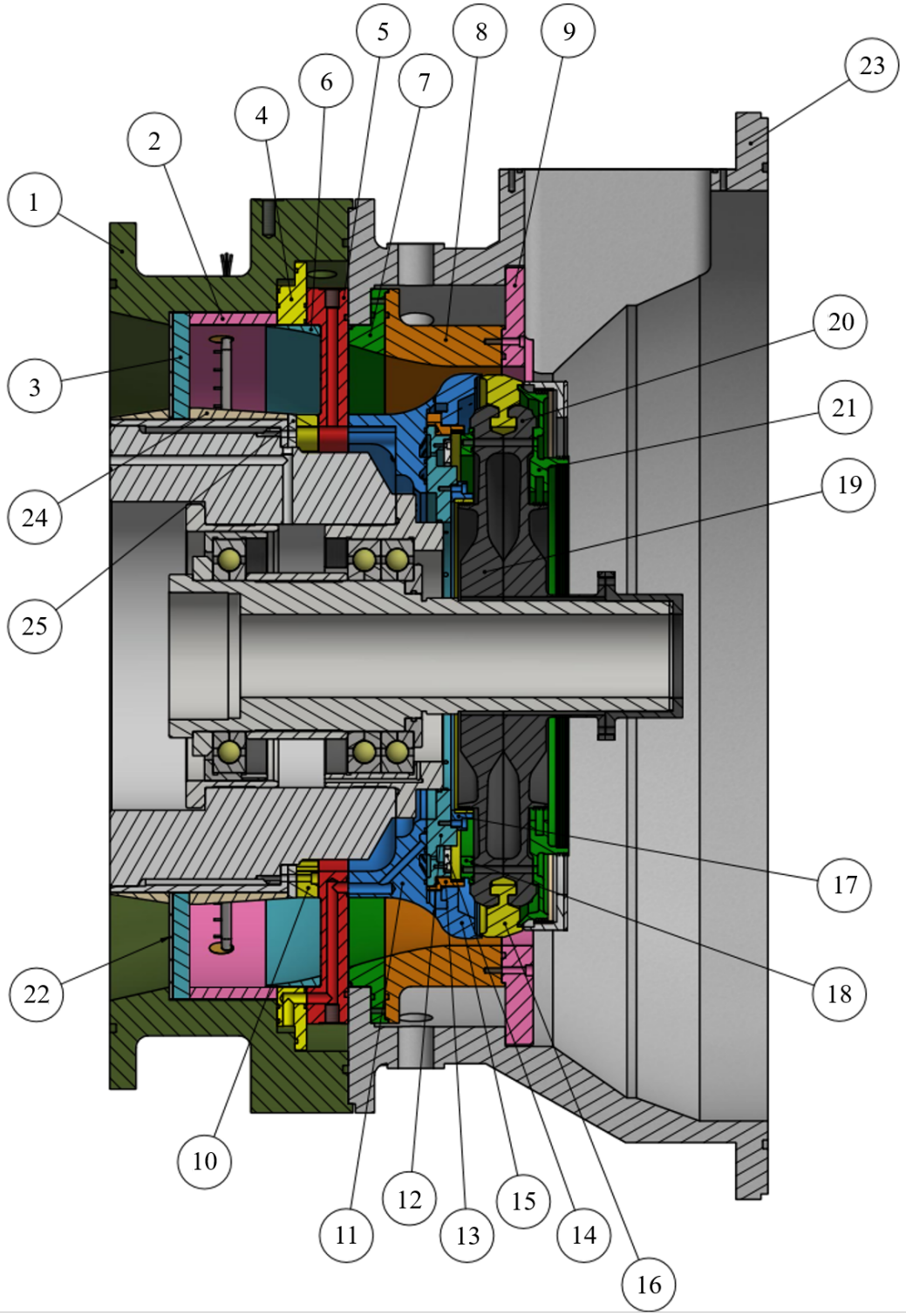

Figure 3.6: Longitudinal cross section of the CAD model.

A main gas path with a simple reduced annulus area free of any blading was initially installed into the test facility with dummy stator and rotor platforms. This study acts as a continuation of the research published by Beard *et al.* [19] and features the same cavity geometry. Their experimental test conditions were first replicated (Stage 1: purge flow and rotor disc rotation only).

Table 3.3: List of modified components in the ORF shown in Fig.3.6.

Item	Description	Item	Description
1	Contraction outer case	14	Hub feed barrier
2	Outer case liner	15	Vane hub ring
3	Mesh support	16	Mini disc
4	Case feed distributor	17	Lower front static seal
5	Feed plate	18	Upper front static seal
6	Reduced annulus part 1	19	Split disc front
7	Reduced annulus part 2	20	Split disc rear
8	Reduced annulus part 3	21	Seal rear
9	Reduced annulus part 4	22	Existing wire mesh plate
10	Hub interface	23	IP blade ring
11	Hub inlet transition	24	Inlet inner annulus liner
12	Hub feed distributor	25	Inlet inner spacer ring
13	Upper hub seal ring		

Details of the working section geometry adopted for this study are presented in Fig 3.7(a). Without blading, the rotor hub platform (1) and the hub vane ring (2) were solid, axisymmetric rings that defined the rim seal design. The ORF includes a split disc (3) allowing modification to the rotor seal geometry by simply replacing the rotor hub platform component. The potential leak path between the rotor disc and rotor hub platform is sealed using flexible silicone. The rim seal purge flow is injected into the rotor disc cavity between the lower labyrinth seal (5) and upper overlapping seal. This flow enters an annular cavity upstream of the feed distributor (4) and through an array of 60 holes of 2.5 mm diameter, it is evenly distributed circumferentially. A blockage ring at the hole exit discourages any jetting and promotes mixing prior to injection into the rotor cavity through a 2.6 mm annular slot.

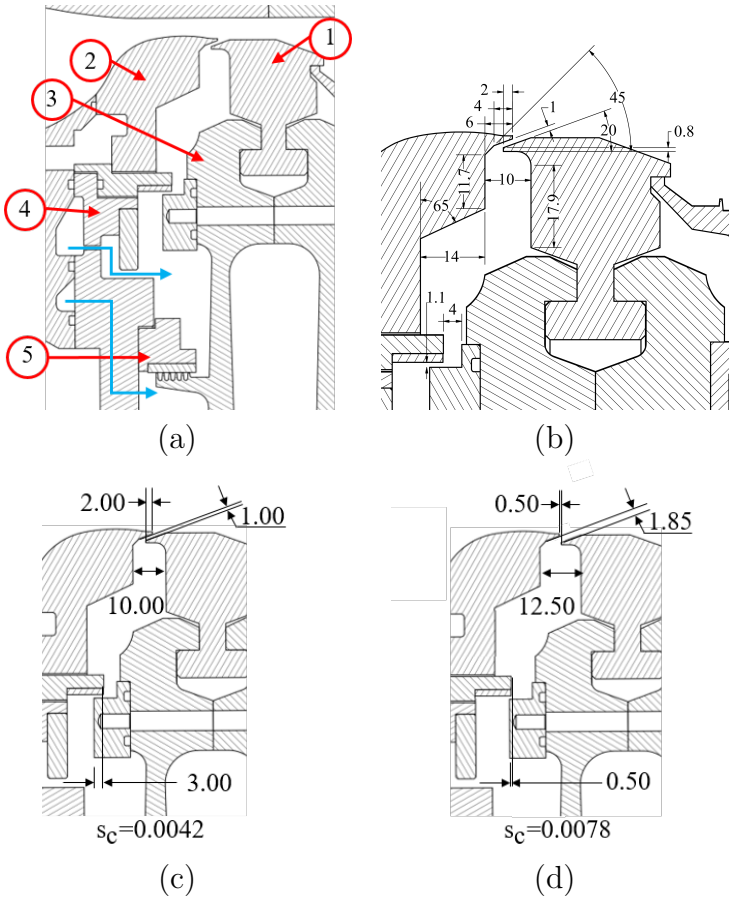

Figure 3.7: (a)Details of the working section geometry and purge flow supply, (b) details of the rim seal geometry (mm), (c) relevant dimensions for the small gap size, $s_c = 0.0042$, and (d) relevant dimensions for the large gap size, $s_c = 0.0078$.

A secondary air supply beneath the rotor labyrinth seal is available to compensate for leakages from this volume. However, Beard *et al.* [19] demonstrated that the volume was well sealed, and therefore the secondary air feed was not used during this study.

The surfaces of the rim seal and rotor disc cavity were axisymmetric and polished to avoid non-uniformities. In particular, all bolt heads were counter-bored, filled and smoothed. The chute seal design used in this study is identical to that investigated by Beard *et al.* [19] and shown in Fig.3.7(b). The nominal seal clearance was designed to be 1 mm at the maximum rotor disc speed of 9000 rpm with an axial overlap of the stator and rotor surfaces at the rim of 2 mm, Fig.3.7(c). The radial growth of the rotor disc was previously evaluated by Beard *et al.* and accounted for in this study. Introducing

a spacer ring between the disc and the shaft increased the axial distance between the stator and rotor ring, leading to a seal gap of 1.85 mm, Fig.3.7(d). The larger seal gap simulates a potential engine off-design condition, where the relative axial displacement between static and rotating components may vary. It is worth highlighting that, from a 2 mm axial overlap between the stator and rotor surfaces, opening the rim seal led to a 0.5 mm axial gap instead.

Enhanced air supply system

The ORF was initially designed as a transient test facility that used an isentropic light piston tube to provide the air supply. This operating mode allowed a running time of approximately 80 ms, which was insufficient for the investigation of hot ingestion here described if sealing effectiveness data were to be obtained. To enable the acquisition of sealing effectiveness data, an air feed system was designed to provide a steady mass flow of up to 6 kg/s over a test period of the order of minutes. A schematic of the installed system is shown in Fig.3.8 below.

In the configuration with no mainstream flow, the purge flow is supplied by an Alicat MC Series 2000 mass flow controller, with a traceable uncertainty of ±0.8% of reading plus ±0.2% of full scale, connected to the air supply line of compressed air at 6.9 bar (100 psi), Fig.3.8(a). Dry air at ambient temperature and 27.6 bar (400 psi) is supplied to the test area through a 101.6 mm (4 inch) diameter pipe. Following isolation valves, the parallel connection of a flow limiter and pressure reducing valve, Fig.3.9(a), ensures constant pressure upstream of separate ISO9300:2015 compliant choked nozzles (uncertainty in $C_{\mathrm{d}} = \pm 0.5\%$). With annulus flow, this arrangement supplies the mainstream and purge flows, thereby achieving constant mass flow conditions for each stream, Fig.3.8(b).

The constant area of the flow limiter is set to supply the required total mass flow with the maximum 27.6 bar feed pressure. As the experiment proceeds, the mass flow

through the limiter decreases since the feed pressure decays during blow down operation mode. However, the regulator mass flow increases accordingly to achieve constant pressure upstream of the metering nozzles and steady mainstream and purge mass flows. The operating principle of this assembly is depicted in Fig.3.10(a). The mainstream and purge flows are initiated by solenoid actuated ball valves located prior to their respective metering nozzles. The mainstream feed passes through two venturi nozzles in parallel and is introduced into a large settling tank before entering the working section through the feed distributor visible in Fig.3.9(b) and (c).

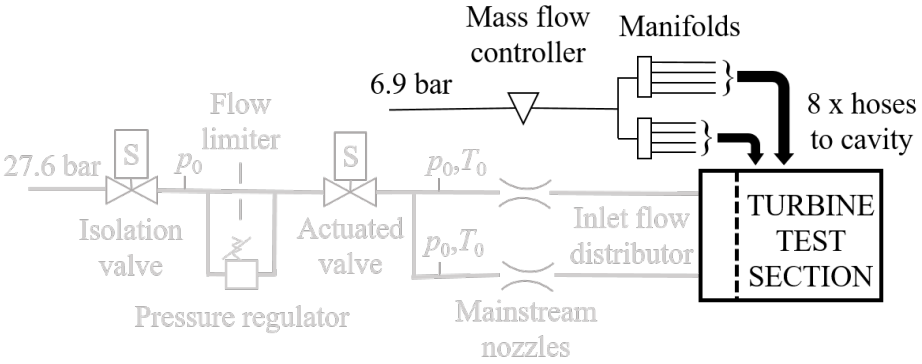

(a)

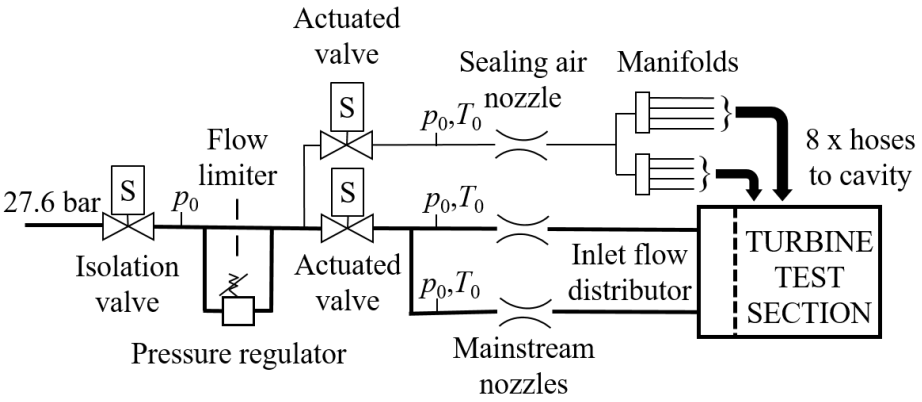

(b)

Figure 3.8: Schematic of the mainstream and purge air feed system for (a) $\mathrm{Re_{ax}} = 0$ (Stage 1) and (b) $\mathrm{Re_{ax}} = 2.6 \times 10^5$ (Stages 2 and 3).

A 50.8 mm (2 inch) diameter pipe line was branched from the main duct downstream the pressure regulator and flow limiter to provide the purge air into the cavity. Another choked venturi nozzle effectively sets the purge supply before it enters a manifold that

introduces the flow in the working section by means of 8 flexible hoses. The hoses are evenly distributed around the circumference of the facility and connected to an annular settling volume in the working section prior to entering the cavity volume.

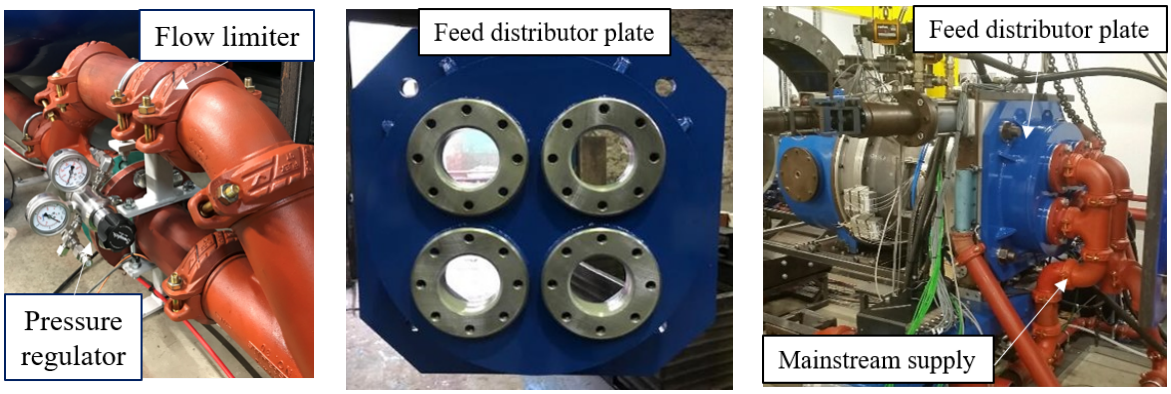

Figure 3.9: (a) Pressure reducing valve and flow limiter assembly, (b) feed distributor plate and (c) feed distributor assembly in the ORF.

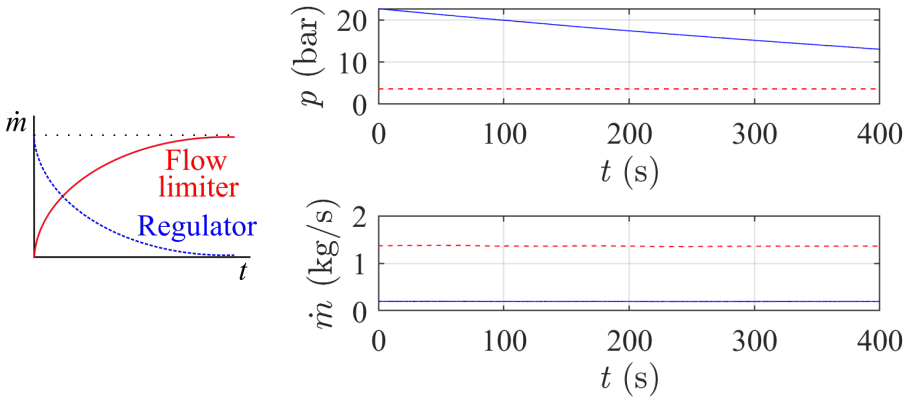

(a) (b)

Figure 3.10: (a) Operation principle of the flow limiter and pressure regulator and (b) typical air feed system pressures and mass flows.

Total pressure and temperature measurements were acquired upstream of each nozzle. The uncertainty associated with the measurement of the mainstream mass flow was ±0.7%, whereas for the purge mass flow it ranged between ±0.75 and ± 2.0% depending on nozzle diameter. To reduce measurement uncertainty, for test conditions with low purge mass flow conditions ($\dot{m}_{\text{purge}} < 0.035$ kg/s) the purge flow was instead metered by an Alicat MC Series 2000 mass flow controller, with a traceable uncertainty of ±0.8% of

reading plus ±0.2% of full scale. Together with the previously described reduced annulus area, a steady test time of up to 20 minutes was possible at the test conditions detailed later. Typical system pressures and mass flows are plotted in Fig.3.10(b).

Venturi flow nozzles Different venturi flow nozzles were designed in accordance to the test conditions and configurations of the working section. For the first scenario, no nozzles were employed since no mainstream flow was supplied, see Fig.3.8(a).

The two parallel nozzles that provided the mainstream flow were dimensioned to supply a maximum air flow of 4 kg/s (2 kg/s each) with an inlet total pressure of 10 bar. Based on these design conditions, and for a standard temperature of 290 K, Eq.3.7 set the diameter of the mainstream flow nozzles.

The effect of the seal to axial velocity ratio, $U_{\mathrm{m}}/U_{\mathrm{ax}}$, on the mechanism of ingestion was experimentally studied covering the range $U_{\mathrm{m}}/U_{\mathrm{ax}} \in [0, 0.6]$ based on typical in-service large civil aero-engines. The target axial velocity in the annulus was kept constant throughout the entire test matrix (design parameter), thus the different values of seal-to-axial velocity ratio were achieved through changes in the purge flow velocity. Based on the continuity equation, Eq.3.9, the flow velocity through the seal given a constant seal clearance was adjusted with the purge mass flow. The size of the nozzles was obtained with Eq.3.7.

$$\dot{m}_{\mathrm{purge}} = \rho \, U_{\mathrm{m}} \, A_{\mathrm{seal}} \tag{3.9}$$

Stage 2: Eq.3.7 set the diameter of the mainstream flow nozzles to 32.8 mm. Table 3.4 summarises the dimensions of the venturi nozzles used to achieve each one of the required purge rates of Stage 2.

Stage 3: The addition of the NGVs introduced a swirl component and the mainstream flow was no longer axial. The Mach Number at the exit of the NGV hub was

approximately $M_{ann} = 0.87$ and the annulus section was transonic. Assuming the static pressure at the rim was maintained, the total pressure upstream of the NGVs was dictated by the total Mach Number setting the total-to-static pressure ratio across the NGVs.

Table 3.4: Purge flow nozzle diameter for axisymmetric annulus flow (Stage 2).

d_{nozzle}	(mm)		5.2	7.3	9.0	10.4	12.7	14.8	16.4	17.8
U_m/U_{ax}	(-)	$s_c = 0.0042$	0.08	0.16	0.23	0.31	0.46	0.63		
		$s_c = 0.0078$		0.1		0.2			0.55	0.63

Based on the results of Stage 2, the highest static pressure at the rim was $p_{rim} = 1.1$ bar achieved at $U_m/U_{ax} = 0.5$ for $s_c = 0.0078$. Assuming choked conditions at the annulus downstream of the NGVs for ease of calculation and to allow for some design margin, the total-to-static pressure ratio across the NGVs was 1.89 giving a required total pressure upstream of the vanes of $p_{0,upstream} = 2.08$ bar. This value ensured an axial Mach number of $M_{ax} = 0.34$ at the exit of the NGVs thus matching the axial flow conditions of Stage 3 to those of Stage 2. To guarantee a constant mass flow rate supply (choked nozzle $M = 1,\ p_0/p = 1.89$) the total pressure upstream the mainstream feed nozzles must be at least 1.89 times higher than the desired pressure at the entrance of the test section (upstream of the NGVs). Taking into account some pressure losses that may occur in the pipeline, the pressure at the outlet of the regulator had to be at least 5 bar. The pressure margin was increased to account for a safety factor and the upstream pressure requirement was set at 6 bar.

Table 3.5: Purge flow nozzle diameter for non-axisymmetric annulus flow (Stage 3).

d_{nozzle}	(mm)		4.5	5.2	6.6	7.8	9.0	10.4
U_m/U_{ax}	(-)	$s_c = 0.0042$	0.1		0.22	0.3	0.35	
		$s_c = 0.0078$	0.07	0.08	0.13	0.18	0.23	0.3

Axial velocity in the annulus (and therefore mass flow rate) were similar to those of Stage 2. However, since the total pressure upstream of the nozzles was higher, new mainstream nozzles with a smaller diameter ($d = 25.5$ mm) were required to deliver the same mainstream mass flow rate. Similarly, nozzles for the purge flow were machined to

account for the increase in upstream pressure and summarised in Table 3.5.

Nozzle guide vanes

The introduction of NGVs in Stage 3 of testing added a strong swirl component into the flow velocity in the main gas path generating variations in the pressure and velocity potential field. A set of NGVs was designed to adjust for the reduction in the annulus cross section The vane design was based on the original engine-realistic geometry previously tested in the ORF [72] with an axial chord of 34 mm, exit flow Mach number and swirl angle of 0.87 and 68° respectively, and radial span of 7.5 mm at the trailing edge. A total of 36 NGVs were included and manufactured using SLA rapid prototyping. The axial distance between the vane trailing edge and the rim seal was 9.4% of the vane axial chord. The stator vanes were introduced into the main gas path through 36 slots machined in the casing ring of the reduced annulus, Fig.3.11. The gas path remained bladeless downstream of the NGVs with an identical rotor disc geometry to that of the experimental set up with and without axisymmetric flow.

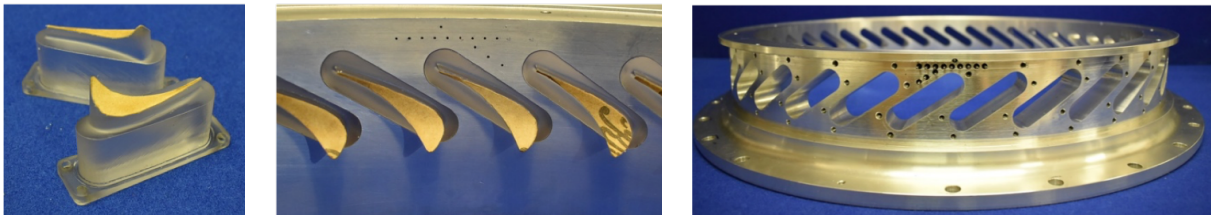

(a) (b) (c)

Figure 3.11: Photographs of (a) SLA NGVs, (b) assembly of NGVs in casing mounting ring with static pressure tappings visible and (c) casing mounting ring.

3.2 Instrumentation set up

Comprehensive low bandwidth pressure and temperature measurements were acquired throughout the working section (including the main gas path, purge flow feed system and the rotor disc and rim seal cavities) to ensure the desired test conditions were achieved in the main gas path and stator-rotor cavity. High bandwidth pressure transducers were

strategically located around the stator wall circumference to study the unsteady flow phenomena inside the cavity. A new measurement system to quantify the sealing effectiveness of the chute seal based on gas concentration measurements was commissioned in the ORF. The low bandwidth data is first described in this section followed by the sealing effectiveness and high bandwidth data. Another subsection is dedicated to the description of the data acquisition system.

3.2.1 Low bandwidth data

This section focuses on the pressures and temperatures acquired by a National Instruments PXI/SCXI data acquisition system logging data at 200 Hz.

Pressure data

All steady pressure measurements were obtained by pneumatic pressure transducers connected to 1.6 mm diameter tappings with flexible vinyl tubing. Absolute measurements were acquired using First Sensor CTE8000 transducers with a nominal uncertainty of $\pm 0.1\%$ of the full-scale output. Differential measurements were acquired using First Sensor BTEM5000 transducers with a nominal uncertainty of $\pm 0.2\%$ of the full-scale output.

Mainstream condition monitoring: The flow velocity in the reduced annulus was calculated from measurements of p_0, p and T_0. Mainstream p_0 was measured using four radial rakes, each including 4 pitot tubes covering the annulus height (15% to 85% approximately), placed upstream of the reduced annulus – see Fig.3.12(a) – and distributed at 90° intervals. The upstream pressure rakes, mounted with Sensor Technics CTE8000 Series $0 - 10$ bar absolute pressure transducers, provided validation that axisymmetric flow conditions in the annulus flow were achieved, Fig.3.13. In addition, higher range $0 - 16$ bar absolute pressure transducers were fitted in the control volume between the pressure reducing valve and upstream the venturi flow nozzles as depicted in Fig.3.8(b). A $0 - 35$ bar pressure transducer of the same series logged the pressure input to the system

from the tanks of compressed air. The typical error band of these sensors is ±0.1% of the full-scale output.

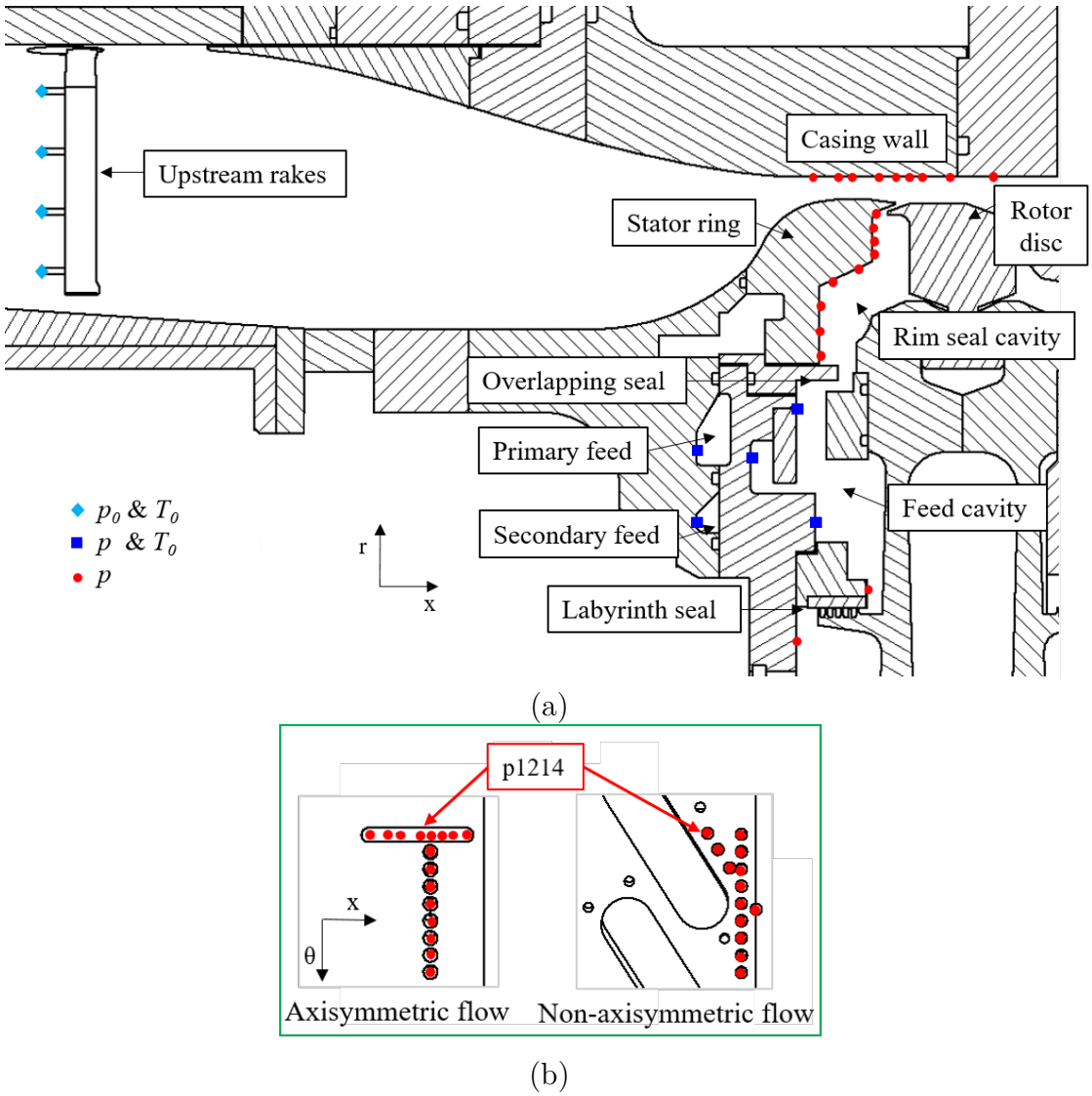

Figure 3.12: (a) Pressure and temperature instrumentation in the main gas path, feed and inner cavities and (b) view of the casing wall circumferential points for axisymmetric and non-axisymmetric annulus flow configurations above the rim seal.

A total of nine pressure tappings (connected to 0−5 bar absolute pressure transducers) were located above the seal following the axial direction at four circumferential locations. The position of the tappings was strategically chosen to capture the significant changes of static pressure expected to occur at the annulus based on the CFD results.

The angled slots in the new casing designed to introduce the NGVs in the annulus hindered the distribution of the axial static pressure measurements thus 5 data points

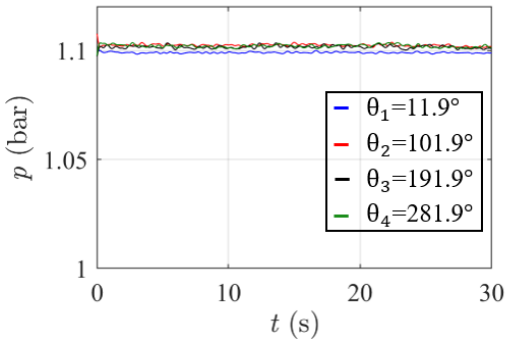

Figure 3.13: Typical upstream pressures ensuring axisymmetric flow in the annulus.

were aligned with the slots. As a result, the axial coordinate remained unchanged whilst a slight circumferential offset was introduced. The difference in measurement position for the axisymmetric (without NGVs) and non-axisymmetric (with NGVs) annulus flow test cases can be seen in Fig.3.12(b). The circumferential pressure asymmetries in the annulus were measured by nine pressure tappings located above the seal at a constant axial position and circumferentially spaced to cover one vane pitch.

Purge flow feed system: The measurement locations in the purge flow feed system and rotor cavity are shown in Fig.3.12(a). Locations with both pressure and temperature measurements are shown in blue, whereas those with only pressure measurements are labelled red. These pressures were acquired using First Sensor Series CTE8000 absolute pressure transducers with a nominal uncertainty of $\pm 0.1\%$ of the full-scale output.

Cavity instrumentation: The position of the radial static pressure tappings on the stator wall at the rim seal and cavity are shown in Fig.3.12(a) and Fig.3.14. Radial distributions of static pressure tappings were installed at four locations, distributed evenly around the cavity. At locations A and B nine radial measurement points extended across the entire radial span of the cavity, whereas at locations C and D a lower resolution of four repeat measurements was included.

The static pressure data were acquired by First Sensor BTEM5000 $0 - 100$ mbar

unidirectional differential pressure transducers with a nominal uncertainty of ±0.2% (or ±0.2 mbar) of the full-scale output. Measurements were referenced to the innermost measurement location (p1011) with this point using the mainstream pressure as reference. Note that the tapping in the furthest outward position in the rim seal, e.g. model point 1110, has not been included in the steady measurements to avoid flow disturbances. Pressures are often non-dimensionalised by the rotor disc dynamic head defining the cavity pressure coefficient, C_{p}, Eq.3.10. The uncertainty associated with this derived parameter is ±0.0017, see Appendix A. Tables 3.6 and 3.7 summarise the pressure measurement coordinates, model point numbers and types of pressure transducer.

$$C_{\mathrm{p}} = \frac{p - p_{1011}}{0.5\rho(\Omega b)^2} \tag{3.10}$$

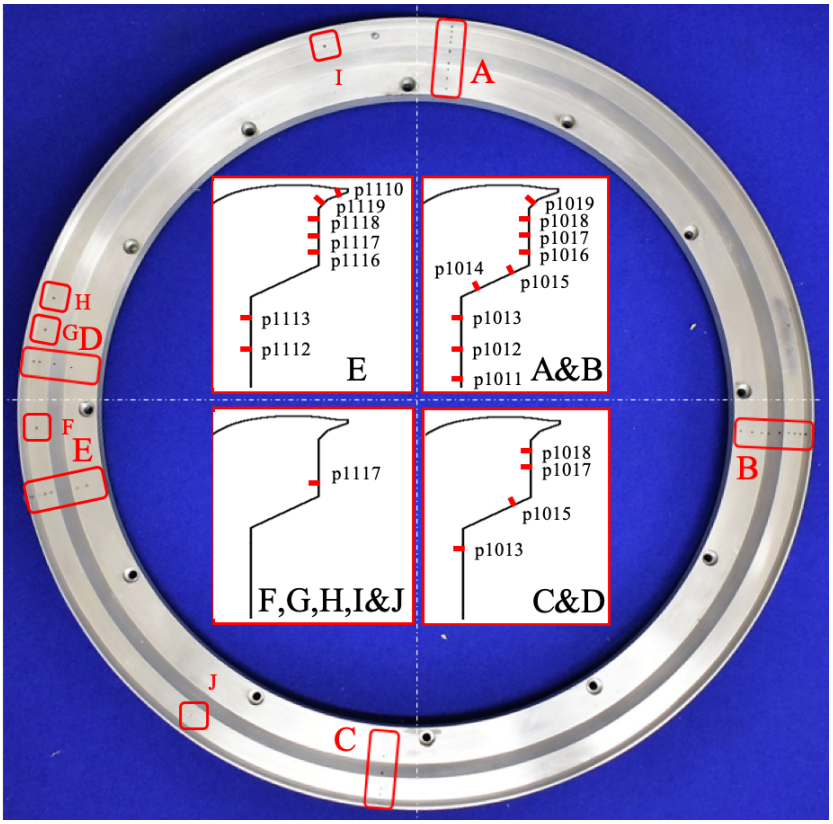

Figure 3.14: Pressure instrumentation in the stator ring.

Table 3.6: Summary of steady pressure measurements in the cavity.

Model point	**Type**	**Description**	**Radius (mm)**	**Sensor**	**Uncertainty (%FS)**
1011, 1021	dp	Cavity position 1	198.7	FS HCE $0-100$ mbar	0.2
1012, 1022	dp	Cavity position 2	205.7	FS HCE $0-100$ mbar	0.2
1013, 1023 1033, 1043	dp	Cavity position 3	211.7	FS HCE $0-100$ mbar	0.2
1014, 1024	dp	Cavity position 4	215.7	FS HCE $0-100$ mbar	0.2
1015, 1025 1035, 1045	dp	Cavity position 5	219.7	FS HCE $0-100$ mbar	0.2
1016, 1026	dp	Cavity position 6	224.2	FS HCE $0-100$ mbar	0.2
1017, 1027 1037, 1047	dp	Cavity position 7	227.7	FS HCE $0-100$ mbar	0.2
1018, 1028 1038, 1048	dp	Cavity position 8	231.2	FS HCE $0-100$ mbar	0.2
1019, 1029	dp	Cavity position 9	234.16	FS HCE $0-100$ mbar	0.2
1051	p	Primary (upper) feed cavity	172	FS CTE8000 0-10 bar	0.1
1052	p	Secondary (lower) feed cavity	157	FS CTE8000 0-10 bar	0.1
1053	p	Overlapping seal	184.5	FS CTE8000 0-10 bar	0.1
1054	p	Underneath overlapping seal	170	FS CTE8000 0-10 bar	0.1
1055	p	Inner cavity	157	FS CTE8000 0-10 bar	0.1
1056	p	Underneath labyrinth seal	127.5	FS CTE8000 0-10 bar	0.1
1057	p	Above labyrinth seal	134.5	FS CTE8000 0-10 bar	0.1

Table 3.7: Summary of steady pressure measurements.

Model point	**Type**	**Description**	**Radius (mm)**	**Sensor**	**Uncertainty (%FS)**
1211-1218	p	Axial mainstream location 1 positions 1-8	244	FS CTE8000 0-5 bar	0.1
1219		location 1 position 9			
1221-1228	p	Axial mainstream location 2 positions 1-8	244	FS CTE8000 0-5 bar	0.1
1325-1395	p	Circumferential locations 2-9 position 2	244	FS CTE8000 0-5 bar	0.1
1411, 1441	p_0	Upstream rakes locations 1, 4 position 1	174	FS CTE8000 0-5 bar	0.1
1412, 1442	p_0	Upstream rakes locations 1, 4 position 2	190	FS CTE8000 0-5 bar	0.1
1511	p_0	Sealing air nozzle	n/a	FS CTE8000 0-16 bar	0.1
1521	p_0	Upper bypass nozzle mainstream air	n/a	FS CTE8000 0-16 bar	0.1
1531	p_0	Lower bypass nozzle mainstream air	n/a	FS CTE8000 0-16 bar	0.1
1541	p_0	System upstream pressure	n/a	FS CTE8000 0-35 bar	0.1
1081	p	Oil bearing	n/a	FS CTE9000 0-10 bar	0.1
1082	dp	Labyrinth seal differential	n/a	ST BTE5000 ±350 mbar	0.1

Temperature data

Gas temperature measurements were acquired by k-type bare bead ($d = 76.2$ μm) thermocouples with exposed tips protruding into the flow. The associated measurement uncertainty was $\pm 0.45\%$ (or ± 1.3 K). The focus of this investigation has not been the temperature distribution inside the cavity, but temperatures at strategic points were used to derive other quantities such as flow density. The exact coordinates of the measurement points together with the model point are shown in Table 3.8.

Table 3.8: Summary of temperature measurements.

Model point	**Type**	**Description**	**Radius (mm)**	**Thermocouple type**	**Uncertainty (K)**
2051	T_0	Primary (upper) feed cavity	172	k-type	1.3
2052	T_0	Secondary (lower) feed cavity	157		
2053	T_0	Overlapping seal	184.5		
2054	T_0	Underneath overlapping seal	170		
2055	T_0	Inner cavity	157		
2411, 2421 2431, 2441	T_0	Mainstream upstream rakes	174	$d = 76.2$ μm	
2412, 2422 2432, 2442	T_0		190		
2413, 2423 2433, 2443	T_0		206		
2414, 2424 2434, 2444	T_0		233		
2511-2513	T_0	Sealing air nozzle	n/a		
2521-2524	T_0	Upper bypass nozzle	n/a		
2531-2534	T_0	Lower bypass nozzle	n/a		

Mainstream condition monitoring: Analogously to the pressure rakes shown in Fig.3.12(a), four radial rakes, each one including four thermocouples, were installed at the same axial coordinate to measure mainstream T_0. Temperature rakes were also located (together with pressure sensors) upstream of the choked venturi nozzles that supplied the air to the mainstream and purge streams, see Fig.3.8(b).

Purge flow feed system: Temperature measurements were also recorded in the purge flow feed system for monitoring purposes. The specific locations where these data were obtained can be seen in Fig.3.12(a).

3.2.2 Sealing effectiveness data

This section provides an introduction to the basic principles and requirements of the tracer gas technique followed by a detailed description of the new system installed in the ORF. Operation and calibration of the system are then explained before the gas sample measurement locations are introduced.

Evidence of hot gas ingestion from pressure measurements or flow visualisation provided qualitative information of the flow behaviour in turbine rim seals. Gas concentration data quantified the performance of the seal. A wide range of flow visualisation techniques were used to study the velocity flow field in the rim cavity such as Particle Image Velocimetry (PIV) (at Arizona State University [74], [55] but also at other research institutions like the University of Darmstadt [67]), Tunable Diode Laser, Laser Doppler Anemometry (LDA) or Velocimetry (LDV) [10], seeded smoke or oil paint. Despite their benefits, these techniques are unsuitable for the current research due to the limitations for optical access to the working section in the ORF. When it comes to experimentally quantifying ingestion, the use of a tracer gas has become the most extended practice ([36], [39], [29]).

Tracer gas technique

The tracer gas technique has proven to be a powerful methodology to quantify the performance of rim seals and the physics that govern the mechanism of hot gas ingestion. For safety reasons, the foreign gas must be non-toxic, environmentally friendly, colorless, odorless, inert, easily detectable and not present in other sources. Early studies reported the use of nitrous oxide ([13], [23], [36]) or helium [75] although carbon dioxide has become the most widespread option ([36], [33], [39], [74]). Clark *et al.* [76] cited that turbulent mixing prevails over molecular diffusion and therefore the use of a tracer gas with higher molecular weight than air is justified. Clark *et al.* described in high detail how to use carbon dioxide as a tracer gas to quantify sealing effectiveness.

Infrared (IR) spectometry in all its varieties (dispersive, non-dispersive (NDIR) and Fourier Transfrom (FTIR)) stands amongst the available techniques to measure gas concentration due to its superior sensitivity, selectivity and stability. The basic principle of this technology relies on the capability of the gas molecules to absorb infrared light, which is directly proportional to the gas concentration in the sample. Dispersive IR detectors use a prism to pre-select the desired wavelength of light to pass through the gas sample before reaching the detector. Non-dispersive sensors however, pass all the light source through the gas sample and a color filter placed before the light detector selects the desired wavelength of the gas, see Fig.3.15.

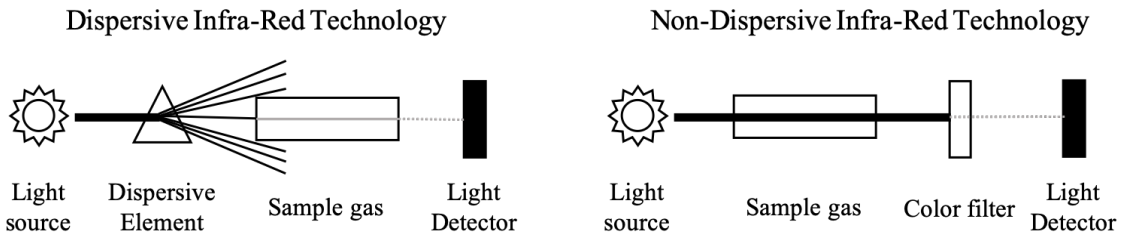

Figure 3.15: Dispersive (left) and non-dispersive (right) infrared technology operation.

The FTIR technique allows a wider spectral resolution although only the range of wavelengths related to carbon dioxide are of interest for the current study. For this

reason, NDIR is the most suitable technique for this investigation. Gentilhomme [36] supported the choice of carbon dioxide as tracer gas based on its high light absorption coefficient, which increases the accuracy of the gas concentration measurements provided by NDIR gas analysers.

Two main options of NDIR devices are available: NDIR sensors (recently used at the University of Cambridge [29]) and the most commonly used off-the-shelf gas analysers (employed at Penn State University [76] and Bath University [53] for instance). On the one hand, NDIR sensors offer high flexibility since the tracking system is customised and built by the user. This option allows simultaneous multiple sampling points (multichannel configuration) inferring a potential reduction in the logging time. However, the long response time of the devices (of the order of 40 s for state-of-the-art NDIR sensors) represents the main drawback. Another major downside is the need to continuously monitor the accuracy of the measurements (calibration drifts over time).

On the other hand, off-the-shelf gas analysers stand out for their shorter response time (order of 2 s) and higher accuracy on the measurements. Notwithstanding, gas analysers cannot simultaneously take multiple measurements due to the limitation in the number of input channels to the device (usually 1 or 2, although it could be up to 5 for multi-gas and multi-channel analysers in which each channel is tuned for one single gas). This restriction can be overcome with a multiplexer that switches between measurement points and is connected to one of the channels of the gas analyser. The logging time will therefore be extended depending on the amount of measurement points to extract data from. In addition, the larger size of the device implies that the equipment will have to be installed potentially far from the measurement point. This could lead to an even further increase of the response time of the gas analyser if the sample gas has to travel a long distance from the working section to the measurement cell of the device.

An emerging technology with large potential, micro electro-mechanical devices, offers the capability to measure gas concentration together with other thermodynamic properties such as pressure and temperature. Nonetheless, the accuracy of this technique is still suboptimal due to its early development stage, thus further improvement is required before it can be successfully implemented in this type of environment. Based on the review of available measurement techniques and equipment, the multi-gas analyser was deemed to offer the best compromise of properties for this application.

Sealing effectiveness data can be used as a measure of ingestion of mainstream annulus flow into the cavities existing beneath the annulus hub. The tracer gas technique consists of seeding the purge flow that is introduced into the cavity with a foreign gas, carbon dioxide in this case, whilst the mainstream flow is kept at atmospheric composition. Measurement of tracer gas concentration in the air mixture then indicates ingestion when the concentration falls below that supplied to the cavity, meaning that the extra air from the mainstream has diluted the air-CO_2 mixture. The performance of the seal against ingestion can be quantitatively represented by the sealing effectiveness, Eq.3.11, which can take values between 0 (100% ingestion – solely mainstream flow) and 1 (no ingestion – only purge flow).

$$\varepsilon = \frac{c_{\text{stator}} - c_{\text{ann}}}{c_{\text{purge}} - c_{\text{ann}}} \tag{3.11}$$

The gas concentration sampled from the static wall of the rim seal cavity is represented by c_{stator} in Eq.3.11, with the concentration of the mainstream flow, c_{ann}, and seeded purge flow, c_{purge}, monitored for reference at the entry of the test section. The readings of CO_2 concentration in the cavity reveal the presence of mainstream flow underneath the hub when the air-gas mixture is diluted.

Sealing flow supply and seeding system in the ORF

Design of a new system to quantify sealing effectiveness based on gas concentration data was required in the ORF. The sealing flow introduced into the cavity was seeded with

carbon dioxide whilst the mainstream flow maintained its atmospheric composition. A schematic of the sealing effectiveness measurement system is shown in Fig.3.16. The CO_2 mass flow was set by an Alicat MCR mass flow controller and recorded as a $0 - 5$ V proportional output signal. The quoted accuracy for the mass flow controller was $\pm 0.8\%$ of reading plus $\pm 0.2\%$ of full scale. An Alicat MCR series 2000 mass flow controller provided the carbon dioxide in the high purge flow test cases (when mainstream flow was present in the annulus). In absence of annulus flow, or for lower purge flow rates in presence of external flow, an Alicat MCR series 50 was used to supply the CO_2 whilst the Alicat MCR series 2000 replaced the metering nozzle in Fig.3.16 to set the air flow.

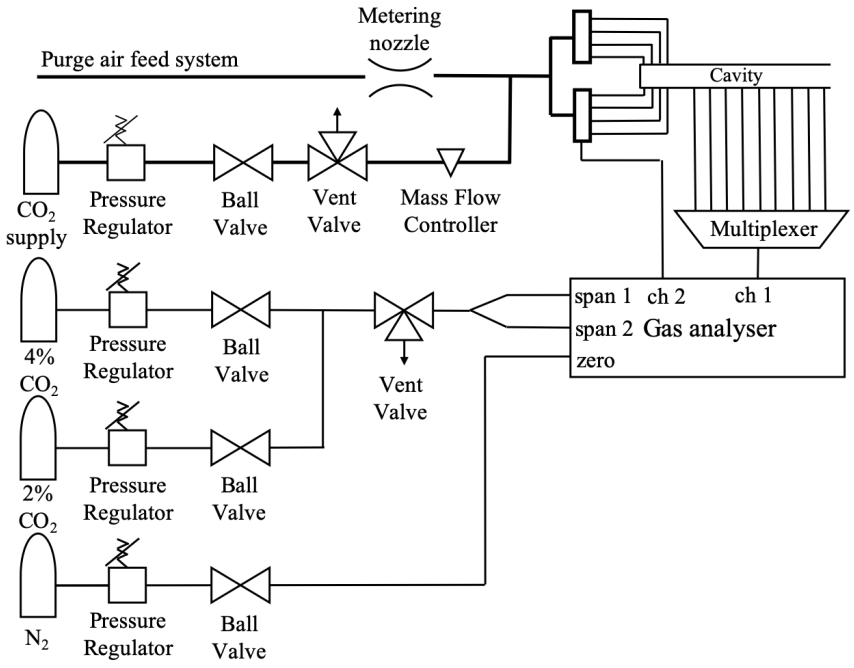

Figure 3.16: ORF sealing effectiveness measurement system for high purge flow rates.

Pure carbon dioxide was introduced into the purge flow downstream of the choked metering nozzle and prior to the distribution manifold with a flexible pipe of 8 mm diameter. Preliminary tests during commissioning of the new system demonstrated that the air and carbon dioxide in the purge flow were fully blended and the gas mixture entering the cavity was homogeneous. Eight hoses of 25.4 mm diameter evenly distributed along the circumference introduced the purge flow from the manifolds into the feed cavity. These

were replaced by 8 mm diameter flexible tubes for the tests with lower purge flow.

CO_2 concentration measurements were acquired using a dual channel Pulsar IV NDIR multi-gas analyser from Signal Group. This device offered a sensor response time of under 2 seconds with linearity and repeatability below ±0.5% and ±0.1% of full scale respectively. A multiplexer allowed sequential sampling of up to 20 measurement points through channel 1, whilst channel 2 was used to continuously monitor the concentration of the purge flow in the manifold upstream of the rim seal cavity entry. A constant input of nitrogen purged the measurement cells expelling the sample gas, as well as defining the zero concentration calibration point. The gas analyser, multiplexer and light tracker to indicate the measurement point the multiplexer was sampling from, were all mounted in a cabinet and located next to the working section as shown in Fig.3.17. The gas cylinders can also be seen at the back of the facility.

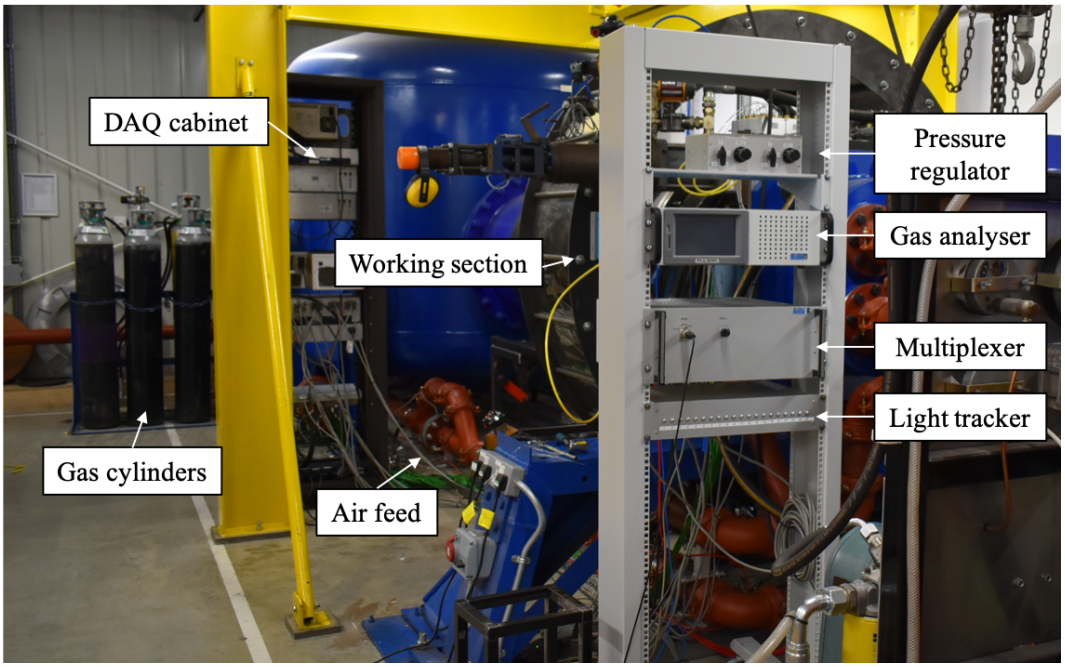

Figure 3.17: View of the ORF equipment distribution.

Gas analyser calibration and operation

Pure nitrogen and pre-set reference CO_2-air gas mixtures were used to calibrate the gas analyser. A constant input of nitrogen purged the measurement cells and expelled the sample gas as well as defined the zero CO_2 calibration point. Clark *et al.* [76] highlighted the importance of maintaining low concentrations of the foreign gas in air so that the heat and mass transfer analogy could still hold. The percentage of CO_2 content in the seeded flow varies from 1% to 30% in the open literature. For this study, the mass flow controllers were set to provide a fraction of 3% carbon dioxide content in air. Compressed gas bottles of certified CO_2-air mixtures of 2% and 4% CO_2 concentration ($\pm$1% uncertainty in concentration percentage) provided the two other span points to complete a three-point calibration curve. Single stage pressure regulators and pressure relief valves ensured that the calibration gases did not exceed the pressure limit of the gas analyser. A ball valve in each line opened/closed the gas supply to allow swapping between calibration gases, see Fig.3.16.

The gas analyser was calibrated daily before the start of testing to eliminate the sensor drift over time. The device manufacturer recommended that the gas analyser was initiated two hours prior to calibration with a continuous flow of nitrogen to purge any residuals in the measurement cells. This good practice improved the accuracy of the measurements and increased the operating life of the equipment. A sample screenshot of the software interface used to communicate with the gas analyser is shown in Fig.3.18. One line per channel indicated the type of gas each channel was set up for and the operation mode, e.g. sample, zero or span. The *Sample, Zero, Span* buttons were used to log the readings of the sample gas and defined the zero and span points of the calibration curve respectively.

Calibration of the gas analyser commenced with the zero CO_2 content point. Oxygen-free-nitrogen was already flowing into the gas analyser therefore the *apply calib. to all*

ranges box would be ticked, the channel selected from the *Select Detector* list and the *Calibrate* button pressed. Next, the two span points were defined with the pre-mixed 2% and 4% CO_2-air gas mixtures. During each test run, the gas analyser read values that ranged from 0% (in the annulus), to 3% CO_2 in the purge reference with values in between for the cavity.

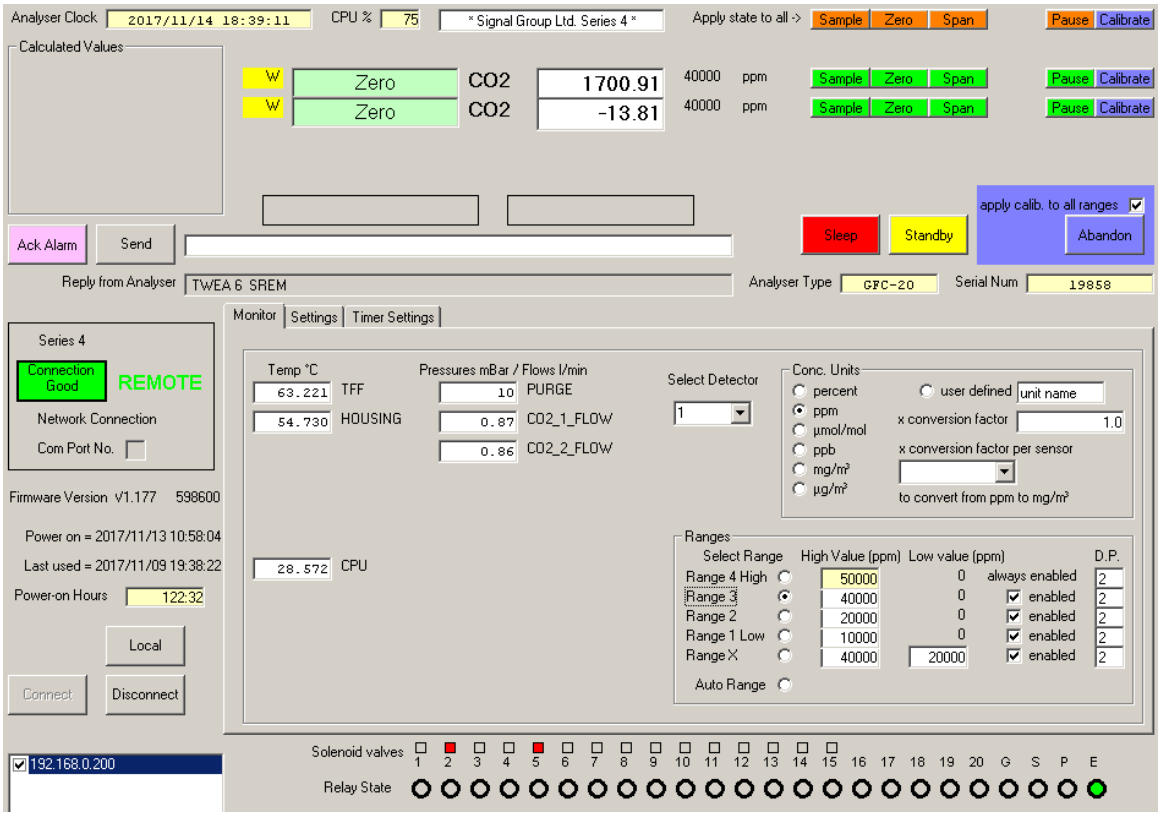

Figure 3.18: Gas analyser software interface.

The span points of the calibration curve were defined by the pre-mixed gas cylinders supplied by speciality BOC industrial gases to an accuracy of 1%. The ball valve allowing the gas to flow was first opened, the *apply calib. to all ranges* box unticked and the *Span* button selected. The pre-mixed 2% CO_2-air mixture was used to calibrate the first point. Next, the ball valve corresponding to this cylinder was closed to open that of the 4% CO_2-air pre-mixed gas cylinder and the same procedure was repeated for the second calibration point. For ease of post-processing, the light tracker box in Fig.3.17 was connected to the data acquisition cabinet in the experimental area to extract the data indicating the multiplexer channel as a 0-10 V output signal in the same LabView file

as the pressure and temperature readings. An example of the calibration data obtained from the gas analyser software interface and LabView can be observed in Table 3.9.

Table 3.9: Sample values from the gas analyser calibration.

	Zero		**Span 1** (2% CO_2 in air)		**Span 2** (4% CO_2 in air)	
	GA (ppm)	LabView (V)	GA (ppm)	LabView (V)	GA (ppm)	LabView (V)
Channel 1	20.25	0.0047	21059.32	5.1697	39992.52	9.8154
Channel 2	14.53	0.0049	21153.47	5.3068	40022.27	10.0302

A sample calibration curve of the gas analyser is included for reference in Fig.3.19. Note each input channel had its sensitivities and a different calibration was required for each one of them. The post-processing script logged the data from Table 3.9 and fitted a linear curve to obtain the calibration equation. The readings from the gas analyser were then imported into MATLAB from the LabView output file. For each of the data points, the script performed an interpolation to obtain the concentration of CO_2 in the sample gas and derived the sealing effectiveness using Eq.3.11. The associated absolute uncertainty with the sealing effectiveness measurement was ± 0.068 (repeatability error of $\pm 8.4 \times 10^{-3}$ that provided good ability to measure differences between test cases), see Appendix A for more detailed information. An example of run-to-run and measurement repeatability can be seen in Fig.5.16.

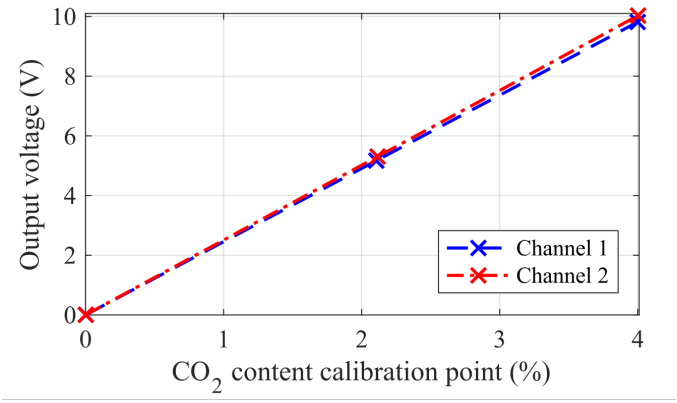

Figure 3.19: Example of the gas analyser calibration curve.

The multiplexer was set to sample gas during 30 s at each measurement point to

allow for stable readings in the gas analyser. The response of the device to changes in gas concentration was quoted to 2 s but the travel time of the sample gas through the pneumatic tubes to the measurement cell of the gas analyser also had to be accounted for. The settling time of the readings was strongly dependent on the change of content of tracer gas thus a preliminary study was conducted with alternating points at the maximum content of carbon dioxide (3%) and those with atmospheric composition. The results of the study of the dwell time of the multiplexer are presented in Fig.3.20. The black lines indicate a change in the measurement point that the multiplexer was sampling from and the red lines indicate the readings of the gas analyser. A dwell time of 10 s was insufficient for the readings to settle and despite an improvement was found with 20 s, Fig.3.20 shows that the measurement cell was not able to fully purge the sample gas and achieve a 0% reading. The study of the dwell time concluded that 30 s provided a stable reading able to capture the changes in concentration. This value offered the best compromise between test duration and stable reading. The multiplexer sequentially sampled from the purge supply, the 9 cavity measurement points, a point in the main gas path, and again from the purge supply to check that the purge conditions had not changed. In total, these added up to 12 points that required a total run time of 360 s.

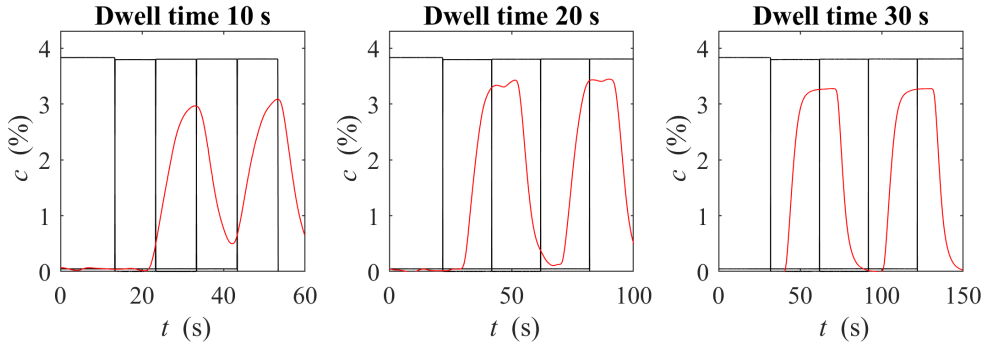

Figure 3.20: Response of the gas analyser for different dwell times.

Measurement points

Gas concentration measurements were taken inside the stator-rotor cavity, at the entry to the test section and in the main gas path. The radial distribution of sealing effectiveness

was first obtained and then the effect of circumferential variations below the hub line was investigated in Stage 3 of testing. The extent of the sealing flow migration in the main gas path was also studied at the rotor blade leading edge during Stage 3. The gas was sampled through the pressure tappings inside the cavity and transported to the gas analyser through flexible vinyl tubing of 1.6 mm diameter.

Cavity radial distribution: Measurements of CO_2 concentration were taken at nine radial positions along the stator wall of the rim seal cavity (c_{stator}) – using the static pressure tappings at location B in Fig.3.14 – along with the concentration of the mainstream flow (c_{ann}) – static pressure tapping p1214 in Fig.3.12 – and the seeded purge flow (c_{purge}) – monitored for reference at the entry of the test section in the manifold, Fig.3.16. The coordinates of the radial positions where the gas was sampled from can be seen in Table 3.6 since they are equivalent to the low bandwidth pressure measurements.

Cavity circumferential distribution: In the configuration with NGVs in the main gas path (Stage 3), egress or ingress regions into the cavity are determined by the pressure distribution in the annulus downstream of the NGVs. Consequently, the relative position of the cavity radial measurement points respect to the NGV trailing edge determines the sealing effectiveness inside the cavity. A second NGV ring with a combination of nine radial measurement points and two sets of nine circumferentially-distributed pressure tappings was machined. The new cavity instrumentation configuration included a set of pressure tappings at the same radial positions as those shown in Fig.3.14 location B. An additional set of radial positions labelled as location K in Fig.3.21(a) was included with a circumferential offset of 5° respect to B. This allowed to investigate the effect of the relative position between measurement point and NGV trailing edge on the radial distribution of sealing effectiveness inside the cavity. The coordinates where the sample gas was sampled from in the second NGV ring are summarised in Table 3.10.

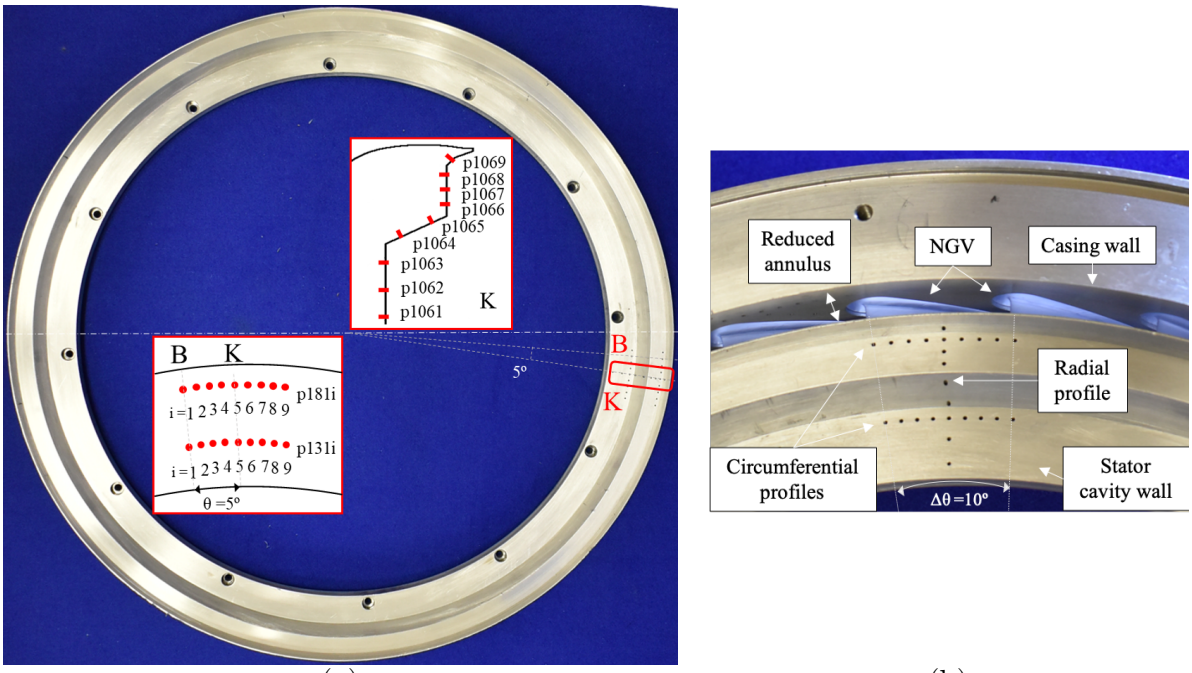

(a) (b)

Figure 3.21: (a) Position of the circumferentially-distributed cavity pressure tappings and (b) relative position of the cavity measurement points respect to the NGVs.

Nine pressure tappings were also circumferentially distributed covering one NGV pitch of $\Delta\theta_{\text{NGV}} = 10°$ at two radial positions, $r/b = 0.98$ and $r/b = 0.89$ as seen in Fig.3.21. This set of data aimed to investigate whether the sealing performance in the vicinities of the rim seal and further inbound into the cavity was conditioned by the circumferential pressure asymmetries in the main gas path or, on the contrary, it was uniform and the external pressure field did not penetrate.

Mainstream traverse: A probe formed by three $d = 1$ mm Scanivalve tubes radially spaced by 2 mm to cover the reduced annulus height was manufactured to acquire gas concentration data in the annulus, see Fig.3.22(a). The probe was located at the equivalent axial position where the rotor leading edge would sit in the gas path to obtain information about the radial migration of the purge flow and the flow distribution the leading edge of the rotor blades would encounter. This test campaign aimed to gain understanding of the behaviour of the sealing flow once it has left the cavity and interacts with the mainstream.

Table 3.10: Summary of concentration measurement data points in the second stator ring.

Model point	**Type**	**Description**	**Radius (mm)**	**Circumferential location (°)**
1061	*c*	Radial position 1	198.7	102
1062	*c*	Radial position 2	205.7	102
1063	*c*	Radial position 3	211.7	102
1064	*c*	Radial position 4	215.7	102
1065	*c*	Radial position 5	219.7	102
1066	*c*	Radial position 6	224.2	102
1067	*c*	Radial position 7	227.7	102
1068	*c*	Radial position 8	231.2	102
1069	*c*	Radial position 9	234.16	102
1881	*c*	Circumferential top location 1	231.2	97
1882	*c*	Circumferential top location 2	231.2	98.25
1883	*c*	Circumferential top location 3	231.2	99.5
1884	*c*	Circumferential top location 4	231.2	100.75
1885	*c*	Circumferential top location 5	231.2	102
1886	*c*	Circumferential top location 6	231.2	103.25
1887	*c*	Circumferential top location 7	231.2	104.5
1888	*c*	Circumferential top location 8	231.2	105.75
1889	*c*	Circumferential top location 9	231.2	107
1831	*c*	Circumferential bottom location 1	211.7	97
1832	*c*	Circumferential bottom location 2	211.7	98.25
1833	*c*	Circumferential bottom location 3	211.7	99.5
1834	*c*	Circumferential bottom location 4	211.7	100.75
1835	*c*	Circumferential bottom location 5	211.7	102
1836	*c*	Circumferential bottom location 6	211.7	103.25
1837	*c*	Circumferential bottom location 7	211.7	104.5
1838	*c*	Circumferential bottom location 8	211.7	105.75
1839	*c*	Circumferential bottom location 9	211.7	107

Data from the annulus at the rotor leading edge was only acquired in the test configuration of non-axisymmetric external flow (Stage 3). In this scenario, the probe was under the influence of the circumferential pressure variations induced by the presence of the NGVs in the gas path. The effect of the pressure asymmetries in the radial migration of the purge flow into the annulus was therefore investigated. The annulus probe was positioned in five different circumferential positions in the annulus that covered one NGV pitch as depicted in Fig.3.22(b). As a result, a traverse of sealing effectiveness data was obtained at fifteen points (3 radial positions at 5 circumferential locations) covering one NGV pitch at the rotor leading edge.

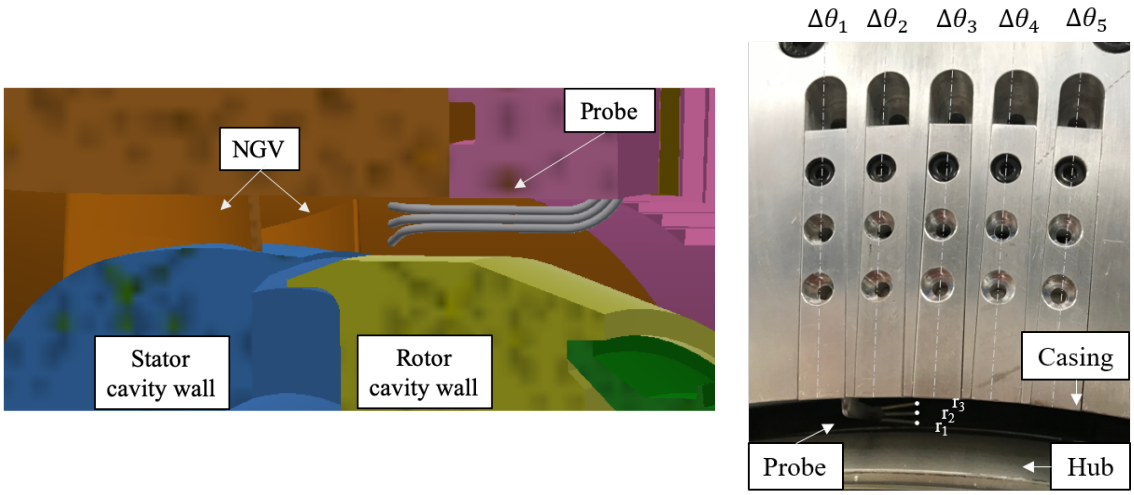

(a) (b)

Figure 3.22: (a) CAD view of the annulus measurement probe assembly and (b) downstream view of the annulus measurement probe installed in the ORF.

A summary of the traverse measurement points can be seen in Table 3.11. The circumferential position here, $\Delta\theta$, is referenced to the NGV trailing edge defined positive in the clockwise direction when seen from downstream.

Table 3.11: Summary of concentration measurement points in the annulus traverse.

Model point	Type	Description	Radius (mm)	Circumferential location (°)
r_1	c	Radial position 1	238.8	$\Delta\theta_1$, $\Delta\theta_2$, $\Delta\theta_3$, $\Delta\theta_4$, $\Delta\theta_5$
r_2	c	Radial position 1	240.8	$\Delta\theta_1$, $\Delta\theta_2$, $\Delta\theta_3$, $\Delta\theta_4$, $\Delta\theta_5$
r_2	c	Radial position 1	242.8	$\Delta\theta_1$, $\Delta\theta_2$, $\Delta\theta_3$, $\Delta\theta_4$, $\Delta\theta_5$
$\Delta\theta_1$	c	Circumferential position 1	r_1, r_2, r_3	-3.35 °
$\Delta\theta_2$	c	Circumferential position 2	r_1, r_2, r_3	-0.85 °
$\Delta\theta_3$	c	Circumferential position 3	r_1, r_2, r_3	1.65 °
$\Delta\theta_4$	c	Circumferential position 4	r_1, r_2, r_3	4.14 °
$\Delta\theta_5$	c	Circumferential position 5	r_1, r_2, r_3	6.62 °

3.2.3 High bandwidth data

Unsteady pressures and rotor disc speed were logged at 1 MHz through the high speed channels of the National Instruments PXI/SCXI data acquisition system. The acquisition and conditioning process of the unsteady pressure signals is described in this section.

A total of eleven ultraminiature Kulite™ XCQ-062 series unsteady pressure sensors were installed in the stator ring. These piezoresistive pressure transducers are temperature compensated up to 80°C and offer high sensitivity and resolution. The pressure transducers of 50psiA and 100psiA were mounted in the stator wall with no protrusions to avoid discontinuities in the cavity surface. The typical natural frequency of the sensor without screen was 300 kHz for the 50 psiA range and 380 kHz for the 100 psiA version. These ultraminiature devices had a very compact size of 1.7 mm diameter and a shortened length of 9.5 mm. The pressure sensors were radially and circumferentially distributed in the cavity wall - seven of these transducers were radially positioned at location E in Fig.3.14 and Fig.3.23 ($\theta = 257°$ in the clockwise direction from top dead center) and five additional sensors at a constant radial coordinate and unevenly spaced in the θ direction.

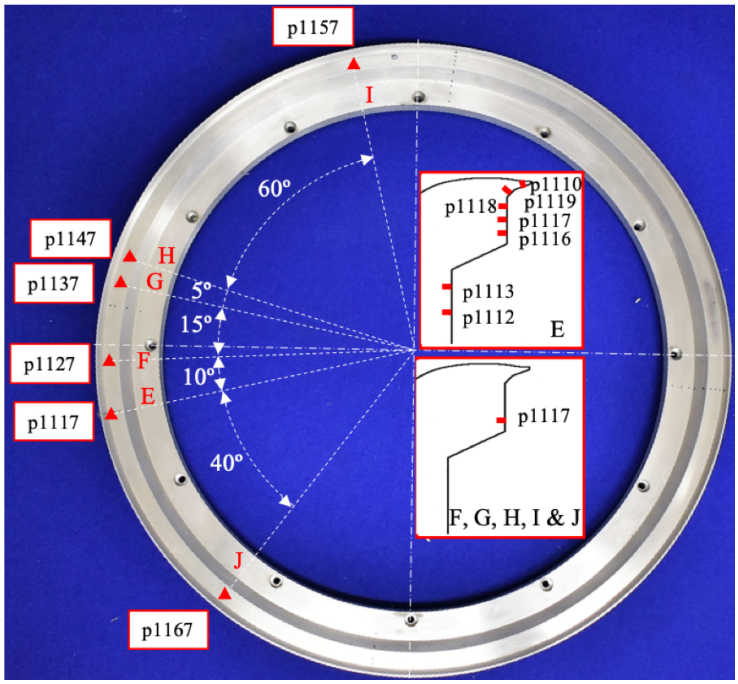

Figure 3.23: High bandwidth pressure measurements distribution in the NGV ring.

The unsteady pressure sensors were installed in the same radial positions as the low bandwidth pressure tappings with an extra measurement point at the rim, see p1110 in Fig.3.23, thus providing a data point in the overlapping region of the chute seal. In the circumferential locations labelled F to J, only one sensor in the equivalent radial position of p1117 was installed. These sensors were strategically distributed along the circumference in such a way that the combinations resulting of the pairing of any two sensors as summarised in Table 3.12 offered increments of 5° in the range $5° - 30°$ and 10° spacing between $30° - 90°$. A previous experimental campaign performed before the modifications to the ORF detailed in section 3.1.2 took place, explored the origin of the unsteady flow structures detected by Beard *et al.* [19] further inbound into the cavity. For that investigation, three Kulite probes were placed at either side of the overlapping seal. They showed no unsteadiness therefore suggesting the overlapping seal in the inner cavity was not the source of the unsteadiness and they were later removed. This is further discussed in chapter 6.

Table 3.12: Angles resulting of the pairing of any two unsteady pressure sensors.

Index	Sensor pairing	$\Delta\theta$ (°)
1	p1117 & p1127	10
2	p1117 & p1137	25
3	p1117 & p1147	30
4	p1117 & p1157	90
5	p1167 & p1117	40
6	p1127 & p1137	15
7	p1127 & p1147	20
8	p1127 & p1157	80
9	p1167 & p1127	50
10	p1137 & p1147	5
11	p1137 & p1157	65
12	p1167 & p1137	65
13	p1147 & p1157	60
14	p1167 & p1147	70
15	p1167 & p1157	130

Table 3.13: Summary of unsteady pressure measurements.

Model point	Description	Radius (mm)	Circumferential location (°)	Sensor	Uncertainty (%FS)
1112	Cavity position 2	205.7	257	XCQ-062-50A	0.1
1113	Cavity position 3	211.7		XCQ-062-50A	
1116	Cavity position 6	224.2		XCQ-062-50A	
1117	Cavity position 7	227.7		XCQ-062-50A	
1118	Cavity position 8	231.2		XCQ-062-50A	
1119	Cavity position 9	234.14		XCQ-77-062-100A	
1110	Cavity position 10	235.87		XCQ-77-062-100A	
1127	Cavity position 7	227.7	267	XCQ-062-50A	
1137			282	XCQ-062-50A	
1147			287	XCQ-062-50A	
1157			347	XCQ-062-100A	
1167			217	XCQ-062-100A	

The ratiometric output voltage of the Kulite XCQ-062 sensors was amplified by a set of Fylde FE-579-TA amplifiers. Previous limitations in the amplifiers restricted the maximum gain to 30 due to the autozero function. This issue was solved with an AC coupling circuit before the amplifiers that allowed to set a gain of up to 1000. A summary of the unsteady pressure measurements coordinates and sensors is provided in Table 3.13.

3.2.4 Data acquisition system

The data acquisition system (DAQ) was comprised of several items including high and low bandwidth measurement systems, power supplies for pressure transducers, amplifiers and thermocouple terminal blocks with cold junction compensation mounted in a 19 inch rack cabinet. A photograph of the DAQ system can be seen in Fig.3.24. The cabinet was connected to the desktop in the control room via an optical fibre link and a LabView program would provide the readings of each one of the different channels in screen. A total of 80 low bandwidth channels, 32 thermocouple channels and 16 high speed channels were available.

Another mounting rack included all the equipment necessary to obtain the sealing effectiveness data and was positioned as close to the working section as possible to reduce the length of the pneumatic tubes and therefore settling time. The sealing effectiveness cabinet was connected to the low bandwidth chassis when gas concentration data were acquired and logged through the first 24 channels of the LabView script alongside pressure and temperature measurements. Simultaneous measurements of all pressures and gas concentration data points were not possible due to a limitation in the number of channels in the low bandwidth chassis.

The rotational speed of the rotor disc is obtained by measuring the position of a toothed disc mounted on the main shaft with an optical encoder sampling at 500 kHz. A one line toothed disc provides a once per revolution disc speed measurement. The

ideal signal from the optical encoder is a periodic square wave that oscillates between set levels of voltage. Modulation of the encoder signal is observed when the rotor disc speed changes. The rotational speed is calculated from the time period for a single revolution, determined by detecting the time at which the signal rises above an arbitrary threshold voltage. The signal sample rate, number of disc lines, performance of the optical sensor and signal processing methodology determine the accuracy of the technique. For a nominal rotational speed of 9500 rpm the uncertainty of the speed encoder is ±24 rpm.

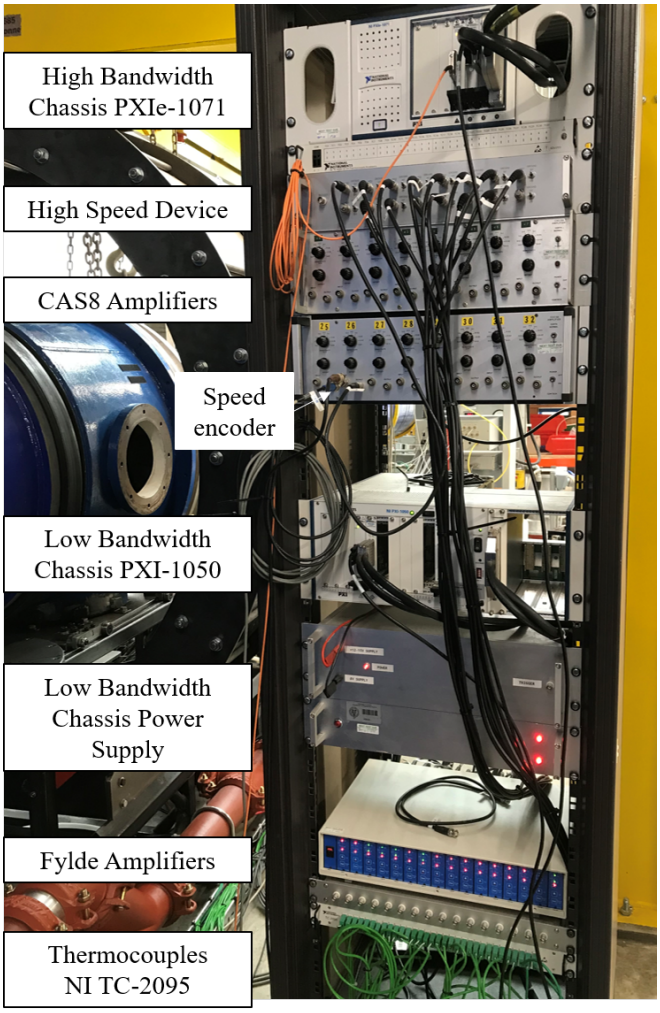

Figure 3.24: DAQ cabinet.

Fig.3.25 provides a detailed schematic of the instrumentation and DAQ arrangements in the ORF. In addition, Fig.3.25 illustrates the increased complexity in the signal conditioning process from the unsteady pressure sensors.

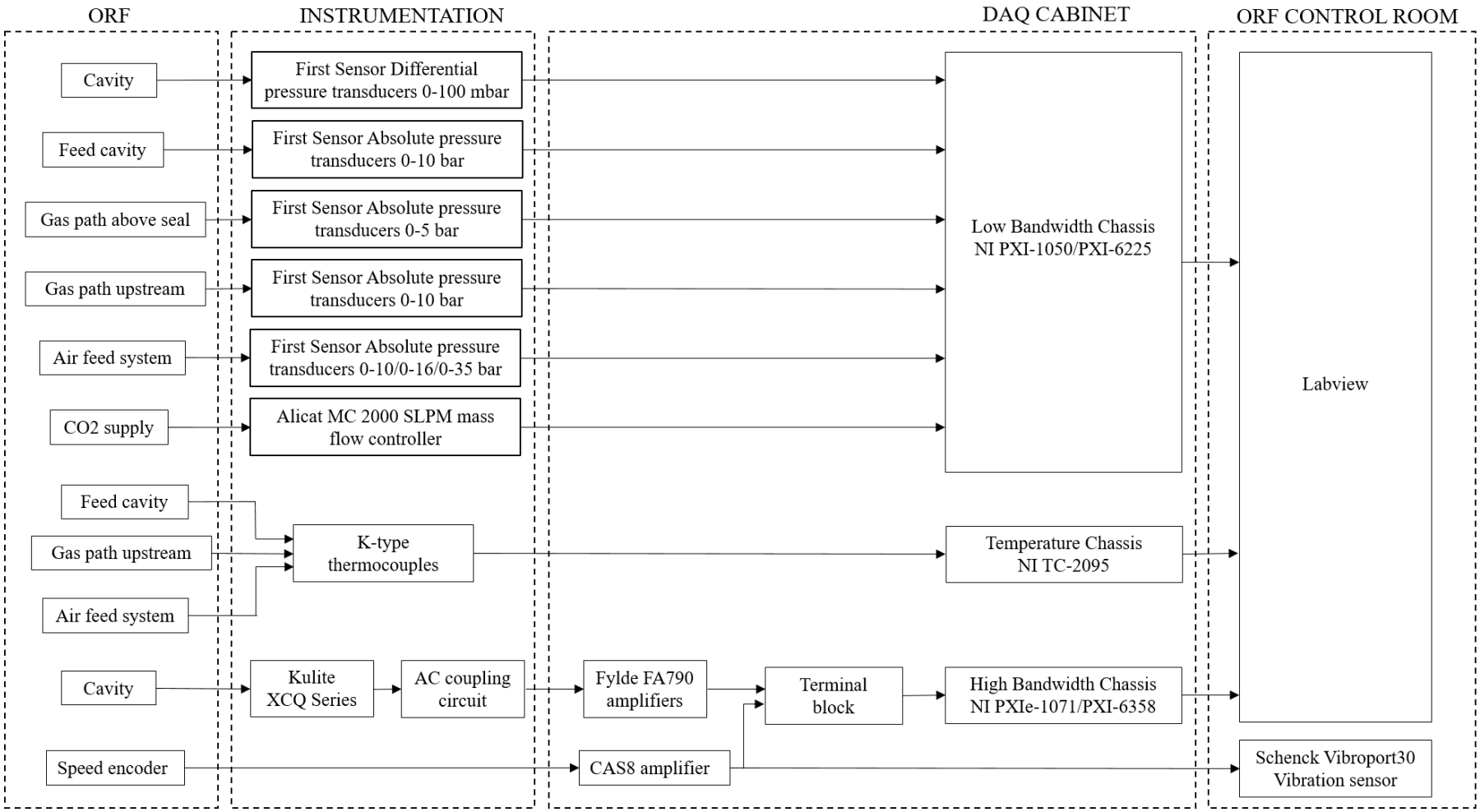

Figure 3.25: Instrumentation systems.

3.3 Summary

The capability of the Oxford Research Facility was upgraded for investigation of turbine rim sealing flows. An extended run time of the order of minutes was achieved by reducing the annulus height to 20% of its original height span and by installing a new feed system to provide steady state flow conditions in blow down mode. These two major modifications allowed gas concentration measurements to be sequentially logged in one run.

The extensive instrumentation installed in the ORF for this research has been described. Low bandwidth pressure and temperature sensors were positioned in the main gas path and purge flow feed system for flow monitoring purposes and in the stator-rotor cavity to investigate the aerodynamics of the cavity flow. A new system to quantify the sealing performance of the chute seal based on the tracer gas technique was installed. The purge flow was seeded with CO_2 as a foreign gas whilst the mainstream flow maintained atmospheric composition of carbon dioxide. A gas analyser determined the amount of tracer gas present in the samples taken in the stator wall. Based on the readings of concentration of CO_2 the sealing effectiveness was derived. The presence of foreign gas in the annulus was also investigated to study the radial migration of the purge flow when it is discharged into the main gas path.

High bandwidth pressure transducers were embedded in the stator cavity wall to investigate unsteady flow features rotating at a fraction of rotor disc speed inside the cavity. The unsteady pressure sensors were distributed circumferentially and radially to investigate the presence, strength, quantity and speed of rotation of these rotating flow features.

Chapter 4

Rotationally-induced ingestion

The mean cavity flow aerodynamics and sealing performance of the chute seal under purely rotationally-induced ingestion are examined in this chapter. The working section configurations investigated here correspond to those named Stage 1 (bladeless main gas path in absence of annulus flow) and Stage 2 (clean annulus but incorporating an axial axisymmetric annulus flow). In absence of external pressure asymmetries, ingress occurs due to the centrifugal forces that expell the flow in the rotor boundary layer radially out establishing a pressure gradient in the cavity that sucks mainstream flow. This is referred to as rotationally-induced ingestion (or disc pumping effect) and is displayed in Fig.4.1.

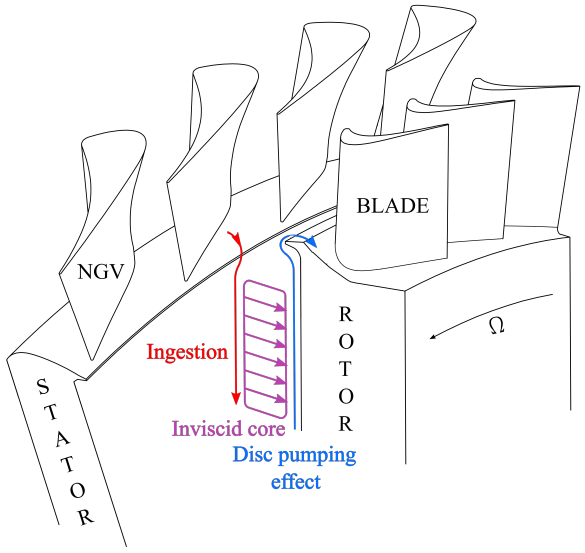

Figure 4.1: Disc pumping effect as the driving mechanism of rim seal ingestion.

The test conditions for each configuration are first summarised before detailed discussion of the results is provided. The mean flow in the rotor-stator cavity based on pressure measurements is examined in section 4.2. Preliminary data is first contrasted against the work by Beard *et al.* [19] confirming that the modifications to the test facility did not affect the aerodynamics of the cavity. Following this, the steady cavity flow behaviour is examined in detail without and with an axial axisymmetric annulus flow. Results from this project are compared to published data for other rim seal geometries studied under rotationally-induced ingestion. The disc pumping effect orifice model correlation from Chew [25] was fitted to the experimental data. The influence of axial annulus flow, seal clearance size, rotor disc speed and purge flow over the sealing capability of the chute seal is also analysed in this chapter.

4.1 Test matrix

The performance of a turbine rim seal operating under rotationally-induced ingestion may be sensitive to changes in seal geometry, seal clearance, purge flow rate, rotational speed, presence of annulus flow, inner cavity geometry, non-uniformities in the annulus, eccentricity and vibrations. The current study focuses on the limiting case of rotationally-driven ingestion for a chute seal, not studied under these conditions before. This particular type of geometry presents an inclined surface in which a simultaneous radial and axial overlap exists between the stator and rotor discs. As in many other rim seal studies, eccentricity, vibrations and unintended circumferential asymmetries in the external flow could arise from practical limits on rig design and manufacture. These are considered to be small with a 0.3% pressure difference within the circumferentially spaced total pressure measurements upstream of the working section (see Fig.3.13), but the possibility of some influence on the finer detail of the results cannot be ruled out. Later results show the importance of the disc pumping effect and the implications in modern aero-engines highlighting the need for a dedicated study of this phenomenon.

The effect of purge mass flow, rotor disc speed, rim seal gap size and annulus mass flow were investigated, analysed and presented in terms of the non-dimensional parameters: non-dimensional (purge) mass flow, C_{w}, rotational Reynolds number, Re_{ϕ}, non-dimensional seal clearance, s_c, and mainstream axial Reynolds number, $\mathrm{Re}_{\mathrm{ax}}$. The test range covered by these non-dimensional groups, defined in the nomenclature, is summarised in Table 4.1. The presence of axial mainstream annulus flow is indicated through the axial Reynolds number, $\mathrm{Re}_{\mathrm{ax}} = 0$ if not present. Low bandwidth data and gas concentration measurements were acquired at all test conditions. It is worth highlighting that in the $\mathrm{Re}_{\mathrm{ax}} = 0$ sealing effectiveness test campaign, the annulus was vented with a weak axial flow to avoid build up of CO_2 in the annulus giving false readings.

Table 4.1: Test conditions for experiments under rotationally-induced ingestion.

$\mathrm{Re}_{\mathrm{ax}}$	C_{w}	Re_{ϕ}	s_c
0	800 – 9000	1.5×10^6 2.1×10^6	4.2×10^{-3}
2.6×10^5	800 – 40000	2.7×10^6 3×10^6	7.8×10^{-3}

4.2 Mean cavity flow

This section provides insight into the flow structure within the rim seal cavity when exclusively subject to the disc pumping effect in two configurations with a clean annulus: (1) in absence of mainstream flow and (2) under axial axisymmetric annulus flow.

4.2.1 Validation of new working section

Results from this research are contrasted against those presented by Beard *et al.* [19]. The test campaign by Beard *et al.* included a full annulus and 30 uncovered disc bolts below the overlapping seal. The frequency spectra of the unsteady pressures revealed the signature of the bolts at the corresponding multiple of disc speed. For this study,

the clamping arrangement of the ORF split disc was modified to ensure an axisymmetric disc geometry without exposed protrusions in the cavity. In addition, this investigation extended previous measurements−which terminated at $r/b = 0.94$ (p1016 in Fig.3.14) – inboard down to $r/b = 0.84$ (p1011 in Fig.3.14).

The radial distributions of mean pressure coefficient, C_{p}, inside the cavity for the full annulus (with and without exposed rotor bolts) and reduced annulus are presented in Fig.4.2. Pressures were obtained under conditions of no purge flow $C_{\mathrm{w}} = 0$ and rotational Reynolds number 3×10^6 for the small seal clearance $s_c = 0.0042$.

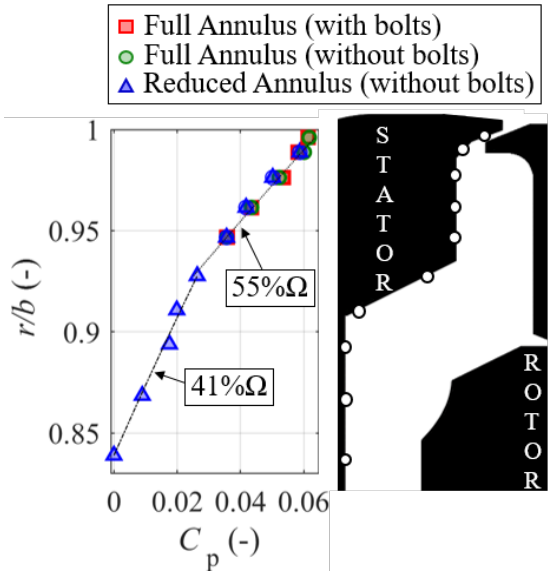

Figure 4.2: Radial distribution of the mean pressure coefficient in the rim seal and stator-rotor cavity for $C_{\mathrm{w}} = 0$, $s_c = 0.0042$ and $\mathrm{Re}_\phi = 3 \times 10^6$.

The pressure coefficient is calculated as the pressure difference to the innermost measurement point available in each test case and non-dimensionalised using the dynamic head at the disc rim speed. C_{p} is included as a measure of the vortex strength in the rim seal cavity. For ease of comparison, an offset has been applied to the results obtained for the full annulus datasets such that values at $r/b = 0.95$ are equal in all test cases. Pressures at $r/b = 0.995$ are only available from the full annulus configuration. In this study, this rim measurement point was removed to avoid the tapping protruding and interacting with the mainstream flow. Previously, without the mainstream flow, this

was not a concern. The excellent agreement of the cavity pressure measurements within various builds of the ORF evidenced that the mean flow aerodynamics in the rim seal cavity remained unaffected by the alterations to the working section (change to rotor disc clamping arrangement, reduction of annulus height, re-assembly and augmented resolution in the stator wall instrumentation). The extended measurements included in this study ($r/b < 0.94$) revealed a change in slope in the radial distribution of C_{p} showing that two different swirl velocities exist at the inner and outer parts of the cavity. Lines corresponding to forced vortices at 41% and 55% of disc speed are also plotted in Fig.4.2. A more thorough analysis is provided in the following section.

4.2.2 Steady cavity flow behaviour

The radial distribution of C_{p} in Fig.4.2 suggests coexistence of two different swirl velocities in the cavity rotating core. The same trends are reproduced in Fig.4.3 for a wider range of operating conditions tested in absence of mainstream flow, Fig.4.3(a), and with an axial axisymmetric annulus flow, Fig.4.3(b). Lines corresponding to forced vortices at several fractions of disc speed are included in Fig.4.2 and Fig.4.3 to aid visualisation. Following the radial direction, a change in slope at $r/b \sim 0.94$ indicates an increase in the vortex strength in the upper part of the cavity. In a shrouded plane disc rotor-stator system with separate turbulent boundary layers on the rotor and stator surfaces, the rotating core between the boundary layers typically rotates at $\sim 40\%$ of the rotor disc speed [8]. The results in Fig.4.3 are consistent with this although they reveal some effects of the non-planar geometry in the stator wall ($0.91 < r/b < 0.93$). A reduction in vortex strength in this region is consistent with an increased surface area for stator drag.

The turbulent flow parameter, $\lambda_{\mathrm{T}} = C_{\mathrm{w}}/\mathrm{Re}_{\phi}^{0.8}$, has previously been shown to characterise the flow in rotor-stator disc cavities. The individual effect of the purge flow rate and rotational Reynolds number in the turbulent flow parameter is analysed in Fig.4.3 for the two configurations under consideration. In absence of external annulus flow, $\mathrm{Re}_{\mathrm{ax}} = 0$,

doubling the rotational Reynolds number appears to have negligible repercussion in the cavity pressures if the purge flow remains constant (halving λ_T), Fig.4.3(a). For a fixed rotor disc speed however, an increase in purge supply strongly modifies the C_p distribution in the cavity. A larger input of radial flow into the cavity rises the pressure to allow the increased mass flow passing through the seal area. Consequently, higher purge flow rates aid the pressurisation of the cavity, thus achieving a more uniform radial profile and reducing the pressure gradient across the stator wall. This translates onto better sealing capability. Since hot gas ingestion is driven by a difference in the pressure across the rim seal (between the gas path above and the cavity below), an increase in the cavity pressure discourages the annulus flow from entering the cavity hence inhibiting ingestion.

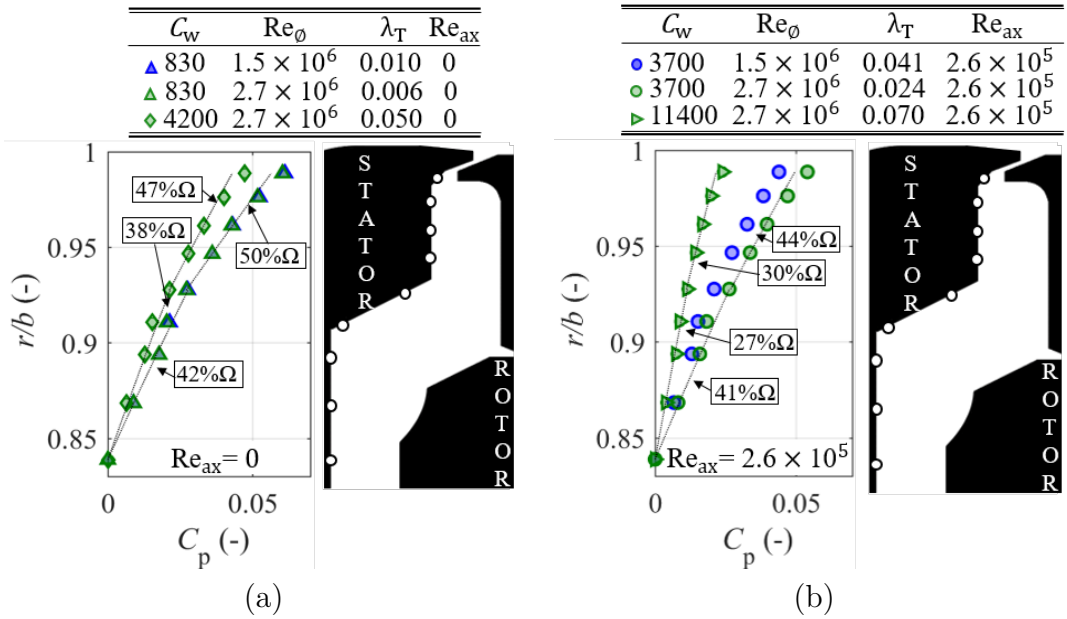

Figure 4.3: Effect of purge flow, C_w, and rotor disc speed, Re_ϕ, in the radial distribution of the mean pressure coefficient in the rim seal cavity for $s_c = 0.0042$: (a) $Re_{ax} = 0$ and (b) $Re_{ax} = 2.6 \times 10^5$.

The introduction of axial mainstream annulus flow, Fig.4.3(b), exacerbates the impact of C_w and Re_ϕ in the pressure coefficient. An increase in rotational Reynolds number strengthens the vortices by transferring angular momentum to the cavity flow. Owen [5] pointed to the swirl inside the cavity as the driving force for the disc pumping effect, therefore the ejection of sealing flow is favoured by large tangential velocities. Similarly

to Fig.4.3(a), a larger supply of radial outflow aids the sealing of the cavity by decreasing the cavity pressure gradient (steeper slopes) and reducing the intensity of the vortices. Fig.4.3 suggests that the vortices may even be suppressed if enough sealing flow is provided. Under rotationally-induced ingestion, Fig.4.3(a) and (b) manifest higher sensitivity of C_{p} to purge flow and annulus flow than to rotor disc speed under rotationally-induced ingestion. This is consistent with the definition of the turbulent flow parameter. The influence of C_{w} and Re_{ϕ} on the pressure coefficient appears to be magnified when external axial annulus flow is present in the system. The data from the ORF aligns with the early study of Bayley and Owen [11] in which a reduction of the purge supply or an increase of the rotor disc speed fostered ingestion due to a rise in the tangential velocity in the cavity.

The mean pressure coefficient at the outer measurement location, $r/b = 0.99$, is plotted in Fig.4.4 against the turbulent flow parameter, λ_{T}, across the full range of test conditions defined in Table 4.1. For values of $\lambda_{\mathrm{T}} < 0.1$, the data collapse to a linear regression regardless of the rotational Reynolds number, seal clearance or the presence of axial flow in the annulus. The scaling of the seal clearance with the disc boundary layer thickness in the minimum flow rate for disc pumping justifies the independence of λ_{T} from the seal clearance [18].

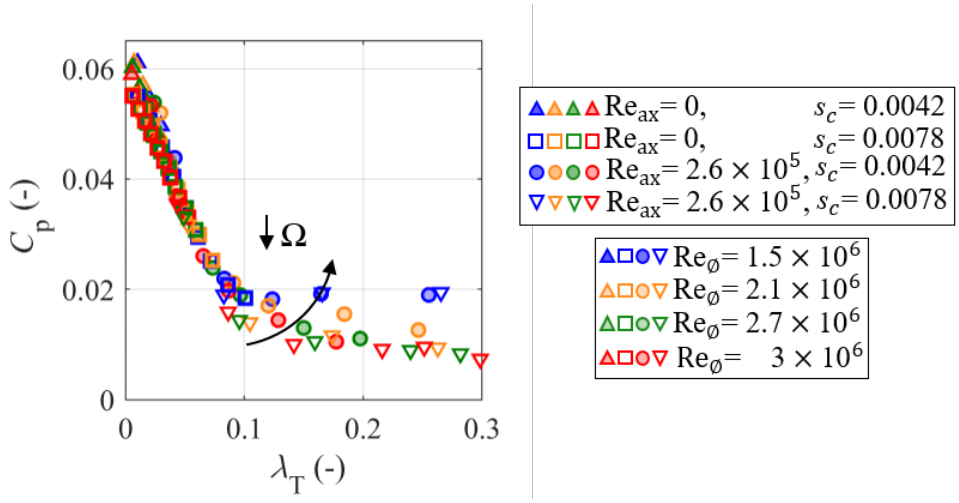

Figure 4.4: Effect of the external flow, Re_{ϕ} and s_c in the mean pressure coefficient at the rim, $r/b = 0.99$, correlated against the turbulent flow parameter.

Higher values of λ_T generate more uniform radial pressure profiles thus inducing a lower pressure difference across the cavity and leading to a reduction of the swirl velocity – see Fig.4.3. Interestingly, Fig.4.4 reveals that for $\lambda_T > 0.1$, the pressure coefficient tends to an asymptotic value that, depending on the rotational Reynolds number, will settle at $0.005 \leq C_p \leq 0.02$. For a sufficiently high turbulent flow parameter, the pressurisation of the cavity achieved by the purge flow is enough to overcome the disc pumping effect and the recirculation of the swirling flow and vortex in the cavity are suppressed. Ultimately, when the effects of the rotor disc lessen and the core region disappears, the vortex flow is ejected into the main gas path as if adjacent to a free disc [11]. The solution for free disc of von Karman's momentum integral equation gives $C_{w,fd} = 0.219 Re_\phi^{0.8} \left(\frac{r}{b}\right)^{2.6}$, which means $\lambda_{T,fd} = 0.219$ when the rotating core flow is suppressed [4]. Estimates of free disc pumping with allowance for the effect of a non-zero inner radius of the disc are consistent with a change of flow behaviour at $\lambda_T \sim 0.1$. Beyond this value, for $C_p < 0.02$ other effects contribute to the flow structure. This distinct behaviour of the flow at the lowest rotational Reynolds number setting is further investigated in section 4.3.3 based on the sealing effectiveness data.

4.3 Sealing performance

Results of sealing effectiveness with and without an axial annulus flow, including comparison against other rim seal designs and the disc pumping model by Chew [25] are presented.

4.3.1 Disc pumping results

Numerous rim seal geometries under pure disc pumping effect have been explored by other research groups, although purely rotationally-induced ingestion for a chute seal of the type considered here has only recently been reported by Bru Revert *et al.* [27]. Results of sealing effectiveness for the ORF chute seal are plotted in Fig.4.5(a) (blue

triangles) as a function of the seal-to-rotor rim velocity ratio, $U_m/(\Omega b)$, also referred to as non-dimensional flow ratio. Fig.4.5(a) also includes experimental data from Sangan *et al.* [28] for an axial seal (red squares) and a radial seal (green circles). Correlation curves (solid lines) derived from the orifice model formulated by Chew [25] – see Eq.2.1 – for rim seal performance exclusively under the disc pumping effect are also plotted for various parameter k values. All experimental results show good agreement for axial and radial seals with the disc pumping model using the k values suggested by Chew *et al.* [26] for these rim seal types. The k parameter was not supplied for the chute geometry investigated here, but the ORF provides experimental data to fit the orifice model and a $k = 1$ has shown to provide the best match. Silhouettes for each geometry are included for ease of comparison with the left component representing the stator wall and the rotor disc being on the right.

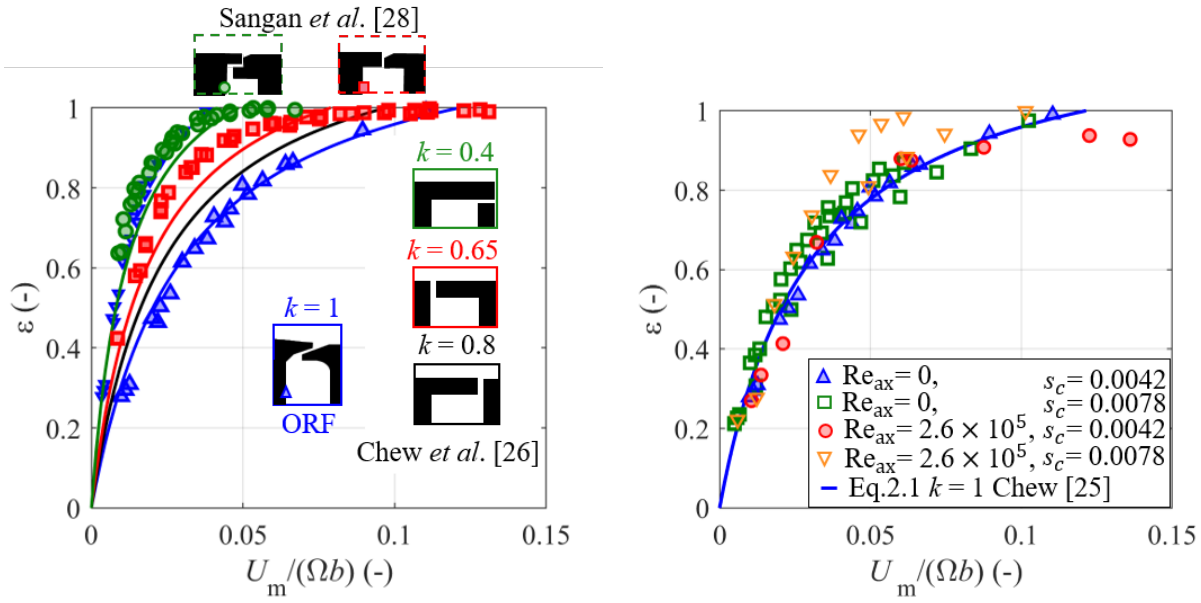

(a) (b)

Figure 4.5: (a) Comparison of the sealing effectiveness of different seal geometries against non-dimensional flow ratio at $r/b = 0.96$ and (b) effect of the annulus flow in the sealing effectiveness as a function of $U_m/(\Omega b)$ at $r/b = 0.96$ for two different gap sizes.

For the radial seal tested by Sangan *et al.*, the experimental results fall close to the model with $k = 0.4$ as associated with the simple radial seal used by Chew *et al.* [26]. Chew *et al.* correlated data for two different axial seal geometries (as depicted in

Fig.4.5(a)) with associated k values of 0.65 and 0.8 depending on whether the overhang lip protruded from the stator or rotor wall. The axial seal tested by Sangan *et al.* shows significantly better sealing performance than predicted by the model. This could be due to the difference in seal geometries or possible re-ingestion of purge air from the gas path associated with incomplete venting of the annulus space during these experiments[1].

The chute seal includes both radial and axial variation so its performance may be expected to lie between that of the axial and radial seals, as demonstrated by Phadke and Owen [21] for their *mitered* seal. Notwithstanding, Fig.4.5(a) indicates that the chute seal performs worse than the radial and axial seal geometries. Based on the analytical predictions obtained with Eq.2.1, the chute, radial and axial seals were fully sealed with $U_{\mathrm{m}}/(\Omega b)$ values of approximately 0.12, 0.05 and 0.079 respectively. The performance of the chute correlates well to the disc pumping model with $k = 1$, compared to $k = 0.4$ and $k = 0.65$ for simple radial and axial seals. Nonetheless, it should be noted that the results from Sangan *et al.* for the radial and the axial seal geometries are based on the axial gap size. The tested chute seal has an axial gap a factor of 2.9 higher than an axial seal with the same clearance. The chute seal data obtained in the ORF has been scaled to an equivalent axial seal clearance and included in Fig.4.5(a) as blue inverted triangles. This proves that the chute seal outperforms the axial seal for the same axial seal gap, with the clearance being much less sensitive to axial movement of the rotor. The chute geometry may also hold significant benefits over the axial and radial types, especially at high purge flow rates, for HPT performance, cycle performance and cooling.

4.3.2 Effect of mainstream annulus flow

The effect of the annulus flow on the sealing performance of the chute seal has been investigated for a wide range of conditions of purge flow rate, rotational speed and seal gap. In this stage of the study, the imposed annulus flow was purely axial with a Mach number

[1]This was confirmed in correspondence with authors.

of 0.34 (axial Reynolds number of 2.6×10^5 referenced to the nominal NGV axial chord), representative of HPT in modern aero-engines.

The effect of the external crossflow is assessed in Fig.4.5(b) based on the sealing effectiveness at radial position $r/b = 0.96$ at the seal clearances of $s_c = 0.0042$ and $s_c = 0.0078$, without and with an external axial axisymmetric annulus flow. The analytical prediction from Eq.2.1 was adjusted with $k = 1$ for best fit to the small seal clearance data without external flow (shown by filled blue triangles). Good agreement is largely observed in the presence of external flow (shown by filled red circles) until departure above $U_\mathrm{m}/(\Omega b) \sim 0.08$. Beyond this point the data reveal that the cavity is never fully sealed even at large supplies of purge, $U_\mathrm{m}/(\Omega b) \sim 0.275$, suggesting that the complex interaction between the sealing and mainstream flows will always lead to some levels of ingestion at the rim. This outcome broadly agrees with the findings of the experimental studies by Chew *et al.* [32] and Bohn *et al.* [33], although mindful comparison across the datasets is required since their experimental set up included pressure asymmetries in the mainstream. The lack of complete sealing in the cavity is suspected to be due to shear effects, and possibly small non-uniformities around the annulus when the external flow is introduced. Chew *et al.* also speculated with larger turbulent diffusion as the underlying cause. These observations align with the findings of other research groups (see Green and Turner [31], Chew *et al.* [32] and Savov *et al.* [29]) for different seal types illustrating the complexity of the flow.

4.3.3 Effect of rotor disc speed

In this section, the sealing effectiveness along the stator cavity wall is correlated against the radial distribution of the pressure coefficient at different conditions of rotational Reynolds number for two flow rates. Initial discussion is based on the results of Fig.4.6 for a flowless annulus and a seal clearance of $s_c = 0.0078$. Similar trends were identified for the smaller gap size.

At low rates of purge flow, Fig.4.6 (left), the strong radial pressure gradient across the cavity draws larger amounts of external flow through the rim seal leading to lower values of sealing effectiveness. As discussed in section 4.2, this is due to the pressurisation of the cavity not being sufficient to overcome the disc pumping effect at any of the rotor disc speeds studied. Fig.4.6 (right) shows how a higher non-dimensional purge flow rate reduces the pressure difference across the cavity volume and provides a more uniform radial pressure distribution. A drastic increase in sealing effectiveness occurs in Fig.4.6 (right) as a direct consequence of the drop in pressure coefficient. A fully sealed cavity is achieved at $\mathrm{Re}_\phi = 1.5 \times 10^6$. Larger sensitivity of both C_p and ε to rotational Reynolds number is observed for the highest purge flow supply. The pressure coefficient values at $C_\mathrm{w} = 830$ show that the disc pumping effect is equally strong at low and high rotor disc speeds.

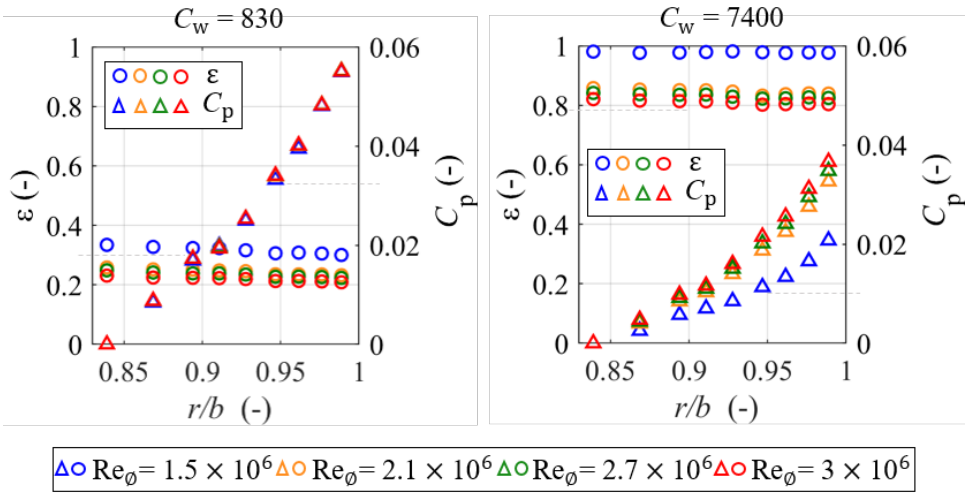

Figure 4.6: Radial distribution of sealing effectiveness and pressure coefficient inside the cavity in absence of annulus flow at different rotational Reynolds numbers for a gap size of $s_c = 0.0078$ at $C_\mathrm{w} = 830$ (left) and $C_\mathrm{w} = 7400$ (right).

Consistently with the findings from the pressure data in Fig.4.3(b), a significant gap between results at $\mathrm{Re}_\phi = 1.5 \times 10^6$ and all the other rotor disc speeds is visible in Fig.4.6 (right). To further explore this effect, the sealing effectiveness as a function of the non-dimensional flow ratio at different Re_ϕ is included in Fig.4.7 without (a) and with (b) axial annulus flow.

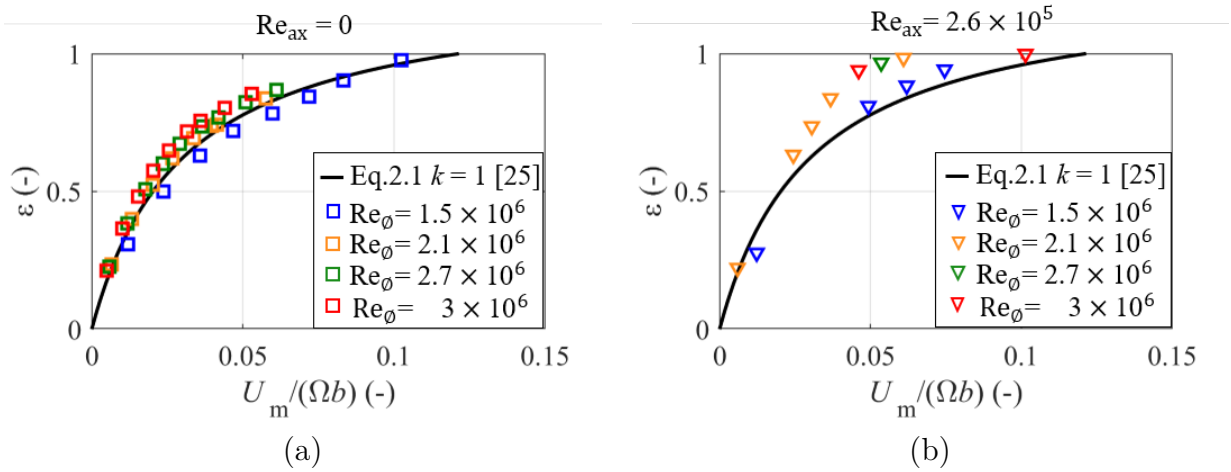

Figure 4.7: Sealing effectiveness as a function of the non-dimensional flow ratio at $r/b = 0.96$ for $s_c = 0.0078$ (a) in absence of annulus flow, $\mathrm{Re_{ax}} = 0$, and (b) with axial axisymmetric annulus flow, $\mathrm{Re_{ax}} = 2.6 \times 10^5$.

As already observed, data from the lowest rotational Reynolds number, $\mathrm{Re}_\phi = 1.5 \times 10^6$, differ from the general trend followed by other rotor disc speeds considered. A slight offset between $\mathrm{Re}_\phi = 1.5 \times 10^6$ (below curve of $k = 1$) and $\mathrm{Re}_\phi > 1.5 \times 10^6$ (above $k = 1$) can be identified in Fig.4.7(a). In Figure 4.7(b) however, a different curve for the sealing effectiveness distribution at $\mathrm{Re}_\phi = 1.5 \times 10^6$ is clearly observed. The unsteady pressures discussed in chapter 6 also display departure from the other datasets at this particular condition. The source of discrepancy is attributed to the unsteadiness arising from the shear between annulus and purge flows being more intense at this condition.

4.3.4 Effect of seal clearance

The results for the large seal clearance, $s_c = 0.0078$ (empty markers in Fig.4.5(b)), display a different nature. Without external flow, the data show reasonable agreement with the plotted correlation although the data genearally sits above the analytical prediction. The 1.85 mm seal clearance was achieved by axially displacing the rotor disc rearwards and, as a consequence, the overlap in the chute seal was lost. This change in configuration intrinsically modified the rim seal geometry. The sealing effectiveness data obtained with the larger gap suggest a superior sealing capability of the open rim geometry. Bayley and

Owen [11] reported a reduction of cavity swirl velocity as a consequence of an increase of the seal clearance that is consistent with the ORF results. However, because the axial displacement increases the seal clearance, it does result in more flow being required to seal the cavity. With the introduction of external flow in the larger gap set up, an improved seal performance is evident especially at high purge flow rates. However, scatter in the data at conditions with high sealing effectiveness makes it difficult to conclude the value of $U_{\mathrm{m}}/(\Omega b)$ for a fully sealed cavity. The effect of the gap size on the radial distribution of sealing effectiveness can be assessed by comparison of the data in Fig.4.8(a) and (b).

4.3.5 Effect of purge flow

Radial distributions of sealing effectiveness on the cavity stator wall are shown in Fig.4.8 for (a) $s_c = 0.0042$ and (b) $s_c = 0.0078$, without and with annulus flow for purge flows varying from $U_{\mathrm{m}}/(\Omega b) = 0.02$ to 0.09 ($C_{\mathrm{w}} = 850$ to 3400) at constant rotational Reynolds number $\mathrm{Re}_\phi = 1.5 \times 10^6$. A rise in sealing effectiveness is observed as purge mass flow increases since the cavity pressure must rise to pass the increased purge flow through the seal area, subsequently inhibiting ingestion. A decrease in sealing effectiveness for the wider gap is evident when comparing data for constant $U_{\mathrm{m}}/(\Omega b) = 0.02$ ($C_{\mathrm{w}} = 850$) looking at the blue markers across the two plots.

The radial distribution of sealing effectiveness can be explained by the cavity flow structure. According to the study presented by Daily and Nece [8], turbulent flow and separate boundary layers are expected to develop inside the cavity. When ingestion occurs, the external flow that reaches the cavity mixes with the outward purge flow in the outer part of the volume. The combined flow then merges with the stator boundary layer and migrates radially downwards. A constant radial distribution of sealing effectiveness is observed in Fig.4.8(a) at the inner part of the cavity ($r/b < 0.94$) indicating that the flow is fully mixed all along the stator boundary layer. On the contrary, at higher radii ($r/b > 0.94$) radial variations in the sealing effectiveness distribution indicate partial

mixing of the ingested and cavity flows. It is also worth noting that the geometrical discontinuity of the stator wall joining the flat vertical and angled faces at $r/b = 0.94$ aids this affect and the trend change consistently takes place at this radial coordinate. The effect also intensifies with increasing purge flow. Generally, variations are small and in Fig.4.8(a) fall within measurement uncertainty.

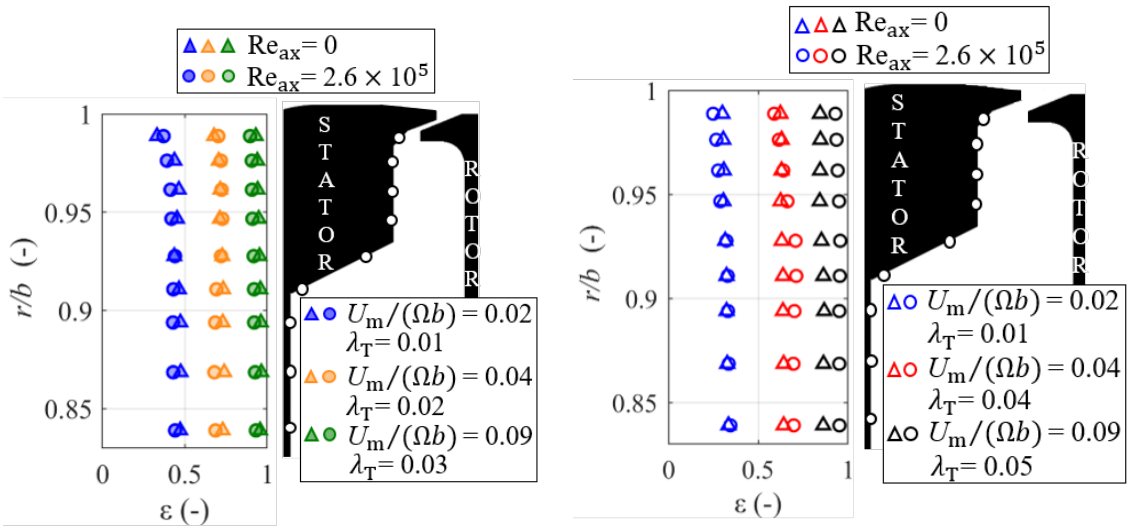

(a) (b)

Figure 4.8: Effect of the purge flow on the sealing effectiveness radial distribution at $\mathrm{Re}_\phi = 1.5 \times 10^6$ without and with annulus flow for: (a) $s_c = 0.0042$ and (b) $s_c = 0.0078$.

The effect of imposing the mainstream annulus flow is in agreement at both seal gap sizes: at low purge flow rates, for example $U_m/(\Omega b) = 0.02$, the effect is small, with a consistent decrease in effectiveness near the rim seal in the mixing region between $0.94 < r/b < 0.99$. For the smaller gap size, the largest change in effectiveness, of approximately 0.03, is observed at $r/b = 0.99$.

As the purge flow is increased, the effect of the mainstream flow becomes more influential in both seal gaps although it is more pronounced for $s_c = 0.0078$ due to the larger supply of purge flow required to achieve the same U_m/U_{ax}. For $U_m/(\Omega b) > 0.04$ in Fig.4.8(b), the change induced at the rim is small, but a positive shift in seal effectiveness is observed in the fully mixed region below $r/b < 0.94$. In combination, these result in

a gradient in the mixing region between $0.94 < r/b < 0.99$. Despite more noticeable in the larger seal clearance, this shift in the lower cavity region appears in $s_c = 0.0042$ as well. Interestingly, the offset also appears to increase with the rate of purge flow supplied into the cavity; at $r/b = 0.84$ it goes up from +0.06 at $U_m/(\Omega b) = 0.04$ to +0.11 at $U_m/(\Omega b) = 0.07$.

Furthermore, Fig.4.8 reveals that further increasing the supply of purge flow leads to an improved rim sealing capability of the chute seal in the presence of mainstream flow. Due to the gradient in sealing effectiveness over $0.93 < r/b < 0.99$ and the offset in the inner region, there is a point in the radial distribution at which the sealing effectiveness under axial annulus flow equals that of the configuration without it. From this point (which depends on the purge supply) upwards, the presence of mainstream flow seems to exert a beneficial effect on the sealing capability of the chute seal. This outcome is studied across a larger range of purge flows and compared to the pressure difference across the cavity volume in Fig.4.9. Data correspond to $\mathrm{Re}_\phi = 1.5 \times 10^6$ (left) and $\mathrm{Re}_\phi = 2.7 \times 10^6$ (right) for the test cases without and with axial annulus flow. The results presented were measured at the rim, $r/b = 0.99$, for the larger seal clearance, $s_c = 0.0078$.

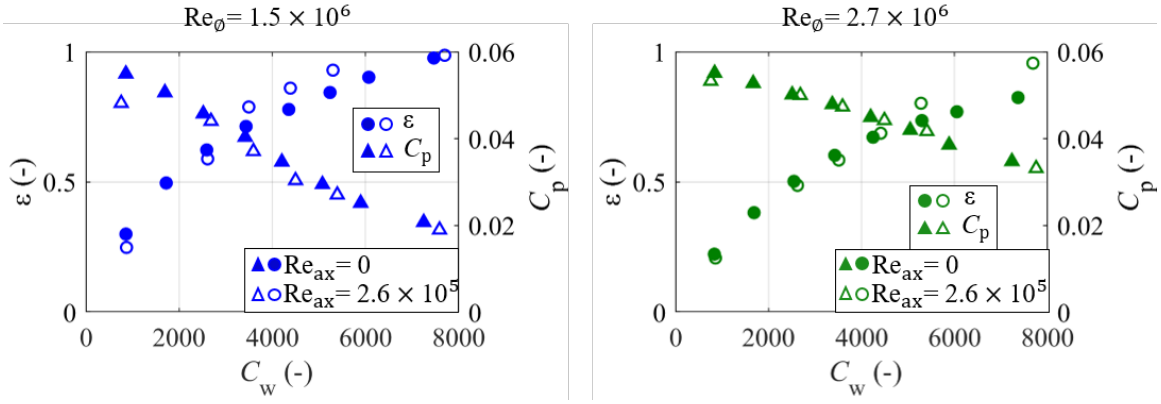

Figure 4.9: Effect of the axial annulus flow on the sealing effectiveness and cavity pressure difference as a function of the purge supply at $\mathrm{Re}_\phi = 1.5 \times 10^6$ (left) and $\mathrm{Re}_\phi = 2.7 \times 10^6$ (right) measured at $r/b = 0.99$ and $s_c = 0.0078$.

The pressure difference across the cavity is inversely proportional to the amount of purge flow rate: the larger the supply of C_w, the more uniform pressure distribution is

achieved inside the cavity and therefore the lower the value of C_{p}. As mentioned earlier, high pressure differences across the cavity yield lower values of sealing effectiveness, indicating substantial levels of ingestion. This outcome is observed regardless of the presence of axial annulus flow, as the pressure coefficient collapses into a linear regression.

Fig.4.9 reveals an interesting effect consistent with what was observed in Fig.4.8: the addition of axial annulus flow aids the sealing performance of the chute seal under certain circumstances. The study conducted by Phadke and Owen [14] reported an improvement of the sealing capability when the external environment presented a weak quasi-axisymmetric flow. Past a certain threshold ($\mathrm{Re}_{\mathrm{ann}} \geq 2 \times 10^5$ for $s_c = 0.01$), their data revealed a detrimental effect of the external flow. These results are in broad agreement with the measurements obtained in the ORF. Bear in mind their experimental set up struggled to achieve an axisymmetric mainstream and that the pressure non-uniformities in the gas path amplified with higher flow rates. In this particular case, it appears that a purge supply able to satisfy $C_{\mathrm{p}} = 0.04$ is sufficient to overcome the disc pumping effect and could benefit the sealing performance. The value of C_{w} for which this occurs depends on the rotor disc speed - a stronger pressure gradient in the cavity will be generated at higher rotational Reynolds number, thus demanding larger flow rates to pressurise the cavity and outbalance the disc pumping effect. In the specific cases depicted in Fig.4.9(a) and (b), values of $C_{\mathrm{w}} \sim 4000$ and $C_{\mathrm{w}} \sim 5000$ respectively are required to satisfy the condition for the low and high rotational Reynolds number.

The observed changes in seal effectiveness – small decreases near the rim at low purge flow rates and comparatively large positive shifts in the lower cavity at higher purge – unveil that the addition of an external axisymmetric flow can infer a beneficial or detrimental effect in the rim seal performance depending on the seal-to-axial mass flow ratio and radial position. This improvement in sealing capability in the presence of external flow could be a consequence of the flow recirculation in the rim seal region

due to the interaction between purge and annulus flows that intensifies at higher rates of sealing air supply. The flow visualisation technique employed by Phadke and Owen [14] revealed a separation bubble at the rim that reduced the effective clearance between the stator and rotor discs therefore restricting ingestion. The CFD analysis of Savov and Atkins [77] showed that the gap recirculation zone reduced in size and was blown out of the rim seal passage into the main gas path at high flow rates. The turbulent mixing of the purge and annulus flow would then occur in the annulus and ingestion would be inhibited. It is clear that the combination of the purge and annulus flows enhances the complexity of the flow structure in the rim region and inside the cavity.

4.4 Summary

The mean cavity pressure coefficient has been contrasted against preliminary data from the ORF confirming that the rebuild of the facility did not affect the cavity aerodynamics. The addition of pressure instrumentation further inbound the stator wall revealed the presence of different core swirl velocities in the inner and outer parts of the cavity suspected to be due to the change in geometry of the stator wall. Higher sensitivity of the C_{p} to purge and annulus flow than rotor disc speed under rotationally-induced ingestion was observed. A sufficiently high purge flow was shown to overcome the disc pumping effect suppressing the vortex in the cavity and expelling the purge flow as free disc flow. This behaviour was identified at $\lambda_{\mathrm{T}} > 0.1$, where the cavity pressure coefficient was almost invariant.

Sealing effectiveness data for a chute seal under purely rotationally-induced ingestion have been reported for the first time by Bru Revert *et al.* [27] as an outcome of this project. Results of sealing effectiveness have been compared to those for axial and radial seal designs available in the published literature. The chute seal performs better than an axial seal of the same axial clearance. The experimental sealing effectiveness data at

$r/b = 0.96$ showed good agreement with the disc pumping effect orifice model derived by Chew [25] for an empirical constant of $k = 1$.

The effect of the annulus flow on seal performance has shown to hinder complete sealing of the cavity due to the complex interaction between the mainstream and purge flows. Strong dependency on the operating conditions has been identified with some test cases showing an improvement of the sealing capability of the chute seal when mainstream flow was present. A significant difference in the sealing effectiveness at low and high rotational Reynolds number has been identified. Further analysis of the data showed the impact of Re_ϕ in the low and high bandwidth pressure signals. It is thought that an increase in the unsteadiness due to the shear between the annulus and purge flows at these conditions is causing this discrepancy. Larger scatter in the results of sealing effectiveness has been observed for the larger seal clearance.

Chapter 5

Externally-induced ingestion

A thorough analysis of the aerodynamic behaviour of the cavity flow and the sealing performance of the chute seal under the influence of a non-axisymmetric external annulus flow is conducted in this chapter. The introduction of nozzle guide vanes in the main gas path adds a swirl component to the mainstream flow generating pressure and potential field asymmetries, Fig.5.1. Ingestion of annulus flow occurs when the pressure downstream of the vanes is above that inside the rotor-stator cavity and the pressure gradient across the seal draws the hot mainstream gas into the cavity. This driving mechanism is known as pressure-driven or externally-driven ingestion (see section 2.4).

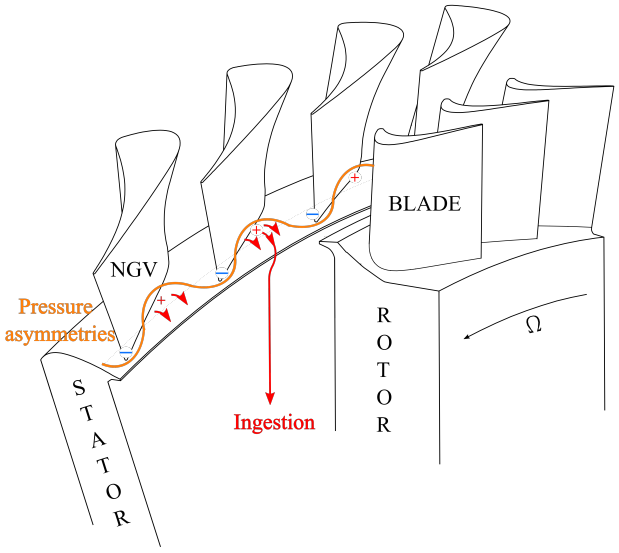

Figure 5.1: Circumferential pressure asymmetries as the driving mechanism of ingestion.

The configuration of the working section studied in this chapter was referred to as Stage 3 in section 1.4. Experimental results in this set up are compared to those presented in chapter 4 so that the disc pumping effect and the influence of the pressure asymmetries can be isolated and studied separately as independent drivers for ingestion but also in juxtaposition.

The experimental conditions are described first and then results of the mean flow structure in the cavity and the main gas path are evaluated. Next, the sealing performance is assessed over a wide range of operating conditions to analyse the effect of the most influential parameters. Following this, the impact of the purge flow in the aerodynamics of the gas path downstream of the seal is investigated at the rotor blade leading edge.

5.1 Test matrix

The different operating conditions investigated in this parametric study are summarised in Table 5.1, whereas Table 5.2 shows the rotational Reynolds numbers and flow coefficients for the tests at each rotor speed. The variation of purge flow is captured by the seal-to-disc rim velocity ratio, $U_\mathrm{m}/(\Omega b)$ (also called non-dimensional flow ratio). Values of non-dimensional (purge) mass flow, C_w, as commonly used in air systems are also given.

Table 5.1: Experimental test matrix for externally-induced ingestion investigation (*denotes test condition for non-axisymmetric annulus flow only).

	$U_\mathrm{m}/(\Omega b)$ (-)	λ_T (-)	C_w (-)	Re_ϕ (-)
No external flow	$0.01 - 0.11$	$0.005 - 0.05$	$820 - 4200$	$3.8 \times 10^{5*}$
Axisymmetric flow	$0.01 - 0.65$	$0.006 - 0.42$	$850 - 40000$	1.5×10^6 2.3×10^6
Non-axisymmetric flow	$0.03 - 1.3$	$0.028 - 0.63$	$3500 - 30000$	2.9×10^6 3.3×10^6

When present, the mainstream axial velocity component was kept constant throughout all the experiments and was identical to Stage 2 ($U_{\mathrm{ax}} = 115$ m/s, $\mathrm{M_{ax}} = 0.34$). Rotational speed, seal clearance ($s_c = 4.2 \times 10^{-3}$ and 7.8×10^{-3}), purge flow rate and annulus flow conditions were the handle variables in this experimental study.

Table 5.2: Rotational Reynolds number and flow coefficient at tested rotor speeds for experiments with non-axisymmetric annulus flow.

N (rpm)	Re_ϕ (-)	$U_{\mathrm{ax}}/(\Omega b)$ (-)
1000	3.8×10^5	4.5
4000	1.5×10^6	1.01
6000	2.3×10^6	0.67
7850	2.9×10^6	0.52
9000	3.3×10^6	0.45

5.2 Mean flow structure

The circumferential pressure coefficient in the mainstream defined with annulus flow velocity and rotor disc speed has been studied to assess the relative contribution of external pressure asymmetries and disc pumping effect. Steady pressure measurements in the cavity and the main gas path are presented in this section. The mean pressure coefficient in the cavity, indicative of vortex strength, has been compared against the test configurations without annulus flow and with axial axisymmetric flow reported in chapter 4.

5.2.1 Annulus pressure asymmetry

The circumferential mean pressure coefficient downstream of the NGVs was inspected on the reduced annulus casing wall, at $r/b = 1.03$. These pressure measurements were obtained at nine equispaced points on the annulus covering a single NGV pitch of 10°. The data are plotted in Fig.5.2 as circumferential mean pressure coefficient, $C_{\mathrm{p},\theta}$, for a purge flow rate corresponding to $U_{\mathrm{m}}/U_{\mathrm{ax}} = 0.08$, $s_c = 0.0042$, and four values of flow

coefficient varying from $U_{ax}/(\Omega b) = 1.01$ (4000 rpm) to $U_{ax}/(\Omega b) = 0.45$ (9000 rpm). Therefore, Fig.5.2 shows the effect of $U_{ax}/(\Omega b)$ on the circumferential distribution of $C_{p,\theta}$ in the annulus. Note that the annulus flow was constant and the rotor disc speed was the only variable parameter. Two approaches for non-dimensionalisation of $C_{p,\theta}$ have been used. In Fig.5.2 left, the dynamic head is calculated using the annulus flow velocity providing values of $C_{p,\theta ann}$, whilst in Fig.5.2 right the dynamic head is based on the rotor disc speed evaluated at the rim to give results of $C_{p,\theta disc}$.

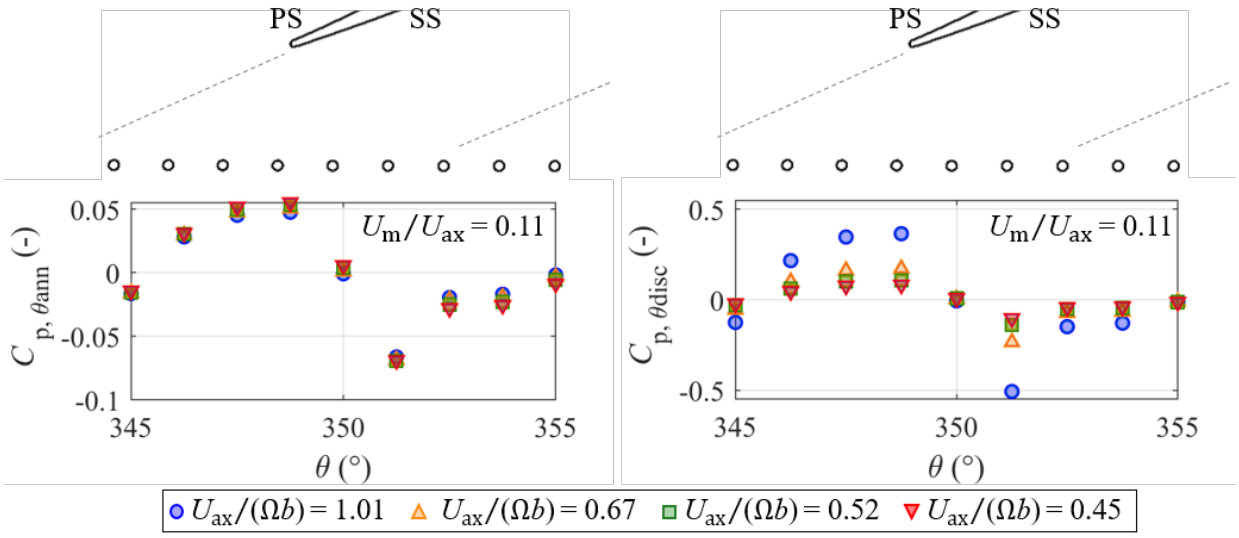

Figure 5.2: Effect of Re_ϕ on $C_{p,\theta}$ over one NGV pitch for $s_c = 0.0042$ and $U_m/U_{ax} = 0.11$ with $C_{p,\theta}$ referenced to the annulus flow (left) and the rotor disc speed (right).

The distribution of $C_{p,\theta ann}$ shows little variation with rotor disc speed implying the vane wakes are unaffected by the purge flow. Looking at the $C_{p,\theta disc}$ circumferential profile instead, Fig.5.2 suggests that the annulus pressure asymmetry should be significant (compared to rotational effects) at all conditions studied. At the highest and lowest tested rotor speeds of 9000 rpm and 4000 rpm, the minimum-to-maximum pressure variation is approximately 20% and 80% respectively of the disc speed dynamic head.

The effect of purge flow in the circumferential pressure coefficient is assessed at two values of flow coefficient in Fig.5.3. A slight decrease in the amplitude of the annulus

pressure variations is found at higher supplies of purge flow rate, represented by an increase in the non-dimensional flow ratio in Fig.5.3. This effect can also be examined by plotting the peak-to-peak pressure coefficient difference over a vane pitch as shown in Fig.5.4.

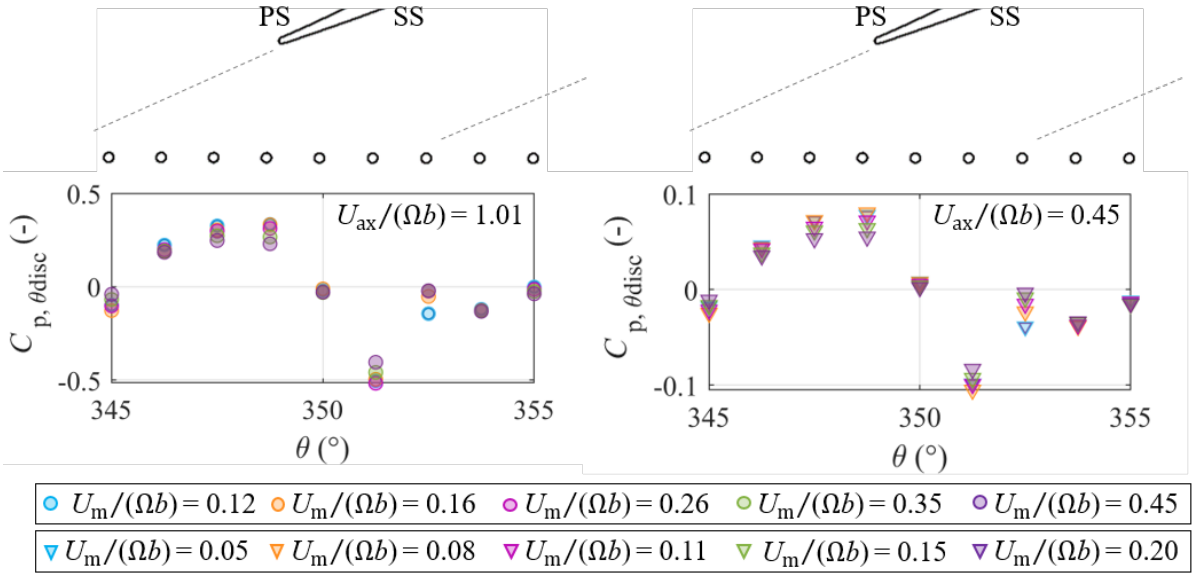

Figure 5.3: Effect of purge flow, $U_m/(\Omega b)$, on $C_{p,\theta disc}$ over one NGV pitch for $s_c = 0.0042$ at $U_{ax}/(\Omega b) = 1.01$ (left) and $U_{ax}/(\Omega b) = 0.45$ (right).

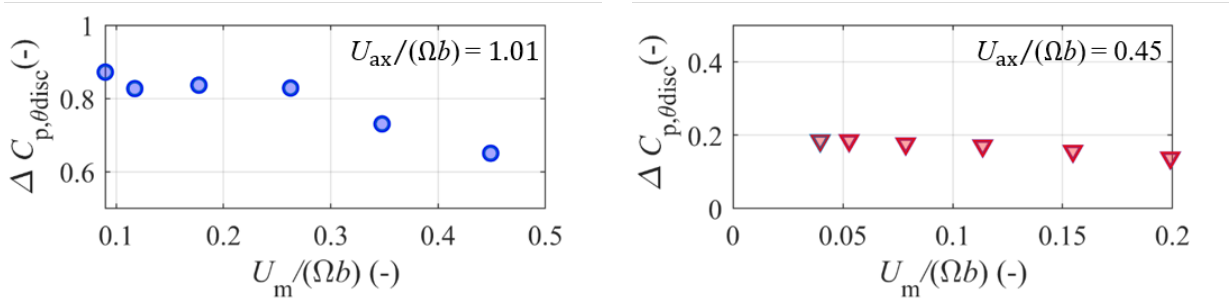

(a) (b)

Figure 5.4: Effect of purge flow, $U_m/(\Omega b)$, on the peak-to-peak circumferential pressure coefficient difference $\Delta C_{p,\theta disc}$ for $s_c = 0.0042$ at (a) $U_{ax}/(\Omega b) = 1.01$ and (b) $U_{ax}/(\Omega b) = 0.45$.

A decay of pressure amplitude with an increase of purge supply is identified. Two constant values of flow coefficient, $U_{ax}/(\Omega b) = 1.01$ and $U_{ax}/(\Omega b) = 0.45$, reveal a lower influence of the purge flow ratio at low flow coefficient. These results align with the

findings of Sangan *et al.* [39] where a small reduction of $C_{\mathrm{p},\theta\mathrm{disc}}$ was identified for higher sealing flows although they both contradict the lack of influence of the purge flow over the pressure asymmetries reported by Roy *et al.* [44]. Nonetheless, the influence of the purge flow is secondary to flow coefficient, see Fig.5.2. The third tapping from the right hand side appears as an anomalous point that departs from the general sinusoidal trend. It is suspected this is due to it falling directly under the influence of the vane wake.

5.2.2 Steady cavity flow behaviour

Examples of radial profiles of the mean pressure coefficient on the stator disc are shown in Fig.5.5. These correspond to the smaller seal clearance and a constant purge flow rate of $C_{\mathrm{w}} = 3500$ ($U_{\mathrm{m}}/U_{\mathrm{ax}} = 0.08$). Results with and without vanes are given at two values of non-dimensional purge flow ratio corresponding to $\mathrm{Re}_{\phi} = 1.5 \times 10^6$ (left) and $\mathrm{Re}_{\phi} = 2.9 \times 10^6$ (right) respectively. The cavity pressure coefficient, C_{p}, has been referenced to the measurement point located furthest inboard in the cavity and the dynamic head at disc rim speed has been used for non-dimensionalisation.

For the rotational Reynolds numbers shown, the flow in the cavity is expected to be fully turbulent with separate boundary layers developing on each wall with a rotating core in between [8]. Typically, for turbulent flow in shrouded rotor-stator cavities, the core vortex rotates at approximately 40% of the rotor disc speed [8]. The vortex strength may be affected by mainstream ingestion, cavity geometry, purge flow rate and rotor speed. The combined effects of purge flow rate and rotor speed can often be captured by the turbulent flow parameter (or throughflow parameter), $\lambda_{\mathrm{T}} = C_{\mathrm{w}}/\mathrm{Re}_{\phi}^{0.8}$, where $C_{\mathrm{w}} = \dot{m}/\mu b$ is the non-dimensional flow rate. This non-dimensional variable was already used in chapter 4 to describe the cavity flow behaviour. The data shown in Fig.5.5 correspond to throughflow parameter values of approximately 0.04 (left) and 0.02 (right) respectively. The two different slopes in all radial profiles of C_{p} in Fig.5.5 suggest a change in the swirl velocity between the outer and inner parts of the cavity at the inflexion point in the ge-

ometry of the stator wall. Lines indicating pressure distributions for various forced vortex strengths are also plotted for reference since they match the slopes in the radial distributions. Fig.4.2 showed that the disc pumping effect in isolation (no purge nor annulus flow) would induce vortices in the cavity rotating at 41% and 55% of the disc speed. Fig.5.5 explores how the purge supply, type of external flow and rotational Reynolds number affect the aerodynamics of the cavity flow.

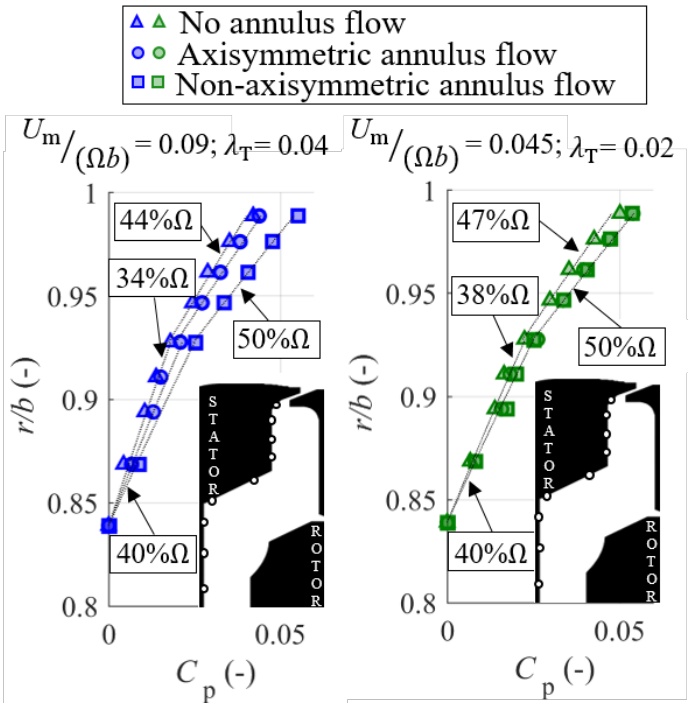

Figure 5.5: Radial profile of C_p inside the cavity without annulus flow, with axisymmetric and with non-axisymmetric annulus flow for $s_c = 0.0042$, $U_m/U_{ax} = 0.08$ at $U_m/(\Omega b) = 0.09$ ($\mathrm{Re}_\phi = 1.5 \times 10^6$) on the left and $U_m/(\Omega b) = 0.045$ ($\mathrm{Re}_\phi = 2.9 \times 10^6$) on the right.

For the test cases without vanes (no annulus flow and axisymmetric annulus flow), Fig.5.5 shows that the outer and inner cavity swirl velocities increase as the rotational Reynolds number is raised. For example, without annulus flow the swirl velocity in the outer cavity goes up from approximately 44% to 47%. This is due to a larger transfer of angular momentum from the rotor disc consistent with a change in throughflow parameter.

Interestingly, results for the vaned configuration are in close agreement implying a suppression of the sensitivity to rotational Reynolds number. This is attributed to inges-

tion of highly swirled annulus flow in this configuration compensating for the increase in vortex strength expected from the reduction in λ_T. Recent studies suggest a beneficial impact of swirling the purge flow to reduce the viscous losses derived from the interaction of the mainstream and sealing flows. The effect of rotation on ingestion is further explored in the following section. The angular momentum of the annulus flow appears to influence the cavity pressure. This explains why an axial annulus flow exerts negligible impact on the cavity pressures when compared to the case of no annulus flow.

The cavity pressure coefficient evaluated near the rim ($r/b = 0.99$) has been plotted as a function of the turbulent flow parameter across the test conditions in Fig.5.6. From the definition, this represents the pressure difference across the cavity in the stator wall. Fig.5.6 compares the cavity pressure gradient as a function of the turbulent flow parameter under the influence of an axisymmetric and non-axisymmetric external annulus flows for two clearance sizes. Therefore, this builds up from Fig.4.4 discussed in chapter 4.

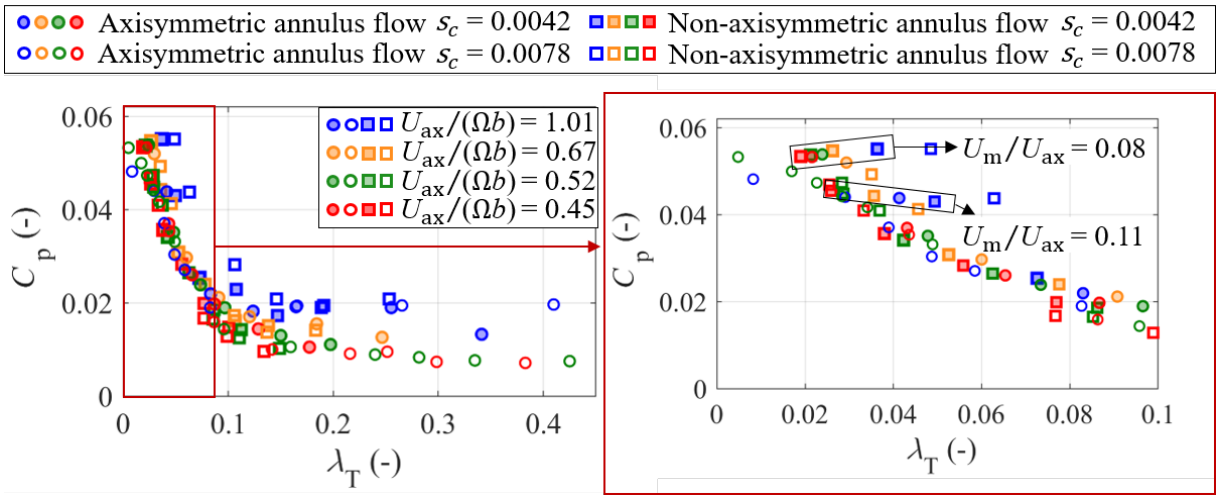

Figure 5.6: Cavity pressure coefficient as a function of λ_T for two seal clearances under axisymmetric and non-axisymmetric conditions of external annulus flow.

Overall, two distinct regimes are identifiable: a linear region for $\lambda_T < 0.1$ and an asymptotic region for $\lambda_T > 0.1$ with larger data scatter. Similarly to what was described in section 4.2, a sufficiently large supply of sealing flow, $\lambda_T > 0.1$, overcomes the disc pumping effect suppressing the rotating core in the cavity and ejecting free vortex flow

into the mainstream. For a free-disc with zero radius this would occur at approximately $\lambda_{T,fd} \sim 0.22$. Accounting for the effect of a non-zero inner radius of the disc, this change in flow behaviour would occur at $\lambda_T \sim 0.1$ in this set up hence agreeing with the experimental data of Fig.5.6.

Under the influence of an axisymmetric annulus flow, section 4.3.3 revealed that the cavity pressure coefficient and the sealing effectiveness were affected by the rotational Reynolds number. This was observed in the distribution of $C_p - \lambda_T$ as different asymptotic values of the cavity pressure coefficient depending on the rotor disc speed. For $\lambda_T > 0.1$, test data obtained at $N = 4000$ rpm asymptotically settled at $C_p \sim 0.02$ whilst a value of ~ 0.01 was observed for higher rotor disc speeds. In the linear region however, all measurements showed satisfactory agreement and such an effect was not identified. In Fig.5.6, data with non-axisymmetric mainstream conditions generally agree with the behaviour above described. Notwithstanding, in the range of $0 < \lambda_T < 0.07$ of the linear regime, rotor disc speed discrepancies are observed. This is consistently recorded for both gap sizes under consideration. A zoomed in view in Fig.5.6 allows for better detailed observation of this region.

At high rates of ingestion (low purge flow supply $U_m/U_{ax} = 0.08$ and $U_m/U_{ax} = 0.11$), the experimental data in Fig.5.6 shows departure from the linear trend thus evidencing an effect of the flow coefficient $U_{ax}/(\Omega b)$. Considering a constant purge supply and change in rotor disc speed, the cavity pressure coefficient experiences a slight increase with turbulent flow parameter. Note that C_p was introduced as a measure of the vortex strength inside the cavity in Fig.5.5 and therefore is proportional to the swirl velocity of the rotating core. Unexpectedly, the dataset of $U_m/U_{ax} = 0.08$ reveals that the swirl velocity (inferred from the C_p) and the rotor disc speed are inversely proportional. This goes against the believed assumption that higher rotational Reynolds numbers would induce a stronger rotating motion in the adjacent fluid. Nonetheless, this effect could be explained if larger

ingress of highly swirled mainstream flow external to the cavity was occurring under these conditions. A slightly higher supply of purge flow, $U_{\mathrm{m}}/U_{\mathrm{ax}} = 0.11$, still shows departure from the trend line in the linear regression but the vortex strength shows direct proportionality with the rotor disc speed. This unusual phenomenon was observed for $s_c = 0.0042$ as well as for $s_c = 0.0078$ at all conditions of $U_{\mathrm{m}}/U_{\mathrm{ax}} < 0.08$.

5.3 Sealing performance

Results of sealing effectiveness under different conditions of purge flow rate, rim seal gap size, rotational speed and annulus flow conditions are assessed in this section. Comparisons against the disc pumping correlation by Chew [25] and the simple orifice model for pressure-driven ingestion by Hamabe and Ishida [30] are included.

5.3.1 Effect of mainstream flow conditions

Radial distributions of sealing effectiveness on the stator wall under three different conditions of annulus flow are represented in Fig.5.7 for constant $\mathrm{Re}_\phi = 1.5 \times 10^6$ (4000 rpm) and $C_{\mathrm{w}} = 3500$ (corresponding to $U_{\mathrm{m}}/U_{\mathrm{ax}} = 0.08$). Silhouettes of the rim seal and cavity geometry are aligned with the radial position of the ordinate. At this operating point, the addition of axisymmetric flow in the annulus induced a 5% reduction in the sealing capability of the chute seal under rotationally-induced ingestion. With non-axisymmetric annulus flow, the introduction of swirl velocity and circumferential variations in pressure in the annulus drastically reduced the sealing effectiveness by 33% in the inner cavity and 60% near the rim seal. Under these circumstances, the ingestion mechanism is clearly driven by the annulus pressure asymmetries. For the cases without annulus flow and with axisymmetric annulus flow, the cavity appears to be almost fully sealed with a uniform radial profile of sealing effectiveness. However, for the vaned configuration, the outer part of the cavity is significantly affected by the entrainment of mainstream flow. This is reflected through high gradients that cause a remarkable decrease in sealing effectiveness

in the proximity of the rim seal. Again, departure from the typical Batchelor flow is observed in the upper cavity due to a larger mixing region where the ingressed external flow dilutes the radially outward purge flow. Similar behaviour was reported by Horwood *et al.* [53] for their study of a chute seal, but not for those previously conducted with other rim seal geometries. This flow structure was attributed to the rotor boundary layer impinging directly upon the stator wall that acted to encourage mixing.

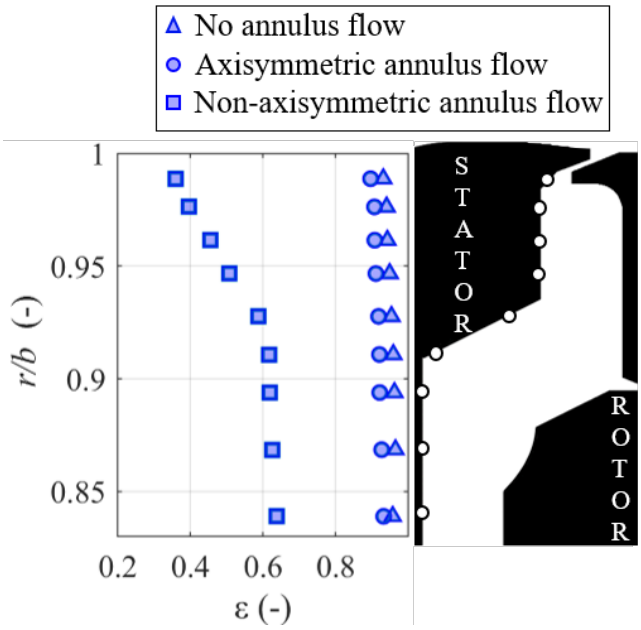

Figure 5.7: Effect of the external flow conditions in the sealing effectiveness radial distribution at $C_{\mathrm{w}} = 3500$ ($U_{\mathrm{m}}/U_{\mathrm{ax}} = 0.08$) at $\mathrm{Re}_{\phi} = 1.5 \times 10^6$ and $s_c = 0.0042$.

The effectiveness profiles with annulus flow (without and with vanes) from Fig.5.7 are reproduced in Fig.5.8(a), alongside results at lower flow coefficients. The purge supply, annulus flow rate and seal clearance are identical for all data in this figure. Therefore, these results show the effect of rotational speed for the cases without and with annulus pressure asymmetries from the NGVs. The speed variation also corresponds to changes in flow coefficient, reflecting the balance of rotational and pressure-driven ingestion when vanes are present, Table 5.2.

Fig.5.7 shows an evident deterioration of the sealing performance at all radial positions when pressure asymmetries in the annulus are induced by the NGVs. However, Fig.5.8(a)

reveals a very interesting inversion of the effect of rotational speed in combination with the external flow conditions. To the author's knowledge, this effect has not been previously identified.

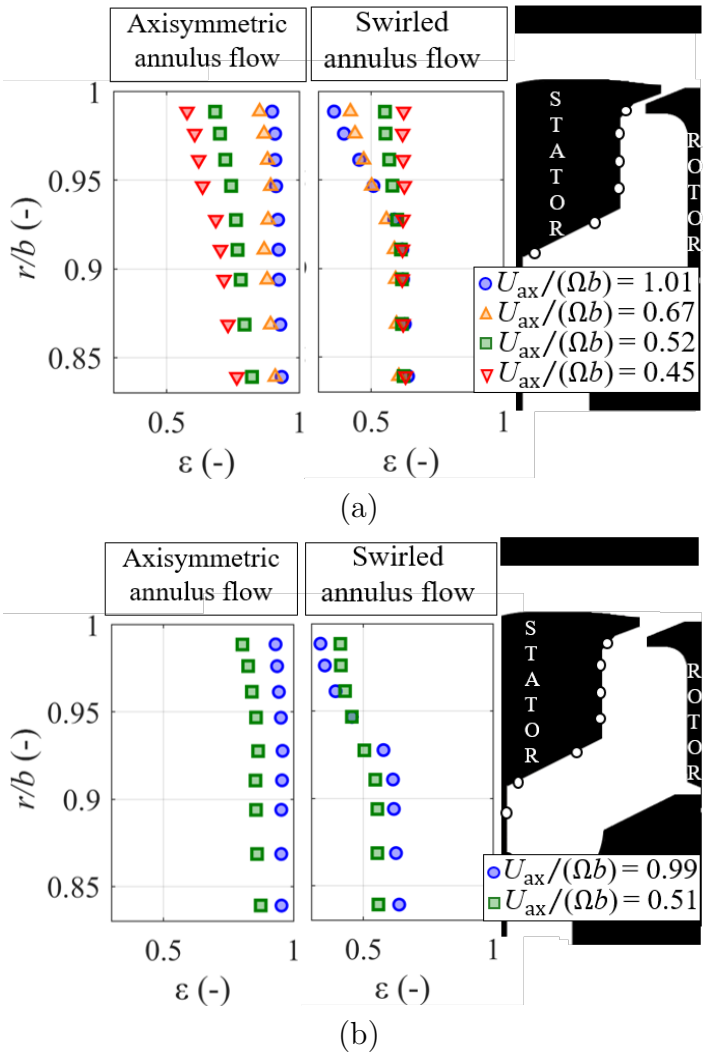

Figure 5.8: Effect of flow coefficient and annulus pressure asymmetries at: (a) $C_w = 3500$ ($U_m/U_{ax} = 0.08$) for $s_c = 0.0042$, (b) $C_w = 4800$ ($U_m/U_{ax} = 0.06$) for $s_c = 0.0078$.

For the case with axisymmetric annulus flow, the increase in rotor speed induces a stronger pressure difference across the rim seal, and more annulus flow is entrained into the cavity – see Fig.5.5. In the case of non-axisymmetric annulus flow, a decrease in the flow coefficient (higher rotational speed), results in an increase of sealing effectiveness, indicative of less annulus flow being entrained into the cavity. Therefore, Fig.5.8(a) suggests that fostering the disc pumping effect with higher rotor speeds prevents ingestion

of mainstream flow. This unexpected outcome was consistently observed across the test matrix for several combinations of purge flow rates and seal clearances. At the lowest flow coefficient tested, $U_{\mathrm{ax}}/(\Omega b) = 0.45$, the sealing effectiveness for the axisymmetric annulus flow dropped just below that for the vaned configuration at the outer radii.

Phadke and Owen [14] postulated that pressure asymmetries in the annulus gas path drive the hot ingestion mechanism when NGVs are present. The disc pumping effect under these circumstances was generally expected to be significantly lower although both mechanisms were thought to co-exist under certain circumstances. The high flow coefficient results presented in Fig.5.7 and Fig.5.8(a) are consistent with this statement. However, at higher rotational speeds (or lower flow coefficients), Fig.5.8 challenges the assumption that ingestion will be dominated by the external pressure asymmetries when vanes are fitted. The data shown in Fig.5.8 suggest that the rotationally-induced flow can suppress pressure-driven ingestion. This was also captured by the numerical study conducted by Palermo *et al.* [78] for similar seal and cavity geometries using URANS.

Fig.5.8(b) shows comparable results for the larger seal gap at a fixed purge flow rate, for flow coefficients of $U_{\mathrm{ax}}/(\Omega b) = 1.01$ and $U_{\mathrm{ax}}/(\Omega b) = 0.51$. For the axisymmetric annulus flow scenario, increasing rotation results in larger ingestion, aligning with Fig.5.8(a). For the case with vanes, the results are consistent with the findings from the smaller clearance: better sealing performance at lower flow coefficient is found near the rim. However, the influence of rotation is weaker for the larger clearance. This could be due to purge and pressure-driven mass flows increasing for the larger clearance while disc pumping flows are less dependent on the gap size. Nevertheless, as the seal clearance is increased by changing the axial spacing between the rotor and stator only, geometrical similarity is lost, particularly in terms of the axial overlap of the chute seal, and this could also account for the different behaviour of the two seals.

5.3.2 Overall sealing effectiveness dependencies

Fig.5.9 presents a summary of the smaller seal clearance studies as a map of sealing effectiveness against the non-dimensional purge flow, $U_m/(\Omega b)$. Data were all obtained at a radius near the rim, $r/b = 0.99$, and included for all rotor speeds and purge flow rates investigated. The colored lines in Fig.5.9 connect results at the same flow coefficient (rotor disc speeds) whilst the dotted black lines join the data at constant purge flow rate for different rotor disc speeds, assessing the effect of flow coefficient. Results are compared against the test case with external axisymmetric flow and the analytical correlation for disc pumping effect given by Eq.2.1 with $k = 1$.

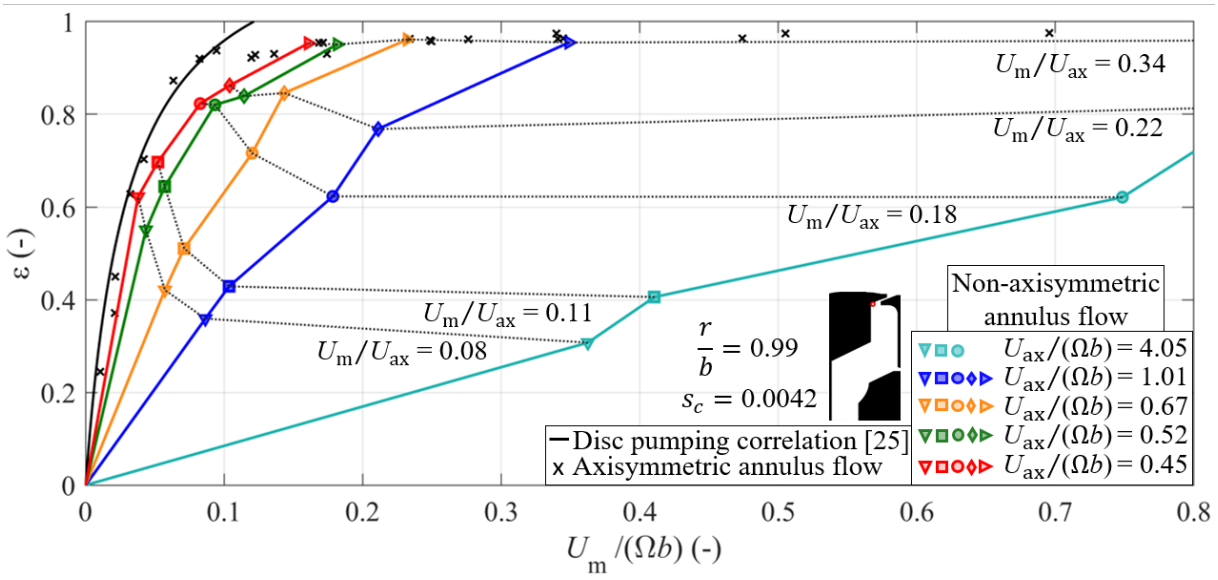

Figure 5.9: Map of sealing effectiveness against non-dimensional purge flow ratio, $U_m/(\Omega b)$, at $r/b = 0.99$ for different seal-to-axial velocity ratios, U_m/U_{ax}, and flow coefficients, $U_{ax}/(\Omega b)$, under axisymmetric and non-axisymmetric external annulus flow.

Effect of flow coefficient

Higher seal-to-axial velocity ratios consistently provide better sealing by increasing the pressure inside the cavity so that less external fluid is drawn into the cavity. The effect of reducing flow coefficient (increasing rotor speed) at a constant purge supply can be analysed by following each of the black dotted lines from right to left. At low values of

U_m/U_{ax} (where significant ingestion occurs) strong sensitivity to flow coefficient is evident. For example, the results for $U_m/U_{ax} = 0.08$ reveal an important 30% improvement of the sealing effectiveness as the flow coefficient decreases from 4.05 to 0.45. This trend was observed along the flat surface of the stator wall (upper cavity volume) in Fig.5.8(a) and it can be related to the reduced amplitude of the non-dimensional annulus pressure asymmetries in Fig.5.2(b). The $U_{ax}/(\Omega b) = 4.05$ test case represents a virtually stopped rotor in which the disc pumping effect is negligible. This scenario is relevant during under-speed of the engine - through engine start-up and part-load operation. The sealing effectiveness values at $U_{ax}/(\Omega b) > 1$ ($N = 1000$ rpm and 4000 rpm) in Fig.5.9 are very similar thus indicating that pressure-driven ingestion dominates at lower speeds.

As shown in Table 5.2, both rotational Reynolds number, Re_ϕ, and flow coefficient, $U_{ax}/(\Omega b)$, vary with rotor speed in the present experiments. Previous rim sealing studies have found that for fixed $U_{ax}/(\Omega b)$ there is little or no dependency on rotational Reynolds number. Thus the effects of rotor speed shown here can be interpreted, at least to first order, as the effects of the flow coefficient which is equivalent to the ratio Re_{ax}/Re_ϕ used by Phadke and Owen [14]. Fig.5.9 shows that ingestion is pressure-driven at high values of the flow coefficient, such as those that might occur in low pressure turbines.

At high purge flow rates, $U_m/U_{ax} \geq 0.22$, Fig.5.9 reveals an almost invariant sealing effectiveness value albeit changes in flow coefficient. It becomes apparent that a fully sealed cavity is not reached under any of the test conditions considered during this investigation, highlighting the complexity of the interaction of the purge and annulus flows in the rim seal region. For low flow coefficients, such as might be found in core turbines, both rotational and pressure-driven effects may be important. As the flow coefficient reduces to 0.45 the sealing effectiveness approaches values associated with rotationally-driven ingestion suggesting that the disc pumping effect prevails. This is particularly the case at low purge flow rates. The effect of disc speed has important implications for engines,

especially high pressure turbines which usually have flow coefficients in the range where the sealing effectiveness is sensitive to rotor disc speed. Indeed, some references in the open literature define the design point flow coefficient in modern high pressure turbine stages at $U_{\mathrm{ax}}/(\Omega b) = 0.5$ (with this value being slightly lower than those found in previous designs due to the increasingly larger flow angles achieved at the exit of the NGVs).

Previous studies investigating the effect of flow coefficient at off-design conditions were published by Savov *et al.* [29] for a single and double lip seal geometry and Scobie *et al.* [71] for single radial and axial seals as well as a double radial seal. Savov *et al.* investigated the effect of modifying the flow coefficient for a constant non-dimensional flow ratio and they identified a reduction of the sealing capability at low rotor disc speeds. The study conducted by Scobie *et al.* [71] at a turbine test rig at the University of Bath consisted of varying the non-dimensional purge flow rate for a constant flow coefficient. This process was then repeated at different flow coefficients as shown in Fig.5.10 for a radial and an axial seal.

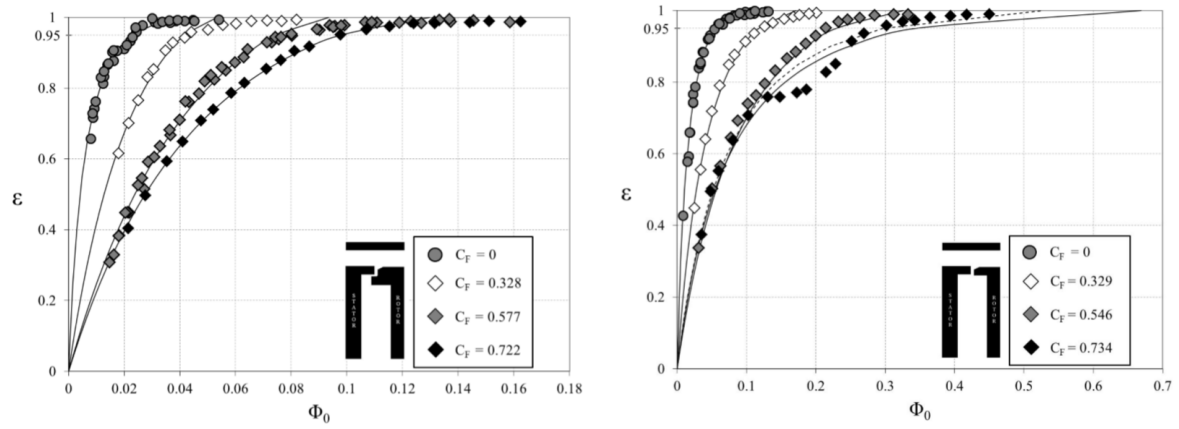

(a) (b)

Figure 5.10: Effect of flow coefficient on the sealing effectiveness for (a) a radial seal and (b) an axial seal [71].

The investigation undergone within this project combined both approaches: firstly, a fixed rotor disc speed maintained a constant value of flow coefficient and by varying the purge flow rate, a sweep through $U_{\mathrm{m}}/(\Omega b)$ was conducted. Secondly, for a constant purge

flow rate, the rotor disc speed was modified based on Table 5.2 providing the different flow coefficients. Nonetheless, it should be noted that, whilst Savov *et al.* had an invariant non-dimensional purge flow ratio (vertical lines in Fig.5.11), the study in the ORF maintained a constant U_{m} and the variations in rotor disc speed led to the inclined blue lines in Fig.5.11.

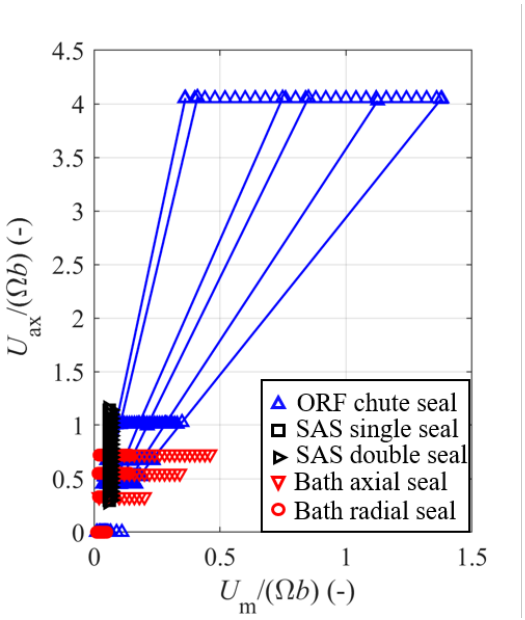

Figure 5.11: Comparison of test conditions of published experimental studies ([29] and [71]) on the influence of the flow coefficient over the sealing performance.

Scobie *et al.* argued that externally-induced ingestion dominates at design point ($U_{\mathrm{ax}}/(\Omega b) = 0.538$ for the Bath test rig) and fitted their experimental results to the orifice model derived by Owen [38] for Combined Ingress (CI). This is an intermediate regime defined by this research group between the externally-induced ingestion and rotationally-induced ingestion for the scenario where the disc pumping effect gains relevance. The data from Scobie *et al.* showed departure of the CI curve at low values of flow coefficient, which was attributed to the effects of separation of the mainstream flow over the turbine blades at large deviation angles between the flow and the blades. Given the similarity in the test conditions between the experiments of Scobie *et al.* and those obtained in this research according to Fig.5.11, the departure from the CI curve could be explained

based on the larger predominance of the disc pumping effect. This could imply that the influence of rotationally-induced ingestion may have been undermined in the CI orifice model and not only it is significant, but it could even be dominant. Notwithstanding, it is important to highlight that the cavity, seal and annulus configurations were different, with blades present in Scobie *et al.*'s experimental set up and not in that investigated here.

Variations in flow coefficient due to changes in tangential velocity at the rotor rim affect the velocity triangles by inducing a variation of the annulus flow angle. The closest agreement between the NGV exit tangential velocity and that of the purge flow is found at $U_{\mathrm{ax}}/(\Omega b) = 0.45$. This could imply that similarity in the swirl component of the mainstream and the outbound purge flow reduces shear between the two streams and improves the sealing capability of the rim seal. CFD prediction from Palermo *et al.* [78] captured some of the trends described here. In particular, at lower flow coefficient, CFD predicted that the chute seal may offer some insensitivity to pressure-driven effects, in agreement with measurements. Nonetheless, the CFD underpredicted the levels of ingestion.

Effect of seal clearance

The influence of the rim seal gap size on the sealing performance of the chute seal at the rim can be assessed by visual comparison of Fig.5.12(a) and Fig.5.12(c). The reader is reminded that, apart from the 1 mm nominal gap size, a second larger seal clearance was studied in order to simulate the rearward displacement of the rotor disc at off-design conditions in an engine, such as an over-speed event. The increase of the seal clearance was achieved by including a spacer between the rotor disc and the shaft. As a consequence of the axial displacement of the rotor disc, maintaining the geometrical similarity in the cavity was not possible: from a 2 mm axial overlap at the chute rim in the configuration of $s_c = 0.0042$ the increase to $s_c = 0.0078$ led to a 0.5 mm axial separation with no overlap of the rotor and stator discs.

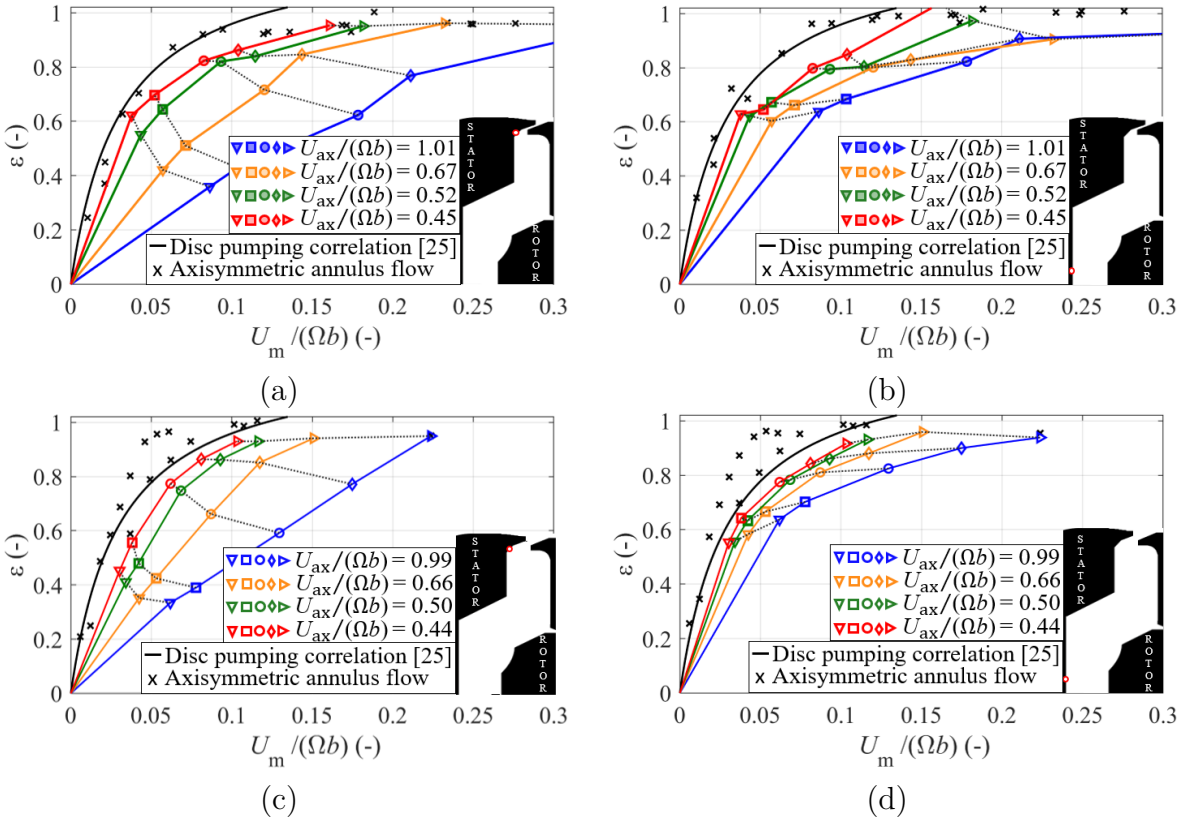

Figure 5.12: Map of sealing effectiveness against the seal-to-rotor disc speed velocity ratio, $U_m/(\Omega b)$, under axisymmetric and non-axisymmetric external flow at: (a) $r/b = 0.99$ and $s_c = 0.0042$, (b) $r/b = 0.84$ and $s_c = 0.0042$, (c) $r/b = 0.99$ and $s_c = 0.0078$ and (d) $r/b = 0.84$ and $s_c = 0.0078$.

At first glance, the same trends observed in Fig.5.12(a) are reproduced in Fig.5.12(c) thus confirming that the improvement in sealing performance detected at low flow coefficients occurs regardless of the seal clearance size and the overlap between the stator and rotor platforms. The sensitivity to flow coefficient at low purge flow rates is lower in the larger gap (smaller gradients in the dotted lines of constant U_m/U_{ax}) especially at low U_m/U_{ax}. It is suspected that the larger ingress of swirled annulus flow (caused by a larger gap area) increases the swirl of the rotating core inside the cavity at all rotor disc speeds. As a result, the annulus pressure asymmetries gain relevance in the detriment of the disc pumping effect at low flow ratios where this was seen to dominate at $s_c = 0.0042$. This is observed by a larger departure of the data for $U_{ax}/(\Omega b) = 0.44$.

An interesting fact shedding from Fig.5.12 is that the non-dimensional purge flow ratio required to seal the cavity volume (taken at $\varepsilon = 0.95$) is lower at $s_c = 0.0078$. This counter-intuitive output might be explained by the change in cavity geometry mentioned above. The 1 mm nominal seal clearance of the chute has been measured in the perpendicular direction to the rotor disc at the rim which, in the axial direction corresponds to a 2.9 mm axial seal clearance. Due to the axial overlap, the flow passing through 2 mm/2.9 mm of this axial distance is experiencing high levels of shear induced by the rotor disc rotation being positioned close to the stationary surface. Increasing the gap in this case removes the shear between rotating and stationary surfaces and leads to a 0.5 mm axial seal clearance. The increase in sealing performance for the wider gap was already identified in the axisymmetric annulus flow configuration (and can be deduced from the crosses in Fig.5.12(a) and Fig.5.12(c)).

Effect of radial position

The sealing effectiveness map in Fig.5.9 was thoroughly analysed for the data obtained near the rim, $r/b = 0.99$, and $s_c = 0.0042$. This section aims to explore the influence of the purge flow and flow coefficient over the sealing effectiveness at a point further inboard in the cavity, $r/b = 0.84$. These data are plotted for $s_c = 0.0042$ and $s_c = 0.0078$ in Fig.5.12(b) and (d) respectively. At this radial position, the ingested mainstream flow, if at all present, is expected to be fully mixed with the stator wall boundary layer and widely independent of the mainstream flow coefficient. Indeed, the radial profiles of sealing effectiveness in Fig.5.8 showed that the ingested mainstream flow was fully mixed as displayed by an invariant profile independent of flow coefficient and radial position. Consistently, Fig.5.12(b) shows an almost constant horizontal line for each $U_{\mathrm{m}}/U_{\mathrm{ax}}$ confirming the external flow coefficient had minimal effect.

For the lowest purge flow rates represented in Fig.5.12(b), a slight increase in the sealing performance is observed for the larger flow coefficients. This effect becomes more

obvious in Fig.5.12(d) for $s_c = 0.0078$. In the inner cavity, the rotor disc pumping effect prevails thus resisting transport of the ingested annulus flow along the stator wall. As a result, the ingested mainstream flow does not reach the inner cavity and the influence of the external annulus flow is hardly felt. Consequently, an improvement of the sealing effectiveness with increasing flow coefficient (similar to that observed for the case of axisymmetric annulus flow shown in Fig.5.8) is identified. These observations are consistent with the findings of Savov *et al.* [29] who detected a decrease followed by a raise in sealing effectiveness in the inner cavity as the rotor disc speed was reduced.

5.3.3 Comparison to previous work

The results from the current research are compared in Fig.5.13 to the data for a chute seal obtained by Horwood *et al.* [53] in a turbine rig at the University of Bath. The flow coefficient for the turbine was 0.35 compared to 0.45 for the results shown from the ORF. Notwithstanding, it is worth mentioning that Horwood *et al.*'s experiments included effects of the rotating blades and a different vane design. Values of effectiveness are obtained at $r/b = 0.96$ in the ORF and the facility at the University of Bath.

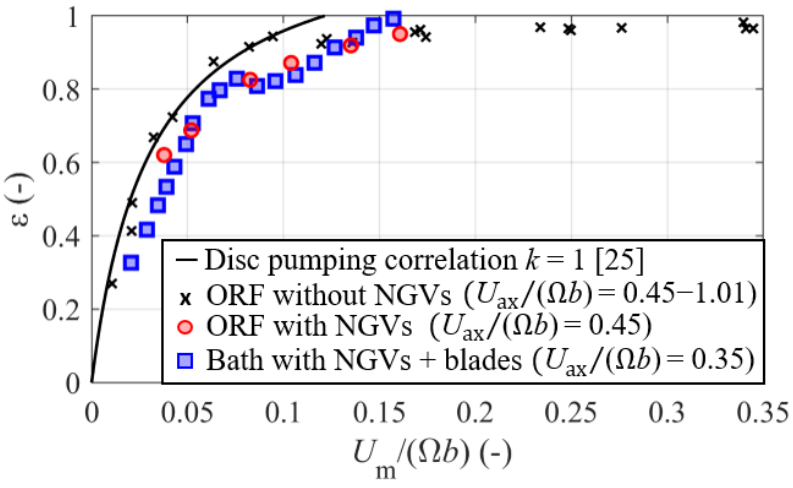

Figure 5.13: Comparison of sealing performance of the ORF chute seal under different external flow conditions at $r/b = 0.96$ against the chute seal from Horwood *et al.* [53] and the disc pumping correlation from Chew [25].

Good agreement is evident despite the different test conditions. Sealing effectiveness

measurements at the University of Sussex for a chute seal by Gentilhomme [79], as presented in references [54] and [78], also show some agreement with the present results. The Sussex experiments were conducted in a turbine rig with a flow coefficient ~ 0.6, and included a significant density difference between the purge and main annulus flows. Calculation of $U_{\mathrm{m}}/(\Omega b)$ for the Sussex data was subject to some uncertainty so these are not shown in Fig.5.13. Nonetheless, the similarity of the results with data from other research facilities suggests some insensitivity to turbine design at low flow coefficients, which is encouraging for extrapolation of rig data to engine conditions. The inflection point in the sealing effectiveness curve was the focus of the study of Hualca *et al.* [64] who attributed it to the presence of rotor blades. The discreet data points from the ORF do not provide enough information to investigate this effect.

Engine representative conditions in scaled test facilities are simulated by matching the relevant non-dimensional parameters. The non-dimensional purge flow $U_{\mathrm{m}}/(\Omega b)$ defines the extent of ingestion and the turbulent flow parameter characterises the flow structure inside the cavity. Values between 0 and 0.1 are typically found in aero-engines for both quantities thus this research is considered to represent the flow behaviour in an engine cavity. Characteristic values of rotational Reynolds number in aero-engines are of the order of 10^7. Despite the range of Re_ϕ covered in this study being an order of magnitude below engine-realistic conditions, Fig.5.9 suggests that extrapolation to values of flow coefficient found at engine operating conditions would intensify the disc pumping effect. This is the case especially for high pressure turbines which usually have flow coefficients in the range where the sealing performance displays high sensitivity to rotational speed.

Considering correlation of results, it is also of interest to compare present measurements with the orifice model. While numerous variations of the orifice model are available, Hamabe and Ishida's version [30] assuming a sinusoidal pressure distribution and constant discharge coefficient has been used for an initial comparison. The amplitude of the cir-

cumferential pressure variations have been obtained from the data shown in Fig.5.2 for $s_c = 0.0042$ and $U_m/U_{ax} = 0.08$. Fig.5.14 compares sealing effectiveness at flow coefficients of 0.45 and 1.01 with the orifice model at a radial position $r/b = 0.96$ assuming discharge coefficients of 0.4 and 0.6 at these two conditions.

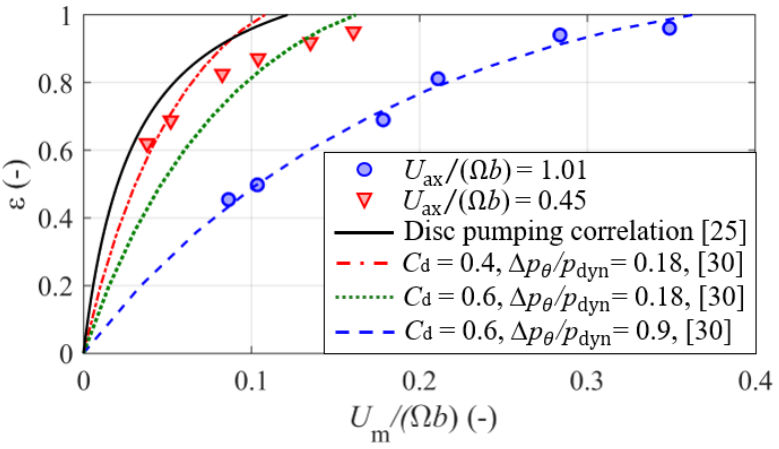

Figure 5.14: Comparison of experimental data against prediction from [30] and [25].

For $U_{ax}/(\Omega b) = 1.01$ (4000 rpm), the orifice model displays satisfactory agreement with $C_d = 0.6$. At $U_m/(\Omega b) = 0.45$ (9000 rpm), $C_d = 0.4$ fits the data better at low effectiveness and $C_d = 0.6$ is more suitable at high sealing effectiveness. The disc pumping effect correlation by Chew [25] is also included for comparison. The experimental data and orifice model predictions approach the disc pumping correlation at low flow coefficients. In addition, Fig.5.14 suggests that discharge coefficients in the orifice model predictions could be redefined and be considered a function of flow coefficient, reducing as the orifice model predictions approach values for rotationally-driven ingestion.

5.3.4 Effect of relative position to NGV trailing edge

The improvement in sealing effectiveness at low $U_{ax}/(\Omega b)$ sparked the question of whether this only occurred because the cavity measurement points were located directly under the influence of the NGV wake or in the middle of the passage. In order to investigate the effect of the relative position between the cavity measurements and the trailing edge of the NGVs, a stator ring was machined with a 5° offset of the radial measurement points

as described in section 3.2.2 and shown in Fig.3.21. In addition, two rows of tappings at $r/b = 0.89$ and $r/b = 0.98$ were included in the circumferential direction covering one NGV pitch of 10°. Tests were repeated for $U_{\mathrm{m}}/U_{\mathrm{ax}} = 0.08$ and $s_c = 0.0042$.

Radial profiles

The dataset obtained at $\Delta\theta_{\mathrm{NGV}} = +1°$ confirmed the previously reported improvement of rim sealing performance at low flow coefficients, see Fig.5.15. The observed trends are consistent with those shown in section 5.3.1. Nonetheless, Fig.5.15 reveals a positive shift towards higher values of sealing effectiveness at all conditions studied. This increase in sealing performance could be attributed to the change in relative position of the cavity measurement points respect to the NGV trailing edge in the annulus. A more in depth analysis is required before drawing any conclusions.

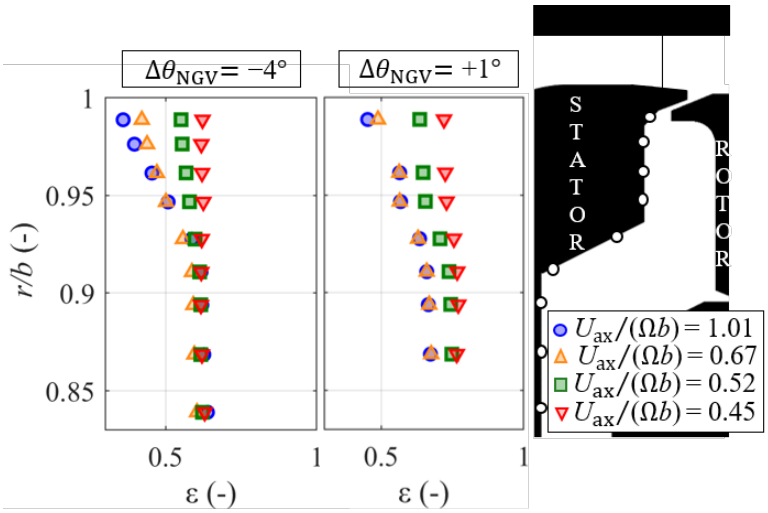

Figure 5.15: Comparison of the sealing effectiveness radial profiles in configuration of Stage 3 for two different circumferential locations $\Delta\theta_{\mathrm{NGV}} = -4°$ and $\Delta\theta_{\mathrm{NGV}} = +1°$ at $U_{\mathrm{m}}/U_{\mathrm{ax}} = 0.08$ and $s_c = 0.0042$.

It is worth highlighting that the higher resolution in the cavity instrumentation resulted in more pneumatic tubes stemming from the NGV ring. Despite all efforts, some of the tubing ended up being totally or partially blocked during installation. These datapoints were not able to provide trustful results and have been removed from the plots ($r/b = 0.84$ and $r/b = 0.98$ for $\Delta\theta_{\mathrm{NGV}} = +1°$in Fig.5.15).

Values of sealing effectiveness inside the cavity were taken at different circumferential positions that covered one NGV pitch. The circumferential distributions of sealing effectiveness did not reflect the $\Delta\varepsilon \sim 20\%$ variation observed in Fig.5.15 for a $\Delta\theta = 5°$. The presence of blocked and partially blocked tubing casted doubt in the validity of the results and therefore these have not been included. The possibility of a leak in the measurement system was explored: the rig was dismantled, pneumatic tubes checked and cleaned, NGV ring removed and components recommissioned. The repeat test campaign reproduced the same effect as before with extraordinary repeatability confirming the improvement in sealing effectiveness at this position, see Fig.5.16.

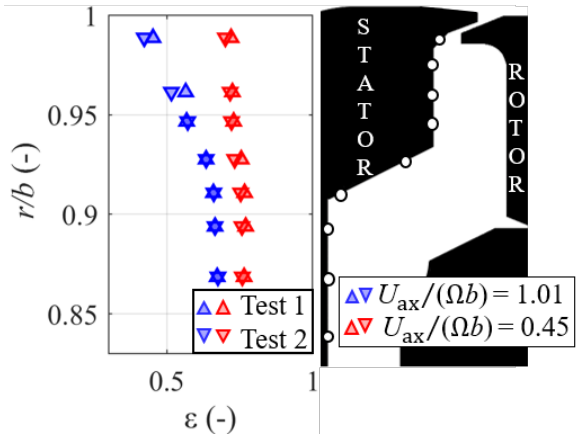

Figure 5.16: Radial profiles of repeat tests for cavity points at $\Delta\theta_{NGV} = +1°$ taken at $U_m/U_{ax} = 0.08$ and $s_c = 0.0042$.

5.4 Spoiling effect on the mainstream aerodynamics

This section aims to analyse the purge flow in the main gas path when it interacts with the mainstream flow. The main objective is to determine the impact of the purge flow at the rotor blade leading edge through measurements of gas concentration in a $\theta - r$ section of the annulus. Previous research reported a strong interaction of the purge and annulus flows causing aerodynamic losses in the main gas path due to a strengthening of the passage vortex. Nonetheless, this may enhance the cooling of the rotor blade due to radial migration of the passage vortex on the suction surface [53].

Before proceeding to the analysis of the mainstream results, it is worth highlighting that the reduced annulus arrangement may be affecting the development of the secondary flows. Therefore, the limitation of the results of this section is acknowledged. A static pressure distribution of both NGV and rotor blades should be included and compared with full span blade passage in order to study a representative flow field.

Following the methodology described in section 3.2.2, sealing effectiveness data were extracted from 15 points that covered the radial span of the reduced annulus (3 points) over one vane pitch (5 points) at the axial position equivalent to the rotor blade leading edge (with no blades). Purge-to-annulus mass flow ratios of 1% and 1.2% were chosen. All test data presented in this section correspond to the seal clearance $s_c = 0.0042$. The circumferential variation in sealing effectiveness at the three radial positions studied are included in Fig.5.17.

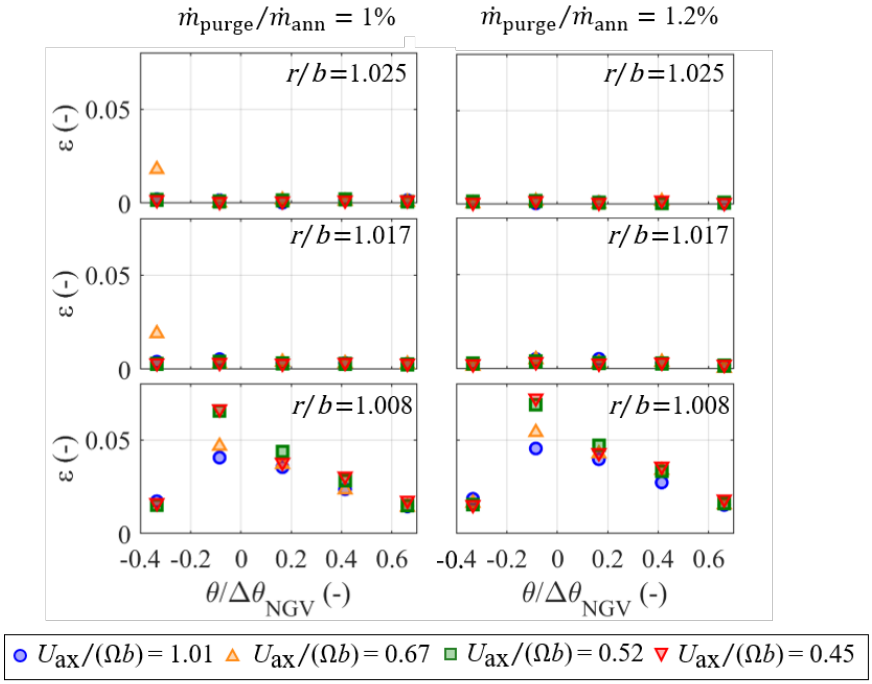

Figure 5.17: Influence of flow coefficient, radial position and purge-to-annulus flow rate on the circumferential variation of sealing effectiveness in the main gas path.

At the closest position to the hub, $r/b = 1.008$, traces of CO_2 from the sealing flow are clearly detected whilst the presence of foreign gas is negligible at the casing wall. The amount of tracer gas in the rim strongly depends on the relative position of the probe respect to the NGV trailing edge, indicating large dependency on the circumferential pressure variations induced by the stator vanes. The effect of the rotor disc speed can also be observed: at higher rotor disc speeds, the disc pumping imposes higher momentum onto the ejected purge flow which then resists mixing with the annulus unseeded flow. Consequently, this leads to higher content of CO_2 at the lowest annulus radial position.

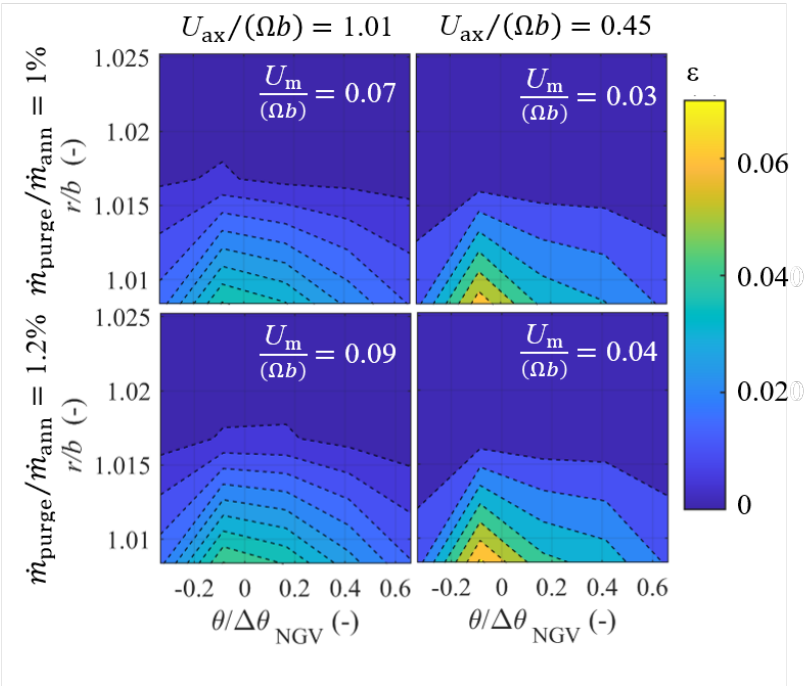

Figure 5.18: Distribution of ε in a traverse plane in the main gas path downstream of the NGVs for two flow coefficients and two ratios of purge-to-mainstream mass flow.

Contour plots of sealing effectiveness along the traverse plane at the rotor leading edge are included in Fig.5.18 for visual aid since the circumferential variations of CO_2 in the main gas path are better depicted. Results are shown for the highest and lowest flow coefficients (corresponding to $U_{ax}/(\Omega b) = 1.01$, 4000 rpm, and $U_{ax}/(\Omega b) = 0.45$, 9000 rpm, respectively). No significant differences arise from increasing the purge-to-mainstream

flow ratio at high flow coefficient (top and bottom left). The peak of tracer gas content observed in Fig.5.17 near the rim is easily identified here as the yellow region in $\theta/\Delta\theta_{\mathrm{NGV}} = -0.1$. Its presence can be sensed at all four conditions in Fig.5.18, although it is more predominant at low flow coefficients and high purge flow rate.

The reader is reminded that, as stated in chapter 3, a study to assess the development of secondary flows in the reduced annulus was not conducted and it is likely that these are not representative due to the boundary layers in the endwalls. Therefore, a cautious analysis of the mainstream flow aerodynamics of this set up and its limitations is required.

5.5 Summary

The performance of a rim chute seal and cavity subject to pressure-driven ingestion has been studied and compared to the behaviour reported in chapter 4 under rotationally-induced ingestion. Main gas path test configurations with no flow and axisymmetric flow simulated conditions of rotationally-driven ingestion. The introduction of turbine vanes upstream of the seal superimposed pressure-driven effects by creating a swirl velocity component in the annulus flow and generating circumferential pressure and velocity asymmetries. Thus two of the main drivers for hot gas ingestion in a turbine stage have been investigated.

Steady pressures have been acquired inside the cavity and on the reduced annulus casing. The radial profile of pressure coefficient on the stator wall revealed the coexistence of two vortices with different swirl velocities in the upper and lower cavities. At all test conditions, the annulus pressure asymmetries were significant compared to rotational effects. At the highest rotor speed tested, the minimum-to-maximum circumferential pressure variation in the annulus was approximately 20% of the dynamic head associated with the rotor rim speed.

Ingestion of mainstream flow into the rotor disc cavity has been evaluated using the tracer gas technique to quantify the sealing effectiveness of the chute seal. The introduction of vanes led to an overall reduction of sealing effectiveness. This effect was most severe at the largest flow coefficients studied. Decreasing the flow coefficient improved the sealing effectiveness. At the lowest flow coefficient tested, the sealing effectiveness approached that associated with rotationally-driven ingestion alone. Comparison of the radial distribution of sealing effectiveness inside the cavity for axisymmetric and non-axisymmetric flow showed opposing trends as rotor disc speed increased. A reduction in sealing performance for higher disc speeds was observed in absence of annulus flow and for an axisymmetric annulus flow. However, with vanes present, the lowest values of sealing effectiveness were found at the slowest rotational speeds investigated, with a considerable improvement at high speeds. This finding is of particular relevance for core turbines since the disc pumping effect would be intensified and sealing capability improved at the low flow coefficients found at engine conditions.

A map of sealing effectiveness against non-dimensional flow ratio showed a remarkable influence of rotor disc speed (or flow coefficient) on the sealing capability of the chute seal, especially at low purge supplies and high rotational speeds. Excellent agreement with the correlation developed by Chew [25] for the purely rotationally-driven ingestion was found at low flow coefficient. Departure from this condition increased with flow coefficient. At the lowest value considered, $U_{\mathrm{ax}}/(\Omega b) = 0.45$, the effectiveness was close to the rotationally-dominated condition. For $U_{\mathrm{ax}}/(\Omega b) > 1$, ingestion was dominated by annulus flow effects. Previous research investigating the sealing performance at off-design conditions also acknowledged a reduction in the capability to prevent ingestion at low rotor speeds. Lower sensitivity to flow coefficient was observed for an increased seal clearance. This was attributed to the ingestion of highly swirled external flow at all conditions. The change in rim geometry (loss of shear in the overlapping region of the chute) originated

by the axial rear displacement of the rotor disc is thought to be the cause of the enhancement in sealing capability observed for $s_c = 0.0078$. The influence of the flow coefficient at a further inbound point in the cavity is minimal as the rotor disc pumping dominates. Consequently, a similar effect of the flow coefficient to that observed for an axisymmetric annulus flow has been detected at $r/b = 0.84$ - the sealing effectiveness improves at higher flow coefficients (lower rotor disc speeds).

Comparison to an orifice model suggests an interesting dependence of the discharge coefficient to flow coefficient. Remarkable agreement was found when the data of this investigation was compared to that from a previously published study of a similar chute seal at the University of Bath. The resemblance of the results from different test facilities reveals a degree of insensitivity to low flow coefficient promising for extrapolation to engine conditions.

The effect of the relative position of the cavity measurements in respect to the NGV trailing edge in the annulus seems to play an important role in the sealing effectiveness results. The improvement in sealing capability at lower flow coefficients still holds regardless of the circumferential position of the measurements. However, a quantitative mismatch suggests that there is a strong dependency on whether the measurements in the cavity are taken under the influence of the NGV wake or in the mid passage. Due to limitations in the instrumentation of key points this study was deemed inconclusive.

A traverse measurement system was installed in the reduced annulus gas path to obtain data of radial migration of the purge flow at the rotor blade leading edge. Presence of tracer gas was detected near the hub (contained within 5% of the real blade span) but it did not reach the casing of the reduced annulus. Significant variations in the circumferential direction were observed especially at low flow coefficient and high purge supply.

Chapter 6

Unsteady rim seal flow structures

Since Cao *et al.*'s [15] breakthrough reporting large-scale unsteady flow structures inside the cavity, this topic has gauged the interest of several research groups. Subsequent studies have followed different approaches to investigate the number of vortices, the speed at which they rotate, the frequencies and amplitude of the peaks they generate in the frequency domain. Research in recent years has demonstrated that the unsteadiness in the rim seal cavity can also be a driving mechanism for hot gas ingestion. The rim seal instabilities are depicted as inertial waves in Fig.6.1.

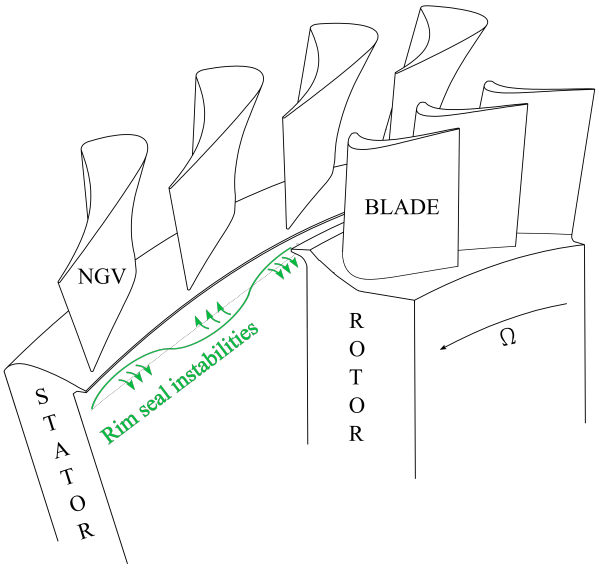

Figure 6.1: Unsteady rim seal flow structures as the driving mechanism of ingestion.

The aim of this project is to provide high quality experimental data that could contribute to improve the understanding of the underlying flow physics governing these complex flow structures also referred as rim seal instabilities. High bandwidth pressure probes have been placed in the stationary wall of the ORF cavity in order to investigate the behaviour of the unsteady cavity modes across a wide range of conditions. The data collected during this investigation could potentially be employed to update existing empirical correlations currently used in the design process of rim seals which do not account for unsteady effects.

The experimental conditions examined in this chapter are first described. The complex nature of the data acquired during these test campaigns requires a section dedicated to explain the methodology followed for the phase analysis. Results collected during the current project are compared to those from previous studies conducted in the ORF to verify the changes undergone in the working section of the facility did not affect the aerodynamic behaviour of the unsteady flow features in the cavity. Next, a study of the mean time-averaged cavity flow pattern is conducted and extended with thorough analysis of the data in the frequency domain. Finally, cross-correlation of the circumferentially-spaced pressure sensors allowed a phase analysis to determine the number and rotating speed of the flow structures.

6.1 Test matrix

Previous studies have shown that the unsteady flow features in the cavity may be sensitive to seal geometry, purge mass flow, rotor disc speed, rim seal gap size, conditions of the annulus flow, radial and circumferential coordinates inside the cavity, eccentricity, protrusions in the geometry and vibrations. The origin and nature of these structures is not fully understood therefore more research is required. In this study, the existence and characteristics of these structures have been analysed in the three working section config-

urations introduced in section 1.4 as Stage 1 (bladeless gas path with no annulus flow), Stage 2 (bladeless gas path with axisymmetric axial annulus flow) and Stage 3 (NGVs in the gas path creating a non-axisymmetric annulus flow).

Unsteady pressure measurements inside the cavity have been logged in the radial and circumferential directions to explore the effect of non-dimensional (purge) mass flow, C_{w} (often replaced by the non-dimensional flow ratio $U_{\mathrm{m}}/(\Omega b)$), rotational Reynolds number, Re_{ϕ}, non-dimensional seal clearance, s_c, and type of annulus flow. The range covered by the sweeps of each one of the handle variables is summarised in Table 6.1 (analogous to the test conditions described in chapter 5). Data was acquired for 1 s (corresponding to 150 revolutions at $N = 9000$ rpm) sampled at 1 MHz.

Table 6.1: Experimental test matrix for unsteady-induced ingestion investigation (*denotes test condition for non-axisymmetric annulus flow only).

	$U_{\mathrm{m}}/(\Omega b)$ (-)	λ_{T} (-)	C_{w} (-)	Re_{ϕ} (-)
No external flow	$0.01 - 0.11$	$0.005 - 0.05$	$820 - 4200$	$3.8 \times 10^{5*}$
Axisymmetric flow	$0.01 - 0.65$	$0.006 - 0.42$	$850 - 40000$	1.5×10^{6} 2.3×10^{6}
Non-axisymmetric flow	$0.03 - 1.3$	$0.028 - 0.63$	$3500 - 30000$	2.9×10^{6} 3.3×10^{6}

6.2 Methodology

Previous studies have reported that the unsteady flow features travel around the annular cavity rotating at a fraction of the rotor disc speed. Numerical investigations have provided good insight into the cavity aerodynamics by showing regions of high and low pressure in the rim region which are understood to be as displayed in Fig.6.2. These regions of high and low pressure are depicted as L lobes of ingress and egress separated an angle β and rotating at an angular speed ω in the same direction as the rotor disc.

Cao *et al.* [15] pointed out that the number of flow structures in the annulus at any given time may vary due to a large degree of randomness in the phenomenon.

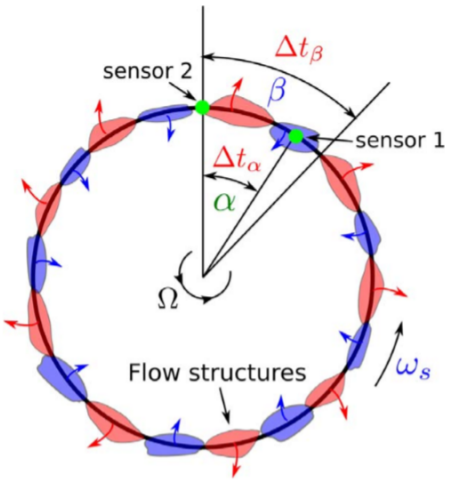

Figure 6.2: Schematic of the rotating cavity flow structure [59].

The number of lobes and the specific angular speed at which they rotate can be obtained from a phase analysis consisting of the cross-correlation of two signals spaced in the circumferential direction that provide the time or phase lag. This methodology is based on the resolution of a system of four equations to find six unknown parameters. The unsteady flow features are modelled as periodic characteristics with L lobes equally spaced in the circumferential direction by an angle $\beta = 2\pi/L$. The time required by one of these flow structures to rotate an angle β is $\Delta t_\beta = \beta/\omega$ as indicated in Fig.6.2. Measurement probes were positioned in the stator cavity wall separated by a known angle α. Assuming the flow structures rotate at a constant angular velocity ω, two stationary probes detect the same lobe with a time lag $\Delta t_\alpha = \alpha/\omega$ that represents the time that took for one same flow structure to travel the distance separating both probes. The sensors would log the same frequency $f = 2\pi/\Delta t_\beta$.

The frequency spectra provides the frequency of the lobes f allowing the calculation of Δt_β. The separation between the probes is a known physical angle, α, and the phase lag between the two, Δt_α, is obtained from the cross-correlation of the two probes under

consideration. These last two parameters (α and Δt_α) allow for the rotating speed of the lobes, ω, to be determined. With it, the angle between flow structures and, subsequently, the number of lobes in the cavity is unveiled. To summarise, the four equations required to find out the number of lobes and their angular speed are shown in Eq.6.1.

$$\Delta t_\beta = 2\pi/f; \qquad \omega = \alpha/\Delta t_\alpha; \qquad \beta = \Delta t_\beta\, \omega; \qquad L = 2\pi/\beta; \tag{6.1}$$

Due to the random nature of the phenomenon, the time lag and characteristics of the flow pattern vary from one revolution to the next. As a result, different values of time lag would be obtained for each revolution (bear in mind that 150 revolutions were logged during an acquisition time of 1 s at 9000 rpm). A histogram visually displays the most concurrent time lag (or band of time lags) for all the revolutions in the dataset under investigation. Two examples of histograms obtained in the same test campaign (conditions of no external flow at $C_\mathrm{w} = 3500$ and $\mathrm{Re}_\phi = 3 \times 10^6$ for $s_c = 0.0042$) are shown in Fig.6.3. The pairing of two sensors spaced 20° is included in Fig.6.3(a) showing a dominant time lag obtained in over 50 of the revolutions. The time lag of two pressure transducers separated by 80° is shown in Fig.6.3(b) displaying a wide spread of the time lag indicative of the high degree of randomness.

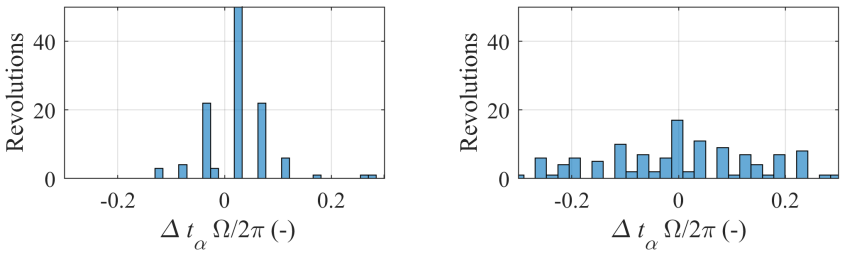

Figure 6.3: Example of histogram (a) with a dominant time lag and (b) with large spread.

Common practice has assumed an average time lag value (Horwood *et al.* [53]) to conduct the calculations above described, although Town *et al.* [58] emphasised the increased source of error that may derive when an average time lag is used instead of the dominant time lag of the flow structures.

Beard *et al.* [19] suggested an alternative methodology that overcomes this inconvenience by plotting the time lag obtained at all rotor revolutions in the summary plot included in Fig.6.4. The non-dimensional time lag provided by the cross-correlation of two spaced signals is shown in the x axis in Fig.6.4. In addition, by spacing several pressure sensors in the circumferential direction and pairing them in different combinations, various α values can be obtained. This is what appears in the y axis. The summary plots generated by Beard *et al.* contained the information for all revolutions and all possible pair of sensors revealing an aligned distribution in which it was possible to fit trend lines. The slope of the trend lines was identified as the angular speed of the flow structures. The horizontal spacing corresponds to the time lag of the flow structures, $\Delta\beta$, whilst the vertical separation of the lines provides information about the angle of the flow structures, β. However, only the positive values of the time lag have been included.

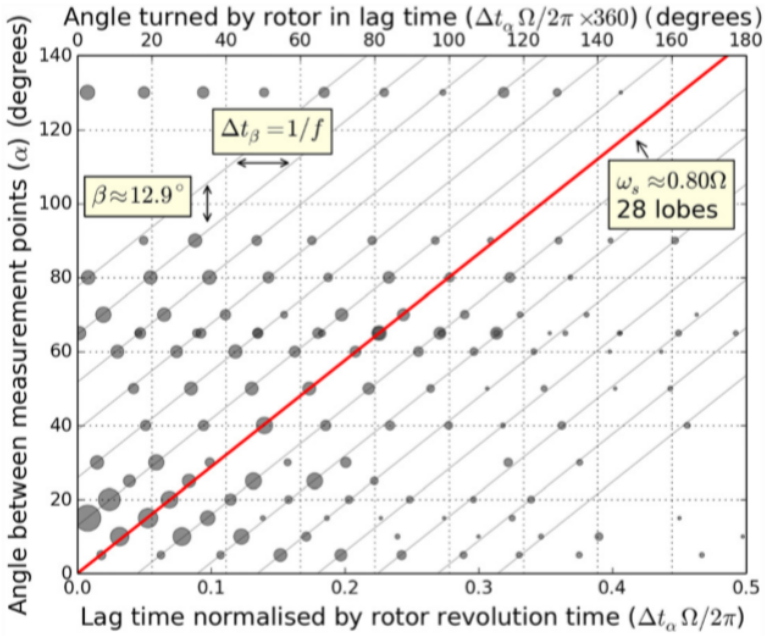

Figure 6.4: Summary plot for $s_c = 1$ mm, $\mathrm{Re}_\phi = 3 \times 10^6$ and $C_\mathrm{w} = 3400$ [19].

The signal recorded with the unsteady pressure transducers required a more complex post-processing methodology than the steady results presented in chapters 4 and 5. The conditioning process of the high bandwidth data sets started with AC coupling of the signal to remove the DC content ($f \sim 5$ Hz) followed by the amplification of the signal

using the Fylde amplifiers FE-579-TA mentioned in section 3.2.3. Small variations in run-to-run test conditions (typically ±1%) were affected by, for example, the drift in the regulated pressure upstream of the feed nozzles, variation in atmospheric conditions at exit of the reduced annulus or the operator's ability to hold a steady rotational speed (usually within ±10 rpm). To account for this, the post-processing of the data resampled the acquired length data in each revolution. By doing this, the ensemble-averaging of the pressures was simplified.

The Fast Fourier Transform (FFT) converted the time-dependent pressure signals into the frequency domain revealing the presence of high amplitude distinct peaks. The characteristic peaks indicate the presence of unsteady flow structures rotating in the cavity. The amplitude of the spike is proportional to the intensity of the perturbance whilst the frequency relates to its angular speed.

6.3 Cavity flow structure

The aerodynamic behaviour of the cavity flow is thoroughly analysed in this section based on the unsteady pressure measurements collected with high bandwidth sensors installed in the stator wall. The nature of the signals allows for a study of the frequency spectra which complements the mean time-averaged flow field and sealing effectiveness results presented in chapter 4.

Firstly, a comparison against previous data obtained in the ORF demonstrates that the modifications to the working section have not altered the unsteady aerodynamics in the cavity and therefore the phenomenon of interest is present. The unsteady cavity flow aerodynamics is then assessed, first based on the mean flow, and then more in depth in the frequency domain. High bandwidth sensors were radially and circumferentially distributed along the annular cavity volume as shown in Fig.3.23. The effect of the

variables of interest (purge flow, annulus flow, rotor disc rotation and gap size) is evaluated from both distributions of high bandwidth sensors. Finally, a phase analysis based on the cross-correlation approach by Beard *et al.* is conducted using data from different pairings of probes spaced in the circumferential direction.

6.3.1 Validation of new working section

The measurements by Beard *et al.* [19] evidenced the presence of unsteady flow structures in the axisymmetric rim cavity geometry of the ORF in an experimental setting without external mainstream flow nor stator/rotor blade pressure fields. The frequency spectra revealed distinct peaks at $f/\Omega \sim 21$ that correspond to large scale flow features rotating inside the cavity at approximately 80% of the rotor disc speed. Distinct frequencies at a higher amplitude also recorded multiples of $f/\Omega = 30$ at all test conditions as observed in Fig.6.5. Subsequent analysis concluded that the source of these highly energetic peaks were the 30 uncovered bolts holding the rotor disc together below the overlapping seal.

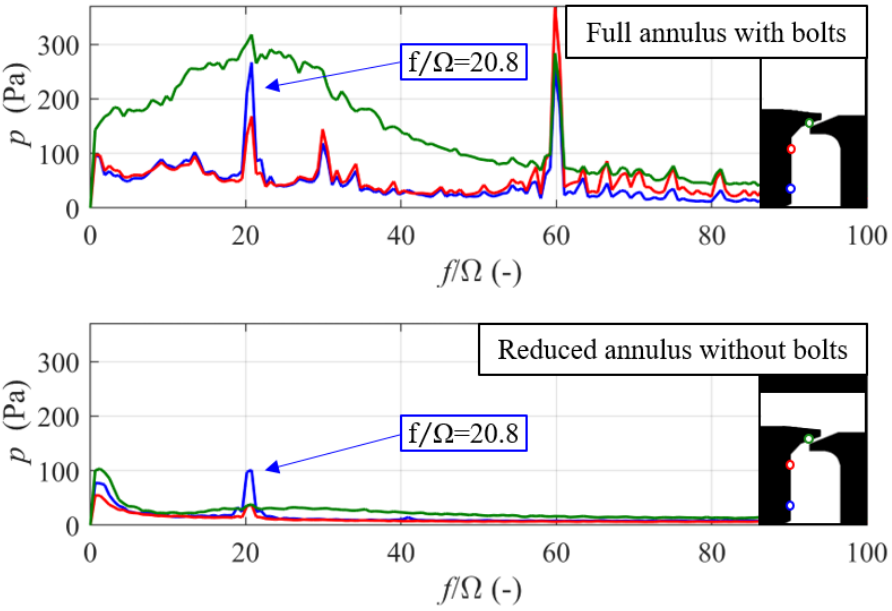

Figure 6.5: Frequency spectra of the unsteady pressure signals at three radial positions inside the cavity ($r/b = 0.95, 0.97, 0.99$) across test campaigns at $C_w = 3500$ and $Re_\phi = 3 \times 10^6$ in the full annulus configuration with bolts (top) and in the reduced annulus without bolts (bottom).

The clamping arrangement of the split rotor disc was changed during a posterior rebuild of the facility to bolt the discs from the downstream component providing an axisymmetric geometry in the front face of the rotor disc. In addition, Beard *et al.* reported an increase in distinct peak amplitude with decreasing radius confirmed by the data of the reduced annulus, Fig.6.5. This suggested that the measured unsteadiness originated further inboard, potentially at the overlapping seal feeding the rim seal cavity. To further investigate this, additional unsteady pressure sensors were installed deeper inbound in the rim cavity at $r/b = [0.84, 0.87, 0.89]$ – see p1111 to p1113 in Fig.3.23 – and above and below of the overlapping seal ($r/b = 0.72$ and $r/b = 0.78$) – see Fig.3.14. Negligible unsteadiness was recorded at either side of the overlapping seal indicating that the unsteady flow features inside the cavity did not originate there, Fig.6.6. This result was consistent with the computational study conducted by Gao *et al.* [59] whose LES simulations of a similar geometry showed that the inner cavity did not excite the unsteady flow features. In a subsequent study in which several rim seal arrangements were numerically investigated under the same conditions, Gao *et al.* [20] speculated that a change in flow radius within the seal is required to generate unsteadiness.

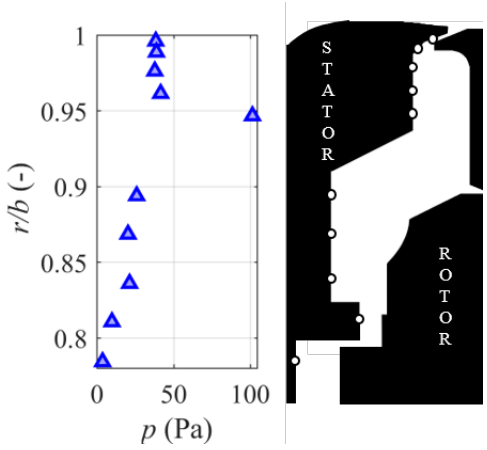

Figure 6.6: Peak amplitude of the distinct cavity frequency against radial position within the cavity at $C_w = 3400$ and $\mathrm{Re}_\phi = 3 \times 10^6$ for $s_c = 0.0042$ in absence of external flow.

Typical frequency spectra of the ensemble-averaged pressure signals with and without the exposed disc bolts are compared in Fig.6.5 for the radial positions $r/b = 0.95$, $r/b = 0.97$ and $r/b = 0.99$ (model points p1116, p1118 and p1110 in location E of

Fig.3.23). The distinct frequency at $f/\Omega \sim 21$ was still evident in the results with the reduced annulus and the frequencies corresponding to the exposed bolts ($f/\Omega = 60$) no longer present. Moreover, these observations were consistent across the entire dataset and the results show better agreement, in terms of amplitude, with the LES simulations of Gao *et al.* [59]. Non-axisymmetric features such as bolts and hooks may be present on real engine hardware, intensifying the strength of the rotating flow structures. Protrusions can severely affect the flow and heat transfer characteristics by inducing losses. The difference in tangential velocity of the fluid core and the bolts in the rotor disc leads to a relative speed that results in drag losses and the increased unsteadiness observed in Fig.6.5. Moreover, owing to the unsteady flow structures rotating in the cavity, it is thought that the presence of the bolts was interacting with the lobes further increasing the unsteadiness. Removal of the frequencies associated with the bolts reduced the amplitude of the peaks by a factor of approximately 2. The overall unsteadiness severely decreased at all measurement points, although most noticeably at the rim. Gao *et al.* [59] speculated that eccentricity may be the cause of the broadband frequencies observed near the rim in the tests of Beard *et al.* However, this could also be associated with the increased shear between the overlapping stator and rotor surfaces in the chute seal.

6.3.2 Unsteady cavity flow behaviour

A more thorough analysis of the unsteady pressure signals in the time and frequency domains is conducted in this section. The influence of each one of the handle variables is individually examined in the radially and circumferentially spaced measurement points.

Time domain

The specific requirements of the data acquisition system did not allow the unsteady and steady pressures to be logged at the same time. The radial profiles of cavity pressure coefficient calculated from unsteady and steady pressure data acquired in different test

runs are compared in Fig.6.7. Results in the three annulus flow configurations prove that the aerodynamics were repeatable, therefore any interpretation of the cavity flow field derived from the unsteady pressure measurements is consistent and directly applicable to the mean flow.

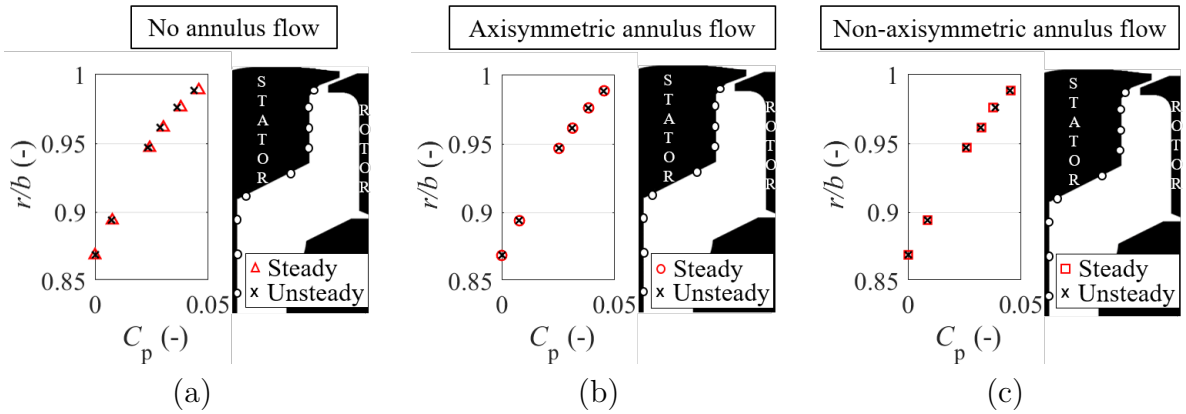

Figure 6.7: Mean pressure coefficient radial distribution obtained in the steady and unsteady runs at $U_m/(\Omega b) = 0.04$ and $s_c = 0.0042$ for: (a) no external annulus flow, (b) axial axisymmetric annulus flow and (c) non-axisymmetric annulus flow.

It is worth highlighting the change in definition of the pressure coefficient, C_p, presented in this section. Section 3.2.3 mentioned that the high bandwidth instrumentation was not installed at radial position $r/b = 0.84$, the point p1011 used in the definition of C_p in previous chapters. To account for this, the pressure coefficient has been redefined based on the lowest radial measurement point available, $r/b = 0.87$ for both data types.

Frequency domain

The aim of this section is to identify the dominating frequencies in the cavity in view to further deepen the understanding of the unsteady cavity flow in terms of origin and sensitivity to the handle variables and mainstream conditions. The wide range of conditions tested provided an extended data set to study the influence of radial and circumferential position, seal clearance, purge supply, rotor disc speed and external pressure asymmetries. For this purpose, the time-dependent high bandwidth signals from the Kulite™ pressure transducers were converted into the frequency domain with the discrete Fast Fourier Transform (FFT) as previously detailed. The frequencies were non-dimensionalised by

the rotor disc speed to assess the results across the test matrix independently of rotation.

Effect of radial position. The frequency spectra of the unsteady pressure signals recorded at different radial positions along the stator wall is presented in Fig.6.8 for different gap sizes. The influence of the radial position is analysed in Fig.6.8.

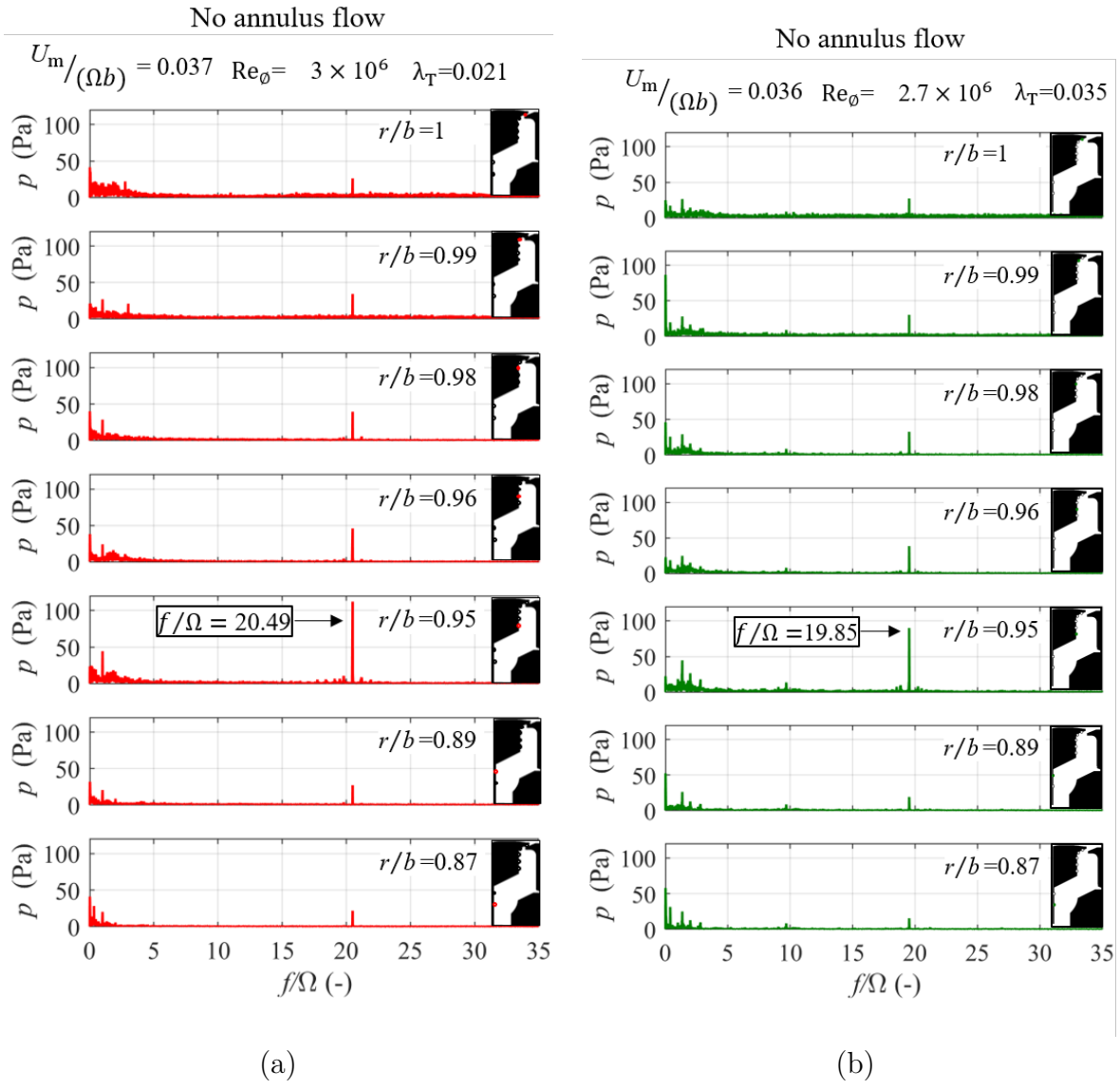

(a) (b)

Figure 6.8: Frequency spectra in absence of external flow at different radial positions inside the cavity at (a) $U_m/(\Omega b) = 0.037$, $s_c = 0.0042$ and (b) $U_m/(\Omega b) = 0.036$, $s_c = 0.0078$.

The data are plotted for approximately constant values of non-dimensional flow ratio at the two seal clearances under investigation. This was achieved with $C_w = 3450$ and $\mathrm{Re}_\phi = 3.3 \times 10^6$ for $s_c = 0.0042$ in Fig.6.8(a) whilst $C_w = 5280$ and $\mathrm{Re}_\phi = 2.9 \times 10^6$

provided the desired $U_{\mathrm{m}}/(\Omega b) = 0.036$ at $s_c = 0.0078$ in Fig.6.8(b). Each subplot presents frequency spectra data for the radial measurement position highlighted in the corresponding silhouette sketch. The reader is referred to section 3.2.3 for the exact positions and specifications of the instrumentation used to collect these data. The abscissa shows the non-dimensional frequency at which the peak is registered and the ordinate axis indicates the magnitude of the FFT peak obtained from the fluctuating component of the pressure signal. Note that the frequency signals shown in Fig.6.8 have not been ensemble-averaged, as opposed to those in Fig.6.5. The analysis has been carried out with the frequency spectra of the signal without manipulation to avoid smoothing of the distinct frequencies and reduce the error that the resampling technique may introduce. Nonetheless, comparable values of the peak frequencies were observed and the discussion is applicable to the ensemble-averaged results.

An outstanding peak in the frequency spectra at $f/\Omega \sim 20$ is easily identified throughout the cavity and for both gap sizes. Moving radially outwards from the innermost measurement point in the cavity (bottom to top in Fig.6.8), the peak initially increases in amplitude, reaches a maximum at $r/b = 0.95$ and then reduces in intensity with proximity to the rim seal. This trend aligns with the findings of the extended instrumentation shown in Fig.6.6, which already dismissed the hypothesis of the unsteadiness emerging further inboard in the cavity at the overlapping seal. The maximum amplitude of the pressure signals in the frequency domain has been observed at $r/b = 0.95$ across all test campaigns performed in the ORF, including the study reported by Beard *et al.* [19]. This coordinate corresponds to the first measurement point (when increasing radius from the inside of the cavity) on the vertical face of the stator wall after the non-planar geometry, therefore suggesting that the geometrical discontinuity may be key in this phenomenon. Relating this increased pressure amplitude of the high bandwidth signal to the mean flow cavity pressure coefficient examined in section 4.2.2 provides further insight into the cavity flow behaviour (acknowledging the change in C_{p} definition).

The C_p radial distributions analysed in sections 4.2.2 and 5.2.2 revealed the presence of two vortices that coexisted inside the cavity volume rotating at different fractions of the disc speed. The change in vortex strength appeared roughly at $r/b \sim 0.94$, in the angled face of the stationary surface. No measurement point is available at this specific coordinate in the high bandwidth data set, but the evidence seems to suggest that the increased shear originating from the interaction of the two vortices rotating at different angular speeds at approximately this radial position may be the cause of the higher unsteady activity registered at this point. Savov *et al.* [29] showed important sensitivity to geometric tolerances and highlighted the need for careful interpretation of the results and prediction of seal performance.

To summarise, the amplitude of the unsteady pressures recorded in the rim seal cavity varies with radial position, with a maximum at the measurement point located in $r/b = 0.95$. No sensitivity of peak non-dimensional frequency with radial position was identified.

Effect of seal clearance. The influence of the seal clearance for a constant non-dimensional flow ratio can be assessed by direct comparison of Fig.6.8(a) and Fig.6.8(b). The amplitude of the distinct frequency peak at $f/\Omega \sim 21$ is very similar at all radial positions for both seal gaps. However, an increase in the seal clearance appears to shift the distinct frequency towards slightly lower frequencies. This is consistent with the observation made by Chew *et al.* [18] who extensively reviewed the available published literature and noticed that generally, lower frequencies were found at higher axial clearances with higher values of f/Ω registered in tighter and more complex types of seal. Nevertheless, it must be stated that the data set of $s_c = 0.0078$ chosen to satisfy the requirement of constant non-dimensional flow ratio was obtained at a lower rotor disc speed ($N = 7850$ rpm) than the smaller clearance (evaluated at $N = 9000$ rpm). Therefore, caution when determining the cause of the decrease in the amplitude and frequency of the peak must be taken until a more thorough analysis of all the key players is complete.

Effect of purge supply. Changes in amplitude and frequency of the distinct frequency peak induced by an increase in the purge flow are scrutinised here. The study of the effect of purge supply is based on the case with no external annulus flow included in Fig.6.9. All variables of interest (other than purge mass flow) remained fixed at $\mathrm{Re}_{\mathrm{ax}} = 0$, $\mathrm{Re}_{\phi} = 3 \times 10^6$ and $s_c = 0.0042$. This analysis is centered on radial position $r/b = 0.95$, expected to be the most sensitive to changes in the operating conditions. The mean cavity pressure coefficient revealed two vortices coexisting in the cavity in chapter 4, and the increased shear between the two different tangential velocities has been pointed as the reason for the increased unsteadiness observed at the position closest to the change in stator wall geometry. A plot of the mean flow cavity pressure coefficient as a function of the turbulent flow parameter is included in Fig.6.9. Similarly, the curve of sealing effectiveness as a function of the non-dimensional flow ratio is also displayed. These are intended to support the interpretation of the flow physics in the cavity by allowing a combined approach that complements the experimental unsteady signals with the mean flow and sealing performance data collected at the same operating point (see chapters 4 and 5 for more details). Note the difference in definition of the mean time-averaged pressure coefficient calculated from the pressure difference between the point of interest and the innermost available measurement in $r/b = 0.87$ (as opposed to $r/b = 0.84$ used in chapter 4) non-dimensionalised by the dynamic pressure based on the rim speed. The frequency spectra is not shown as a pressure amplitude but as the amplitude pressure non-dimensionalised by the dynamic head at the rotor rim.

The first detail stemming from Fig.6.9 is a slight reduction of the non-dimensional frequency peak with increasing non-dimensional purge flow. This effect was also observed by Beard *et al.* [19] in the published work that preceded this project. Section 4.2.2 reported a contraction of the core region at large purge supplies that imposed higher resistance to the free rotation of the core due to a thicker rotor boundary layer. The same principle applies to the rotation of the unsteady cavity flow structures which is restricted

at high sealing flow rates and appears reflected as lower frequencies (thus angular speeds if the number of lobes is unaffected). This trend has been identified across all configurations (no external flow, axisymmetric and non-axisymmetric annulus flow) regardless of the seal clearance. No clear trend has been identified when assessing the impact of the purge supply on the amplitude of the principal frequency. Fig.6.9 shows that the magnitude of the peak initially drops and then increases with larger sealing flow. Nonetheless, the highest value of C_w appears of lower amplitude than the previous one.

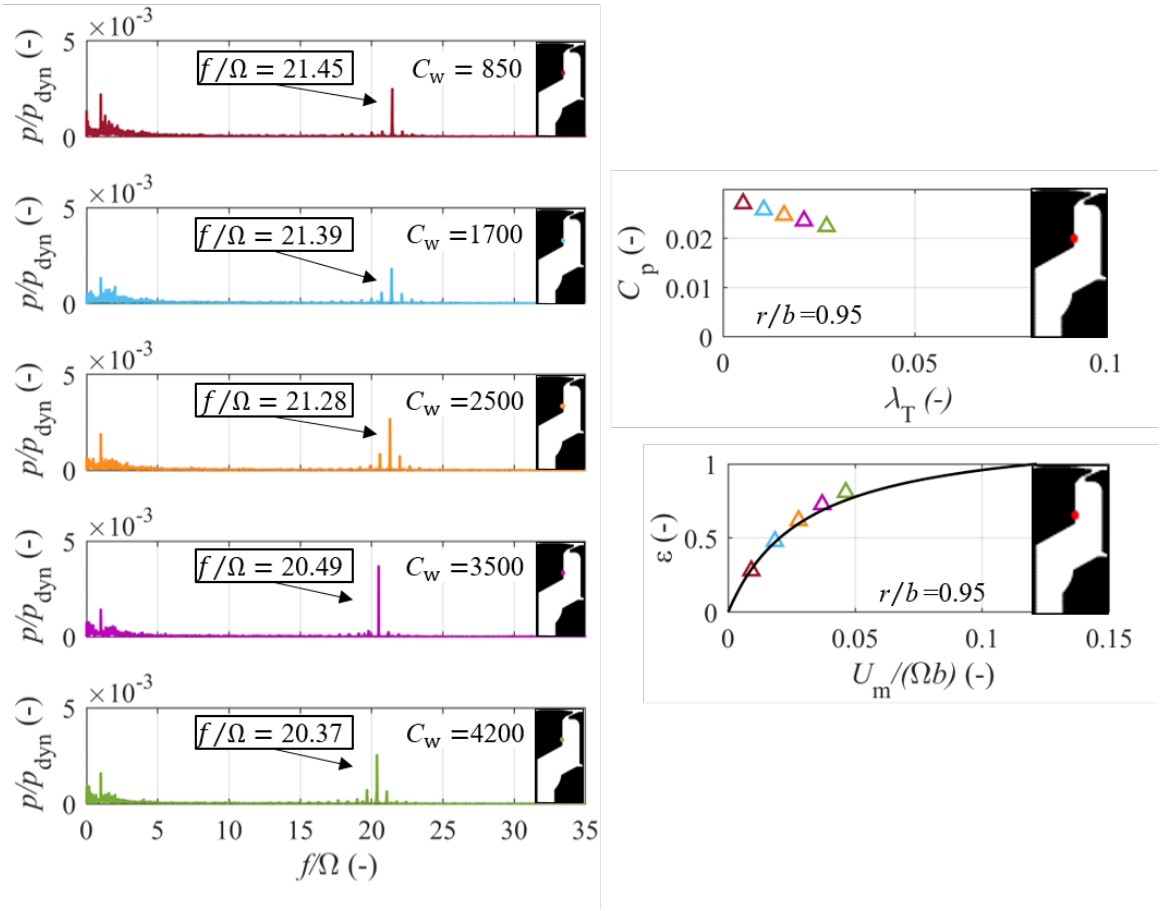

Figure 6.9: Effect of the purge supply on the frequency spectra at $r/b = 0.95$ in absence of external annulus flow for constant $\mathrm{Re}_\phi = 3 \times 10^6$, $s_c = 0.0042$.

Effect of rotor disc speed. The influence of the rotor disc speed is studied in isolation for a more in depth analysis that complements what was described above. Beard *et al.* [19] speculated that the non-dimensional frequency of the peak was independent of rotor disc speed. The range of rotational Reynolds numbers covered in their study has been

twofolded in the current investigation therefore a wider span of operating conditions is analysed here. The frequency spectra from the signal measured with the pressure probe at $r/b = 0.95$, with a constant rate of sealing flow ($C_w \sim 3500$) and seal clearance $s_c = 0.0042$ is examined in Fig.6.10 under changing conditions of rotational Reynolds number. Note that the x axis in Fig.6.10 (left) has not been non-dimensionalised by the rotor disc speed to allow comparison with a stopped rotor, $\mathrm{Re}_\phi = 0$. The non-rotating disc in absence of external flow represents the baseline scenario in which the frequency spectra does not identify any unsteadiness. Fig.6.10 (right) shows the non-dimensional frequency f/Ω in the abscissa.

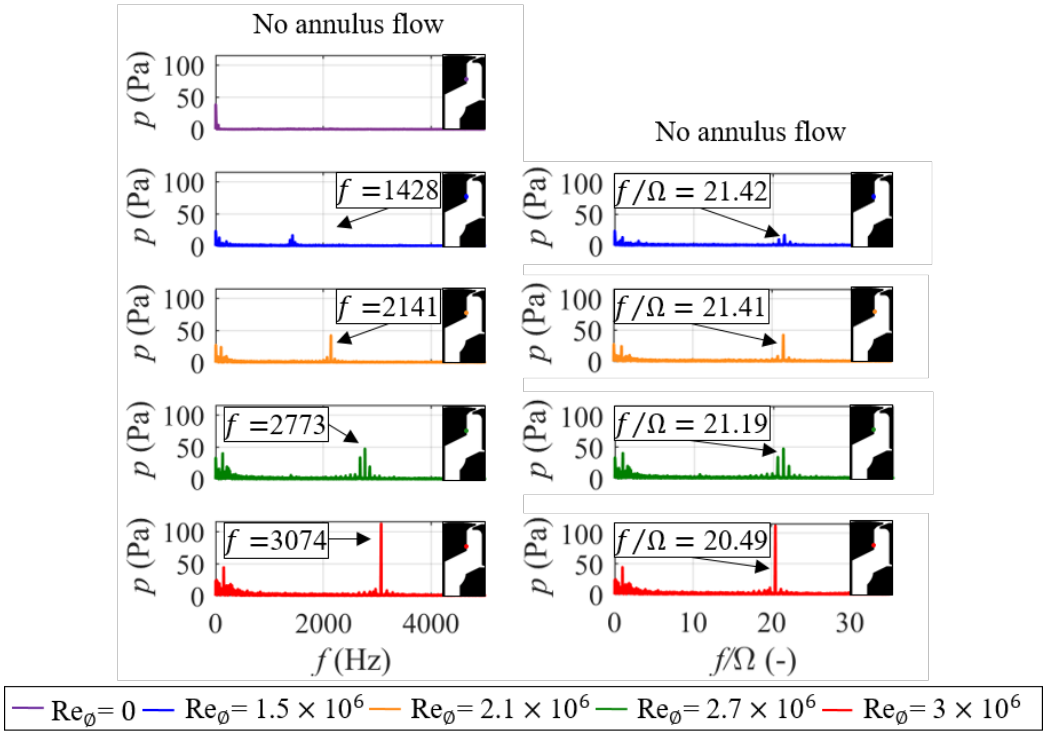

Figure 6.10: Effect of the rotational Reynolds number on the frequency spectra for constant $C_w = 3500$ at $r/b = 0.95$, $s_c = 0.0042$ in absence of external annulus flow.

A distinct peak with high energy content appears as the rotor disc spins faster, increasing its amplitude and frequency proportionally. Under disc pumping predominance, higher rotor disc speeds induce a stronger pressure gradient in the cavity which translates into an isolated outstanding peak of higher amplitude. One main conclusion may be drawn from Fig.6.10: an increase in the angular velocity shifts the unsteady frequency

towards higher values. This is reflected in Fig.6.10 (right) as a slight decrease when non-dimensionalised against rotor disc speed. Beard *et al.* showed that the peaks almost align with varying conditions of angular speed, but a slight offset consistent with the findings of this research can also be identified. Cao *et al.* [15] reported minor and proportional changes in peak frequency due to variations in rotor speed consistent with the results presented here.

For a constant ratio of $U_{\mathrm{m}}/(\Omega b)$ different peak values are observed depending on rotational Reynolds number. A clear effect of rotor disc speed on the non-dimensional frequency of the distinct peak reflects that the rotor disc angular speed and the purge flow rate are relevant. The latter has already been discussed based on Fig.6.9 and the effect of rotor speed from Fig.6.10. Variations of the non-dimensional amplitude and frequency of the distinct peaks have been thoroughly studied under different operating conditions in absence of external flow in Fig.6.11. The influence of non-dimensional flow ratio at different radial positions in the cavity for four rotational Reynolds numbers and two seal clearances are analysed.

Good collapse of the peak amplitude results is observed at most locations. However, the scatter of the data, particularly at $r/b = 0.95$, reveals high sensitivity to changes at this position, in concordance with previous discussions about the largest peak detected in the cavity. The non-dimensional peak amplitude displays a slight increase with non-dimensional purge flow ratio at $r/b = 0.95$ which contrasts with the invariance registered by the rest of the sensors. This weak raise of $p/p_{\mathrm{dyn,p}}$ observed in Fig.6.11(a) for $s_c = 0.0042$ appears magnified at $s_c = 0.0078$ in Fig.6.11(b). In fact, not only it is observed at $r/b = 0.95$ but it can also be appreciated at $r/b = 0.98$. A reduction in overlap at the rim seal region is suspected to be the reason for a greater influence of the sealing flow at the larger clearance.

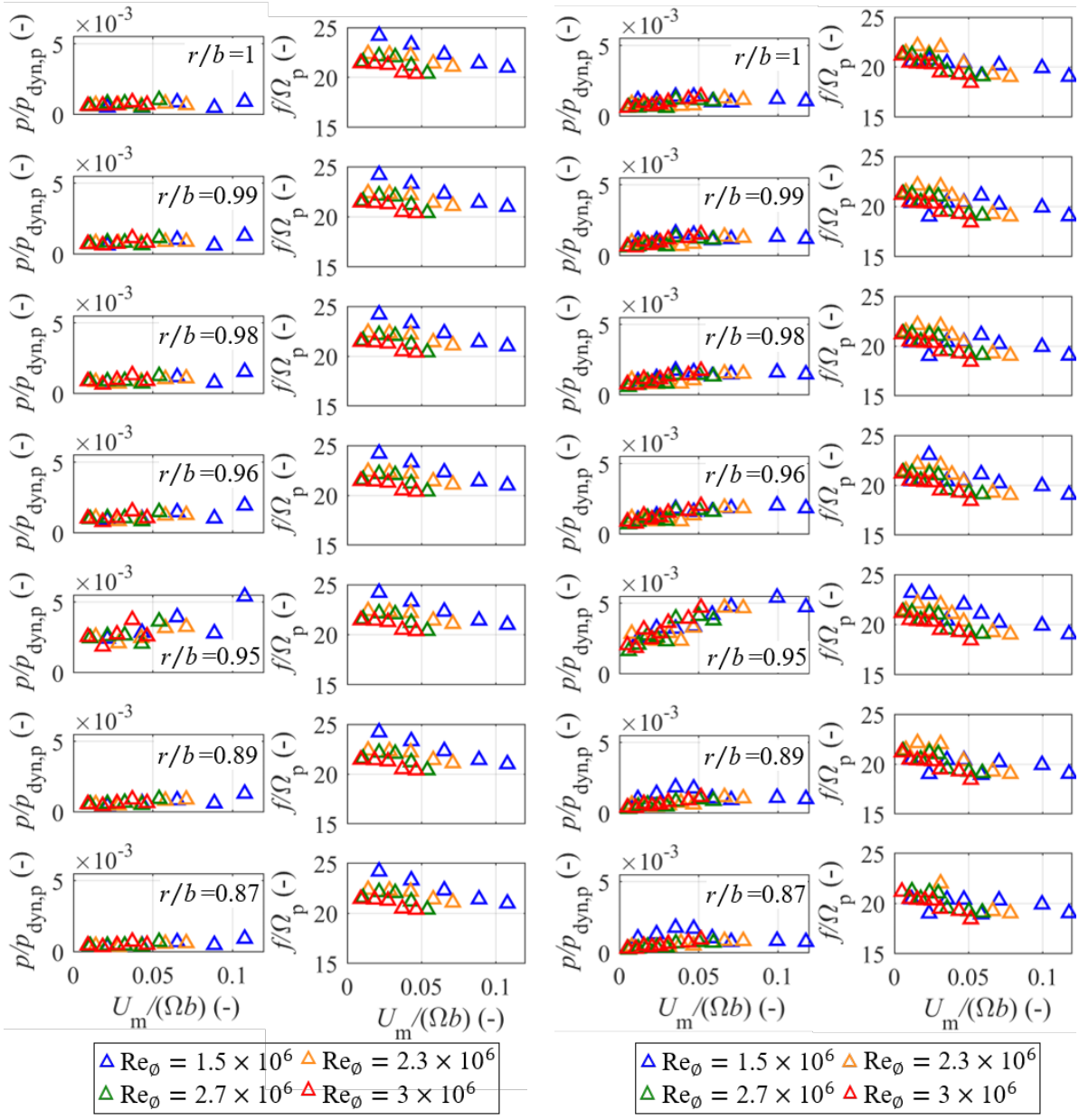

(a) $s_c = 0.0042$ (b) $s_c = 0.0078$

Figure 6.11: Non-dimensional pressure and frequency of the distinct peak for different rotational Reynolds numbers and $U_\mathrm{m}/(\Omega b)$ in absence of annulus flow at two gap sizes (a) $s_c = 0.0042$ and (b) $s_c = 0.0078$.

The non-dimensional peak frequency appears to be more sensitive to non-dimensional purge flow ratio at low rotor disc speeds, based on a more acute reduction of the blue triangles in Fig.6.11 across $U_\mathrm{m}/(\Omega b)$ over a wider range of f/Ω_p. In addition, Fig.6.11 reveals that an acceleration of the rotor disc speed from $\mathrm{Re}_\phi = 2.7 \times 10^6$ to $\mathrm{Re}_\phi = 3 \times 10^6$ supports the claim of Beard *et al.* of insensitive non-dimensional frequency peak to

rotational Reynolds number. Albeit this, when the rotational Reynolds number is reduced beyond their lower limit (7000 rpm) discrepancies arise.

Effect of external annulus flow conditions. The introduction of flow in the main gas path directly impacts the cavity flow dynamics. The influence of the purge supply for a constant rotational Reynolds number is analysed under axial annulus flow in Fig.6.12.

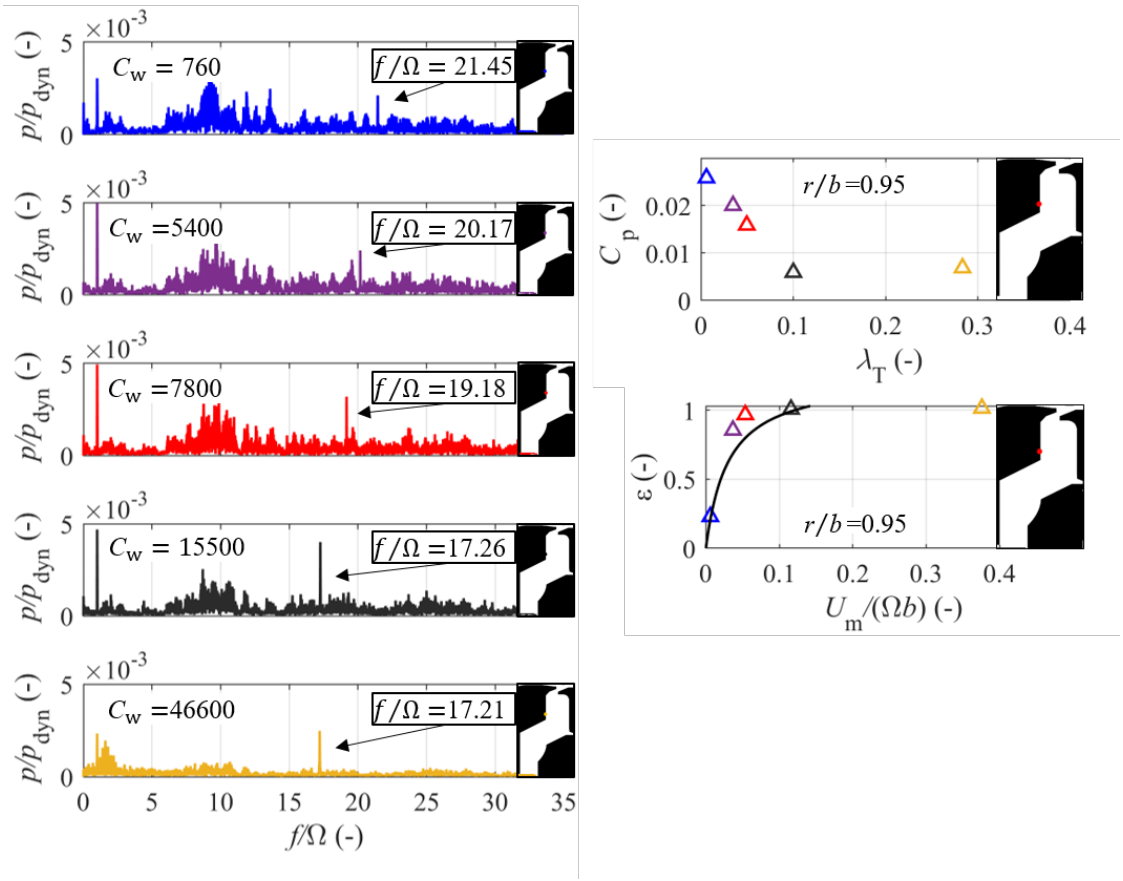

Figure 6.12: Effect of the purge supply on the frequency spectra at $r/b = 0.95$ with external axisymmetric flow at $\mathrm{Re}_\phi = 3.1 \times 10^6$, $s_c = 0.0078$.

A shift towards slightly lower peak non-dimensional frequencies with increasing purge supply was identified in absence of external flow. Under an axial axisymmetric annulus flow, this is only observed for values of $\lambda_\mathrm{T} < 0.1$ where the disc pumping effect dominates the cavity flow aerodynamics. Beyond this value, the sealing effectiveness curve shows that the purge supply is sufficient to seal the cavity and the sealing flow is expelled as free vortex flow to the external environment. The asymptotic trend observed in the $C_\mathrm{p} - \lambda_\mathrm{T}$

distribution of Fig.6.12 for a turbulent flow parameter above 0.1 (see discussion in section 4.2.2) is linked to an insensitivity of the peak non-dimensional frequency to further increases in the purge flow. Indeed, the non-dimensional frequency appears to plateau at $C_w > 15500$ in Fig.6.12.

With the introduction of external axial flow an increase in the unsteady activity is registered around $f/\Omega \sim 10$. The broadband unsteadiness is highly reduced at high rates of non-dimensional purge flow ($C_w = 46600$ in Fig.6.12). This points towards the ingress of mainstream flow and annulus/sealing flow interaction as potential sources of this unsteadiness indicating that a fully sealed cavity may have the potential to cancel the excitation of these frequencies.

The influence of the mainstream flow is evaluated for a constant value of purge supply, $C_w = 3500$, with changing conditions of rotational Reynolds number and annulus flow configurations in Fig.6.13. At high rotational Reynolds number, the disc pumping effect still prevails thus characteristic peaks associated with the presence of cavity modes continue to stand out in the frequency spectra. As the angular momentum of the rotor disc is reduced, the distinct frequency associated with the rotation-induced unsteady flow instabilities in the cavity decreases in amplitude and frequency reflecting a loss of strength and angular speed. The frequencies identified at $f/\Omega \sim 10$ in Fig.6.12 that emerged with the introduction of annulus flow are observed at a constant frequency $f \sim 1400$ Hz invariant across rotor disc speed and annulus flow settings. The energy content of this unsteadiness is registered even when the rotor is not spinning therefore confirming it arises from the interaction of mainstream and purge flows and is not related to disc rotation. It is suspected that large levels of shear in the rim region originated by the difference in tangential velocities between the purge flow and the mainstream could induce large scale asymmetries that could excite this band of frequencies.

Length scales larger than the sector size used in the CFD models could explain why these frequencies are detected in the experiments but not captured computationally. Small asymmetries in the annulus flow from the experimental set up were also investigated as a potential cause. The vortex shedding frequency of the struts located upstream of the working section was found to be of the order of $\sim$ 400 Hz and therefore dismissed as the potential origin of the localised increase in unsteadiness. The resonance frequency of the diaphragm of the pressure sensor was also considered a potential trigger, but it was orders of magnitude larger (300 kHz). The spike originated from the rotating flow structures blended with the broadband frequencies at low rotor disc speeds. From close examination of the different conditions, the distinct frequency peak was observed to be very small for $N = 4000$ rpm in Fig.6.10 and disappear (or be camouflaged by the larger broadband unsteadiness) at low rotational Reynolds number in Fig.6.13 where the disc pumping was not dominating the cavity flow physics.

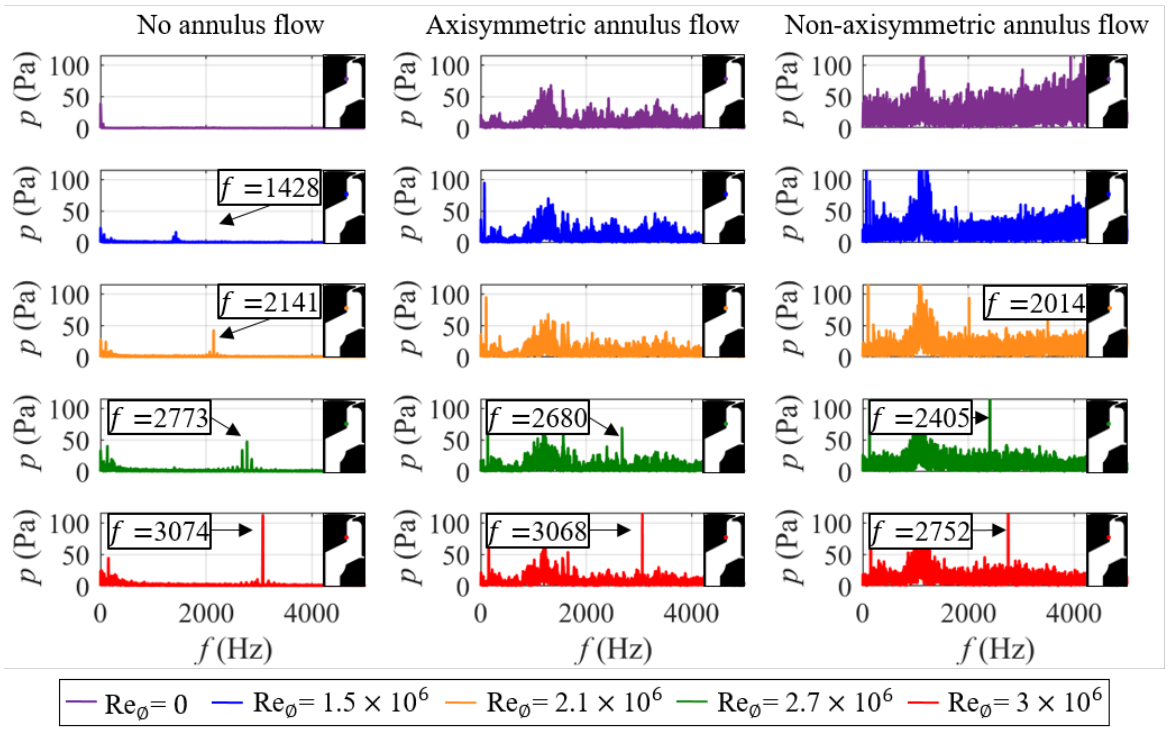

Figure 6.13: Effect of the rotational Reynolds number on the frequency spectra for constant $C_w = 3500$ at $r/b = 0.95$, $s_c = 0.0042$ in absence of external annulus flow, under an axisymmetric annulus flow and under non-axisymmetric annulus flow.

In the most complex gas path configuration studied within the scope of this project, the introduction of the pressure asymmetries in the main gas path further intensifies the broadband unsteadiness already observed in the axial annulus flow configuration, see Fig.6.13. Moreover, the non-axisymmetric annulus flow frequency spectra shows an increased excitation of the frequencies around $f \sim 1400$ Hz that become the most energetic phenomena at the lowest rotational Reynolds number. Nonetheless, the spike related to the rim seal instabilities still stands out at the highest rotor disc speed. To summarise, the main conclusions that can be extracted from Fig.6.13 are:

1. The peak frequency of the rotating structures in the cavity increases with disc speed.

2. Two sources of unsteadiness are identified at different frequency ranges. The first one, invariant with rotor disc speed, appears as a spread in a range of frequencies around $\sim$ 1400 Hz and is attributed to the interaction between purge and mainstream flow. The second one, associated with the disc pumping effect and the presence of rotating structures in the cavity, can be seen as an outstanding peak that appears at different frequencies depending on rotor disc speed.

The effects deduced from Fig.6.13 and Fig.6.15 are in close alignment with previous research publications. For instance, Cao *et al.* [15] reported a minor increase of the peak frequency with speed and demonstrated that the annulus swirl velocity had larger impact than rotational speed.

The rotationally-dominated test cases of each annulus configuration shown in the last row of Fig.6.13 have been analysed based on spectograms in Fig.6.14. The non-dimensional peak frequency is included in the y axis, the amplitude of the peak is represented by the colour contour and the rotor revolutions during which data was taken are shown in the x axis. In absence of external flow, a band of high frequency content is identified at $f/\Omega \sim 20$ across all rotor revolutions that corresponds to the unsteady flow structures. The introduction of an axial axisymmetric flow in the annulus significantly

changes the frequency spectra. As aforementioned, a highly energetic region corresponding to the unsteady interaction of mainstream and purge flows is observed at $f/\Omega \sim 8-10$. The band of frequencies related to the unsteady cavity flow structures dominated by the disc pumping effect can still be identified at $f/\Omega \sim 20$, although they are less distinct for all rotor revolutions and have been relegated to second most energetic phenomenon. Including NGVs in the main gas path to add a swirl component to the annnulus flow increases the amplitude of the overall unsteadiness in the frequency spectra. The frequency spectra distribution appears to be very similar to that of the previous test case, with high unsteadiness across a range of frequencies between approximately $f/\Omega \sim 8-10$ and a narrower line at $f/\Omega \sim 20$ in which the phenomenon appears to have a higher degree of randomness.

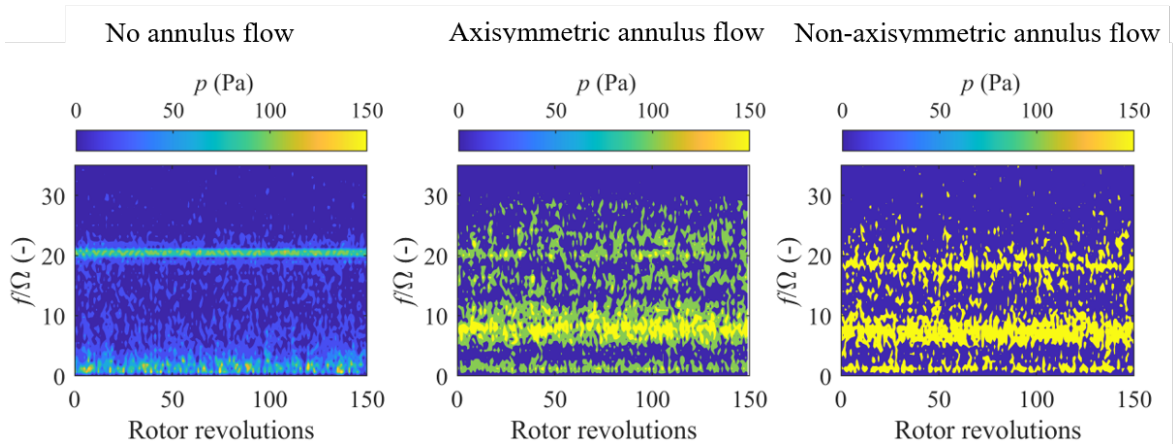

Figure 6.14: Frequency spectra for constant $C_w = 3500$, $\mathrm{Re}_\phi = 3 \times 10^6$ at $r/b = 0.95$, $s_c = 0.0042$ in absence of external annulus flow, under an axisymmetric annulus flow and under non-axisymmetric annulus flow.

Previous investigations by Cao *et al.* [15], Chilla *et al.* [49] and Savov *et al.* [29] showed that the specific geometry and dimensions of the rim seal cavity would determine the frequency of the unsteadiness. The latter study concluded that the narrower double lip seal tested registered higher frequencies (of the order of $30 \leq f/\Omega \leq 40$) than the wider single lip arrangement ($25 \leq f/\Omega \leq 35$), consistent with Chew *et al.* [18]. In addition, these authors presented an expanded spectrogram in which they detected a range of low

frequency unsteadiness at the rim seal region similar to those described here. For their specific geometry, they appeared at $\sim 3 \leq f/\Omega \leq 5$.

Fig.6.15 shows another method to interrogate the influence of the mainstream flow over the frequency spectra. Frequency spectra at various radial positions for all three mainstream conditions are shown alongside sealing effectiveness results for $C_{\mathrm{w}} = 3500$. Data for different non-dimensional flow ratios and flow coefficients were achieved through changes in the rotor disc speed (4000 rpm in Fig.6.15(a) and 9000 rpm in Fig.6.15(b)). Results derived from steady pressure transducers and gas concentration measurements are also included to assist interpretation of the results.

On the one hand, the frequency spectra in Fig.6.15(a) shows an enlarged overall unsteadiness when annulus flow is included, particularly in the upper cavity ($r/b \geq 0.95$). The obvious distinct peak reported in absence of annulus flow at $f/\Omega \sim 21$ may still be present with annulus flow, but it no longer stands out owing to the larger overall activity across the frequency spectra. The largest levels of unsteadiness were suspected to be found at the rim for a non-axisymmetric annulus flow configuration. This is because ingress of highly swirled external flow into the cavity was found in this case due to the strongest pressure gradient across the cavity. However, the increased shear between the two vortices detected in the cavity and the separation zone in the corner of the stator wall (discussed in chapter 5) increased the unsteadiness at $r/b = 0.95$.

On the other hand, Fig.6.15(b) displays a significantly lower overall unsteadiness across all radial positions and test configurations, with distinct peaks and a clear effect of the pressure asymmetries in the annulus over the non-dimensional frequency. The introduction of an axial flow through the main gas path increased the overall unsteadiness and activity in the frequencies around $f/\Omega \sim 8$. However, this did not affect the amplitude nor frequency of the peak (behind the purple one in Fig.6.15(b)).

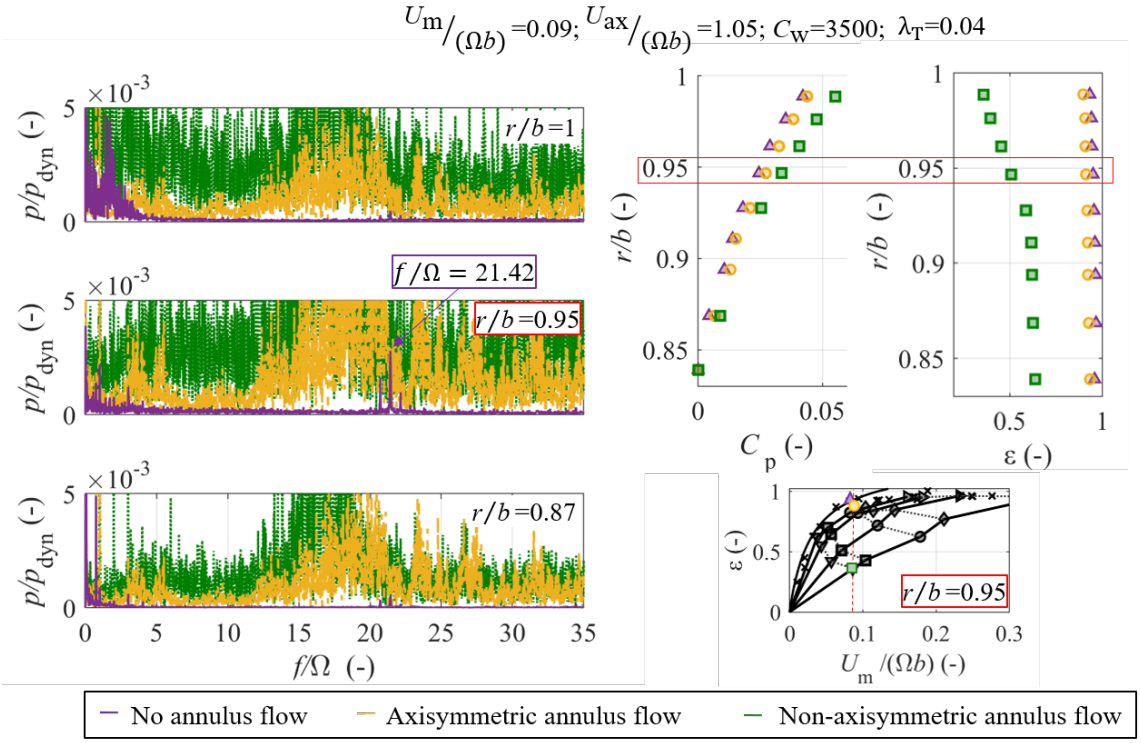

(a)

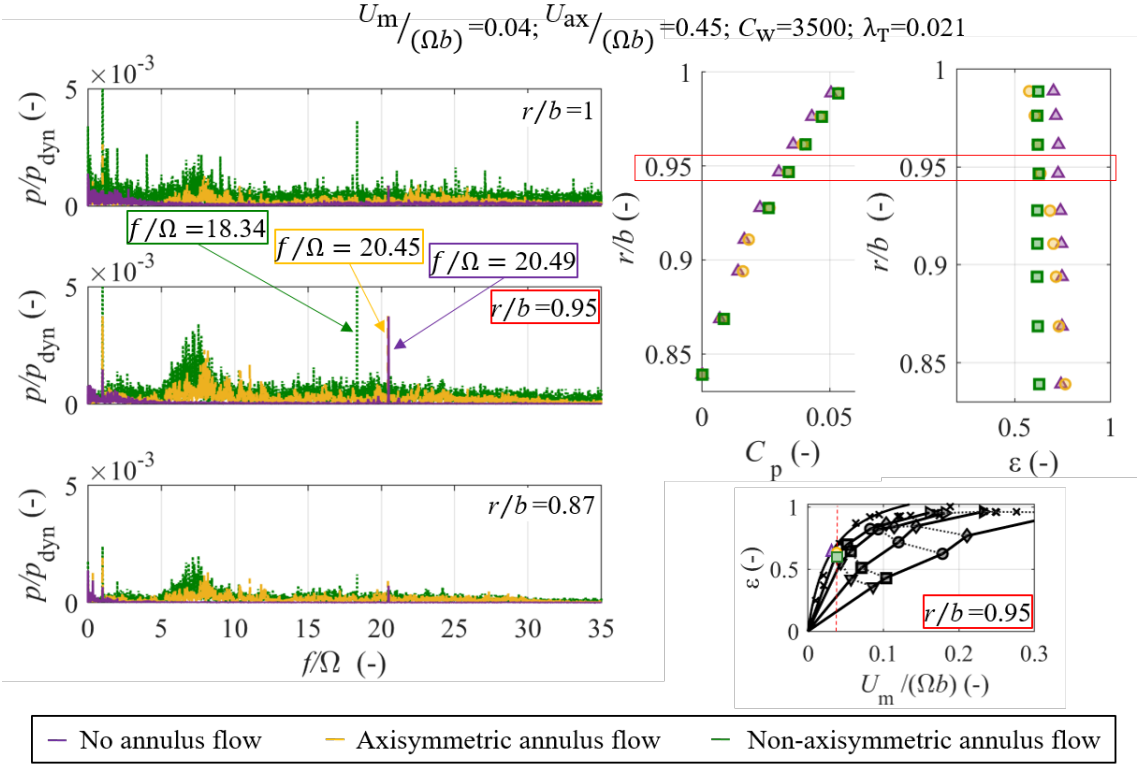

(b)

Figure 6.15: Effect of the external annulus flow conditions on the frequency spectra for constant $C_w = 3500$ and $s_c = 0.0042$ at (a) $U_{ax}/(\Omega b) = 1.05$ and (b) $U_{ax}/(\Omega b) = 0.45$.

Incorporating a swirl component to the external flow velocity further increases the overall unsteadiness in the cavity. The characteristic peak is amplified and shifted towards lower frequencies. The radial profiles of pressure and sealing effectiveness show how, at this particular test condition, there is good agreement in the lower part of the cavity between the results from the test campaigns without and with an axial annulus flow and a slight mismatch with the case of swirled mainstream flow. This is confirmed in the plot of sealing effectiveness as non-dimensional flow ratio where the three data points fall on top of each other. Following on previous discussions, displacements of the spike towards higher frequencies are observed for lower rotor disc speeds in all three configurations when comparing across Fig.6.15(a) and (b).

The behaviour observed in the frequency spectra can be explained based on the sealing effectiveness map discussed in chapter 5 (and included in Fig.6.15). The same flow pattern is identified in absence of mainstream flow in Fig.6.15(a) and (b). This test configuration was included as the scenario of pure disc pumping effect. The rotation of the rotor disc dominated ingestion and the sealing performance was theoretically correlated to the Chew orifice model for $k = 1$, [25]. The flow coefficient is a concept not applicable to this case due to the lack of external flow. In the two other annulus flow configurations however, and especially under externally-induced ingestion, chapter 5 reported that the flow coefficient became the most influential parameter, therefore the analysis is continued based on $U_{\mathrm{ax}}/(\Omega b)$.

For years, the extended assumption within the turbine rim seal community was that the pressure asymmetries and potential field interaction of the NGVs and rotor blades in the main gas path would dominate the mechanism of ingestion. Chapter 5 however, provided evidence that contradicted this hypothesis. The ability of the Chew orifice model to fit the sealing effectiveness experimental data was good for the configurations without annulus flow, with an axial axisymmetric annulus flow and under a swirled non-axisymmetric

mainstream at low flow coefficients. Nevertheless, the disc pumping correlation failed to match the sealing effectiveness data at high flow coefficients in an environment with swirled external flow, Fig.6.15(a) and Fig.5.9. The ingestion mechanism was deemed to be dominated by the pressure asymmetries in the annulus flow therefore aligning with the widespread assumption of pressure-driven ingress mentioned above. Ingestion of highly swirled annulus flow into the cavity intensifies the mismatch in the tangential velocity component between the ingested flow and that of the rotating fluid core, therefore leading to high levels of shear that translate into the increased unsteady activity detected in Fig.6.15(a). In this case, the region of higher frequency content falls between $f/\Omega \sim 15$ and 20 whilst it was observed at $f/\Omega \sim 8$ for the rotationally-induced dominated test scenario in (b). This is due to the non-dimensionalisation with rotor disc speed, since Fig.6.13 showed that the frequency originating from the interaction between the mainstream and the purge flow was invariant across the different rotational Reynolds numbers.

Finally, the distinct frequency peak attributed to the unsteady large scale structures rotating in the cavity may be merged and/or dissipated by the overall increased unsteadiness but it can also be reduced or even suppressed. The higher broadband frequencies observed in Fig.6.13 with the addition of external annulus flow (axial and swirled) surpassed that of the distinct peak so that it was no longer detectable in the frequency spectra. This suggests that the effects arising in the annulus-purge interface could be used to neutralise the rotating cavity structures. The work of some research groups has provided evidence of increased levels of ingestion led by the unsteadiness in the rim. Therefore, suppressing the rim seal instabilities may have a beneficial effect on engine performance. Previous published studies have suggested a stabilisation of the cavity modes with high purge supplies ([47]) until they were completely eliminated with a fully sealed cavity. Nonetheless, results presented in this chapter have provided evidence of the distinct peak being detected in a fully sealed cavity, see Fig.6.12. Gao *et al.* [20] showed the importance of the choice of rim seal geometry when aiming to suppress the cavity modes or

the rim seal instabilities. Evidence of suppression of the unsteadiness arising from the interaction between the annulus and purge streams has also been provided in this chapter, where Fig.6.12 showed that a fully sealed cavity significantly reduced the excitation of the frequencies around $f/\Omega \sim 8$.

Effect of circumferential position. High bandwidth pressure transducers were also distributed along the circumferential direction in the annular wall of the stator at uneven angular distances (but at the same radial coordinate, $r/b = 0.96$). The frequency spectra of these data points at two conditions of non-dimensional flow ratio are included in Fig.6.16. The presented data correspond to $U_{\mathrm{m}}/(\Omega b) = 0.09$ and $U_{\mathrm{m}}/(\Omega b) = 0.04$ obtained with a constant purge supply of $C_{\mathrm{w}} = 3500$ and different rotor disc speeds ($N = 4000$ rpm and $N = 9000$ rpm respectively) for $s_c = 0.0042$ in absence of external annulus flow.

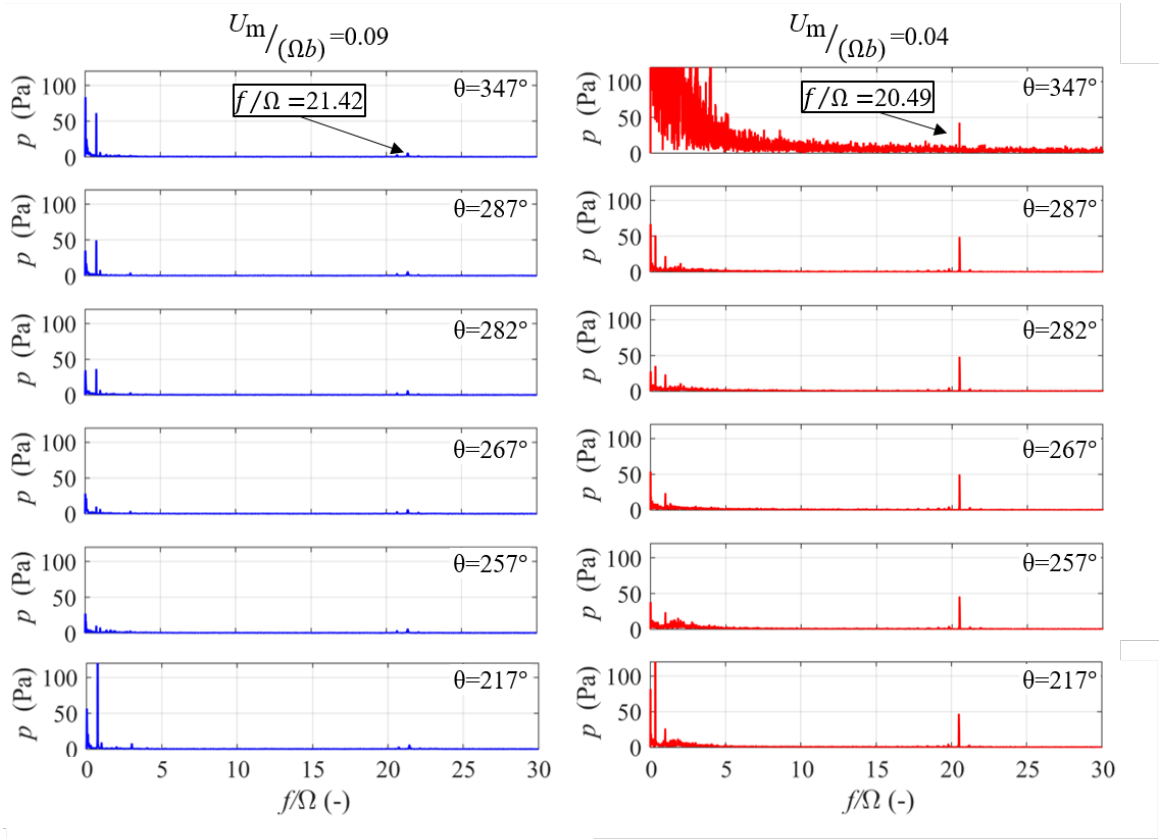

Figure 6.16: Effect of the circumferential position on the the frequency spectra for constant $C_{\mathrm{w}} = 3500$, $s_c = 0.0042$ in absence of external annulus flow.

The same trends described above have been identified at all operating conditions of the test matrix studied: reduced amplitude of the distinct peak at low rotational Reynolds number with a more obvious peak as the disc pumping effect gains relevance and dominates the aerodynamics in the cavity at high rotational Reynolds numbers.

No significant changes in non-dimensional frequency or amplitude of the peaks are reported with circumferential position. Of particular interest are the higher levels of unsteadiness present in the signal from the Kulite transducer located at $\theta = 347°$ measured in the clockwise direction from top dead center when viewed from downstream (model point p1157 in Fig.3.23). It is suspected that higher levels of noise arose in this sensor at these specific operating conditions.

6.3.3 Phase analysis

The unsteady flow features developing in the rim seal cavity are further investigated through phase analysis of circumferentially distributed pressure signals. The methodology followed here was described in section 6.2 and it allows to determine the number of flow structures in the annular cavity and angular speed at which they travel. Cross-correlation of two signals separated by a known angle provides the time lag of the flow structure to travel from one measurement point to the next, therefore allowing to calculate its rotational speed.

The non-dimensional frequencies of the distinct peaks presented in Fig.6.11 appeared to be contained within the range of $f/\Omega = [15, 25]$. Prior to the phase analysis, the pressure signals were filtered to remove the components outside this region of frequencies of interest with a 3rd order bandpass Butterworth filter. The output signal of this intermediate step can be seen in Fig.6.17(a). Cross-correlation of all possible combinations of Kulites (15 pairing possibilities in total) was calculated across all revolutions and summary plots similar to those of Beard *et al.* are discussed in Fig.6.18 and Fig.6.19.

Model points p1117 and p1127 installed 10° apart in the stator ring have been selected to describe the process in more detail and an example from the cross-correlation of their signals is provided in Fig.6.17(b). The time lag has been non-dimensionalised by the time taken by the rotor to complete one revolution. Further analysis of the signal reveals the presence of a rotating pattern as indicated by the equispaced peaks. The separation between two peaks represents the time lag between two neighbouring vortical structures.

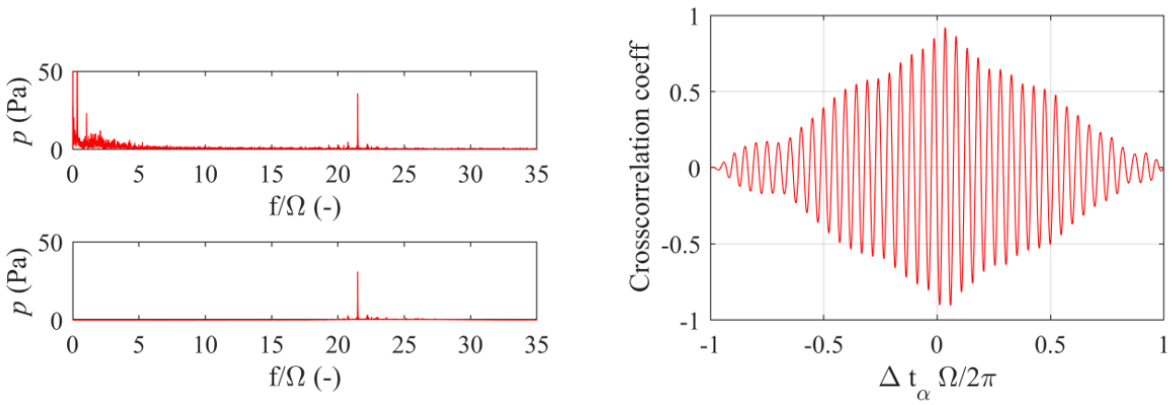

(a) (b)

Figure 6.17: (a) Example of an unfiltered (top) and filtered (bottom) FFT case and (b) model cross-correlation distribution for $\alpha = 10°$.

Summary plots for the configuration without external flow are included in Fig.6.18 for a low and high rotational Reynolds numbers and the two seal clearance sizes under investigation. Following the approach by Beard *et al.* [19], the slope of the trend line that unites the measurements of all pressure transducers has been adjusted for best fit in each case and provides the rotational speed of the flow structures.

Minimal differences are observed across the different test cases in Fig.6.18. An increase in the scatter of the results appears when the azimuthal distance between the pair of cross-correlated pressure sensors increases, especially in Fig.6.18(b). However, this does not seem to be replicated in the other conditions (Fig.6.18(a), (c) and (d)).

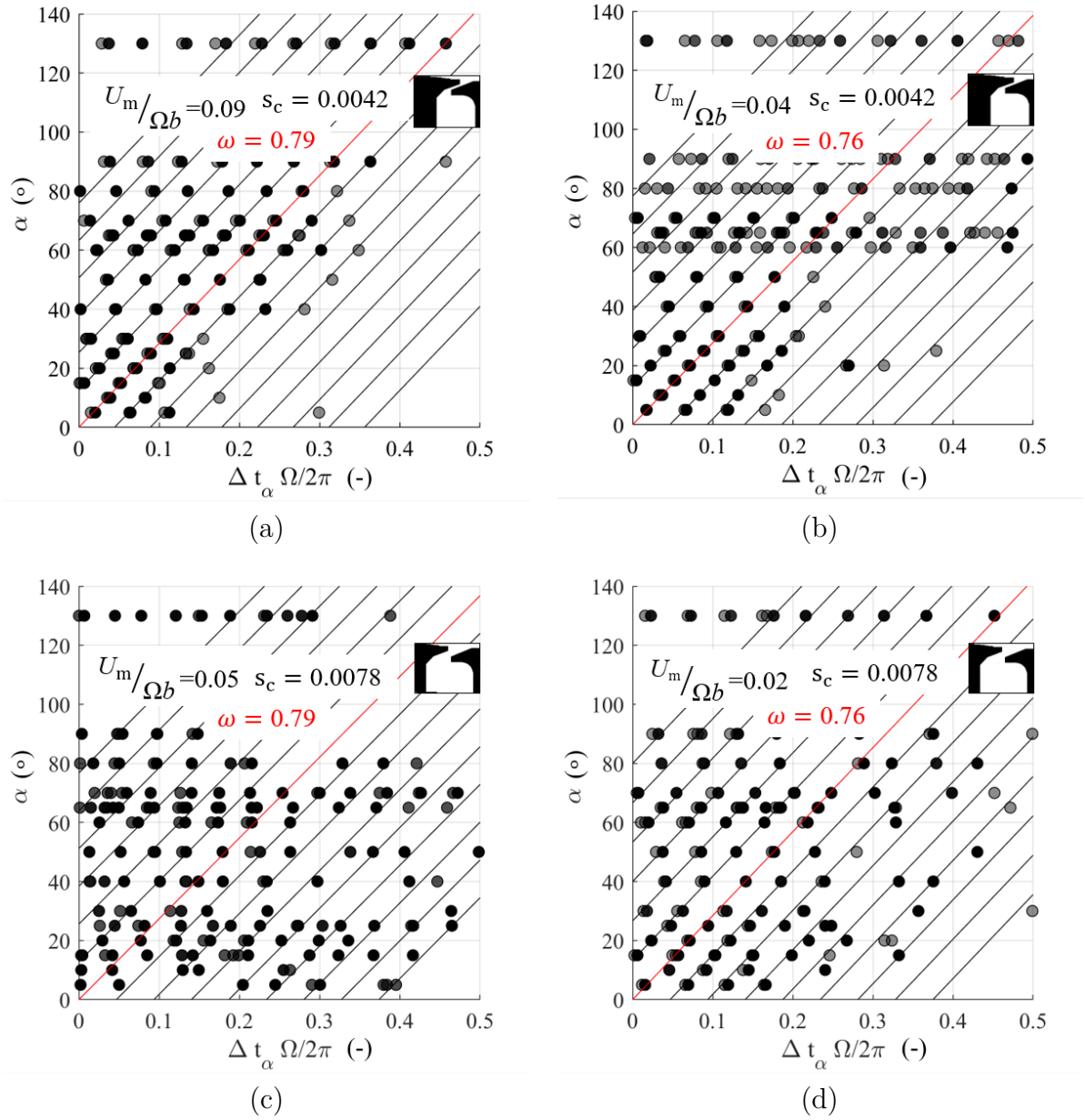

Figure 6.18: Summary plots of cross-correlation results for $C_w = 3500$ in absence of external flow at (a) $Re_\phi = 1.5 \times 10^6$ and $s_c = 0.0042$, (b) $Re_\phi = 3 \times 10^6$ and $s_c = 0.0042$, (c) $Re_\phi = 1.5 \times 10^6$ and $s_c = 0.0078$ and (d) $Re_\phi = 3 \times 10^6$ and $s_c = 0.0078$.

The plots indicate that the flow structures rotate around the cavity at $\omega = 79\%$ of rotor disc speed for the test cases at low rotational Reynolds number, $Re_\phi = 1.5 \times 10^6$ in Fig.6.18(a) and (c). These derive in 28 flow structures in the cavity. Increasing the seal clearance (from Fig.6.18(a) to Fig.6.18(c)) at this condition appears to add scatter to the data, but the angular speed of the flow structures remains unchanged. When the

rotor spins faster, $\mathrm{Re}_\phi = 3 \times 10^6$ in Fig.6.18(b) and (d), the slope for best fit reduces to $\omega = 0.76$ leading to a count of 28 and 27 flow structures for $s_c = 0.0042$ and $s_c = 0.0078$ respectively. These values are consistent with those of Beard *et al.* who found between 26 to 29 lobes rotating at $79 - 80\%$ of rotor disc speed.

The same methodology has been applied to the datasets obtained with an axisymmetric (Fig.6.19(a), (b)) and non-axisymmetric external annulus flow (Fig.6.19(c), (d)). In this instance, a constant rotor disc speed, $\mathrm{Re}_\phi = 3 \times 10^6$, and low and high purge cases are analysed. Fig.6.13 demonstrated that the addition of the mainstream flow increased the broadband frequencies and, at low rotor disc speeds, the distinct peak indicative of the rotationally-induced cavity modes would no longer be visible in the frequency spectra. For this reason, only cases under the disc pumping effect dominance are analysed.

The configuration with an axisymmetric annulus flow presents a more clear pattern in which the best fit line is more obvious at high rates of sealing flow. It appears that, for a fully sealed cavity with external axial flow, Fig.6.18, the flow behaviour shows higher resemblance to that of the pure disc pumping effect in a quiescent environment. The angular speed of the unsteady flow structures is the same as that observed in Fig.6.18(b) for the strongest case of disc pumping effect in absence of external flow. Larger purge supplies cause a reduction in the speed at which the flow structures travel in the cavity volume, that goes down from $\omega = 0.78$ at $U_\mathrm{m}/(\Omega b) = 0.04$ to $\omega = 0.76$ at $U_\mathrm{m}/(\Omega b) = 0.32$. This translates into a decrease in the number of lobes that goes down from 27 to 26.

The addition of a tangential velocity component in the annulus flow increases the scatter at low sealing flow rates, where large ingestion takes place. Ingress of highly swirled flow seems to transfer part of that tangential velocity to the cavity flow structures which appear to travel faster in Fig.6.19(c).

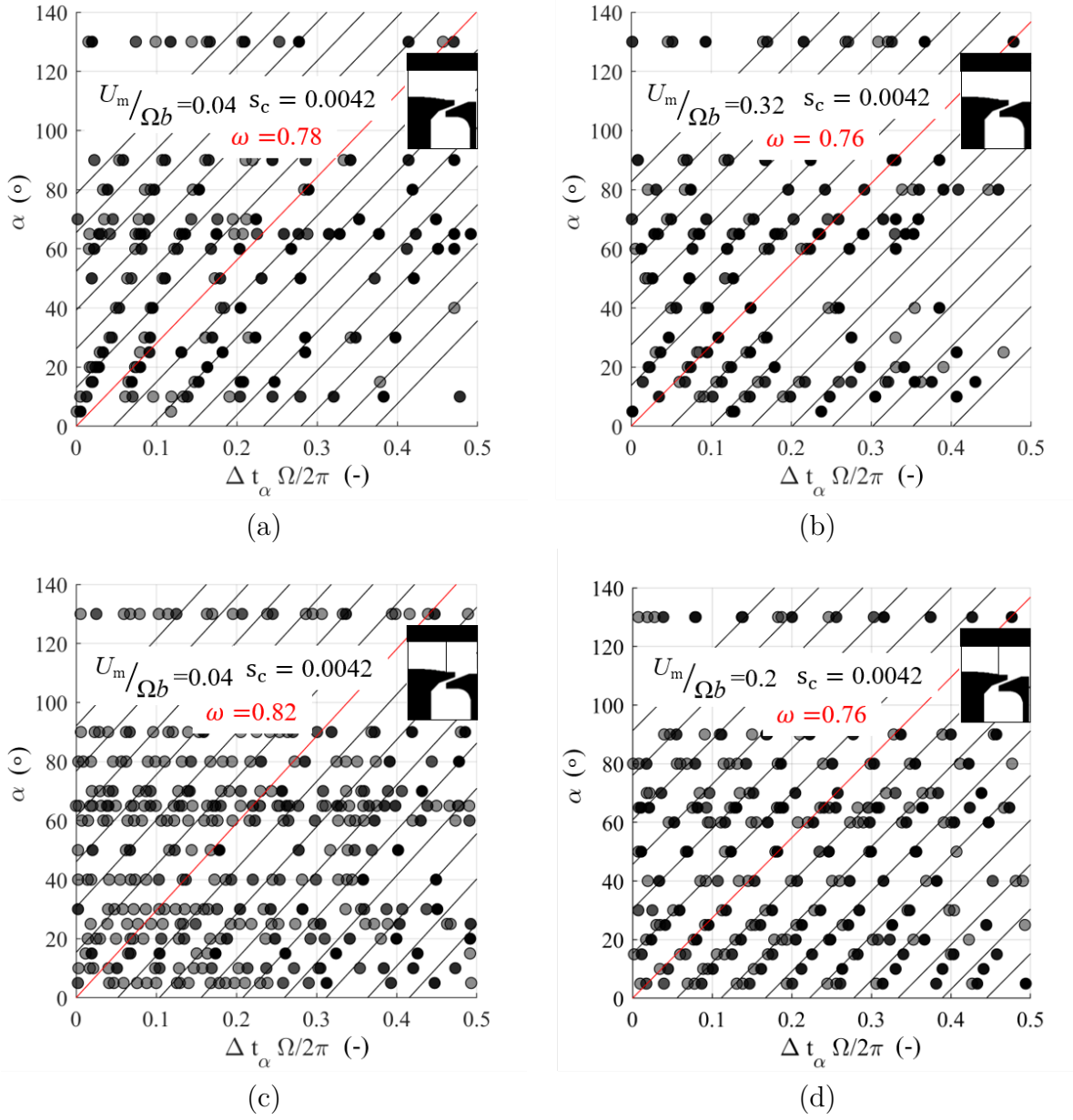

Figure 6.19: Summary plots of cross-correlation results at $\mathrm{Re}_\phi = 3 \times 10^6$ and $s_c = 0.0042$ in (a) axisymmetric annulus flow at $C_w = 3800$, (b) axisymmetric annulus flow at $C_w = 31800$, (c) non-axisymmetric annulus flow at $C_w = 3800$ and (d) non-axisymmetric annulus flow at $C_w = 20800$.

Nonetheless, it should be noted that the higher scatter in the datapoints introduces larger error in the adjustment of ω. The scatter and the angular speed reduce for larger supplies of purge in which the sealing effectiveness of the cavity is expected to be close to unity. Again, this scenario appears to reproduce the pure disc pumping effect in absence of external flow where the rotating structures travelled at 76% of the rotor disc speed.

Interestingly, despite the variation in ω, the lobe count is mostly unaffected, revealing 23 lobes at $U_{\mathrm{m}}/(\Omega b) = 0.04$ and $U_{\mathrm{m}}/(\Omega b) = 0.2$. This fact suggests that ingress of swirled flow does not influence the count of flow structures but it does impact the speed at which they travel.

A summary of the rotational speed and lobe count of each of the test cases presented in this section is included in Table 6.2. From the information gathered in this table and the discussions above, it can be inferred that:

- **Effect of rotor disc speed**. A faster spinning rotor tends to induce a slight reduction in the number of lobes that rotate inside the cavity. The disc pumping effect has been shown to dominate the flow behaviour at $\mathrm{Re}_\phi = 3 \times 10^6$ with the unsteady structures travelling at a constant $\omega = 76\%$ of rotor disc speed regardless of the external flow configuration.

- **Effect of seal clearance**. Increasing the seal clearance did not influence the angular speed of the rotating structures but caused a decrease in the number of lobes.

- **Effect of purge flow**. Overall, larger purge supplies lead to a slight reduction of the lobe count but most importantly, a reduction in the angular speed of the flow structures that seems to tend towards an asymptotic value of $\omega = 0.76$ regardless of the test configuration.

- **Effect of annulus flow**. The number of flow structures in the cavity decreased with each incremental increase of complexity of the system. Generally, the addition of an axial external flow reduced the lobe count by approximately 3.5% compared to the baseline case, but including a swirl component had the largest impact with a decrease of $\sim 18\%$ to the number of rotating flow structures.

Table 6.2: Summary of rotating flow structures.

Annulus flow	Re_ϕ	$U_\mathrm{m}/(\Omega b)$	s_c	ω	L
No external flow	1.5×10^6	0.09	0.0042	0.79	28.44
No external flow	3×10^6	0.04	0.0042	0.76	28.27
No external flow	1.5×10^6	0.05	0.0078	0.79	28.14
No external flow	3×10^6	0.02	0.0078	0.76	27.00
Axisymmetric flow	3×10^6	0.04	0.0042	0.78	27.49
Axisymmetric flow	3×10^6	0.32	0.0042	0.76	26.15
Non-axisymmetric flow	3×10^6	0.04	0.0042	0.82	23.47
Non-axisymmetric flow	3×10^6	0.20	0.0042	0.76	23.68

6.4 Summary

A thorough analysis of the high bandwidth pressure signals collected from the stationary wall of the rim seal cavity volume in the ORF has been conducted. The time history data has been converted to the frequency domain through the Fast Fourier Transform to focus the study in the frequencies corresponding to the unsteady flow structures developing in the cavity. A phase analysis of these frequencies determined the number and rotating speed at which these structures travel around the annular cavity.

Results obtained in the new working section have been contrasted against those from previous test campaigns prior to the rebuild of the facility. The frequencies corresponding to the 30 bolts clamping the split rotor disc were successfully removed. As a consequence, the high broadband levels of unsteadiness, attributed to the presence of such bolts in the cavity, reduced. Three more pressure transducers were introduced further inboard across the overlapping seal to investigate the origin of the unsteady frequency peaks, confirming that this was not the source of such flow structures.

From the seven radially-spaced sensors, the most intense frequency peak was detected at a radial position corresponding to $r/b = 0.95$ with the amplitude decreasing with proximity to the rim region. This trend was consistently observed across the test matrix and

has been related to the change in swirl velocity in the cavity reported in chapter 4. Based on this, it is speculated that the difference in tangential velocity of the vortices coexisting in the cavity increases the shear at this region. A reduction in the non-dimensional frequency of the distinct peak was identified for a larger seal clearance and constant flow ratio.

Large purge supplies have shown to shift the non-dimensional frequency of the peak towards lower values. This was observed across all configurations of annulus flow and seal clearance. Interpretation of these results has been aided by comparison to the steady pressures and sealing effectiveness values described in chapters 4 and 5. This approach has allowed to identify that, for values of turbulent flow parameter beyond that corresponding to the free disc, the peak non-dimensional frequency plateaus owing to the purge flow being ejected as free vortex flow in a fully sealed cavity.

The rotational Reynolds number has proved to be one of the most influential parameters on the frequency of the distinct peak. In terms of absolute frequencies, faster spinning discs induce higher frequencies in the flow structures that slightly decrease when non-dimensionalised with the rotor angular speed.

Changes in the conditions of the flow in the main gas path provoke the most noticeable variations in the frequency spectra. Introduction of an axial flow increases the overall unsteadiness but most significantly, it excites the frequencies around $\sim$ 1400 Hz. This does not change when the external flow is swirled. Therefore, the source of these energetic frequencies has been attributed to the interaction between the annulus and purge flow that generated large scale fluctuations in the rim region. Moreover, it has been demonstrated that in the conditions at which ingestion is largest, the energy content of these frequencies rises, thus further supporting this statement.

Albeit some specific differences potentially due to tolerances and sensitivities of the instrumentation, no significant changes have been identified across the data from the circumferentially spaced sensors.

A phase analysis study has revealed that when the disc pumping effect dominates, the rotating flow structures in the cavity tend to a unique angular speed of 76% of the rotor disc speed regardless of the configuration, seal clearance and purge supply. Nonetheless, the count of unsteady structures strongly depends on the settings of the external annulus flow showing a clear reduction when the NGVs turn the flow. Overall, slight reductions of the rotating speed of the flow features have been observed when the disc spins faster and more sealing air is provided, whilst the seal clearance and rotor disc speed also showed a slight decrease in the number of unsteady events.

Chapter 7

Conclusions

The concluding remarks of each one of the relevant chapters are summarised here to wrap up the discussion reported in this thesis. Suggestions for potential lines of future research are made based on the outcome of this investigation.

7.1 Experimental method

The capability of the Oxford Research Facility was upgraded for investigation of turbine rim sealing flows. The geometry of the working section was modified with a reduction of the annulus casing line to 20% of its original span. A basic CFD study concluded that the mainstream aerodynamics near the hub remained unchanged. Higher resolution in the pressure and temperature instrumentation in the main gas path and purge flow feed system allowed better monitoring of the flow conditions. The air feed system was redesigned to satisfy the new mass flow requirements and allow for steady state conditions in blow down mode for longer run times (of the order of minutes).

A new measurement system to quantify the sealing performance of the chute seal based on the tracer gas technique was installed. The purge flow was seeded using CO_2 as a foreign gas whilst the mainstream flow remained at atmospheric content. Gas was sampled from the stator wall and its concentration of carbon dioxide determined by the

gas analyser. One channel of the gas analyser was used to monitor the purge supply whilst the other one was connected to a multiplexer that sequentially sampled the gas from the measurement points in the stator wall. The gas analyser was calibrated at the start of each day to reduce the time drift. Based on the readings of CO_2 content the sealing effectiveness was derived to an accuracy within ± 0.0068. The presence of foreign gas in the annulus downstream of the rim seal was also investigated to study the radial migration of the purge flow in the main gas path.

High bandwidth pressure transducers were embedded in the stator cavity wall to investigate the unsteady flow features rotating inside the cavity. The unsteady pressure sensors were distributed in the radial and circumferential directions to investigate the presence, strength, quantity and speed of rotation of these rotating structures.

7.2 Rotationally-induced ingestion

The steady pressure measurements under rotationally-induced ingestion revealed the presence of different swirl velocities in the inner and outer parts of the cavity. Sealing effectiveness data unveiled a very complex effect of the annulus flow on the seal performance in which the cavity never sealed fully even at high purge supplies. Strong dependency on the test conditions was identified thus challenging extrapolation of the observed trends.

Results of sealing effectiveness have been compared to other seal designs available in published literature and existing correlations to validate the new methodology. Good agreement with the disc pumping orifice model of Chew [25] was found with an empirical constant of $k = 1$. The chute seal performs considerably better than an axial seal of the same axial clearance.

7.3 Externally-induced ingestion

The introduction of NGVs led to an overall reduction of the sealing effectiveness when compared against Stage 1, with the largest decrease of 60% found in the rim seal. This effect was most severe at the largest flow coefficients studied. Comparison of the radial distribution of sealing effectiveness inside the cavity for axisymmetric and non-axisymmetric flow showed opposing trends as rotor disc speed increased: with vanes present, the lowest values of sealing effectiveness were found at the highest flow coefficient. A reduction of the flow coefficient displayed an improvement in the sealing effectiveness.

A map of sealing performance displayed a remarkable influence of flow coefficient on the sealing capability of the chute seal, especially at low purge rates and high rotational speeds. Excellent agreement with the disc pumping orifice model developed by Chew [25] was found at low flow coefficients. Departure from this condition increased with flow coefficient suggesting that the disc pumping effect dominates at low flow coefficients with the pressure asymmetries in the annulus becoming the governing mechanism at high flow coefficients. Lower sensitivity to flow coefficient was observed for an increased seal clearance. This outcome was attributed to the ingestion of highly swirled external flow at all conditions. The influence of the flow coefficient at a further inbound point in the cavity is minimal as the rotor disc pumping dominates.

Comparison to a pressure-driven orifice model suggests an interesting dependence of the discharge coefficient to flow coefficient. Remarkable agreement was found when the data of this investigation was compared to that from previously published studies of similar chute seals conducted in turbine rigs with vanes and rotor blades present. The resemblance of the results from different test facilities reveals a certain degree of insensitivity to low flow coefficient, which is promising for extrapolation to engine conditions.

The effect of the relative position of the cavity measurements to the NGV trailing

edge in the annulus seems to play an important role in the sealing effectiveness results. The improvement in sealing capability at lower flow coefficients still holds regardless of the circumferential position of the measurements.

A traverse measurement system was installed in the reduced annulus gas path to study the radial migration of the purge flow at the rotor blade leading edge axial position. Presence of tracer gas was detected near the hub but it did not reach the casing of the reduced annulus (therefore being contained within 5% of the real blade span). Significant variations in the circumferential direction were observed especially at low flow coefficient and high purge supply.

7.4 Unsteady rim seal flow structures

Results obtained in the new working section have been contrasted against those from previous test campaigns prior to the rebuild of the facility. Measurements across the overlapping seal confirmed that the unsteady flow structures did not originate further inboard agreeing with the study of Gao *et al.* [59].

The most intense frequency peak was detected at a radial position corresponding to $r/b = 0.95$ with the amplitude decreasing with proximity to the rim region. This effect was observed across the test matrix. It is speculated that the difference in tangential velocity of the vortices that were found to coexist in the cavity increased the shear in this region. A reduction in the non-dimensional frequency of the distinct peak was identified for larger seal clearance and constant flow ratio.

Larger purge supplies shifted the non-dimensional frequency of the peak towards lower values. This was observed across all configurations of annulus flow and seal clearances.

Interpretation of these results was aided by comparison to the steady pressures and sealing effectiveness values described in chapters 4 and 5. For values of turbulent flow parameter beyond that corresponding to the free disc, the peak non-dimensional frequency plateaued owing to the purge flow being ejected as free vortex flow in a fully sealed cavity.

Higher rotational Reynolds numbers induced higher frequencies in the flow structures. Changes in the main gas path flow conditions produced the most noticeable variations in the frequency spectra. Introduction of an axial flow increased the overall unsteadiness but most significantly, it excited the frequencies around $\sim$ 1400 Hz. The introduction of a swirl component to the annulus flow further excited this band of frequencies and increased the overall unsteadiness. The source of these energetic frequencies has been attributed to the interaction between the annulus and purge flow.

Albeit some specific differences potentially due to tolerances and sensitivities of the instrumentation, no significant changes have been identified across the data from the circumferentially spaced sensors.

A phase analysis has revealed that when the disc pumping effect dominated, the rotating flow structures in the cavity tended to an angular speed of 76% of the rotor disc speed regardless of the configuration, seal clearance and purge supply. Nonetheless, the count of unsteady structures strongly depends on the settings of the external annulus flow showing a clear reduction when the NGVs turn the flow.

Overall, larger purge supplies led to a slight reduction of the lobe count but most importantly, to a reduction in the angular speed of the flow structures to an asymptotic value of $\omega = 0.76$ regardless of the test configuration. The number of flow structures in the cavity decreased with each incremental increase of complexity of the system. Generally, the addition of an axial external flow reduced the lobe count by approximately 3.5%

compared to the baseline case, but including a swirl component had the largest impact with a decrease of $\sim 18\%$ to the number of rotating flow structures (please note these are rough estimates).

7.5 Future research studies

Future lines of work are suggested in this chapter based on the most relevant parameters intervening in the hot gas ingestion mechanism that Johnson *et al.* [16] listed. Focus is on those effects which have not been thoroughly investigated as well as some new findings from the most recent studies.

The current project has provided evidence that challenges the widely accepted dominance of the pressure-driven ingestion over the disc pumping effect when pressure asymmetries exist in the annulus. Experimental data collected at the ORF in a vaned gas path suggests that the disc pumping effect induced may play a key role, and prevail over the pressure asymmetries, in the ingestion of hot mainstream air. These results are of significant relevance if extrapolation to engine conditions is sought, especially for high pressure turbines in modern aero-engines. Further research to push the limits of the test conditions to achieve even more engine realistic environments would be recommended as well as to explore whether this effect is geometry-dependent and linked to the particular rim seal arrangement investigated in this testing facility. The effect of varying the axial Reynolds number of the annulus flow could also be of value. During this research the flow coefficient was only modified by the rotor disc speed maintaining the axial annulus velocity constant. A step further in this research would contemplate increasing the axial Reynolds number in the main gas path through higher pressure ratios to achieve a flow environment more representative of that found in a real gas turbine. This would allow extrapolation of rig data to engine-realistic conditions with a higher degree of confidence.

The numerical study of Gao *et al.* [20] showed that the cavity unsteadiness was damped out with a radial seal geometry. This result has not been experimentally validated yet, therefore testing other seal arrangements at the same range of operating conditions, with particular interest in a radial seal, could be of high interest.

The study of the effects in the circumferential direction in the annular cavity was deemed incomplete due to limitations in the instrumentation that derived from the installation of the equipment. The presence of different numbers of unsteady flow structures in the rim region and in the cavity has been highlighted by some authors. An interesting study would be to include high bandwidth pressure measurement spread along the circumferential direction at two radial positions to investigate the interaction of the cavity modes and the unsteady rim seal instabilities.

Following on the work conducted by previous research groups, Green and Turner [31] showed that the presence of rotor blades improved the sealing performance of an axial seal clearance. Hills *et al.* [35] questioned the validity of this outcome and proved through a CFD study that albeit the circumferential pressure asymmetry introduced by the rotor blades was smaller than that due to the stationary vanes, it had a large impact on ingestion. They concluded that the rotor blades would detriment the sealing performance. The experiments of Bohn *et al.* [33] agreed with Green and Turner's results in a configuration with a shrouded stator and unshrouded rotor, whilst a working section with two unshrouded discs aligned with the findings of Hills *et al.* The contradictory results evidence the complexity of the topic and highlight the need for further research. More recent studies by Savov *et al.* [29] and Hualca *et al.* [64] have addressed this topic through experimental campaigns in which the rotor blades were removed and their effect evaluated. Hualca *et al.* identified an interesting relationship between a *kink* in the sealing effectiveness - flow ratio curve that was attributed to the effect of the blades. The investigation of the chute seal sealing performance under the potential field interactions of stator

vanes and rotor blades is considered of high value. Therefore, a recommended next step would be to complete the investigation with the Stage 4 configuration that included rotor blades in the ORF. This would imply major modifications to the test facility to return the working section to its original capability with a full annulus and rotor blades. Work towards this goal was initiated during this project, such as a redesigned rotor disc and clamping arrangement to preserve the geometry of the cavity as much as possible. The light piston tube would need to be recommissioned and tests would have to be conducted under transient operation.

Moving onto a full annulus transient operation of the ORF would not allow sealing performance data to be obtained in its current form. A high frequency concentration measurement technique would be required to log CO_2 concentration data in a runtime of ms. The development of such measurement technique was initiated in the early stages of this project but was abandoned when it was confirmed that tests with blades would not take place.

Protrusions in the annular cavity act to increase the broadband frequency spectra as described in chapter 6. Manufacturing tolerances, rig installation misalignments and vibrations during operation may also effect the highly sensitive aerodynamics in the cavity. Savov *et al.* [29] captured greater broadband noise in a brief study of the effect of eccentricity that would be interesting to expand.

The suggested lines for further research that could be of high value to the current understanding of rim sealing flows are summarised below.

1. Expand experimental capability to achieve more engine-representative environments.
2. Experimentally investigate different rim seal arrangements, with special interest in the radial seal.

3. Further explore the effect of the circumferential pressure asymmetries inside the cavity.

4. Include rotor blades in the main gas path.

5. Develop a concentration measurement technique with a high frequency response to run in transient facilities.

6. Study the influence of protrusions and experimental inaccuracies (eccentricty and vibrations) over the cavity aerodynamics.

7.6 Research impact

The findings of this research are considered to contribute to the current understanding of the aerodynamics of rim sealing flows. The sealing performance map has provided experimental data that challenges the extended assumption that the pressure asymmetries govern the flow physics in the rim seal. The influence of the disc pumping effect in a full turbine stage has been often neglected as it was thought to be orders of magnitude lower. However, this study has revealed that rotationally-induced ingestion coexists and may even dominate over the pressure asymmetries of the gas path under certain operating conditions.

During this investigation, the flow coefficient has been found to be a critical parameter when assessing the driving mechanism for hot gas ingestion. Over the years, various analytical correlations have been developed to assess the sealing capability of a specific rim seal geometry based on rig data. These models are often used by the engine manufacturers during the design process. The results of the sealing performance map presented in this thesis have been contrasted against real engine data confirming the findings of this research: the disc pumping effect dominates in the HP turbine which operate at low values of flow coefficient whilst the LP turbine results sit within the region of pressure-driven

ingestion defined at high flow coefficients. Therefore, the outcome of this study allows the engine designer to define the operating regime of the turbine stage under consideration to support a better choice of modelling strategy, eventually allowing higher levels of fidelity during the early stages of design.

In addition, the dynamic pressure data collected during this investigation has revealed a high degree of unsteadiness arising from the interaction between the mainstream and purge flows that the engine designer can now account for. The wide parametric study reported here also provides unsteady experimental data over an extensive range of operating conditions that could potentially help the designer if suppressing the unsteadiness in the cavity or the rim seal region was deemed of interest.

Appendix A

Uncertainty analysis

An uncertainty analysis has been performed with the reported bias error of the instrumentation and the precision error registered during tests. Due to the complex definition of most of the variables of interest, propagation of error resulted in an increase of the uncertainty of the derived quantities. The approach followed has been based on the linear terms of a Taylor series expansion that approximates the error of the total quantity as the uncertainty in each measurement with the root sum square of the sensitivity indexes of each of the variables involved multiplied by the uncertainty in each measurement. The same process is repeated for the calculation of the bias and precision error and then the root sum square of both provides the total uncertainty of the derived quantity. In general terms, the process is detailed below using a compound variable Q which is a function of z variables x_1 to x_z.

$$Q = f(x_1, x_2, ..., x_z)$$

The uncertainty of the derived quantity Q is calculated with Eq.7.1 to Eq.7.4.

- **Bias error**

  Denoted by B is obtained directly from the manufacturer of the measuring device.

$$\Delta Q_B = \pm \sqrt{\left(\frac{\partial Q}{\partial x_1} B_{x_1}\right)^2 + \left(\frac{\partial Q}{\partial x_2} B_{x_2}\right)^2 + ... + \left(\frac{\partial Q}{\partial x_z} B_{x_z}\right)^2} \tag{7.1}$$

- **Precision error**

  The precision error of the measurement is calculated based on the standard deviation with Eq.7.2, where x_i is the reading of Q at each one of the i samples evaluated at the design point test case specified in Table 7.1.

$$\sigma = \sqrt{\frac{1}{Z}\sum_{i=1}^{Z}(x_i - \mu)^2} \quad \text{with} \quad \mu = \frac{1}{Z}\sum_{i=1}^{Z} x_i \tag{7.2}$$

Table 7.1: Design point conditions for uncertainty analysis.

Parameter	**Symbol**	**Value**	**Units**
Sample time	t_s	30	s
Sample frequency	f_s	200	Hz
Samples	Z	6000	samples
Non-dimensional purge flow	C_w	3500	(-)
Rotor disc speed	N	7850	rpm
Axial Reynolds number	Re_{ax}	0	(-)
Disc radius	b	0.2368	m

  The uncertainty associated to the precision error for the 95% confidence interval is $\pm 2\sigma$. The precision error must be calculated for each one of the x_z variables involved in the definition of R to provide the total precision error following Eq.7.3.

$$\Delta R_S = \pm\sqrt{\left(\frac{\partial R}{\partial x_1}S_{x_1}\right)^2 + \left(\frac{\partial R}{\partial x_2}S_{x_2}\right)^2 + ... + \left(\frac{\partial R}{\partial x_z}S_{x_z}\right)^2} \tag{7.3}$$

- **Total error**

  The total uncertainty of the sealing effectiveness was derived from the root sum square of the bias and precision errors as shown in Eq.7.4.

$$\Delta R = \sqrt{2\left(\Delta R_B^2 + \Delta R_S^2\right)} \tag{7.4}$$

The uncertainty analysis carried out for the most relevant derived quantities used throughout the discussion of this thesis are listed in this chapter.

Sealing effectiveness, ε

The uncertainty of the sealing effectiveness derived quantity is calculated in this section from the bias and precision errors of the gas analyser. The gas analyser was calibrated for a range of carbon dioxide content in air of $0 - 4\%$. The design point test case chosen corresponded to $\varepsilon = 0.75$.

- **Bias error**

  The gas analyser uncertainty had a linearity error of $\pm 0.5\%$ and repeatability error below $\pm 1\%$ of the full scale. The drift error was neglected since the device was calibrated every day before a run. The total uncertainty of the device was calculated with the sum for the calibrated range of $0 - 4\%CO_2$ content in air. As a result, the total bias error of the gas analyser is $B_c = \pm 0.06\%\ CO_2$.

Linearity error	$\pm 0.5\% \times 4\%CO_2$	$= \pm 0.02\%\ CO_2$
Repeatability error	$\pm 1\% \times 4\%CO_2$	$= \pm 0.04\%\ CO_2$
Total bias error	B_c	$= \pm 0.06\%\ CO_2$

$$B_{c_{\text{stator}}} = B_{c_{\text{purge}}} = B_{c_{\text{ann}}} = \pm 0.06\%$$

- **Precision error**

  The test case chosen as design point yields $\mu = 1.5585$ and $\sigma = 0.0053$. The uncertainty associated to the precision error in the gas concentration measurement for the 95% confidence interval is $\pm 2\sigma = \pm 0.0106$.

$$S_{c_{\text{stator}}} = S_{c_{\text{purge}}} = S_{c_{\text{ann}}} = \pm 0.0106\%$$

- **Total error**

  The partial derivatives of the sealing effectiveness respect to each one of these variables were required and are shown in Eq.7.5 to Eq.7.7.

$$\frac{\partial \varepsilon}{\partial c_{\text{stator}}} = \frac{1}{c_{\text{ann}} - c_{\text{purge}}} \tag{7.5}$$

$$\frac{\partial \varepsilon}{\partial c_{\text{ann}}} = \frac{c_{\text{purge}} - c_{\text{stator}}}{(c_{\text{ann}} - c_{\text{purge}})^2} \tag{7.6}$$

$$\frac{\partial \varepsilon}{\partial c_{\text{purge}}} = \frac{c_{\text{stator}} - c_{\text{ann}}}{(c_{\text{ann}} - c_{\text{purge}})^2} \tag{7.7}$$

Gas concentration readings from the gas analyser at the design point are seen below.

$$c_{\text{purge}} = 1.9881\%; \qquad c_{\text{stator}} = 1.5624\%; \quad c_{\text{ann}} = 0.1207\%;$$

$$\frac{\partial \varepsilon}{\partial c_{\text{purge}}} = -0.4134; \quad \frac{\partial \varepsilon}{\partial c_{\text{stator}}} = 0.5355; \quad \frac{\partial \varepsilon}{\partial c_{\text{ann}}} = 0.4134;$$

Total uncertainty of the sealing effectiveness measurement is:

$$\Delta\varepsilon = \sqrt{2\left(\Delta\varepsilon_B^2 + \Delta\varepsilon_S^2\right)} = \sqrt{2\left((0.0475)^2 + (8.404 \times 10^{-3})^2\right)} = 0.068$$

Pressure coefficient, C_p

The cavity pressure coefficient is defined as the difference of pressure across the stator wall non-dimensionalised by the dynamic head at rotor rim speed as indicated in Eq.7.8 and is evaluated at the conditions shown in Table 7.2. The density used for the calculation of the dynamic head is obtained from the experimental measurements of pressure and temperature in the feed cavity for higher accuracy.

$$C_p = \frac{p - p_{1011}}{0.5\rho(\Omega b)^2} = \frac{p - p_{1011}}{0.5 p_{1051}/(RT_{2051})(\Omega b)^2} \tag{7.8}$$

The values of the variables of interest at the point of evaluation are:

- **Bias error**

  The bias error of the variables of interest for the calculation of C_{p} are summarised in Table 7.3.

Table 7.2: Design point conditions for the cavity pressure coefficient uncertainty analysis.

Parameter	Symbol	Value	Units
Pressure at the rim	p_{1019}	1.087×10^5	Pa
Pressure at the inner cavity	p_{1011}	1.075×10^5	Pa
Pressure at the feed cavity	p_{1051}	1.0054×10^5	Pa
Temperature at the feed cavity	T_{2051}	289.138	K

Table 7.3: Bias error of variables for C_p.

Parameter	Instrumentation	Bias error	
p_{1019}, p_{1011}	FS HCE 0-100 mbar 0.2% FS	$B_{\mathrm{p1019}} = B_{\mathrm{p1011}}$	$= 2 \times 10^{-4}$ bar
p_{1051}	FS HCE 0-10 bar 0.1% FS	B_{p1051}	$= 10^{-2}$ bar
T_{2051}	k-type thermocouple $d = 76.2\mu$m	B_{T2051}	$= 1.1$ K
Ωb	speed encoder	$B_{\Omega\mathrm{b}}$	$= 0.0248$ m/s

- **Precision error**

  The precision error of the relevant parameters is summarised below in Table 7.4.

Table 7.4: Precision error of variables for C_p.

Parameter	Precision error	
p_{1019}	S_{p1019}	$= 1.6524$ bar
p_{1011}	S_{p1011}	$= 1.6881$ bar
p_{1051}	S_{p1051}	$= 1.3763$ bar
T_{2051}	S_{T2051}	$= 2.8 \times 10^{-3}$ K
Ωb	$S_{\Omega\mathrm{b}}$	$= 0.2729$ m/s

- **Total error**

  The partial derivatives evaluated at the design point provide a total uncertainty of the cavity pressure coefficient of ± 0.0017.

$$\frac{\partial C_\mathrm{p}}{\partial p_{1019}} = 37.7; \quad \frac{\partial C_\mathrm{p}}{\partial p_{1011}} = -37.7; \quad \frac{\partial C_\mathrm{p}}{\partial p_{1051}} = -0.4;$$
$$\frac{\partial C_\mathrm{p}}{\partial T_{2051}} = 0.1499; \quad \frac{\partial C_\mathrm{p}}{\partial \Omega b} = -0.4139;$$

$$\Delta C_{\mathrm{p,B}} = 0.0012$$

$$\Delta C_{\mathrm{p,S}} = 1.4379 \times 10^{-4}$$

Total uncertainty of the cavity pressure coefficient measurement is:

$$\Delta C_{\mathrm{p}} = \sqrt{2\left(\Delta C_{\mathrm{p,B}}^2 + \Delta C_{\mathrm{p,S}}^2\right)} = \sqrt{2\left((0.0012)^2 + (1.4379 \times 10^{-4})^2\right)} = 0.0017$$

Mass flow through the nozzles

As detailed in chapter 3 the mainstream annulus flow and the purge flow in the configurations corresponding to Stages 2 and Stage 3 were provided by choked venturi nozzles. The uncertainty of the diameter measurement was $B = 0.05$ mm.

The dimensions of the nozzles providing the flow depended on the upstream pressure and therefore were different for Stages 2 and 3. Two mainstream flow nozzles of diameter $d_{\mathrm{nozzle}} = 32.8$ mm provided the axial annulus flow of Stage 2 and were replaced by $d_{\mathrm{nozzle}} = 25.5$ mm nozzles for the tests in Stage 3. Similarly, the sealing flow nozzles for Stage 2 had diameters ranging from 5.2 to 22.4 mm. For Stage 3, three more nozzles were added to this list to complete the wanted seal-to-axial velocity ratios, with sizes $d_{\mathrm{nozzle}} = [4.5, 6.6, 7.8]$ mm. The uncertainty of the nozzles machined for the experimental campaign of Stage 3 ranged from 0.7% to 2.31% depending on the size of the nozzle.

First of all, the uncertainty in the nozzle diameter was accounted for and the area and area uncertainty for each one of the nozzles was calculated based on Eq.7.9.

$$A_{\mathrm{nozzle}} = \frac{\pi}{4}(d_{\mathrm{nozzle}})^2; \qquad \Delta A_{\mathrm{nozzle}} = \frac{A_{\mathrm{nozzle}_{\pm}} - A_{\mathrm{nozzle}}}{A_{\mathrm{nozzle}}} 100 \tag{7.9}$$

The uncertainty of the discharge coefficient, pressure and temperature measurements was estimated in $\Delta C_{\mathrm{d}} = 0.5$, $\Delta p = 0.1$ bar and $\Delta T = 0.45$ K respectively as shown in Tables 7.5 and7.6. The mass flow for a choked nozzle was calculated according to Eq.3.8 assuming a discharge coefficient of 0.99. The derived total uncertainty of the mass flow passing through the nozzles was then obtained from the individual uncertainty of the

discharge coefficient, pressure and temperature as show in Eq.7.6.

$$\Delta\dot{m} = \sqrt{\Delta A_{\text{nozzle}}^2 + \Delta C_{\text{d}}^2 + \Delta p^2 + 0.5\ \Delta T^2} \tag{7.10}$$

Table 7.5: Uncertainty quantification for the mass flow through Stage 2 nozzles.

d (mm)	$d \pm \Delta d$ (mm)	A_{nozzle} (mm)	ΔA_{nozzle} (mm)	C_{d}	p (bar)	T (K)	$\Delta\dot{m}$ (g/s)
	32.75	842.3886	-0.3046	0.5	0.1	0.45	0.6738
32.8	32.8	844.9628	0	0.5	0.1	0.45	0.6010
	32.85	847.5408	0.3051	0.5	0.1	0.45	0.6740
	5.15	20.8307	-1.91386	0.5	0.1	0.45	2.0059
5.2	5.2	21.2371	0	0.5	0.1	0.45	0.6010
	5.255	21.6475	1.9323	0.5	0.1	0.45	2.0236
	22.35	392.3241	-0.4459	0.5	0.1	0.45	0.7484
22.4	22.4	394.0814	0	0.5	0.1	0.45	0.6010
	22.45	395.8426	0.4469	0.5	0.1	0.45	0.7489

Table 7.6: Uncertainty quantification for the mass flow through Stage 3 nozzles.

d (mm)	$d \pm \Delta d$ (mm)	A_{nozzle} (mm)	ΔA_{nozzle} (mm)	C_{d}	p (bar)	T (K)	$\Delta\dot{m}$ (g/s)
	25.45	508.7044	-0.3918	0.5	0.1	0.45	0.7175
25.5	25.5	510.7052	0	0.5	0.1	0.45	0.6010
	25.55	512.7099	0.3925	0.5	0.1	0.45	0.7178
	4.55	15.55285	-2.2098	0.5	0.1	0.45	2.2901
4.5	4.5	15.9043	0	0.5	0.1	0.45	0.6010
	4.45	16.2597	2.2345	0.5	0.1	0.45	2.3139
	10.35	84.13381	-0.9592	0.5	0.1	0.45	1.1319
10.4	10.4	84.9486	0	0.5	0.1	0.45	0.6010
	10.45	0.9638	0.4469	0.5	0.1	0.45	1.1359

Non-dimensional sealing flow, C_{w}

The sealing mass flow is often non-dimensionalised to provide a parameter that can be compared across configurations and geometries, see Eq.7.11.

$$C_{\mathrm{w}} = \frac{\dot{m}_{\mathrm{purge}}}{\mu\, b} \tag{7.11}$$

The purge supply was provided by an Alicat MC Series 2000 SLPM mass flow controller whose quoted accuracy was set by the manufacturer of the device to ±0.8% of reading plus ±0.2% of full scale. The viscosity of the fluid is temperature-dependent and has been calculated with the temperature measurement available underneath the overlapping seal, model point 2054, following the Sutherland Law introduced in Eq.3.6.

Table 7.7: Design point conditions for the C_{w} uncertainty analysis.

Parameter	**Symbol**	**Value**	**Units**
Output voltage (MFC)	V_{4002}	1.992	V
Temperature at feed cavity	T_{2054}	310.399	K

- **Bias error**

  The bias error from the MFC and the thermocouple are summarised in Table 7.8.

Table 7.8: Bias error of variables for C_{w}.

Parameter	**Instrumentation**	**Bias error**	
V_{4002}	Alicat MC series 0.8% reading + 0.2% FS	B_{V4002}	= 0.29 V
T_{2054}	k-type thermocouple $d = 76.2\ \mu$m	B_{T2051}	= 1.1 K

- **Precision error**

  The precision error of the measurement is detailed in Table 7.9.

- **Total error**

  The partial derivatives are shown below, and the calculated total uncertainty of the sealing flow coefficient is 62.385. note that this is a non-dimensional parameter.

Table 7.9: Precision error of variables for C_{w}.

Parameter	Precision error	
V_{4002}	S_{V4002}	$= 9.2093 \times 10^{-5}$ V
T_{2054}	S_{T2054}	$= 0.0032$ K

Where the partial derivatives evaluated at the conditions in Tab.7.7 are:

$$\frac{\partial C_{\mathrm{w}}}{\partial V_{4002}} = 1.665 \times 10^{3}; \quad \frac{\partial C_{\mathrm{w}}}{\partial T_{2054}} = -8.172;$$
$$\Delta C_{\mathrm{w,B}} = 44.107; \qquad \Delta C_{\mathrm{w,S}} = 0.716;$$

The total uncertainty of the sealing flow coefficient is:

$$\Delta C_{\mathrm{w}} = \sqrt{2\left(\Delta C_{\mathrm{w,B}}^2 + \Delta C_{\mathrm{w,S}}^2\right)} = \sqrt{2\left[(44.107)^2 + (0.716)^2\right]} = 62.385$$

Non-dimensional sealing flow ratio, $\Phi = U_{\mathrm{m}}/(\Omega b)$

The sealing flow can also be non-dimensionalised as a velocity ratio between the average velocity of the purge flow exiting through the rim seal and the rotor rim speed, $U_{\mathrm{m}}/(\Omega b)$. The average velocity through the rim clearance was calculated from the continuity equation Eq.7.12.

$$\Phi = \frac{U_{\mathrm{m}}}{(\Omega b)} = \frac{\dot{m}_{\mathrm{seal}}}{\rho A_{\mathrm{seal}}(\Omega b)} = \frac{\dot{m}_{\mathrm{seal}}\, R\, T_{2051}}{p_{1051}\, A_{\mathrm{seal}}(\Omega b)} \tag{7.12}$$

The values of each one of the required variables at the evaluation point together with the bias and precision errors were already detailed in Tables 7.2, 7.3 and 7.4 respectively. The uncertainty associated with the purge supply is $B_{\mathrm{mseal}} = 2.0256 \times 10^{-4}$ kg/s and $S_{\mathrm{mseal}} = 7.175 \times 10^{-7}$ kg/s. Evaluation of the partial derivatives in the point specified in Tab.7.2 provides:

$$\frac{\partial \Phi}{\partial p_{1051}} = -4.07 \times 10^{-7}; \quad \frac{\partial \Phi}{\partial T_{2051}} = 1.415 \times 10^{-4}; \quad \frac{\partial \Phi}{\partial \dot{m}_{\mathrm{seal}}} = 2.628; \quad \frac{\partial \Phi}{\partial (\Omega b)} = -1.954 \times 10^{-4};$$
$$\Delta \Phi_{\mathrm{B}} = 6.88 \times 10^{-4}; \qquad \Delta \Phi_{\mathrm{S}} = 5.308 \times 10^{-5};$$

The total uncertainty of the sealing flow coefficient is:

$$\Delta\left[\frac{U_{\mathrm{m}}}{(\Omega b)}\right] = \sqrt{2\left(\Delta\Phi_{\mathrm{B}}^2 + \Delta\Phi_{\mathrm{S}}^2\right)} = \sqrt{2\left((6.88\times10^{-4})^2 + (5.308\times10^{-5})^2\right)} = 9.76\times10^{-4}$$

Rotational Reynolds number, Re_ϕ

The rotational Reynolds number has been used as an indication of the strength of the disc pumping effect since its definition is based on the ratio of inertial over viscous forces in the cavity. The rotor disc speed at the rim has been used as the representative velocity in this case and the rim radius, b as the characteristic length, Eq.7.13. The density of the purge flow has been calculated with the closest available pressure to the rim and the temperature measurement of the flow in the cavity. The viscosity of the cavity flow was accounted to be dependent on the temperature by the Sutherland law, Eq.3.6.

$$\mathrm{Re}_\phi = \frac{\rho\,(\Omega b)\,b}{\mu} = \frac{p_{1019}/(R\,T_{2054})(\Omega b)b}{\mu} \tag{7.13}$$

The rotational Reynolds number is a function of the temperature, pressure and rotor rim speed which have already been detailed in Tab.7.2 at the point of evaluation. In the same way, the bias and precision errors of this measurements were summarised in Tab.7.3 and Tab.7.4 respectively. The evaluation of the partial derivatives at the design point under consideration yields to:

$$\frac{\partial \mathrm{Re}_\phi}{\partial p_{1019}} = 28.15; \qquad \frac{\partial \mathrm{Re}_\phi}{\partial T_{2054}} = -1.737\times10^{-7}; \quad \frac{\partial \mathrm{Re}_\phi}{\partial(\Omega b)} = 1.462\times10^{4};$$
$$\Delta\mathrm{Re}_{\phi,\mathrm{B}} = 1.912\times10^{4}; \quad \Delta\mathrm{Re}_{\phi,\mathrm{S}} = 3.967\times10^{3};$$

The total uncertainty of the rotational Reynolds number is:

$$\Delta\mathrm{Re}_\phi = \sqrt{2\left(\Delta\mathrm{Re}_{\phi,\mathrm{B}}^2 + \Delta\mathrm{Re}_{\phi,\mathrm{S}}^2\right)} = \sqrt{2\left[(1.912\times10^4)^2 + (3.967\times10^3)^2\right]} = 2.762\times10^4$$

Axial Reynolds number, $\mathrm{Re_{ax}}$

The axial Reynolds number of the annulus flow was calculated with the axial component of the annulus flow velocity considering the axial chord of the NGVs as the characteristic length. The relevant flow density in this case was that of the mainstream flow and therefore calculated with values in the casing of the reduced annulus, see Eq.7.14. The Sutherland law was used again to find the annulus flow viscosity.

$$\mathrm{Re_{ax}} = \frac{\rho\, U_{\mathrm{ax}}\, C_{\mathrm{ax}}}{\mu} = \frac{p_{1215}}{R\, T_{1215}\, \mu} cos(\alpha_{\mathrm{NGVexit}}) \sqrt{\gamma\, R\, T_{1215}} \sqrt{\frac{2}{\gamma - 1}\left[\frac{1}{\left(\frac{p_{1215}}{p_{\mathrm{rakes}}}\right)^{\frac{\gamma-1}{\gamma}}} - 1\right]} \tag{7.14}$$

The point of evaluation of the previous quantities corresponded to the configuration of Stage 1 in which there was no external annulus flow. In order to assess the properties of the mainstream axial component, the operating conditions of Stage 3 (with NGVs) have been used at the same purge flow, gap size and rotor disc speed as the previously evaluated cases.

Evaluating the partial derivatives at the specified operating conditions leads to an uncertainty quantification of:

$$\frac{\partial \mathrm{Re_{ax}}}{\partial p_{1215}} = -0.2945; \qquad \frac{\partial \mathrm{Re_{ax}}}{\partial T_{1215}} = -1.5153 \times 10^3; \quad \frac{\partial \mathrm{Re_{ax}}}{\partial (p_{\mathrm{rakes}})} = 1.959;$$
$$\Delta \mathrm{Re_{ax,B}} = 2.589 \times 10^3; \quad \Delta \mathrm{Re_{ax,S}} = 9.009;$$

The total uncertainty of the rotational Reynolds number is:

$$\Delta \mathrm{Re_{ax}} = \sqrt{2\,(\Delta \mathrm{Re}^2_{\mathrm{ax,B}} + \Delta \mathrm{Re}^2_{\mathrm{ax,S}})} = \sqrt{2\,[(2.589 \times 10^3)^2 + (9.009)^2]} = 3.661 \times 10^3$$

Flow coefficient, $\frac{U_{\text{ax}}}{(\Omega b)}$

The flow coefficient is defined as the ratio of the axial velocity component of the annulus flow over the rotor rim speed therefore the point of evaluation will be that defined in section 7.6 from the configuration of Stage 3.

$$\Psi = \frac{U_{\text{ax}}}{(\Omega b)} = \cos(\alpha_{\text{NGVexit}})\sqrt{\gamma\ R\ T_{1215}}\ \sqrt{\frac{2}{\gamma-1}\left[\frac{1}{\left(\frac{p_{1215}}{p_{\text{rakes}}}\right)^{\frac{\gamma-1}{\gamma}}}-1\right]}\frac{1}{(\Omega b)} \tag{7.15}$$

$$\frac{\partial\Psi}{\partial p_{1215}} = -6.247\times10^{-6}; \quad \frac{\partial\Psi}{\partial T_{1215}} = 9.737\times10^{-4}; \quad \frac{\partial\Psi}{\partial p_{rakes}} = 1.6032; \quad \frac{\partial\Psi}{\partial(\Omega b)} = -0.003;$$

$$\Delta\Psi_{\text{B}} = 0.0063; \qquad \Delta\Psi_S = 1.714\times10^{-5};$$

The total uncertainty of the sealing flow coefficient is:

$$\Delta\left[\frac{U_{\text{ax}}}{(\Omega b)}\right] = \sqrt{2\ (\Delta\Psi_B^2 + \Delta\Psi_S^2)} = \sqrt{2\ [(0.0063)^2 + (1.714\times10^{-5})^2]} = 0.009$$

Bibliography

[1] European Union Aviation Safety Agency. European aviation environmental report 2019. https://ec.europa.eu/transport/sites/transport/files/2019-aviation-environmental-report.pdf, 2019.

[2] Moore, A. Gas Turbine Engine Internal Air Systems: A Review of the Requirements and the Problems. volume ASME 1975 Winter Annual Meeting: GT Papers of *Turbo Expo: Power for Land, Sea, and Air*, 11 1975.

[3] Chupp, R E, Hendricks, R C, Lattime, S B, and Steinetz, B M. Sealing in Turbomachinery. *NASA reports NASA/TM-2006-214341*, 2006.

[4] Childs, P R N. *Rotating Flow*. Elsevier Science, 2010.

[5] Owen, J M. Prediction of Ingestion Through Turbine Rim Seals—Part I: Rotationally Induced Ingress. *Journal of Turbomachinery*, 133(3), 11 2010.

[6] Owen, J M and Rogers, R H. *Flow and Heat Transfer in Rotating-disc Systems: Rotor-stator systems*. Flow and Heat Transfer in Rotating-disc Systems. Research Studies Press, 1989.

[7] Bayley, F J, Long, C A and Turner, A B. Discs and drums: The thermo-fluid dynamics of rotating surfaces. *Proceedings of the Institution of Mechanical Engineers, Part C: Journal of Mechanical Engineering Science*, 207(2):73–81, 1993.

[8] Daily, J W and Nece, R E. Chamber Dimension Effects on Induced Flow and Frictional Resistance of Enclosed Rotating Disks. *Journal of Basic Engineering*, 82(1):217–230, 03 1960.

[9] Dahlqvist, J and Fridh, J. Experimental Investigation of Turbine Stage Flow Field and Performance at Varying Cavity Purge Rates and Operating Speeds. *Journal of Turbomachinery*, 140(3), 12 2017.

[10] Bohn, D E, Decker, A, Ma, H and Wolff, M. Influence of sealing air mass flow on the velocity distribution in and inside the rim seal of the upstream cavity of a 1.5-stage turbine. volume Volume 5: Turbo Expo 2003, Parts A and B of *Turbo Expo: Power for Land, Sea, and Air*, pages 1033–1040, 06 2003.

[11] Bayley, F J and Owen, J M. The Fluid Dynamics of a Shrouded Disk System With a Radial Outflow of Coolant. *Journal of Engineering for Power*, 92(3):335–341, 07 1970.

[12] Kikuchi, A and Takeuchi J. An Investigation of Turbine Disc Cooling (Experimental Investigation and Observation of Hot Gas Flow into a Wheelspace). In *3rd CIMAC Conference Vienna*, 1979.

[13] Phadke, U P and Owen, J M. Aerodynamic aspects of the sealing of gas-turbine rotor-stator systems: Part 1: The behavior of simple shrouded rotating-disk systems in a quiescent environment. *International Journal of Heat and Fluid Flow*, 9(2):98 – 105, 1988.

[14] Phadke, U P and Owen, J M. Aerodynamic aspects of the sealing of gas-turbine rotor-stator systems: Part 2: The performance of simple seals in a quasi-axisymmetric external flow. *International Journal of Heat and Fluid Flow*, 9(2):106 – 112, 1988.

[15] Cao, C, Chew, J W, Millington, P R and Hogg, S I. Interaction of Rim Seal and Annulus Flows in an Axial Flow Turbine. *Journal of Engineering for Gas Turbines and Power*, 126(4):786–793, 11 2004.

[16] Johnson, B V, Mack, G J, Paolillo, R E and Daniels, W A. *Turbine rim seal gas path flow ingestion mechanisms.* 1994.

[17] Scobie, J A, Sangan, C M, Owen, J M and Lock, G D. Review of Ingress in Gas Turbines. *Journal of Engineering for Gas Turbines and Power*, 138(12), 07 2016.

[18] Chew, J W, Gao, F and Palermo, D M. Flow mechanisms in axial turbine rim sealing. *Proceedings of the Institution of Mechanical Engineers, Part C: Journal of Mechanical Engineering Science*, 233(23-24):7637–7657, 2019.

[19] Beard, P F, Gao, F, Chana, K S and Chew, J W. Unsteady Flow Phenomena in Turbine Rim Seals. *Journal of Engineering for Gas Turbines and Power*, 139(3), 09 2016.

[20] Gao, F, Chew, J W and Marxen, O. Inertial waves in turbine rim seal flows. *Phys. Rev. Fluids*, 5:024802, Feb 2020.

[21] Phadke, U P and Owen, J M. An Investigation of Ingress for an "Air-Cooled" Shrouded Rotating Disk System With Radial-Clearance Seals. *Journal of Engineering for Power*, 105(1):178–182, 01 1983.

[22] Phadke, U P and Owen, J M. Aerodynamic aspects of the sealing of gas-turbine rotor-stator systems: Part 3: The effect of nonaxisymmetric external flow on seal performance. *International Journal of Heat and Fluid Flow*, 9(2):113 – 117, 1988.

[23] Dadkhah, S, Turner, A B and Chew, J W. Performance of Radial Clearance Rim Seals in Upstream and Downstream Rotor–Stator Wheelspaces. *Journal of Turbomachinery*, 114(2):439–445, 04 1992.

[24] Daniels, W A, Johnson, B V, Graber, D J and Martin, R J. Rim Seal Experiments and Analysis for Turbine Applications. *Journal of Turbomachinery*, 114(2):426–432, 04 1992.

[25] Chew, J W. A Theoretical Study of Ingress for Shrouded Rotating Disk Systems With Radial Outflow. *Journal of Turbomachinery*, 113(1):91–97, 01 1991.

[26] Chew, J W, Dadkhah, S and Turner, A B. Rim Sealing of Rotor–Stator Wheelspaces in the Absence of External Flow. *Journal of Turbomachinery*, 114(2):433–438, 04 1992.

[27] Bru Revert, A, Beard, P F, Chew, J W and Bottenheim, S. Submitted to the 18th International Symposium on Transport Phenomena and Dynamics of Rotating Machinery.

[28] Sangan, C M, Pountney, O J, Zhou, K, Owen, J M, Wilson, M and Lock, G D. Experimental Measurements of Ingestion Through Turbine Rim Seals—Part II: Rotationally Induced Ingress. *Journal of Turbomachinery*, 135(2), 11 2012.

[29] Savov, S S, Atkins, N R and Uchida, S. A Comparison of Single and Double Lip Rim Seal Geometries. *Journal of Engineering for Gas Turbines and Power*, 139(11), 07 2017.

[30] Hamabe, K and Ishida, K. Rim Seal Experiments and Analysis of a Rotor-Stator System With Nonaxisymmetric Main Flow. volume Volume 1: Turbomachinery of *Turbo Expo: Power for Land, Sea, and Air*, 06 1992.

[31] Green, T and Turner, A B. Ingestion Into the Upstream Wheelspace of an Axial Turbine Stage. *Journal of Turbomachinery*, 116(2):327–332, 04 1994.

[32] Chew, J W, Green, T and Turner, A B. Rim Sealing of Rotor-Stator Wheelspaces in the Presence of External Flow. volume Volume 1: Turbomachinery of *Turbo Expo: Power for Land, Sea, and Air*, 06 1994.

[33] Bohn, D, Rudzinski, B, Sürken, N and Gärtner, W. Influence of Rim Seal Geometry on Hot Gas Ingestion Into the Upstream Cavity of an Axial Turbine Stage. volume Volume 3: Heat Transfer; Electric Power; Industrial and Cogeneration of *Turbo Expo: Power for Land, Sea, and Air*, 06 1999.

[34] Bohn, D, Rudzinski, B, Sürken, N and Gärtner, W. Experimental and Numerical Investigation of the Influence of Rotor Blades on Hot Gas Ingestion Into the Upstream Cavity of an Axial Turbine Stage. volume Volume 3: Heat Transfer; Electric Power; Industrial and Cogeneration of *Turbo Expo: Power for Land, Sea, and Air*, 05 2000.

[35] Hills, N J, Chew, J W and Turner, A B. Computational and Mathematical Modeling of Turbine Rim Seal Ingestion. *Journal of Turbomachinery*, 124(2):306–315, 04 2002.

[36] Gentilhomme, O, Hills, N J, Turner, A B and Chew, J W. Measurement and Analysis of Ingestion Through a Turbine Rim Seal. *Journal of Turbomachinery*, 125(3):505–512, 08 2003.

[37] Zlatinov, M B, Tan, C S, Little, D and Montgomery, M. Effect of purge flow swirl on hot-gas ingestion into turbine rim cavities. *Journal of Propulsion and Power*, 32(5):1055–1066, 2016.

[38] Owen, J M. Prediction of Ingestion Through Turbine Rim Seals—Part II: Externally Induced and Combined Ingress. *Journal of Turbomachinery*, 133(3), 11 2010.

[39] Sangan, C M, Pountney, O J, Zhou, K, Wilson, M, Owen, J M and Lock, G D. Experimental Measurements of Ingestion Through Turbine Rim Seals—Part I: Externally Induced Ingress. *Journal of Turbomachinery*, 135(2), 11 2012.

[40] Sangan, C M, Pountney, O J, Zhou, K, Wilson, M, Owen, J M and Lock, G D. Experimental Measurements of Ingestion Through Turbine Rim Seals—Part III: Single and Double Seals. *Journal of Turbomachinery*, 135(5), 06 2013.

[41] Bru Revert, A, Beard, P F, Chew, J W and Bottenheim, S. Performance of a Turbine Rim Seal Subject to Rotationally-Driven and Pressure-Driven Ingestion. In *Submitted to ASME Turbo Expo 2020: Power for Land, Sea and Air*, Turbo Expo: Power for Land, Sea, and Air. ASME, 2020.

[42] Roy, R P, Xu, G and Feng, J. A Study of Convective Heat Transfer in a Model Rotor–Stator Disk Cavity . *Journal of Turbomachinery*, 123(3):621–632, 03 2001.

[43] Smout, P D, Chew, J W and Childs, P R N. ICAS-GT: A European Collaborative Research Programme on Internal Cooling Air Systems for Gas Turbines. volume Volume 3: Turbo Expo 2002, Parts A and B of *Turbo Expo: Power for Land, Sea, and Air*, pages 907–914, 06 2002.

[44] Roy, R P, Feng, J, Narzary, D and Paolillo, R E. Experiment on Gas Ingestion Through Axial-Flow Turbine Rim Seals . *Journal of Engineering for Gas Turbines and Power*, 127(3):573–582, 06 2005.

[45] Jakoby, R, Zierer, T, Lindblad, K, Larsson, J, deVito, L, Bohn, D E, Funcke, J and Decker, A. Numerical Simulation of the Unsteady Flow Field in an Axial Gas Turbine Rim Seal Configuration. volume Volume 4: Turbo Expo 2004 of *Turbo Expo: Power for Land, Sea, and Air*, pages 431–440, 06 2004.

[46] Julien, S, Lefrancois, J, Dumas, G, Boutet-Blais, G, Lapointe, S, Caron, J F and Marini, R. Simulations of Flow Ingestion and Related Structures in a Turbine Disk Cavity. volume Volume 4: Heat Transfer, Parts A and B of *Turbo Expo: Power for Land, Sea, and Air*, pages 1071–1080, 06 2010.

[47] Schädler, R, Kalfas, A I, Abhari, R S, Schmid, G and Voelker, S. Modulation and Radial Migration of Turbine Hub Cavity Modes by the Rim Seal Purge Flow. *Journal of Turbomachinery*, 139(1), 09 2016.

[48] Horwood, J T M, Hualca, F P, Wilson, M, Scobie, J A, Sangan, C M and Lock, G D. Unsteady Computation of Ingress Through Turbine Rim Seals. volume Volume 5B: Heat Transfer of *Turbo Expo: Power for Land, Sea, and Air*, 06 2018.

[49] Chilla, M, Hodson, H and Newman, D. Unsteady Interaction Between Annulus and Turbine Rim Seal Flows. *Journal of Turbomachinery*, 135(5), 06 2013.

[50] Boudet, J, Hills, N J and Chew, J W. Numerical Simulation of the Flow Interaction Between Turbine Main Annulus and Disc Cavities. volume Volume 6: Turbomachinery, Parts A and B of *Turbo Expo: Power for Land, Sea, and Air*, pages 553–562, 05 2006.

[51] Queguineur, M, Gicquel, L Y M, and Staffleback, G. Modes Identification and Interactions in a Rotor-Stator Academic Cavity. In *Proceedings of 13th European Conference on Turbomachinery Fluid Dynamics and Thermodynamics ETC13*, 2019.

[52] Mirzamoghadam, A V, Heitland, G, Morris, M C, Smoke, J, Malak, M and Howe, J. 3D CFD Ingestion Evaluation of a High Pressure Turbine Rim Seal Disk Cavity. volume Volume 4: Heat Transfer, Parts A and B of *Turbo Expo: Power for Land, Sea, and Air*, pages 1443–1452, 06 2008.

[53] Horwood, J T M, Hualca, F P, Wilson, M, Scobie, J A, Sangan, C M, Lock, G D, Dahlqvist, J and Fridh, J. Flow Instabilities in Gas Turbine Chute Seals. *Journal of Engineering for Gas Turbines and Power*, 142(2), 01 2020.

[54] Boudet, J, Autef, V N D, Chew, J W and Hills, N J. Numerical simulation of rim seal flows in axial turbines. *The Aeronautical Journal*, 109:373–383, 2005.

[55] Zhou, D W, Roy, R P, Wang, C Z and Glahn, J A. Main Gas Ingestion in a Turbine Stage for Three Rim Cavity Configurations. *Journal of Turbomachinery*, 133(3), 12 2010.

[56] Mirzamoghadam, A V, Heitland, G and Hosseini, K M. The Effect of Annulus Performance Parameters on Rotor-Stator Cavity Sealing Flow. volume Volume 3: Heat Transfer, Parts A and B of *Turbo Expo: Power for Land, Sea, and Air*, pages 1163–1172, 06 2009.

[57] Paniagua, G, Dénos, R and Almeida, S. Effect of the Hub Endwall Cavity Flow on the Flow-Field of a Transonic High-Pressure Turbine . *Journal of Turbomachinery*, 126(4):578–586, 12 2004.

[58] Town, J, Averbach, M and Camci, C. Experimental and Numerical Investigation of Unsteady Structures Within the Rim Seal Cavity in the Presence of Purge Mass Flow. volume Volume 2B: Turbomachinery of *Turbo Expo: Power for Land, Sea, and Air*, 06 2016.

[59] Gao, F, Chew, J W, Beard, P F, Amirante, D and Hills, N J. Large-eddy simulation of unsteady turbine rim sealing flows. *International Journal of Heat and Fluid Flow*, 70:160 – 170, 2018.

[60] O'Mahoney, T S D, Hills, N J, Chew, J W and Scanlon, T. Large-Eddy Simulation of Rim Seal Ingestion. volume Volume 4: Heat Transfer, Parts A and B of *Turbo Expo: Power for Land, Sea, and Air*, pages 1155–1165, 06 2010.

[61] Rabs, M, Benra, F K, Dohmen, H J and Schneider, O. Investigation of Flow Instabilities Near the Rim Cavity of a 1.5 Stage Gas Turbine. volume Volume 3: Heat Transfer, Parts A and B of *Turbo Expo: Power for Land, Sea, and Air*, pages 1263–1272, 06 2009.

[62] Schuepbach, P, Abhari, R S, Rose, M G, Germain, T, Raab, I and Gier, J. Effects of Suction and Injection Purge-Flow on the Secondary Flow Structures of a High-Work Turbine. *Journal of Turbomachinery*, 132(2), 01 2010.

[63] O'Mahoney, T S D, Hills, N J and Chew, J W. Sensitivity of les results from turbine rim seals to changes in grid resolution and sector size. *Progress in Aerospace Sciences*, 52:48 – 55, 2012. Applied Computational Aerodynamics and High Performance Computing in the UK.

[64] Hualca, F P, Horwood, J T M, Sangan, C M, Lock, G D and Scobie, J A. The Effect of Vanes and Blades on Ingress in Gas Turbines. *Journal of Engineering for Gas Turbines and Power*, 142(2), 01 2020.

[65] McLean, C, Camci, C and Glezer, B. Mainstream Aerodynamic Effects Due to Wheelspace Coolant Injection in a High-Pressure Turbine Stage: Part I—Aerodynamic Measurements in the Stationary Frame . *Journal of Turbomachinery*, 123(4):687–696, 02 2001.

[66] McLean, C, Camci, C and Glezer, B. Mainstream Aerodynamic Effects Due to Wheelspace Coolant Injection in a High-Pressure Turbine Stage: Part II—Aerodynamic Measurements in the Rotational Frame . *Journal of Turbomachinery*, 123(4):697–703, 02 2001.

[67] Schrewe, S, Werschnik, H and Schiffer, H P. Experimental Analysis of the Interaction Between Rim Seal and Main Annulus Flow in a Low Pressure Two Stage Axial Turbine. *Journal of Turbomachinery*, 135(5), 06 2013.

[68] Patinios, M, Scobie, J A, Sangan, C M, Owen, M J and Lock, G D. Measurements and Modeling of Ingress in a New 1.5-Stage Turbine Research Facility. *Journal of Engineering for Gas Turbines and Power*, 139(1), 08 2016.

[69] Johnson, B V, Jakoby, R, Bohn, D E and Cunat, D. A Method for Estimating the Influence of Time-Dependent Vane and Blade Pressure Fields on Turbine Rim Seal Ingestion. *Journal of Turbomachinery*, 131(2), 01 2009.

[70] Patinios, M, Ong, I L, Scobie, J A, Lock, G D and Sangan, C M. Influence of Leakage Flows on Hot Gas Ingress. *Journal of Engineering for Gas Turbines and Power*, 141(2), 09 2018.

[71] Scobie, J A, Sangan, C M, Teuber, R, Pountney, O J, Owen, J M, Wilson, M and Lock, G D. Experimental Measurements of Ingestion Through Turbine Rim Seals: Part 4 — Off-Design Conditions. volume Volume 3A: Heat Transfer of *Turbo Expo: Power for Land, Sea, and Air*, 06 2013.

[72] Ainsworth, R W, Schultz, D L, Davies, M R D, Forth, C J P, Hilditch, M A, Oldfield, M L G and Sheard, A G. A Transient Flow Facility for the Study of the Thermofluid-Dynamics of a Full Stage Turbine Under Engine Representative Conditions. volume Volume 4: Heat Transfer; Electric Power; Industrial and Cogeneration of *Turbo Expo: Power for Land, Sea, and Air*, 06 1988.

[73] Atkins, N R. *Aerodynamic Performance Measurements in a Transient Turbine Test Facility*. PhD thesis, University of Oxford, 2005.

[74] Roy, R P, Zhou, D W, Ganesan, S, Wang, C Z, Paolillo, R E and Johnson, B V. The Flow Field and Main Gas Ingestion in a Rotor-Stator Cavity. volume Volume 4: Turbo Expo 2007, Parts A and B of *Turbo Expo: Power for Land, Sea, and Air*, pages 1189–1198, 05 2007.

[75] McGreehan, W F, Haaser, F G and Sherwood, L T. Labyrinth Seal Flow Measurement by Tracer Gas Injection. volume Volume 1: Turbomachinery of *Turbo Expo: Power for Land, Sea, and Air*, 05 1987.

[76] Clark, K, Barringer, M, Thole, K, Clum, C, Hiester, P, Memory, C and Robak, C. Effects of Purge Jet Momentum on Sealing Effectiveness. *Journal of Engineering for Gas Turbines and Power*, 139(3), 10 2016.

[77] Savov, S S and Atkins, N R. A Rim Seal Ingress Model Based on Turbulent Transport. volume Volume 5B: Heat Transfer of *Turbo Expo: Power for Land, Sea, and Air*, 06 2017.

[78] Palermo, D M, Gao, F, Chew, J W and Beard, P F. Effect of Annulus Flow Conditions on Turbine Rim Seal Ingestion. volume Volume 5B: Heat Transfer of *Turbo Expo: Power for Land, Sea, and Air*, 06 2019.

[79] Gentilhomme, O J P. *Turbine rim seal ingestion*. PhD thesis, University of Sussex, 2004.